pharmaceutics

MDPI

Article

Silibinin-Loaded Liposomes: The Influence of Modifications on Physicochemical Characteristics, Stability, and Bioactivity Associated with Dermal Application

Amjed Abdullah Karkad [1,2], Andrea Pirković [3], Milena Milošević [4], Bojan Stojadinović [5], Katarina Šavikin [6], Aleksandar Marinković [1] and Aleksandra A. Jovanović [3,*]

[1] Faculty of Technology and Metallurgy, University of Belgrade, 11000 Belgrade, Serbia; marinko@tmf.bg.ac.rs (A.M.); 20214044@estudent.tmf.bg.ac.rs (A.A.K.)
[2] Faculty of Medical Technology, Elmergib University, Msallata 7310500, Libya
[3] Institute for the Application of Nuclear Energy INEP, University of Belgrade, 11080 Belgrade, Serbia; andrea.pirkovic@inep.co.rs
[4] Institute of Chemistry, Technology and Metallurgy—National Institute of the Republic of Serbia, University of Belgrade, 11000 Belgrade, Serbia; milena.milosevic@ihtm.bg.ac.rs
[5] Institute of Physics Belgrade, University of Belgrade, 11080 Belgrade, Serbia; bojans@ipb.ac.rs
[6] Institute for Medicinal Plants Research "Dr Josif Pančić", 11000 Belgrade, Serbia; ksavikin@mocbilja.rs
* Correspondence: ajovanovic@inep.co.rs; Tel.: +381-64-148-1978

Abstract: Background/Objectives: The aims of the presented study were the development of four types of silibinin-loaded liposomes (multilamellar liposomes—MLVs, sonicated small unilamellar liposomes—SUVs, UV-irradiated liposomes, and lyophilized liposomes) and their physicochemical characterization and biological potential related to skin health benefits. Methods: The characterization was performed via the determination of the encapsulation efficiency (EE), particle size, polydispersity index, zeta potential, conductivity, mobility, storage stability, density, surface tension, viscosity, FT-IR, and Raman spectra. In addition, cytotoxicity on the keratinocytes and antioxidant and anti-inflammatory potential were also determined. Results: UV irradiation significantly changed the rheological and chemical properties of the liposomes and increased their cytotoxic effect. The lyophilization of the liposomes caused significant changes in their EE and physical characteristics, decreased their ABTS and DPPH radical scavenging potential, and increased their potential to reduce the expression of interleukin 1 beta (IL-1β) in cells treated with bacterial lipopolysaccharide. Sonication significantly changed the EE and physical and rheological properties of the liposomes, and slightly increased their cytotoxicity and reduction effect on IL-1β, while the anti-ABTS and anti-DPPH capacity of the liposomes significantly increased. All developed liposomes showed an increasing trend in particle size and a decreasing trend in zeta potential (absolute values) during storage. Conclusions: Silibinin-loaded liposomes (MLVs and lyophilized) showed promising antioxidant activity (toward reactive oxygen species generated in cells) and anti-inflammatory effects (reducing macrophage inhibitory factor expression) on keratinocytes and did not lead to a change in their viability. Future perspectives will focus on wound healing, anti-aging, and other potential of developed liposomes with silibinin in sophisticated cell-based models of skin diseases, wounds, and aging.

Keywords: anti-inflammatory activity; antioxidant activity; encapsulation; liposomes; silibinin; skin; stability

check for updates

Citation: Karkad, A.A.; Pirković, A.; Milošević, M.; Stojadinović, B.; Šavikin, K.; Marinković, A.; Jovanović, A.A. Silibinin-Loaded Liposomes: The Influence of Modifications on Physicochemical Characteristics, Stability, and Bioactivity Associated with Dermal Application. *Pharmaceutics* **2024**, *16*, 1476. https://doi.org/10.3390/pharmaceutics16111476

Received: 24 October 2024
Revised: 8 November 2024
Accepted: 15 November 2024
Published: 19 November 2024

1. Introduction

Products from plant material are of great interest to researchers, not only as a source of new biologically active ingredients for use in the pharmaceutical and cosmetic industries but also as a valuable addition to the formulations for improving the aesthetic properties of wounds, burns, scars, and skin as a whole [1,2]. Silibinin, the flavonolignan compound, is the major active constituent of silymarin, a group of polyphenols from milk thistle (*Silybum marianum*), which, apart from silibinin, contains isosilybin, silydianin, and silychristand [3]. Silibinin is also found in artichokes (*Cynara scolymus*) [4]. Due to their antioxidant, antimicrobial, anti-inflammatory [3,5], antiviral [6], immunomodulatory [7], and anticancer potential [8], the mentioned polyphenols exhibit plenty of bioactivities that can promote human health and wellbeing. Silibinin was used as a chemo-preventive and therapeutic agent in human lung cancer [9], while studies have reported that it also showed significant chemo-preventive activity in animal models of carcinogenesis, including prostate and skin cancer [4,10]. According to the Song et al. study [11], silibinin can also protect liver cells against toxins, while García-Viñuales et al. [12] suggest that it can inhibit amyloid-beta aggregation by affecting the human islet amyloid polypeptide. The study of Matsumura and Ananthaswamy [13] shows a protective effect of silibinin against ultraviolet B-induced skin injuries. Namely, silibinin protects from photo-carcinogenesis, sunburns, UVB-caused epidermal hyperplasia, and deoxyribonucleic acid damage, and changes cell cycle regulation in favor of maintaining the genetic integrity of the skin cells [4,5]. However, its application is quite limited due to its poor water solubility, limited absorption, and consequently, low bioavailability [14]. Thus, silibinin requires encapsulation for further application with the aim of its enhanced bioavailability.

The encapsulation of biologically active components represents a technique that has been widely used in the food, pharmaceutical, and cosmetic industries to strengthen and supplement formulations by enhancing stability and bioavailability and controlling the delivery of active compounds [3,15–17]. Liposomes, as spherical micro- or nanoparticles formed by one or multiple phospholipid layers, are widely used as carriers for delivering drugs, antioxidants, proteins, enzymes, polyphenols, vitamins, flavors, and aromas, due to their non-toxicity, biodegradability, and ability to encapsulate hydrophilic, amphiphilic, and lipophilic compounds [16,18–21]. Liposomes can provide a controlled release of biologically active compounds, as well as aiding their protection from modification and degradation caused by light, oxygen, UV irradiation, free radicals, enzymes, changes in pH values, etc. [3,16]. Additionally, several studies have shown that liposomes provide a higher bioavailability of various compounds, including drugs, proteins, nutraceuticals, and polyphenols, due to their lipid composition being similar to that of epithelial cells [22–25]. The liposomal particles can be formulated using the common thin film hydration procedure, micro-emulsification, membrane extrusion, proliposome method, ether or ethanol injection, a reverse phase evaporation method, etc. [16,19,26]. Among all the previously mentioned techniques, the proliposome technology may be suitable for large-scale production [19]. Additionally, the sonication and cavitation effects can increase the dispersion of lipid molecules, consequently, reducing the particle size of the lipid droplets; thus, the mentioned process is widely employed for obtaining small unilamellar liposomes [26–28]. Liposomal vesicle size displays an important influence on the delivery and penetration of encapsulated compounds through the skin, as well as the efficiency of the applied formulation [29]; thus, that was one of the criteria for choosing modification methods during liposome development. Since UV irradiation is used in the food, pharmaceutical, and cosmetic industries as a sterilization technique, and can enhance the release of active compounds from the liposomes and cause changes in the physicochemical properties of the liposomes, its influence should be investigated as well [30]. Also, the potential application of silibinin-loaded liposomes for the dermal and transdermal delivery of silibinin and, consequently, exposure of the formulation to UV rays from the sun, significantly affected the selection of this specific liposome modification technique. Lyophilization (freeze drying), as a simple and frequently employed procedure for drying thermosensitive components, uses freezing and low pressure with the addition of heat (only to cause the sublimation of ice) and can be applied to liposomal vesicles. Namely, the obtained lyophilized products with active compounds (e.g., polyphenols) are stable over a long period, due to the prevention of hydrolytic and oxidative degradation, which can occur in the surrounding water [26,31,32]. Considering that liposomal formulation can contain between 70 and 95% of the water phase, hydrolytic and oxidative reactions, as well as microbiological contamination (which occurs in an aqueous medium), are frequent causes of products' degradation and spoilage and their short shelf life. With the aim to improve storage stability and provide prolonged shelf life of the liposomal preparations, freeze drying can be used as a simple preservation procedure. However, the lyophilization process can result in significant modifications of the liposomal particles; thus, its effect should be examined as well. Hence, due to all mentioned above related to lyophilization, this process was selected as one of the methods that could potentially have positive or negative impacts on liposome characteristics and bioactivities.

Therefore, the present study aimed to develop silibinin-loaded liposomes using the proliposome procedure, as well as additional steps for liposome modification (sonication by the ultrasound probe, UV irradiation, or lyophilization): multilamellar vesicles (MLVs), sonicated small unilamellar vesicles (SUVs), UV-irradiated liposomes, and lyophilized liposomes, respectively. The encapsulation efficiency (EE), particle size, polydispersity index (PDI), zeta potential, conductivity, mobility, storage stability, density, surface tension, viscosity, FT-IR (Fourier Transform Infrared) and Raman spectra, cytotoxicity, antioxidant and anti-inflammatory activity of the obtained liposomes were investigated. To the best of our knowledge, the influence of all previously mentioned processes on physicochemical characteristics, stability, and bioactivity associated with the dermal application of silibinin-loaded liposomes was not investigated. Specifically, the influence of UV irradiation (present during the production process and dermal application) and sonication or lyophilization (widely employed in industrial conditions) on the cytotoxic, antioxidant, and anti-inflammatory potential of silibinin-loaded liposomes on keratinocytes, the liposome stability, and fingerprint spectra were examined for the first time in the present study.

2. Materials and Methods

2.1. Reagents

Distilled water was purified through a Simplicity UV® water purification system (Merck Millipore, Merck KGaA, Darmstadt, Germany). Phospholipon 90G (Ph, phosphatidylcholine from soybean) was from Nattermann Phospholipids (Cologne-Bocklemünd, Germany) and ethanol was from Thermo Fisher Scientific (Loughborough, UK), while silibinin (≥98%, HPLC grade), 2,2′-azino-*bis* (3-ethylbenzothiazoline-6-sulphonic acid) or ABTS, ascorbic acid, and 2,2-diphenyl-1-picrylhydrazyl or DPPH were from Sigma Aldrich (Steinheim, Germany). HaCaT cells (spontaneously immortalized human keratinocytes) were kindly provided by the Institute for Biological Research "Siniša Stanković", National Institute of the Republic of Serbia, University of Belgrade, Belgrade, Serbia. Bacterial lipopolysaccharide (LPS; *Escherichia coli* 055:B5), phosphate-buffered saline (PBS), sodium dodecyl sulfate (SDS), and MTT reagent (thiazolyl blue tetrazolium bromide, 1 mg/mL) were from Sigma-Aldrich (St. Louis, MA, USA) and DMEM/F12 cell culture medium (1:1 mixture of Dulbecco's Modified Eagle's Medium and Ham's F-12 nutrient mixture) was from Pan-Biotech (Aidenbach, Germany), while 0.5% Tween was from Thermo Fisher Scientific (Waltham, MA, USA). Cells were maintained in RPMI 1640 (GIBCO BRL, Thermo Fisher Scientific, Waltham, MA, USA) supplemented with 10% fetal bovine serum (FBS) and containing 1% antibiotic–antimycotic mixture (Capricorn Scientific, Ebsdorfergrund, Germany), hereafter referred to as complete medium. Cell-permeable oxidation-sensitive probe-H2DCFDA (2′,7′-dichlorofluorescin diacetate-Calbiochem) was from Merck Millipore, Darmstadt, Germany. Dulbecco's Modified Eagle Medium/Nutrient Mixture F-12 Ham (DMEM F 12, Biowest, Nuaillé, France), 10% fetal calf serum (FCS, Gibco, Waltham, MA, USA), and 0.25% trypsin-EDTA solution (Institute for Virology, Vaccines, and Serum "Torlak", Belgrade, Serbia) were also used.

2.2. Cell Culture

HaCaT human keratinocytes were kept in 25 cm^2 tissue culture flasks in a humidified incubator at 37 °C, with 5% CO_2. They were grown in a complete medium containing DMEM F 12, 10% fetal calf serum, and 1% antibiotic–antimycotic solution. After reaching

70% confluence, the cells were trypsinized (0.25% trypsin-EDTA solution) and seeded in 96-well plates (1.5×10^4 cells/well). They were left to attach to wells for 24 h at 37 °C, 5% CO_2, before the treatment.

2.3. Preparation of the Liposomes

Silibinin-loaded liposomes as multilamellar vesicles (MLVs) were prepared using the proliposome method according to Jovanović et al. [33]. Specifically, a mixture of 10 g of phospholipids, 1 g of silibinin, and 40 mL of ethanol was stirred and heated to 50–60 °C for 15 min. After cooling to 25 °C, 80 mL of ultrapure water was added in small portions. Subsequently, the mixture was stirred for 1 h at 800 rpm. Plain (empty) liposomes (MLVs) were prepared as a control using 2.5 g of phospholipids, 10 mL of ethanol, and 20 mL of ultrapure water. Due to the complete evaporation of ethanol (from loaded and unloaded liposomes), the concentration of phospholipids in a final formulation was 125 mg/mL.

2.3.1. Sonication of the Liposomes

With the aim to reduce vesicle size and obtain SUVs, the samples (MLVs, 20 mL) were sonicated for 15 min (on 30 s-off 10 s) using the ultrasound probe Sonopuls (Bandelin, Berlin, Germany) at 40% amplitude and 25 °C (a flask with the sample was continuously cooled using ice coating during sonication and the temperature was measured and controlled) [28].

2.3.2. UV Irradiation of the Liposomes

The liposomal sample (MLVs, 20 mL) in a thin layer was exposed to UV-C irradiation (253.7 nm) for 15–90 min in uncovered Petri dishes using a laminar flow cabinet (AC2-4G8, ESCo, Singapore) [30,34].

2.3.3. Lyophilization of the Liposomes

The influence of lyophilization on liposomes was investigated as well. Freshly prepared silibinin-loaded liposomes and empty liposomes (MLVs, 10 mL) were centrifuged, the supernatant was discarded, and the pellet was frozen in the freezer at −80 °C for 1 h and freeze dried at −75 °C and pressure of 0.011 mbar for 24 h and at −65 °C and pressure of 0.054 mbar for one additional hour (Alpha 2–4 LSCplus, Christ, Osterode am Harz, Germany). The lyophilized liposomes were then reconstructed with ultrapure water to their original volume before further analysis of encapsulation efficiency, photon correlation spectroscopy, antioxidant methods, and assays in the cell culture. For FTIR and Raman spectroscopy, UV-irradiated liposomes and SUVs with silibinin were lyophilized in the same way, as were empty and loaded MLVs, to obtain appropriate samples for analysis.

2.4. Determination of the Encapsulation Efficiency

The EE was determined using an indirect method and calculated by the amount of silibinin in the supernatant, as shown in Equation (1):

$$\mathrm{EE}\ [\%] = (C_i - C_{sup})/C_i \times 100 \quad (1)$$

where C_i is the initial content of silibinin used for the preparation of liposomes and C_{sup} is the content of silibinin determined in the supernatant.

The free silibinin was removed from the liposome dispersions (MLVs, UV-irradiated, and lyophilized samples) by centrifugation at 17,500 rpm and 4 °C for 45 min in Thermo Scientific Sorval WX Ultra series ultracentrifuge (Thermo Fisher Scientific, Waltham, MA, USA). The free silibinin was removed from SUVs' dispersion using ultracentrifugation at 10,000 rpm and 4 °C for 5 h (Optima L-90K Ultracentrifuge, Beckman Coulter, Brea, CA, USA). The concentration of silibinin in the supernatants was determined spectrophotometrically at 280 nm (UV Spectrophotometer UV-1800, Shimadzu, Kyoto, Japan).

2.5. Photon Correlation Spectroscopy and Storage Stability

The mean size, PDI, zeta potential, conductivity, and mobility of liposomal droplets (MLVs, SUVs, UV-irradiated, and lyophilized samples with silibinin and unloaded MLVs) were measured by photon correlation spectroscopy (PCS). Zetasizer Nano Series, Nano ZS (Malvern Instruments Ltd., Malvern, UK) with the measurement range of 0.6 nm to 6 mm used for the measurement of all the above-mentioned parameters. The analyses were performed at 25 °C, and each sample was diluted 200 times with ultrapure water. Each sample was measured three times, and the results obtained were given as the mean value. The conductivity values are presented as the conductivity factor (1 CF = 10 μS/cm).

All previously mentioned parameters of the silibinin-loaded liposomes (MLVs, SUVs, UV-irradiated, and lyophilized samples) were monitored for 60 days of storage at 4 °C. The measurements were repeated on the 1st, 7th, 14th, 21st, 28th, and 60th days using PCS. During the stability study, lyophilized samples were stored in their dried form and reconstituted before every measurement.

2.6. Density, Surface Tension, and Viscosity Analyses

The density and surface tension of three types of silibinin-loaded liposomes (MLVs, SUVs, and UV-irradiated samples) were determined using silicon crystal as the immersion body and Wilhelmy plate, respectively, in Force Tensiometer K20 (KRÜSS, Hamburg, Germany). Each sample (20 mL) was examined three times at 25 °C. The viscosity of the same silibinin-loaded liposomes was also examined using Rotavisc lo-vi device equipment with VOL-C-RTD chamber, VOLS-1 adapter, and spindle (IKA, Staufen, Germany). Each sample (6.7 mL) was examined three times at 25 °C.

2.7. FT-IR and Raman Spectroscopy

FT-IR spectra of pure Phospholipon, UV-irradiated Phospholipon, silibinin, and lyophilized MLVs, SUVs, and UV-irradiated samples (since the used spectrometer requires the samples without water) were recorded in the wavenumber between 400 and 4000 cm^{-1} using Nicolet™iS™10spectrometer (Thermo Fisher Scientific, Waltham, MA, USA) with Smart iTR™ Attenuated Total Reflectance (ATR), in 20 scans mode, and at a resolution of 4 cm^{-1}. The liposomes were exposed to UV irradiation for 15, 30, 45, 60, 75, and 90 min to detect the duration of the irradiation, which caused the chemical changes in the samples. Additionally, deconvolution of the FT-IR spectra, as a means of more powerful detection with the aim to identify changes in bonding, was performed as well.

The micro-Raman spectra of pure Phospholipon, silibinin, and lyophilized MLVs, SUVs, and UV-irradiated liposomes were collected in a backscattering configuration using a Jobin-Yvon T64000 triple spectrometer equipped with a liquid-nitrogen-cooled CCD camera. Raman scattering spectra were recorded in the range of 150–3400 cm^{-1}. The spectral resolution was 2 cm^{-1} and accuracy for all measured wavenumbers is ±3 cm^{-1}. The argon/krypton ion laser with an emitting line at λ = 514.5 nm was used as an excitation source, with the output laser power kept at less than 1 mW to avoid the heating effects and/or sample degradation.

2.8. Antioxidant Capacity of the Liposomes

The antioxidant capacity of all prepared liposomal samples was examined using two antioxidant assays, ABTS and DPPH tests. In addition, the antioxidant potential of the liposomes was investigated in the cell line with generated intracellular free radicals (described in Section 2.9.3).

2.8.1. ABTS Assay

The ABTS radical scavenging potential of silibinin-loaded liposomes was determined using the assay described by Zuhair et al. [35] with a slight modification. The mixture of ABTS solution (5 mL of water and 0.019 g of ABTS powder) and potassium persulfate solution (88 μL) was left to react for 24 h at 4 °C. The ABTS$^{\bullet+}$ working solution was diluted using ethanol (an absorbance of ~0.700 at 734 nm). The $ABTS^{\bullet+}$ solution (2 mL) was mixed with the liposomes (20 µL). After 6 min of incubation, the absorbance was measured, and the radical scavenging activity of the extract was calculated using the following equation (Equation (2)):

$$\Delta A = A_0 - A_x \tag{2}$$

where A_0 is the absorbance of the $ABTS^{\bullet+}$ solution, while A_x is the absorbance of the $ABTS^{\bullet+}$ solution and the liposomes. The scavenging capacity was expressed as IC_{50} (mg of silibinin/mL of liposomal suspension), which represented the concentration required to neutralize 50% of $ABTS^{\bullet+}$ radicals. Ascorbic acid was used as a positive control.

2.8.2. DPPH Assay

The antioxidant capacity of the liposomal samples was measured via hydrogen donating using the stable $DPPH^{\bullet}$ radicals [35]. Various concentrations of the liposomes (200 µL) were mixed with 2 mL of ethanol $DPPH^{\bullet}$ radical solution (an absorbance of ~0.800 at 517 nm). The absorbance was recorded after 20 min of incubation and the percentage of inhibition was calculated using the following equation (Equation (3)):

$$\%\ \text{inhibition} = (A_0 - A_x) \times 100/A_0 \tag{3}$$

where A_0 is the absorbance of the control and A_x is the absorbance of the $DPPH^{\bullet}$ solution and the liposomes. The results were expressed as IC_{50} (mg of silibinin/mL of liposomal suspension), which represented the concentration required to neutralize 50% of $DPPH^{\bullet}$ radicals. Ascorbic acid was used as a positive control.

2.9. Assays on Cell Culture

2.9.1. Treatments Preparation

The stock solution of liposomes with silibinin (MLVs, SUVs, UV-irradiated, and lyophilized samples with silibinin and unloaded MLVs) was prepared, at a concentration of 10 mg/mL and kept at 4 °C. For the experiment, final concentrations of each treatment were prepared from the stock solution by dissolving in fresh complete cell medium to reach final concentrations of 0.1, 1, 10, 25, 50, and 100 µg/mL. These concentrations were further used for cell treatments.

2.9.2. Cytotoxicity Evaluation

The HaCaT cells in complete RPMI medium were seeded in 96-well plates at a density of 1.5×10^4 cells/well, in a final volume of 100 µL per well. The medium was exchanged after 24 h, and treatments were added in a total volume of 100 µL/well. Following the incubation with the treatments (empty MLVs and silibinin-loaded liposomes) or solvent (control) at 37 °C for 24 h, an MTT assay was performed. MTT reagent was added (10 µL per well), and the cells were left for 2 h in the dark at 37 °C for the reaction to occur. Further, purple formazan crystals were dissolved with SDS [36]. Finally, the absorbance was measured at 570 nm on a microplate reader (Epoch, BioTek, Shoreline, WA, USA) after the complete solubilization of the crystals. The data were expressed as percentage viability concerning control (100%). Mean values were represented on bars, from three independent experiments performed in triplicate (n = 9).

2.9.3. H2DCFDA Assay (2′,7′-Dichlorofluorescin Diacetate)

HaCaT cells were left overnight to attach to the wells and kept in a humified incubator at 5% CO_2 and 37 °C. The next day, the medium was exchanged and silibinin-loaded liposomes (MLVs, SUVs, UV-irradiated, and lyophilized samples) or empty MLVs at final concentrations (0.1, 1, 10, 25, 50, and 100 µg/mL) in complete medium were added to the cells (100 µL per well). After 24 h, treatments were removed, and cells were rinsed with PBS. Next, the assay was performed in line with the manufacturer’s instructions [37].

Using PBS as the diluent, 5 μM of the cell-permeable oxidation-sensitive probe, H2DCFDA was added to the cells and left for 45 min in the dark. Next, the cells were washed with PBS and exposed to PBS alone (control) or the 200 μM H_2O_2, used as the positive control. After an incubation time of 2 h, and the conversion of non-fluorescent H2DCFDA to the highly fluorescent 2′,7′-dichlorofluorescein (DCF), the generation of intracellular ROS (reactive oxygen species) level in cells was determined by measuring the fluorescence on a fluorescent plate reader (Wallac 1420 multilabel counter Victor 3V, PerkinElmer Life and Analytical Sciences, Boston, MA, USA) at excitation and emission wavelengths of 485 and 535 nm, respectively. Data were expressed as relative fluorescence intensity and the mean value was represented in figures, from three independent experiments performed in triplicate (n = 9).

2.9.4. Determination of Protein Expression Using the CELISA (CELL-BASED ELISA) Method

Analysis of the anti-inflammatory potential of the obtained liposomal samples was performed using cell-based ELISA according to the previously described method [38]. Namely, HaCaT cells were seeded in 96-well plates at a density of 2×10^5 cells per well and grown for 24 h at 37 °C and 5% CO_2. The following day, the medium was replaced with treatments containing MLVs, SUVs, UV-irradiated, and lyophilized samples or empty MLVs at a final concentration of 10 μg/mL in a complete medium and incubated for 24 h with the cells. At the end of the treatment, the medium was removed, and the cells were exposed to 2.5 μg/mL of LPS in a complete medium for 4 h at 37 °C and 5% CO_2. Afterwards, cells were washed twice with PBS and the plate was dried. After drying, the cells were fixed with ice-cold acetone-methanol (1:1) for 10 min. Next, endogenous peroxidases were blocked by adding 0.3% H_2O_2, 100 μL per well for 30 min in the dark. Then, the wells were washed with PBS and blocked with the addition of 1% BSA in PBS for 30 min at 37 °C. After blocking, 50 μL of each primary antibody (PA5-27238, source: rabbit, 1:500, Invitrogen, Waltham, MA, USA) for interleukin 1 beta (IL-1β), macrophage inhibitory factor (MIF), or cyclooxygenase-2 (COX-2) was added in PBS with 1% BSA to the wells and incubated 2 h at room temperature. Following the incubation with antibodies, the plate was washed three times with PBS containing 0.5% Tween, and a secondary antibody (1:2000, anti-rabbit IgG, HRP-linked Antibody 7074P2, Cell Signaling Technology, Danvers, MA, USA; or 1:2000, anti-mouse IgG, HRP-linked Antibody 7076S, Cell Signaling Technology, Danvers, MA, USA) in PBS with 1% BSA was added to the wells and incubation lasted 2 h at room temperature. Finally, the plate was washed three times with PBS, 50 μL of substrate was added to each well, and color development was monitored. When the color developed, 50 μL of the stop reagent was added and the plate was read at 450 nm wavelength on a plate reader (ELx800, BioTek, Shoreline, WA, USA).

2.10. Statistical Analysis

All measurements and analyses were performed in triplicate and statistical analyses were carried out using the statistical software STATISTICA 7.0. The statistical significance was determined using analysis of variance (one-way ANOVA), followed by Duncan's *post hoc* test. The data in the table and graphs are presented as mean value ± standard deviation. The differences were considered statistically significant at $p < 0.05$.

In the cell assays, one-way analysis of variance (ANOVA) with the Tukey *post hoc* test was used to assess differences in treatments *versus* control after data were tested for normality. All results are expressed as mean ± standard error of the mean (mean ± SEM). GraphPad Prism 6.0 (GraphPad Software, Inc., La Jolla, CA, USA) was used for statistical analysis, where $p < 0.05$ was considered significant.

3. Results

The first step of the present research was the formulation of silibinin-loaded liposomes and the investigation of the influence of sonication, UV irradiation, and lyophilization on liposome physicochemical properties, including the EE, particle size, PDI, zeta potential, conductivity, mobility, and storage stability. In the case of liquid samples, density, surface tension, and viscosity were also measured. The second step was the analysis of FT-IR and Raman spectra. The third step was the examination of the biological activity of all developed silibinin-loaded liposomes, including their antioxidant, cytotoxic, and anti-inflammatory potential.

3.1. Encapsulation Efficiency in the Silibinin-Loaded Liposomes

Regarding the fact that the efficiency of the encapsulation process, i.e., the amount of the encapsulated target compounds, represents one of the essential parameters, the EE of silibinin in four prepared liposomal systems is shown in Table 1.

Table 1. The encapsulation efficiency (EE), particle size, polydispersity index (PDI), zeta potential (ζ), conductivity (presented as the conductivity factor, CF), and mobility (μ) of multilamellar liposomes (MLVs), UV-irradiated liposomes, lyophilized liposomes, and small unilamellar liposomes (SUVs) with encapsulated silibinin, and unloaded MLVs.

Samples	EE [%]	Particle Size [nm]	PDI	ζ [mV]	CF	*μ* [μmcm/Vs]
MLVs with silibinin	$89.7 \pm 1.4^{\text{a},*}$	$1675.0 \pm 44.3^{\text{a}}$	$0.310 \pm 0.019^{\text{b}}$	$-35.5 \pm 0.7^{\text{a}}$	$0.38 \pm 0.01^{\text{d}}$	$-2.78 \pm 0.02^{\text{a}}$
UV-irradiated with silibinin	$88.1 \pm 1.2^{\text{a}}$	$1701.5 \pm 58.7^{\text{a}}$	$0.272 \pm 0.034^{\text{b}}$	$-36.5 \pm 0.7^{\text{a}}$	$1.15 \pm 0.02^{\text{b}}$	$-2.89 \pm 0.07^{\text{a}}$
Lyophilized with silibinin	$62.5 \pm 1.9^{\text{c}}$	$724.9 \pm 27.5^{\text{c}}$	$0.334 \pm 0.031^{\text{b}}$	$-14.9 \pm 0.5^{\text{c}}$	$2.64 \pm 0.30^{\text{a}}$	$-0.70 \pm 0.06^{\text{c}}$
SUVs with silibinin	$74.9 \pm 1.0^{\text{b}}$	$277.8 \pm 2.7^{\text{d}}$	$0.520 \pm 0.059^{\text{a}}$	$-21.6 \pm 0.1^{\text{b}}$	$1.24 \pm 0.08^{\text{c}}$	$-1.58 \pm 0.04^{\text{b}}$
Unloaded MLVs	n.a.	$1435.8 \pm 22.1^{\text{b}}$	$0.287 \pm 0.022^{\text{b}}$	$-10.3 \pm 0.4^{\text{d}}$	$0.32 \pm 0.02^{\text{e}}$	$-0.51 \pm 0.03^{\text{d}}$

* Values with the same letter in each column showed no statistically significant difference between different developed liposomes with silibinin ($p > 0.05$; n = 3; analysis of variance, Duncan's *post hoc* test); 1 CF = 10 μS/cm; n.a., not applicable.

The EE of silibinin in MLVs amounted to 89.7 ± 1.4% and UV irradiation did not significantly influence the mentioned parameter (88.1 ± 1.2%) (Table 1). SUVs with silibinin showed a significantly lower value of EE (74.9 ± 1.0%) in comparison to larger particles but a significantly higher value compared to lyophilized liposomes, whose EE was 62.5 ± 1.9% (Table 1).

3.2. The Particle Size, PDI, Zeta Potential, Conductivity, and Mobility of the Silibinin-Loaded Liposomes

Since the average size of liposomal particles represents an essential and relevant parameter for liposome biodistribution and the release of the encapsulated compounds [20], the measurement of the mentioned variable was performed (Table 1). The average size of the MLVs was 1675.0 ± 44.3 nm. UV irradiation did not affect the vesicle size of silibinin-loaded liposomes, 1701.5 ± 58.7 nm, while sonication caused a significant decrease in the vesicle size, 277.5 ± 10.0 nm. The size of lyophilized liposomes was 724.9 ± 27.5 nm, showing that the lyophilization process led to a diameter decrease. The PDI values for MLVs, UV-irradiated, and lyophilized samples amounted to ~0.3 (Table 1). The highest PDI value, i.e., a narrow range of particle size distribution, was recorded for the SUVs (0.520 ± 0.059) which can mean the presence of MLVs along with SUVs. The zeta potential of the liposomes was measured as the third physical characteristic (Table 1). The zeta potential is used for the determination of the electrical charge present on the surface of the liposomal membrane and all developed liposomes have negative values of zeta potential, demonstrating that the liposome surfaces were negatively charged. The zeta potential of MLVs and their UV-irradiated parallels did not significantly differ and amounted to −35.5 ± 0.7 and −36.5 ± 0.7 mV, respectively. On the other hand, lyophilization and sonication significantly changed the values of liposome zeta potential (−14.9 ± 0.5 and −21.6 ± 0.1 mV, respectively). The conductivity of the liposomes was determined using PCS as well (Table 1). The conductivity factor of the MLVs, UV-irradiated, lyophilized, and SUVs liposomes with silibinin immediately after the preparation was 0.38 ± 0.01, 1.15 ± 0.02, 2.64 ± 0.30, and 1.24 ± 0.08, respectively. The mobility of all four developed liposomal formulations was determined as the fifth physical property (Table 1). The mobility of the MLVs, UV-irradiated, lyophilized, and SUVs liposomes with silibinin immediately after the formulation was −2.78 ± 0.05, −2.89 ± 0.07, −0.70 ± 0.06, and −1.58 ± 0.04 µmcm/Vs, respectively.

3.3. Storage Stability of the Silibinin-Loaded Liposomes

One of the most important challenges in the application of liposomal systems within food, functional food, supplements, pharmaceutical, and cosmetic products is their relative physical and chemical instability in water dispersions and under environmental conditions due to their lipid composition, which can lead to unwanted effects, including oxidation and hydrolysis and a reduction in encapsulation efficiency [39,40]. According to the literature data, their physicochemical instability resulted in membrane combination, aggregation, and changes in particle size, rigidity, and membrane compounds, as well as a decrease in encapsulation efficiency [40,41]. Therefore, the storage stability of the developed liposomes was monitored for 60 days at 4 °C, and the results are presented graphically in Figure 1.

The instability of the liposomes can be attributed to the physical collision of the vesicles and membrane fusion, as well as chemical interactions, lipid oxidation, and production of aldehydes. The higher stability of the liposomes at the temperature of 4 °C was due to the permeability and less flexibility of their membranes, consequently causing lower mobility of phospholipids, and the delayed oxidative process of the unsaturated fatty acids and decomposition of the liposomes [42,43]. However, a significant increase in particle size was noticed in all liposomes with encapsulated silibinin during a 60-day storage study at 4 °C (Figure 1A). The initial mean size of liposomal vesicles was 1675.0, 1701.5, 724.9, and 277.8 nm, which, after 60 days of storage at 4 °C, were increased up to 2466.0 nm (by 32%), 2601.0 nm (by 34%), 2104.0 nm (by 65%), and 538.7 nm (by 48%) for MLVs, UV-irradiated, lyophilized, and sonicated forms, respectively. PDI values measured for all liposomal samples during the time (Figure 1A, numbers above bars) show two different behaviors: (i) PDI remained between 0.33 and 0.47 for lyophilized samples, reflecting a slight increase in the heterogeneity and (ii) PDI value significantly increased with storage time for MLVs (from 0.31 to 0.60), UV-irradiated liposomes (from 0.27 to 0.65), and SUVs (from 0.52 to 0.83), indicating less homogeneity and more aggregation. As can be seen in Figure 1B, a significant decrease in the absolute value of zeta potential was observed in all liposomal forms with silibinin for 60 days. The initial zeta potential was −35.5, −36.5, −14.9, and −21.6 mV, which, after the 60-day storage study, were decreased to −16.6 mV (by 53%), −23.1 mV (by 36%), −6.0 mV (by 60%), and −12.7 mV (by 41%) for MLVs, UV-irradiated, lyophilized, and sonicated samples, respectively (Figure 1B). It can be seen that there was a significant increase in the conductivity factor in MLVs and SUVs with silibinin during a 60-day storage study (from 0.38 to 1.20 µmcm/Vs and from 1.24 to 2.02 µmcm/Vs, respectively), while, in the case of the UV-irradiated parallel, the conductivity was not changed (table in Figure 1B). In addition, there was a significant drop in the conductivity factor of the lyophilized sample, from 2.64 to 1.43 µmcm/Vs during storage. The mobility of MLVs and UV-irradiated liposomes significantly decreased during 60 days of storage, whereas in the case of SUVs and lyophilized samples, the decrease in mobility was slower (Figure 1B, numbers above bars). In the MLVs system, mobility decreased from −2.78 to −1.30 µmcm/Vs, while in the UV-irradiated formulation, the mentioned parameter decreased from −2.89 to −1.81 µmcm/Vs. The mobility of SUVs decreased from −1.58 to −1.31 µmcm/Vs, while in the lyophilized liposomal form, it can be seen that there was a drop from −0.70 to 0.47 µmcm/Vs.

oxidation and hydrolysis and a reduction in encapsulation efficiency [39,40]. According to the literature data, their physicochemical instability resulted in membrane combination, aggregation, and changes in particle size, rigidity, and membrane compounds, as well as a decrease in encapsulation efficiency [40,41]. Therefore, the storage stability of the developed liposomes was monitored for 60 days at 4 °C, and the results are presented graphically in Figure 1.

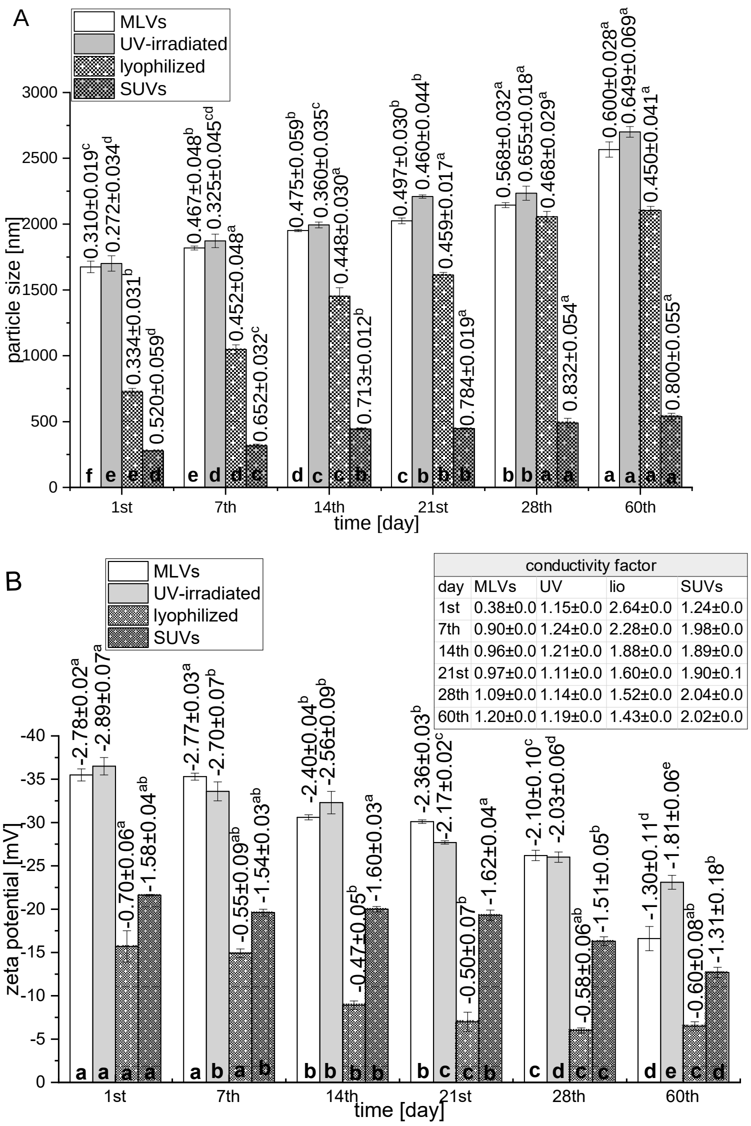

conductivity factor				
day	MLVs	UV	lio	SUVs
1st	0.38±0.0	1.15±0.0	2.64±0.0	1.24±0.0
7th	0.90±0.0	1.24±0.0	2.28±0.0	1.98±0.0
14th	0.96±0.0	1.21±0.0	1.88±0.0	1.89±0.0
21st	0.97±0.0	1.11±0.0	1.60±0.0	1.90±0.1
28th	1.09±0.0	1.14±0.0	1.52±0.0	2.04±0.0
60th	1.20±0.0	1.19±0.0	1.43±0.0	2.02±0.0

Figure 1. Particle size bars and polydispersity index numbers above bars (**A**) and zeta potential-bars, mobility-numbers above bars [μmcm/Vs], and conductivity-table (**B**) of multilamellar liposomes (MLVs), UV-irradiated liposomes, lyophilized liposomes, and small unilamellar liposomes (SUVs) with encapsulated silibinin monitored for 60 days of their storage at 4 °C; values with the same letter showed no statistically significant difference ($p > 0.05$; n = 3; analysis of variance, Duncan's *post hoc* test).

3.4. The Density, Surface Tension, and Viscosity of the Silibinin-Loaded Liposomes

The physical properties of liquid silibinin-loaded liposomes (density, surface tension, and viscosity) were investigated before and after UV irradiation and sonication. As can be seen in Table 2, the density of MLVs, UV-irradiated liposomes, and SUVs was 0.939 ± 0.005, 0.917 ± 0.004, and 0.916 ± 0.006 g/cm^3, respectively.

Table 2. The density (ϱ), surface tension (γ), and viscosity (η) of multilamellar liposomes (MLVs), UV-irradiated liposomes, and small unilamellar liposomes (SUVs) with encapsulated silibinin.

Samples	ϱ [g/mL]	γ [mN/m]	η [mPa·s]
MLVs	$0.939 \pm 0.005^{a,*}$	28.7 ± 0.1^{a}	3.45 ± 0.02^{a}
UV-irradiated	0.917 ± 0.004^{b}	27.1 ± 0.2^{b}	3.28 ± 0.03^{b}
SUVs	0.916 ± 0.006^{b}	26.5 ± 0.2^{c}	3.43 ± 0.02^{a}

[*1] Values with the same letter in each column showed no statistically significant difference ($p > 0.05$; n = 3; analysis of variance, Duncan's *post hoc* test).

MLVs possessed a significantly higher value of surface tension (28.7 ± 0.1 mN/m) compared with UV-irradiated liposomes and SUVs (27.1 ± 0.2 and 26.5 ± 0.2 mN/m, respectively). The viscosity of all prepared liquid formulations varied in a narrow range, from 3.28 to 3.45 mPa·s.

3.5. FT-IR Study

The FT-IR is an easy and versatile analytical tool used for studying the structure and intermolecular interaction in liposome-based systems. Also, the influence of UV irradiation of 2-(oleoyloxy)-3-(stearoyloxy) propyl (2-(trimethylammonio)ethyl) phosphate (phosphatidylcholine), empty liposomes, and silibinin-loaded liposomes was studied using the FT-IR technique. The FT-IR spectra of Phospholipon (phosphatidylcholine, Ph) and empty liposomes (non-loaded liposomes), before and after UV treatment, are shown in Figure S1. The structure of phosphatidylcholine and silibinin A are given in Figure S2. The analysis of the structural changes was based on the inspection of characteristic peaks of intensity change and using deconvolution methodology to separate them into well-resolved structures of functional groups absorption that emerged as a result of the applied treatment.

In the spectrum of Ph broad peak, the range 3600–3000 cm^{-1} is assigned to the O-H stretching vibration (from glycerol and phosphate groups residues) (Figure S1). The small and sharp peak at 3010 cm^{-1} is due to the ethylenic C-H stretching vibration in oleic acid residue in phosphatidylcholine as the main compound of Ph [44]. Additionally, the strong and intensive peaks observed at 2923 cm^{-1} and 2853 cm^{-1} are due to the methyl and methylene groups' asymmetric and symmetric stretching vibration of the fatty acids residue of phosphatidylcholine. The absorption mode at 1735 cm^{-1}, observed in all spectra containing phosphatidylcholine, is assigned to the C=O present in the ester group. The small peak at 1652 cm^{-1} is due to the deformation vibrations of the O-H group and the low contribution of the absorption from the C=C stretching vibration in oleic acid residue. The absorption in the spectral range from 1466 cm^{-1} to 1375 cm^{-1} was assigned to the C-H deformations vibration of the methyl and methylene groups in phosphatidylcholine. The stretching vibration of C-O and C-O-C, as well as the P=O phosphate group in the hydrophilic part of phosphatidylcholine, was observed at 1246 cm^{-1}, 1171 cm^{-1}, 1086 cm^{-1}, and 1063 cm^{-1}, respectively. The band at 1062 cm^{-1} was assigned to the C-O and P-O-C stretching band from the phospholipid structure. Also, the peak at 872 cm^{-1} arises from the P-O asymmetric stretching vibration. The stretching vibration of γ(=C-H) in the *cis*-unsaturated double bond of phospholipids appeared in the 730–770 cm^{-1} region, which is overlapped with the O-CO-C bending vibrations that originate from a molecule of phosphatidylcholine (usually observed at a wavenumber of 734 cm^{-1}) [45].

No observable differences were found by comparison of the FT-IR spectra of Ph and liposomes, for both empty liposomes and MLVs with silibinin (Figures 2 and S1). It means that the established intra/intermolecular interaction in the packed structure of phosphatidylcholine is not reflected in observable peak shifting or intensity change. Moreover, the absence of new modes on the FTIR spectra of silibinin-loaded liposomes in comparison to empty liposomes (Figure 2) indicates that there is no chemical reaction between the silibinin and phospholipids, therefore indicating their compatibility. Figure S3 shows the FT-IR spectra of silibinin, empty liposomes, silibinin-loaded liposomes as MLVs, and UV-treated liposomes with silibinin for different periods (15–90 min of UV irradiation) in the 1550–1800 cm^{-1} spectral region.

The presence of silibinin in liposomes, i.e., the contribution of aromatic structure absorption before and during UV irradiation, does not noticeably bring intensity peak change in the region 1550–1675 cm^{-1}. Also, a hardly observable intensity increase of the valley at 1693 cm^{-1} was observed as a result of oxidation/peroxidation processes causing the formation of oxygen-containing functionalities. Allylic hydrogen is activated to radical group reaction reactive oxygen hydroxyl radical [46]. The formation of hydroperoxides and cyclic forms could undergo C–C scission with the formation of an aldehyde that can then react with oxygen to oxidize to carboxylic groups [47]. To make a more visible and

No observable differences were found by comparison of the FT-IR spectra of Ph and liposomes, for both empty liposomes and MLVs with silibinin (Figure S1 and Figure 2). It means that the established intra/intermolecular interaction in the packed structure of phosphatidylcholine is not reflected in observable peak shifting or intensity change. Moreover, the absence of new modes on the FTIR spectra of silibinin-loaded liposomes in comparison to empty liposomes (Figure 2) indicates that there is no chemical reaction between the silibinin and phospholipids, therefore indicating their compatibility. Figure S3 shows the FT-IR spectra of silibinin, empty liposomes, silibinin-loaded liposomes as MLVs, and UV-treated liposomes with silibinin for different periods (15–90 min of UV irradiation) in the 1550–1800 cm^{-1} spectral region.

measurable peak of interest, the deconvolution of these peaks was performed in absorbance mode, and the obtained results are given in Figure S4.

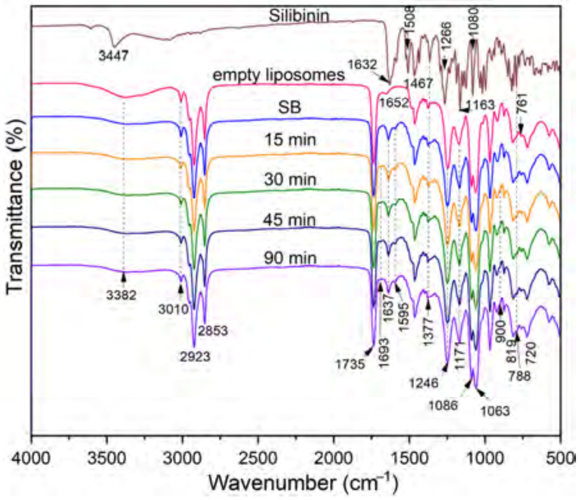

Figure 2. FT-IR spectra of silibinin, empty liposomes, silibinin-loaded liposomes (MLVs), and UV-treated liposomes with silibinin for different periods of 15–90 min of UV irradiation.

Figure 2. FT-IR spectra of silibinin, empty liposomes, silibinin-loaded liposomes (MLVs), and UV-treated liposomes with silibinin for different periods of 15–90 min of UV irradiation.

The presence of silibinin in liposomes, i.e., the contribution of aromatic structure absorption before and during UV irradiation, does not noticeably bring intensity peak change in the region 1550–1675 cm^{-1}. Also, a hardly observable intensity increase of the valley at 1693 cm^{-1} was observed as a result of oxidation/peroxidation processes causing the formation of oxygen-containing functionalities. Allylic hydrogen is activated to radical group reaction reactive oxygen hydroxyl radical [46]. The formation of hydroperoxides and cyclic forms could undergo C–C scission with the formation of mainly aldehyde that can then react with oxygen to oxidize to carboxylic groups [47]. To make a more visible and measurable peak of interest, the deconvolution of these peaks was performed in absorbance mode, and the obtained results are given in Figure S4.

A similar phenomenon and trend were observed for both Ph and liposome, indicating that analogous processes but at different intensities take place in these systems. There is a known dependence between two more or less concomitant processes: the disappearance of double bond (Figure S1) and peak structure/intensities change at ~1652 and ~1702 cm^{-1} because of ethylenic bond oxidation/hydroperoxidation by forming oxygen reach species of low stability. The final step is the structural rearrangement to, mainly, aldehyde groups, which easily, under oxidative conditions, transform into carboxylic groups. A similar conclusion can be drawn from the deconvoluted spectra of MLVs with silibinin and their UV-irradiated parallels (Figure S5).

A similar phenomenon and trend were observed for both Ph and liposome, indicating that analogous processes but at different intensities take place in these systems. There is a known dependence between two more or less concomitant processes: the disappearance of double bond (Figure S1) and peak structure/intensities change at ~1652 and ~1702 cm^{-1} because of ethylenic bond oxidation/hydroperoxidation by forming oxygen reach species of low stability. The final step is the structural rearrangement to, mainly, aldehyde groups, which easily, under oxidative conditions, transform into carboxylic groups. A similar conclusion can be drawn from the deconvoluted spectra of MLVs with silibinin and their UV irradiated parallels (Figure S5).

In this way, silibinin can act as a crosslinking agent for phosphatidylcholine by intramolecular cross-linking being incorporated into a hydrophobic bilayer. At the same time, the phosphatidylcholine protects silibinin from external sources, and thus, only the structural transformation of phosphatidylcholine was noticed.

In this way, silibinin can act as a crosslinking agent for phosphatidylcholine by intramolecular cross-linking being incorporated into a hydrophobic bilayer. At the same time, the phosphatidylcholine protects silibinin from external sources, and thus, only the structural transformation of phosphatidylcholine was noticed.

A similar analysis was applied for the UV-initiated structural change of the studied systems phosphatidylcholine, empty liposomes (Figure S6) and silibinin-loaded liposomes (Figure 3). Here, it was not possible to perform the deconvolution procedure.

A similar analysis was applied for the UV-initiated structural change of the studied systems phosphatidylcholine, empty liposomes (Figure S6) and silibinin-loaded liposomes (Figure 3). Here, it was not possible to perform the deconvolution procedure.

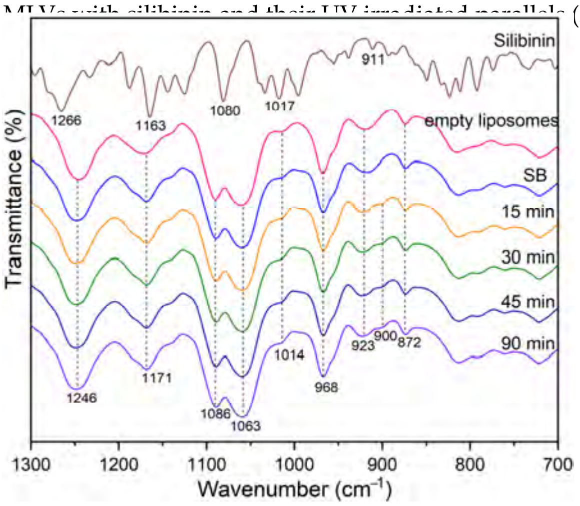

Figure 3. The UV-initiated time-dependent change of the peaks in the 700–1300 cm^{-1} region for silibinin-loaded liposomes.

Figure 3. The UV-initiated time-dependent change of the peaks in the 700–1300 cm^{-1} region for silibinin-loaded liposomes.

The UV irradiation of Ph, liposomes, and silibinin-loaded liposomes leads to spectral change due to the appropriate structural change of treated material (exemplified for silibinin-loaded liposome):

(1) The disappearance of the ethylenic bond was observed as a decrease in the peak intensity at 3010 cm^{-1} (Figure 2),

(2) The change of the peak structure in the region 1600–1750 cm^{-1} related to carbonyl

The UV irradiation of Ph, liposomes, and silibinin-loaded liposomes leads to spectral change due to the appropriate structural change of treated material (exemplified for silibinin-loaded liposome):

(1) The disappearance of the ethylenic bond was observed as a decrease in the peak intensity at 3010 cm^{-1} (Figure 2),
(2) The change of the peak structure in the region 1600–1750 cm^{-1} related to carbonyl groups stretch vibration of different origins (ester, carboxy, aldehyde carbonyl, etc.) (Figure S3),
(3) The appearance of small shoulder peaks in the region 800–1300 cm^{-1} (Figures 3 and S6).

Due to hardly observable peaks of shifting/intensity change or the appearance of new ones, created because of UV-initiated radical reaction causing the chemical transformation, two methods were applied in this study: the deconvolution of selected peaks and the quantification of peaks area as a measure of the appropriate group presence in the studied molecule.

No noticeable change of the peak at 1735 cm^{-1}, originating from the ester carbonyl group of phospholipids, indicates an appropriate stability against oxidative attack. Thus, the height/area of the peak was used as the internal standard value for the calculation of the relative intensities of the peak change. A small noticeable shoulder at 900 and 800 cm^{-1} (Figure S1) indicates the presence of hydroperoxide species, but the position and intensities of other peaks were unchanged. The results obtained based on the applied deconvolution procedure are given in Table S1.

The increased content of oxygen-containing functionalities was reflected as the peak area increased (the peak centered at 1702 cm^{-1}) concerning time (30 min). An analogous trend was observed for the silibinin-loaded MLVs system at a lower extent, which indicates the scavenging capability of present silibinin in liposomes.

As can be seen from Figure 4, sonication did not cause changes in the FTIR spectra of silybin-loaded liposomes. Although ultrasound waves can affect the physical and structural characteristics of liposomes, the degree of the changes depends on ultrasound parameters [48]. In the case of liposomes with silibinin, the sonication period was short (15 min) and included pauses in sonication, which probably prevented the degradation of the bilayer caused by cavitation with a desired reduction in particle size. A prolonged time of ultrasound exposure can show the phase change expanding effect of the phospholipid membrane, and, consequently, chemical and physical changes [48].

As can be seen from Figure 4, sonication did not cause changes in the FTIR spectra of silybin-loaded liposomes. Although ultrasound waves can affect the physical and structural characteristics of liposomes, the degree of the changes depends on ultrasound parameters [48]. In the case of liposomes with silibinin, the sonication period was short (15 min) and included pauses in sonication, which probably prevented the degradation of the bilayer caused by cavitation with a desired reduction in particle size. A prolonged time of ultrasound exposure can show the phase change expanding effect of the phospholipid membrane, and, consequently, chemical and physical changes [48].

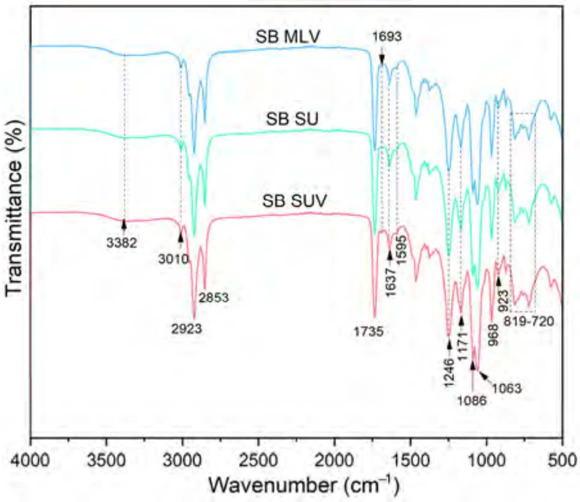

Figure 4. FT-IR spectra of silibinin-loaded liposomes: multilamellar liposomes (MLV), UV-irradiated liposomes, and small unilamellar liposomes (SUV).

Figure 4. FT-IR spectra of silibinin-loaded liposomes: multilamellar liposomes (MLV), UV-irradiated liposomes, and small unilamellar liposomes (SUV).

Several studies have shown that silibinin is a potent sensitizer of UVA radiation-induced oxidative stress and apoptosis and provides strong protection against UV-induced damage in the epidermis [4,5,13,49,50]. Also, considering that silibinin was encapsulated in liposomes as a carrier that has constituent components potentially sensitive to UV irradiation, sonication, and lyophilization, the stability and chemical changes of free silibinin after UV irradiation, lyophilization, and ultrasound treatment were not examined. The first-mentioned process (UV irradiation) was not used for the treatment of

Several studies have shown that silibinin is a potent sensitizer of UVA radiation-induced oxidative stress and apoptosis and provides strong protection against UV-induced

damage in the epidermis [4,5,13,49,50]. Also, considering that silibinin was encapsulated in liposomes as a carrier that has constituent components potentially sensitive to UV irradiation, sonication, and lyophilization, the stability and chemical changes of free silibinin after UV irradiation, lyophilization, and ultrasound treatment were not examined. The first-mentioned process (UV irradiation) was not used for the treatment of free silibinin because studies have shown not only its stability under UV irradiation but also its protective effects [4,5,13,49,50], and the second-mentioned process (freeze-drying) did not apply to the free silibinin because it is not a common procedure used for a powdered component such as silibinin. Additionally, the sonication of silibinin as a powder would not be feasible using the ultrasonic probe that was employed for liposome sonication.

3.6. Raman Spectra

Raman spectroscopy was applied to investigate the presence of various interactions between silibinin, Ph, liposomes with loaded silibinin, and liposome UV-irradiated and sonicated counterparts. The Raman spectra of pure silibinin and Ph are presented in the Supplementary Materials (Figure S1), while the Raman spectra of MLVs, UV-irradiated liposomes, and SUVs with encapsulated silibinin (all lyophilized samples due to device

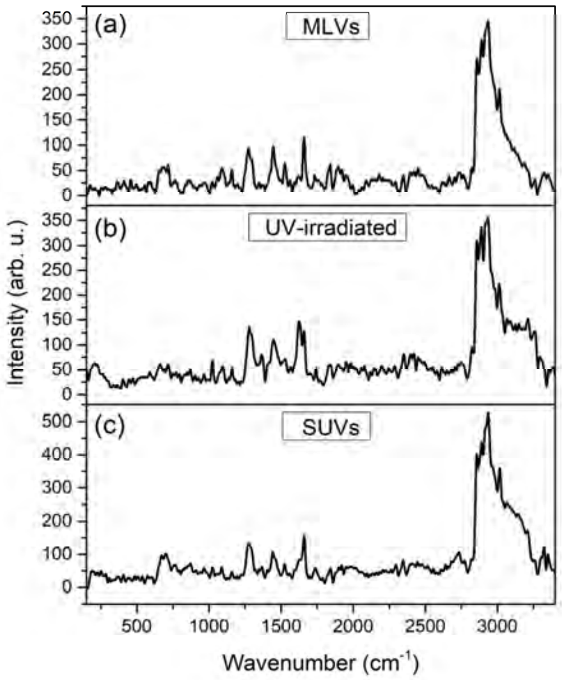

Figure 5. Raman spectra of (**a**) multilamellar vesicles with silibinin (MLVs), (**b**) UV-irradiated liposomes with silibinin, and (**c**) small unilamellar vesicles with silibinin (SUVs).

Figure 5. Raman spectra of (**a**) multilamellar vesicles with silibinin (MLVs), (**b**) UV-irradiated liposomes with silibinin, and (**c**) small unilamellar vesicles with silibinin (SUVs).

The Raman spectra of MLVs with encapsulated silibinin (Figure 5a) mostly resembled Ph (Figure S7A), with both showing characteristic bands of phospholipids. When encapsulated almost exclusively show peaks originating from the carrier, i.e., the liposomal bilayer in the case of silibinin-loaded liposomes, it indicates the efficient entrapment of the active compound [51]. The Raman features of the MLVs with silibinin and Ph spectra (Figures 5a and S7A) correspond to the presence of the esters of palmitic and stearic acids, (bands between 400 and 500 cm^{-1} [52], phospholipid head-group C–N symmetric stretching of choline at ~720 cm^{-1} [53], the most characteristic feature of stearic acid at ~850 cm^{-1} [52], C–C–O stretching at ~980 cm^{-1} [45], the skeletal stretching of the C–C vibrations at 1025 cm^{-1} [53], the symmetric stretching of PO_2^- group at 1080 cm^{-1}, and the asymmetric stretching of the PO_2^- at ~1200 cm^{-1} [54]. The C–H mode from

The Raman spectra of MLVs with encapsulated silibinin (Figure 5a) mostly resembled Ph (Figure S7A), with both showing characteristic bands of phospholipids. When encapsulates almost exclusively show peaks originating from the carrier, i.e., the liposomal bilayer in the case of silibinin-loaded liposomes, it indicates the efficient entrapment of the active compound [51]. The Raman features of the MLVs with silibinin and Ph spectra (Figure 5a and Figure S7A) correspond to the presence of the esters of palmitic and stearic acids, bands between 400 and 500 cm^{-1} [52], phospholipid head-group C–N symmetric stretching of choline at ~720 cm^{-1} [53], the most characteristic feature of stearic acid at ~850 cm^{-1} [52], C–C–O stretching at ~980 cm^{-1} [45], the skeletal stretching of the C–C vibrations at ~1025 cm^{-1} [53], the symmetric stretching of PO_2^- group at 1080 cm^{-1} and the asymmetric stretching of the PO_2^- at ~1200 cm^{-1} [54]. The C–H mode from the lipid acyl chains of phospholipids can be related to the *in-plane* CH_2 twisting mode in the oleoyl chain (1280 cm^{-1}) and CH_2 scissoring mode of the fatty acid chain (1450 cm^{-1}) in both MLVs and Ph spectra [55,56]. The band at ~1525 cm^{-1} corresponds to the N-O stretching, while the mode at ~1670 cm^{-1} is related to the C=C stretching vibration in both spectra [53]. The peak at ~1750 cm^{-1} can be associated with the carbonyl group (C=O) of the ester bond among glycerol and fatty acids [57] (Figure 5a and Figure S7A). The peaks

the oleoyl chain (1280 cm^{-1}) and CH_2 scissoring mode of the fatty acid chain (1450 cm^{-1}) in both MLVs and Ph spectra [55,56]. The band at ~1525 cm^{-1} corresponds to the N-O stretching, while the mode at ~1670 cm^{-1} is related to the C=C stretching vibration in both spectra [53]. The peak at ~1750 cm^{-1} can be associated with the carbonyl group (C=O) of the ester bond among glycerol and fatty acids [57] (Figures 5a and S7A). The peaks in a region of 2100–2750 cm^{-1} in MLVs spectra originate from phospholipids with the fact that they are of a more pronounced intensity than in the case of Ph spectra. The Raman mode in MLVs and Ph spectra at ~2850 cm^{-1} can be related to the symmetric and asymmetric stretching of the C–H bonds of CH_2 and CH_3 groups in the alkyl chains, whereas the band at 3015 cm^{-1} can correspond to the CH stretching of the N-CH_3 [53,57]. The band at ~3350 cm^{-1} is associated with bound water in both spectra [53]. The obtained Raman spectra of pure silibinin (Figure S2B) is in accordance with the literature data in a range of 500–1700 cm^{-1} and 3000–3500 cm^{-1} [58,59], while peaks in a region from 2000 to 2800 cm^{-1} can originate from impurities. As can be seen from Figure 1B, UV irradiation has caused changes in the Raman spectra of silibinin-loaded liposomes. Namely, changes can be noticed in the region of 500–1600 cm^{-1} in the peaks' intensity (higher intensity in UV-irradiated sample). The phenomenon shown is in agreement with the literature data where there were peaks with strongly higher intensities in the UV-irradiated liposomes in comparison to their non-treated counterparts [33]. In FTIR spectroscopy, the changes are visible in a region of 800–1300 cm^{-1}. In addition, the structure of peaks at 1600–1750 cm^{-1} was changed after UV irradiation, which is proven in FTIR analysis as well. The changes are also visible in the region at around 2000 cm^{-1} and 3100–3250 cm^{-1}. The mode at 3015 cm^{-1} in MLVs spectra was moved below 3000 cm^{-1} after UV irradiation. The FTIR analysis showed changes in the same region. Ultrasound treatment of silibinin-loaded liposomes did not lead to a change in the Raman spectra, except in terms of peaks' intensity (Figure 5). Namely, Chotphruethipong et al. [60] reported that the intensity of the peaks of CH_2 stretching and the C=O group of liposomes (modes at 2800–2900 cm^{-1} and ~1750 cm^{-1}, respectively) increased and shifted to a higher wavenumber due to the oxidation of unsaturated fatty acids in the phospholipid membrane. The reason for the absence of the shift of peaks to a higher wavenumber in the case of liposomes with silibinin can be the antioxidant potential of silibinin. Namely, polyphenol compounds are observed to be effective at inhibiting lipid oxidation [48].

3.7. ABTS and DPPH Radical Scavenging Potential of Silibinin-Loaded Liposomes

Liposomal vesicles can be employed as carriers for antioxidant compounds with the aim of increasing their bioavailability and providing controlled release, while liposome oxidation can be prevented [61]. Therefore, the antioxidant potentials of MLVs, UV-irradiated liposomes, lyophilized liposomes, and SUVs with encapsulated silibinin were investigated via ABTS and DPPH radical scavenging capacity tests, as well as in the cell line with generated ROS (described in Section 3.9). The data from ABTS and DPPH assays are presented in Figure 6.

The ABTS radical scavenging activity of developed liposomes with silibinin, expressed as the IC_{50} value, was 22.99 ± 0.32, 23.08 ± 1.62, 20.36 ± 0.56, and 29.44 ± 2.13 mg of silibinin/mL of liposomal suspension for MLVs, UV-irradiated liposomes, SUVs, and lyophilized liposomes, respectively (Figure 6). The antioxidant capacity determined in the DPPH assay, expressed as the IC_{50} value, was 27.80 ± 0.21, 28.21 ± 1.42, 24.86 ± 1.54, and 33.46 ± 2.64 mg of silibinin/mL of liposomal suspension for MLVs, UV-irradiated liposomes, SUVs, and lyophilized liposomes, respectively (Figure 6). The determined IC_{50} value of ascorbic acid, as a control, was 0.217 mg/mL in the ABTS test, and 0.052 mg/mL in the DPPH test. UV irradiation did not cause changes in the antioxidant potential of liposomes measured in both employed assays, while the lyophilization process significantly decreased the radical scavenging activity of liposomes with silibinin. In contrast, sonication positively influenced the antioxidant capacity of liposomes with silibinin (lower IC_{50} value = higher antioxidant potential) (Figure 6). The antioxidant potential of pure silibinin was 15.69 ± 1.61 and 3.65 ± 0.76 mg of silibinin/mL of ethanol, in ABTS and DPPH assays, respectively (Figure 6).

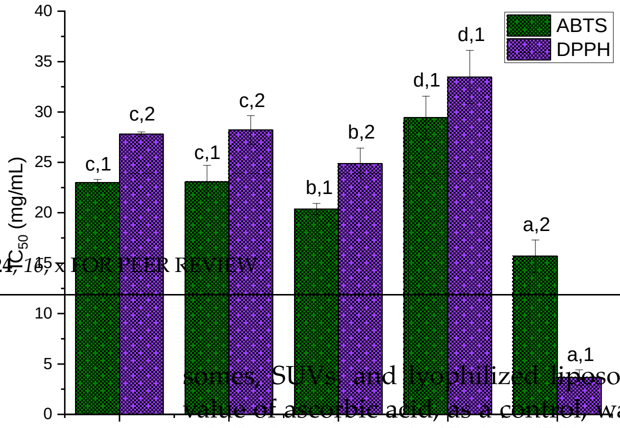

Figure 6. Antioxidant potential of multilamellar vesicles with silibinin (MLVs), UV-irradiated liposomes with silibinin, small unilamellar vesicles with silibinin (SUVs), lyophilized liposomes with silibinin, and pure silibinin; values with the same letter for each assay separately and the same number in each sample separately showed no statistically significant difference ($p > 0.05$; n = 3; analysis of variance, Duncan's *post hoc* test); IC_{50} (mg of silibinin/mL of liposomal suspension) represented the concentration required to neutralize 50% of free radicals.

3.8. Cytotoxicity of Silibinin-Loaded Liposomes

In view of silibinin activities toward skin presented in various studies [4,5,13], the effect of developed liposomes on keratinocyte viability was examined. Figure 7 graphically shows the results obtained.

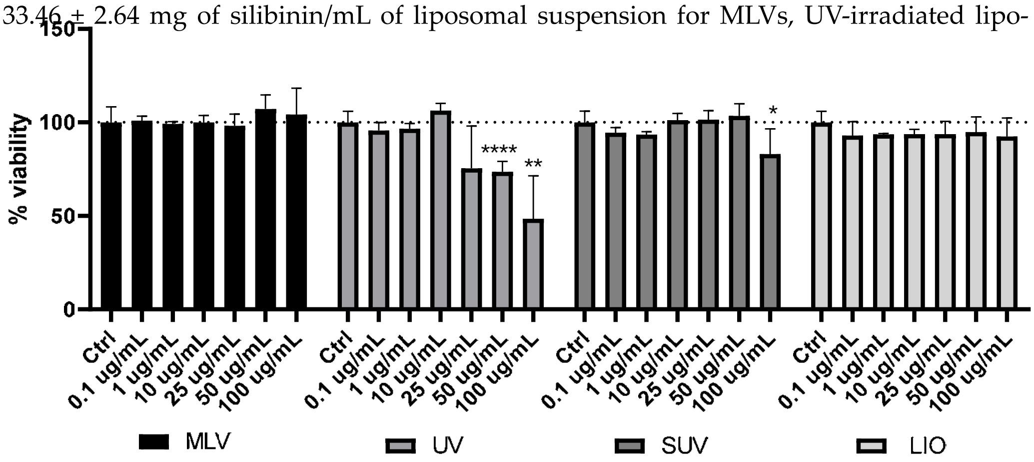

Figure 7. Cytotoxicity of multilamellar liposomes (MLVs), UV-irradiated liposomes, lyophilized liposomes, and small unilamellar liposomes (SUVs) with encapsulated silibinin in a range of concentrations (0.1, 1, 10, 25, 50, and 100 µg/mL) determined by MTT assay in HaCaT cells. Data are expressed as mean + SEM relative to the unexposed control (dashed line); * $p < 0.05$, ** $p < 0.01$, **** $p < 0.0001$ by one-way analysis of variance (ANOVA) with Tukey's multiple comparison *post hoc* test.

Figure 7 represents the effect of MLVs, UV-irradiated liposomes, lyophilized liposomes, and SUVs with encapsulated silibinin on cell viability in HaCaT cells. The treatment of cells with the liposomes for 24 h produced diverse effects on cells, depending on the type of liposomes. Namely, MLVs and lyophilized samples did not lead to a significant change in cell viability compared to the unexposed control in any of the concentrations used. On

served to be effective at inhibiting lipid oxidation [48].

3.7. ABTS and DPPH Radical Scavenging Potential of Silibinin-Loaded Liposomes

Liposomal vesicles can be employed as carriers for antioxidant compounds with the aim of increasing their bioavailability and providing controlled release, while liposome oxidation can be prevented [61]. Therefore, the antioxidant potentials of MLVs, UV-irradiated liposomes, lyophilized liposomes, and SUVs with encapsulated silibinin were investigated via ABTS and DPPH radical scavenging capacity tests, as well as in the cell line with generated ROS (described in Section 3.9). The data from ABTS and DPPH assays are presented in Figure 6.

Figure 6. Antioxidant potential of multilamellar vesicles with silibinin (MLVs), UV-irradiated liposomes with silibinin, small unilamellar vesicles with silibinin (SUVs), lyophilized liposomes with silibinin, and pure silibinin; values with the same letter for each assay separately and the same number in each sample separately showed no statistically significant difference ($p > 0.05$; n = 3; analysis of variance, Duncan's *post hoc* test); IC_{50} (mg of silibinin/mL of liposomal suspension) represented the concentration required to neutralize 50% of free radicals.

The ABTS radical scavenging activity of developed liposomes with silibinin, expressed as the IC_{50} value, was 22.99 ± 0.32, 23.08 ± 1.62, 20.36 ± 0.56, and 29.44 ± 2.15 mg of silibinin/mL of liposomal suspension for MLVs, UV-irradiated liposomes, SUVs, and lyophilized liposomes, respectively (Figure 6). The antioxidant capacity determined in the DPPH assay, expressed as the IC_{50} value, was 27.80 ± 0.21, 28.21 ± 1.42, 24.86 ± 1.54, and 33.46 ± 2.64 mg of silibinin/mL of liposomal suspension for MLVs, UV-irradiated lipo-

Pharmaceutics **2024**, *16*, x FOR PEER REVIEW 17

somes, SUVs and lyophilized liposomes, respectively (Figure 6). The determine
value of ascorbic acid, as a control, was 0.217 mg/mL in the ABTS test, and 0.052 m
in the DPPH test. UV irradiation did not cause changes in the antioxidant poten
liposomes measured in both employed assays, while the lyophilization process s
in. In co
with sil
ant poten
, in ABT
DPPH assays, respectively (Figure 6).

3.8. Cytotoxicity of Silibinin-Loaded Liposomes

In view of silibinin activities toward skin presented in various studies [4,5,13
Figure 7 g

Figure 7. Cytotoxicity of multilamellar liposomes (MLVs), UV-irradiated liposomes, lyop
liposomes, and small unilamellar liposomes (SUVs) with encapsulated silibinin in a range c
centrations (0.1, 1, 10, 25, 50, and 100 µg/mL) determined by MTT assay in HaCaT cells. D
expressed as mean + SEM relative to the unexposed control (dashed line); * $p < 0.05$; ** $p < 0.01$
< 0.0001 by one-way analysis of variance (ANOVA) with Tukey's multiple comparison post ho

Figure 7 represents the effect of MLVs, UV-irradiated liposomes, lyophilized
somes, and SUVs with encapsulated silibinin on cell viability in HaCaT cells. The
ment of cells with the liposomes for 24 h produced diverse effects on cells, dependi
the type of liposomes. Namely, MLVs and lyophilized samples did not lead to a s
cant change in cell viability compared to the unexposed control in any of the conc
tions used. On the other hand, the UV-irradiated sample showed cytotoxic effe
concentrations above 25 µg/mL and significantly reduced cell viability at 50 an
µg/mL in a concentration-dependent manner, where a greater reduction in cell via
was observed with increasing concentrations. Finally, SUVs showed a significan
crease in the percentage of live cells in the treatment with the highest concentration

the other hand, the UV-irradiated sample showed cytotoxic effects in concentrations above 25 µg/mL and significantly reduced cell viability at 50 and 100 µg/mL in a concentration-dependent manner, where a greater reduction in cell viability was observed with increasing concentrations. Finally, SUVs showed a significant decrease in the percentage of live cells in the treatment with the highest concentration of 100 µg/mL, compared to the cells exposed to medium alone (control). The cytotoxic influence of non-loaded liposomes (data in Supplementary Materials, Figure S8) was also noticed but using a concentration of phospholipids of 1000 µg/mL.

3.9. Antioxidative Effect of Silibinin-Loaded Liposomes in H_2O_2-Induced Oxidative Stress

Pharmaceutics **2024**, *16*, x FOR PEER REVIEW

The antioxidative effect of MLVs, UV-irradiated liposomes, lyophilized liposomes, and SUVs with encapsulated silibinin on H_2O_2-induced oxidative stress in HaCaT cells was investigated as well. The obtained data are presented graphically in Figure 8.

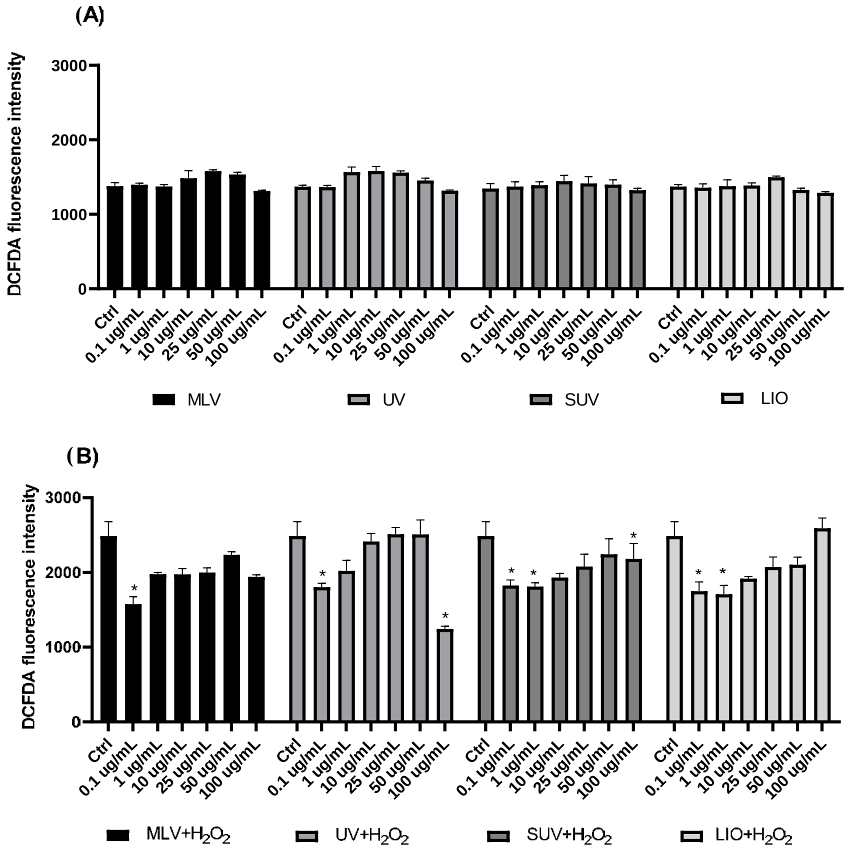

Figure 8. Effect of 24 h pre-incubation with multilamellar liposomes (MLVs), UV-irradiated liposomes, lyophilized liposomes, and small unilamellar liposomes (SUVs) with encapsulated silibinin in a range of concentrations (0.1, 1, 10, 25, 50, and 100 µg/mL) on the production of reactive oxygen species in HaCaT cells *versus* control (**A**) without H_2O_2 and (**B**) after the exposure to H_2O_2, determined by H2DCFDA assay, expressed as relative fluorescence intensity. The data are expressed as mean + SEM; * $p < 0.05$ by one-way analysis of variance (ANOVA) with Tukey's multiple comparison *post hoc* test.

Figure 8. Effect of 24 h pre-incubation with multilamellar liposomes (MLVs), UV-irradiated liposomes, lyophilized liposomes, and small unilamellar liposomes (SUVs) with encapsulated silibinin in a range of concentrations (0.1, 1, 10, 25, 50, and 100 µg/mL) on the production of reactive oxygen species in HaCaT cells *versus* control (**A**) without H_2O_2 and (**B**) after the exposure to H_2O_2, determined by H2DCFDA assay, expressed as relative fluorescence intensity. The data are expressed as mean + SEM; * $p < 0.05$ by one-way analysis of variance (ANOVA) with Tukey's multiple comparison *post hoc* test.

Figure 8 represents the effects of 24 h treatment with MLVs, UV-irradiated liposomes, lyophilized liposomes, and SUVs with encapsulated silibinin on the levels of ROS in the HaCaT cells. The analysis of the effects of all liposomal samples (Figure 8A), after 24 h incubation in the HaCaT cells without exposure to H_2O_2, showed that all examined types of liposomes with silibinin did not significantly alter endogenous ROS production. It should also be mentioned that empty liposomes were tested for ROS production in the HaCaT cells after 24 h, and the results showed that the highest concentration of phospholipids (1000 µg/mL, empty liposomes, i.e., phospholipid liposomes without silibinin) induced an

Figure 8 represents the effects of 24 h treatment with MLVs, UV-irradiated liposomes, lyophilized liposomes, and SUVs with encapsulated silibinin on the levels of ROS in the HaCaT cells. The analysis of the effects of all liposomal samples (Figure 8A), after 24 h incubation in the HaCaT cells without exposure to H_2O_2, showed that all examined types of liposomes with silibinin did not significantly alter endogenous ROS production. It should also be mentioned that empty liposomes were tested for ROS production in the HaCaT cells after 24 h, and the results showed that the highest concentration of phospholipids (1000 µg/mL, empty liposomes, i.e., phospholipid liposomes without silibinin) induced an elevated production of ROS, while smaller concentrations did not affect ROS levels (data in Supplementary Materials, Figure S9).

After exposure to 200 µM H_2O_2 for 2 h, the production of ROS was elevated almost two-fold in HaCaT cells (H_2O_2 bar in Figure 8B). The treatment by pre-incubation of cells with the silibinin-loaded liposomes resulted in reduced ROS levels compared to cells exposed to H_2O_2 alone in a concentration-dependent manner, where smaller concentrations were more efficient in reducing ROS. MLVs and UV-irradiated liposomes with

elevated production of ROS, while smaller concentrations did not affect ROS levels (data in Supplementary Materials, Figure S9).

After exposure to 200 μM H_2O_2 for 2 h, the production of ROS was elevated almost two-fold in HaCaT cells (H_2O_2 bar in Figure 8B). The treatment by pre-incubation of cells with the silibinin-loaded liposomes resulted in reduced ROS levels compared to cells exposed to H_2O_2 alone in a concentration-dependent manner, where smaller concentrations were more efficient in reducing ROS. MLVs and UV-irradiated liposomes with silibinin showed a significant decrease in the ROS levels at 0.1 μg/mL concentration, while SUVs and lyophilized liposomes with silibinin showed a reduction at 0.1 and 1 μg/mL. Additionally, UV-irradiated liposomes and SUVs with silibinin also displayed a significant decrease in ROS levels at the highest concentration of 100 μg/mL.

3.10. Anti-Inflammatory Potential of Silibinin-Loaded Liposomes

Since it is known that COX-2, IL-1β, and MIF play important roles in the regulation of inflammatory response in skin cells, the effects 24 h pre-incubation with MLVs, UV-irradiated liposomes, lyophilized liposomes, and SUVs with encapsulated silibinin at a final concentration of 10 μg/mL were examined in cells challenged with LPS.

The results presented in Figure 9 show that LPS treatment induced a significant elevation of IL-1β and MIF, and only a slight rise in COX-2 levels in LPS-exposed cells compared to non-treated cells. In cells exposed to liposomes alone, without LPS, there was a moderate inhibition of COX-2 expression in HaCaT cells treated with SUVs and lyophilized liposomes and inhibition of IL-1β by SUVs. The results showed that plain liposomes (phospholipid liposomes without silibinin) at a concentration of 10 μg/mL did not induce protein expression of IL-1β, MIF, and COX-2 in comparison to the control, i.e., treatment without liposomes (data in Supplementary Materials, Figure S10). Furthermore, all four types of liposomes significantly reduced MIF expression in cells incubated with liposomes alone for 24 h. Next, in cells exposed to LPS, there was a significant difference in MIF levels at pre-treatments with liposomes at 10 μg/mL compared to LPS alone, confirming the inhibitory effect of MLVs, UV-irradiated liposomes, lyophilized liposomes, and SUVs with encapsulated silibinin on MIF expression after the LPS challenge. Considering IL-1β levels in cells treated with LPS, pre-incubation of lyophilized liposomes significantly reduced the protein expression, while other types of liposomes did not show significant change, although SUVs also showed a reducing trend. Since COX-2 levels were not significantly elevated after LPS treatment, the change in pre-treatments with liposomes could not be observed.

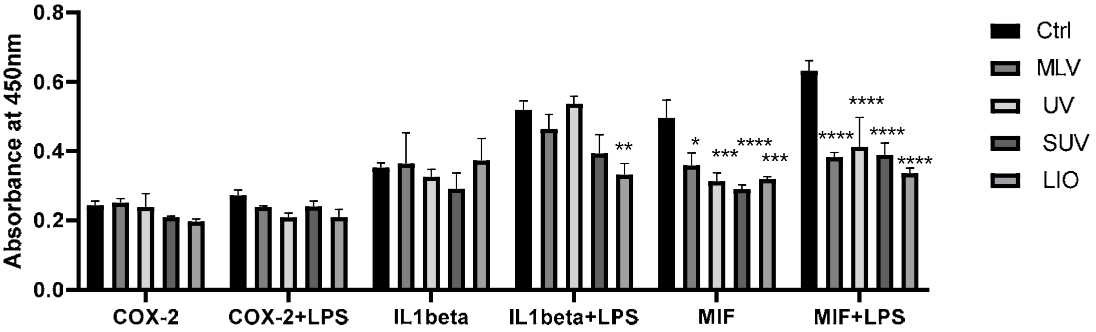

Figure 9. Effect of 24 h pre-treatments with multilamellar liposomes (MLVs), UV-irradiated liposomes, lyophilized liposomes, and small unilamellar liposomes (SUVs) with encapsulated silibinin at final concentration of 10 μg/mL in complete medium on the protein expression of cyclooxygenase-2 (COX-2), interleukin-1 beta (IL-1β), and macrophage inhibitory factor (MIF) in HaCaT cells with or without lipopolysaccharide (LPS) exposure, using the ELISA method; * $p < 0.05$, ** $p < 0.01$, *** $p < 0.001$, **** $p < 0.0001$ by one-way analysis of variance (ANOVA) with Tukey's multiple comparison *post hoc* test.

4. Discussion

The EE of different silibinin-loaded liposomes, as a significant parameter of the encapsulation process, follows the following trend: MLVs and UV-irradiated liposomes > SUVs > lyophilized liposomes. A significantly lower EE of the lyophilized liposomal vesicles was expected since the process of freeze-drying is harmful to the integrity of the bilayer membrane. According to the literature data, a decrease in encapsulation efficiency

4. Discussion

The EE of different silibinin-loaded liposomes, as a significant parameter of the encapsulation process, follows the following trend: MLVs and UV-irradiated liposomes > SUVs > lyophilized liposomes. A significantly lower EE of the lyophilized liposomal vesicles was expected since the process of freeze-drying is harmful to the integrity of the bilayer membrane. According to the literature data, a decrease in encapsulation efficiency is noticed for lyophilized formulations of liposomes, particularly in the absence of the cryoprotectant, as in the case of silibinin-loaded liposomes developed in the present study. Namely, lyophilization results in liposome degradation caused by ice crystals, destruction of the phospholipid membrane function, and consequently, leakage of encapsulated compounds [60,62]. Prolonged exposure to ultrasound waves can also cause a higher decrease in EE (as in liposomes with silibinin) due to higher cavitation effects and the rupture of the vesicles, consequently leading to a potentially excessive release of encapsulated silibinin. Nevertheless, sonication can be used to improve the EE and stability of the liposomal particles in the presence of protein hydrolysates adhering to the membrane internally [63]. The exposure to UV irradiation did not result in a change in the EE of silibinin since UV rays do not create ruptures on the liposomal bilayer, which agrees with the literature data where UV irradiation did not cause a leakage of encapsulated plant bioactives [33].

The average size of liposomal vesicles is significantly affected by the type of used lipids, the liposomal preparation technique, and the physicochemical characteristics of the encapsulated compounds [16,19,28]. In addition, the appropriate diameter of liposomes is essential in terms of the delivery of active components through the skin since larger vesicles cannot diffuse through the skin layers (stratum corneum and deep skin) and achieve the target location. For example, liposomes with a size of 50 nm show a higher diffusion rate in comparison to the vesicles of 200 nm. Small liposomes (diameter of 120 nm) provided a higher accumulation of encapsulated compounds in the stratum corneum and deeper skin in comparison to bigger particles [29]. In the case of silibinin-loaded liposomes, the mentioned parameter follows the following trend: MLVs and UV-irradiated liposomes > lyophilized liposomes > SUVs. UV irradiation did not affect the diameter of liposomes, whereas sonication caused a significant decrease in the particle size. The size of the lyophilized liposomes shows that the lyophilization process led to a decrease in the size of the liposome particles with silibinin in comparison to MLVs. In the case of smaller liposomes (50–300 nm), the freeze-drying process increases the chance of membrane apposition and the creation of larger particles (fusion/aggregation of vesicles) due to the higher liposome concentration by the propagating ice front and the absence of the hydration barrier to fusion [64]. On the other hand, for larger liposomes (such as the silibinin-loaded liposomes developed in the present research), the fragmentation of particles (decreasing in size) is possible during lyophilization [65]. The obtained value of vesicle size of SUVs agrees with the literature data where the mentioned parameter varied between 250 and 280 nm after the ultrasound treatment of the liposomes due to the efficient conversion of larger multilayered vesicles (multilamellar) into single-layered (unilamellar) ones [63]. Namely, the size of liposomes depends on the number of their layers, which can vary in a very wide range (from nm to mm) in thickness [66]. A short ultrasound treatment period (15 min was used for silibinin-loaded liposomes) was required to obtain nano-sized particles, while prolonged sonication time can cause the complete rupture of the liposomal membrane, causing the leakage of encapsulated components, as well as the easy binding of broken integrity membranes, leading to an increase in particle size [48,63]. Silva et al. [67] have also obtained nano-sized liposomes (~200 nm) after 15 min of sonication. UV irradiation can change the physical properties of liposomal bilayers by disturbing the order and phospholipid packing, as well as causing an increase in membrane fluidity and permeability [68,69]. UV irradiation also excites vibrational motions in molecules of the complex, changing the lengths and angles of bonds and causing electronic transitions and the cleavage of chemical bonds. However, the mentioned changes were not visible when measured immediately after UV radiation of silibinin-loaded liposomes. The encapsulation of silibinin can affect membrane integrity and avoid further disintegration under UV irradiation, due to silibinin incorporation between the two imperfect adjoining chains within lipid bilayers of mono- and polyunsaturated phospholipid chains [69]. Silibinin, as a highly hydrophobic compound, can be "sandwiched" between the two monolayers, providing the stabilization of the membrane structure and preventing extra damage.

The PDI values for MLVs, UV-irradiated, and lyophilized liposomes are ~0.3, indicating the mono-dispersity or homogeneity of the system [42]. PDI also remained around 0.3 for liquid and lyophilized phospholipid liposomes with rutin, showing that freeze drying did not cause the changes in PDI values [70], as in the case of liposomes with encapsulated silibinin. The highest PDI was recorded for the SUVs, which can mean the presence of MLVs along with SUVs. The main disadvantages of sonication, as the most extensively employed technique for the preparation of SUVs, are the low encapsulation efficacy, possible degradation of phospholipids and encapsulated compounds, metal pollution from the probe tip, and presence of MLVs along with SUVs [26]. The measured value of PDI of SUVs agreed with the results of the Silva et al. study [67] where the PDI was ~0.5 after 18 min of sonication. According to the literature data, a higher uniformity of liposomal vesicles can be achieved by prolonged ultrasound treatment or the usage of higher amplitude [63,67]. However, ultrasound waves can promote phospholipid hydrolysis and oxidation via the production of free radicals in the cavitation bubbles collapse, while a high temperature that arises due to long-term sonication can accelerate phosphocholine hydrolysis as well [67]. The Arias-Alpizar et al. study [71] has also shown that the measured size and PDI of liposomes were unchanged before and after UV irradiation. In addition, potential membrane reorganization does not always have to lead to a change in liposome integrity, size, size distribution, or the leakage of liposome-encapsulated compounds during and after UV irradiation, which was also proven by measurement of EE after irradiation (Table 1).

The zeta potential of all tested silibinin-loaded liposomes possessed negative values and reached the highest level (absolute value) in the case of MLVs and UV-irradiated liposomes. The values of the zeta potential of MLVs and UV-irradiated samples were not significantly different. Zeta potential values were negative due to the anionic phospholipids, including phosphatidylcholine, and higher (absolute value) than −30 mV, indicating that the MLVs and UV-irradiated samples are considered stable due to the relatively high repulsive forces, preventing the aggregation, flocculation, or sedimentation of their vesicles [70]. However, freeze drying and ultrasound waves significantly decreased the zeta potential (absolute value) of the obtained liposomes. The decrease in zeta potential after ultrasound treatment can be explained by the release of a small extent of the hydrophobic core or molecules due to the cavitation covering the negatively charged surface [63]. In the freeze-drying process, the temperature changes can decrease the zeta potential value and consequently, the crystal structure of the lipids was altered, and the release of encapsulated compounds from the liposomes was increased (that is also shown in Section 3.1.); in addition, the liposomal stability was reduced [48]. Chotphruethipong et al. [60] have also reported that active compounds plausibly liberated from liposomes can interact with a negative charge of phospholipids that, subsequently, can be partially neutralized, resulting in decreased negative surface charge. Several studies showed that the presence of hydrophobic compounds in the bilayer, particularly on the surface, can mask the negative charge [63,72,73]. The drop in the values of zeta potential after ultrasound treatment and lyophilization can result in decreased repulsive interactions between liposomal particles, low stability, and flocculation occurrence, since the negative charge was below −30 mV [63]. The conductivity of liposomal suspension follows the following trend: lyophilized liposomes > SUVs > UV-irradiated liposomes > MLVs. Since UV irradiation caused water evaporation from the liposome sample, the increase in the conductivity factor in the mentioned formulation should be explained by higher lipid and ion concentrations. On the other hand, a significantly higher conductivity factor of lyophilized liposomes and SUVs should be correlated with a lower EE. Namely, the increase in the conductivity factor in the liposome sample can be related to the release of entrapped components [74]. Since the mobility of liposomes is a function of the diameter, surface charge, and lipid composition of liposome vesicles, as well as the characteristics of encapsulated compounds [75], variations between different liposomal formulations were expected. The lower mobility of SUVs and lyophilized liposomes with silibinin compared to the MLV and UV-irradiated samples can be due to the potentially adsorbed flavonoid compound, such as silibinin, at the surface of the liposomal bilayer. Since ultrasound treatment and lyophilization cause the leakage of encapsulated compounds, which are proven by the lower EE in SUVs and lyophilized samples with silibinin (Table 1), the presence of silibinin from the outer membrane of the liposome is possible. Namely, according to Yang et al. [76], the presence of flavonoids on the liposome surface can result in decreased mobility.

A significant increase in vesicle size was noticed in all developed liposomes with silibinin during 60 days of storage at 4 °C. According to Hamadou et al. [43], the aggregation generated by the accumulation of liposomal vesicles can significantly influence liposome size and distribution. The most prominent increase can be noticed in the lyophilized sample, which showed the lowest absolute value of zeta potential (Table 1), i.e., the lowest potential to prevent the aggregation of particles. In the case of SUVs with encapsulated silibinin, the absolute value of zeta potential lower than 30 mV can be also responsible for a significant increase in particle diameter due to the decrease in repulsive interactions, both electrostatic and steric, creating a system that is prone to accumulation [42]. Additionally, the particle size of UV-irradiated liposomes showed consequential variations and, after the 21st day, their size was significantly higher in comparison to the non-treated parallel, suggesting the photochemical destruction of products due to absorption of photon energy and change in the liposome bilayer conformation [68,69]. Also, the predominant effect of UV light on the bilayer damage, i.e., photodegradation from highly disordered polyunsaturated fatty acids chains of phospholipids and the exposition of hydrophobic patches, could promote particle aggregation during storage time [69]. Moreover, physical factors can influence the shelf life of liposomes, such as aggregation/flocculation and fusion/coalescence, size changes, and drug loss, which represents an important disadvantage of liposome usage. Although lyophilization is suitable for liposomal bilayers with heat-sensitive compounds, the stability of lyophilized liposomes can be lost and depends on the freezing rate, liposome formulation technique, and membrane composition, as well as the residual moisture content. Thus, the optimization of the mentioned factors and/or the utilization of appropriate cryoprotectants can improve the stability, encapsulation efficiency, and biological potential of freeze-dried liposomal particles [77]. The potential strategies to mitigate these negative effects that occur during the freeze drying of liposomes for future studies can include the addition of cryoprotectants, such as carbohydrates (monosaccharides, disaccharides, polysaccharides, or synthetic saccharides), proteins (amino acids), and alcohols, as well as additional encapsulation of active compounds in various carriers, e.g., cyclodextrins (double loading technology). The addition of the mentioned cryoprotectants or cyclodextrins to the liposome formulation can prevent particle aggregation and the leakage of the encapsulated compounds and protect the liposomal bilayer from degradation caused by ice crystals [77,78]. The PDI value of the lyophilized sample showed a slight increase in heterogeneity, while the PDI significantly increased in MLVs and UV-irradiated and SUV liposomal suspensions, indicating less homogeneity and more aggregation. The PDI significantly affects the physical stability of the liposomal suspension and, therefore, the value should be as low as possible to provide the long-term stability of the nanosuspension vesicle size distribution [42]. A significant decrease in the zeta potential (absolute value) was noticed in all liposomal forms during the 60-day storage study. The Lopez-Polo et al. study [70] reported that the zeta potential of liquid and lyophilized liposomes (absolute value) decreased during storage at 4 °C, particularly in the case of dried form. All developed liposome formulations have retained negative values of zeta potential in the 60-day storage study. Since the polar heads or phosphate groups of phospholipids (mainly phosphatidylcholine) are responsible for the negative charge of the surface, it can be concluded that the reorganization of phospholipids in the lipid bilayer did not occur over time [63,72]. In addition, the decrease in zeta potential values during time can be explained by the size changes. Namely, according to the literature, the charge can be associated with the liposomal vesicle size, and the smallest size is correlated with a larger surface area, providing the exposure of the phosphate groups to the aqueous surrounding, which results in an increased negative charge [63]. Considering that over time, the particle size of all developed liposomes was significantly increased (Figure 1A), the values of zeta potential consequently decreased due to the lower surface area. The surface charge of liposomes might be partially neutralized via the interaction of negatively charged phospholipids with potentially released compounds, which lead to the enhanced aggregation of liposomal particles [60]. It was also evidenced by the decreased zeta potential and increased diameter of the vesicles of silibinin-loaded liposomes. In the 60-day storage study, the conductivity significantly increased in MLVs and SUVs with silibinin, whereas the mentioned parameter was not changed in the UV-irradiated sample. A significant drop in the conductivity of the lyophilized liposomes might be explained by the greater surface area (smaller liposomal vesicles on the 1st day) exposing a greater percentage of head groups of phospholipids that most notably affected the conductivity (higher conductivity factor on the 1st day) in comparison to larger vesicles at the end of the storage study [79]. The mobility of MLVs and UV-irradiated lipid vesicles with silibinin significantly decreased during storage, while the decrease in the mobility of SUVs and lyophilized samples was more gradual. A significant increase in vesicle size during storage (Figure 1A) can explain the drop in the mobility of all prepared liposomal formulations. Yanagihara et al. [80] have reported that liposomes' size affects their migration behavior in tissues, cells, and blood circulation.

A significantly lower density of liposomal suspension after UV irradiation and ultrasound treatment is probably due to the occurrence of hydrolytic reactions in aqueous surroundings. In addition, decreased density results in higher fluidity and less stability, which is important for the application in preparations that are intended for longer usage and storage [81,82]. The obtained values of surface tension are higher in comparison to the surface tension of different liposomes in the literature [53,83], probably due to the presence of various lipids in their liposomal bilayer, such as lecithin, which can have the role of surfactant and variations in the characteristics of encapsulated compounds. Since flavonoid compounds can be good stabilizers of emulsion systems, due to their adsorption at the surface [84], and SUVs showed a higher amount of silibinin in aqueous surroundings (lower EE, Table 1), it can explain the significantly lower surface tension in the mentioned sample. All developed liposomes with silibinin showed very low viscosity. According to the literature data, liposomal suspension with lower viscosity showed a significant change in the vesicle size of liposomes [81], which was also proven in the stability study of silibinin-loaded liposomes (Figure 1A). Based on Stoke's law, viscosity values are in reverse relation with the sedimentation of vesicles, i.e., an increment in viscosity can decrease the rate of sedimentation; the size distribution of high viscosity liposomes remained unchanged for a longer time and, therefore, more viscous formulations are more stable [81]. Thus, in the case of silibinin-loaded liposomes, viscosity modifiers should be used to decrease the chance of size separation and changes, as well as sedimentation.

UV irradiation did not cause significant changes in the ABTS and DPPH radical scavenging potential of silibinin-loaded liposomes, confirming the protective role of liposomal particles on bioactive compounds. On the other hand, freeze drying significantly decreased the antioxidant capacity of silibinin-loaded liposomes. A slow freezing rate can damage the lipid bilayer due to the formation of large ice crystals and induce deformations via mechanical stresses and osmotic pressure, resulting in the release of encapsulated antioxidants, i.e., lower EE [77] which is also determined in the case of silibinin-loaded liposomes (Table 1). Among all developed liposomes in the present study, the lyophilized sample possessed the lowest amount of encapsulated silibinin. In addition, since the antioxidant tests were performed after the reconstruction of lyophilized liposomes in water, it can lead to the rearrangement of the liposome structure, as well as the incomplete re-suspension of phospholipid particles, which can cause a decrease in the overall antioxidant potential of the liposomes [77]. Although SUVs also showed lower EE compared to MLVs and UV-irradiated liposomes, the effect of ultrasound waves positively influenced the antioxidant potential of liposomes with silibinin, probably due to a larger contact surface of smaller liposomal particles with free radicals. The antioxidant activity of pure silibinin was higher in both antioxidant tests. Therefore, it can be noticed that the liposome surroundings significantly influenced the antioxidant capacity of silibinin.

MLVs and lyophilized liposomes with silibinin did not cause a significant change in the viability of the HaCaT cells, while the UV-irradiated parallel possessed cytotoxic effects. On the other hand, SUVs showed a significant decrease in the viability of HaCaT cells. The obtained result can be related to potential free radicals and lipid peroxidation in liposomal suspension that can be produced due to UV irradiation and ultrasound treatment. UV irradiation caused the chemical changes in developed liposomes that were proven in the FT-IR and Raman analyses (Sections 3.5 and 3.6). Namely, free radicals (produced by ultrasound probe or under UV irradiation) can change the protein structure and induce apoptosis and the release of cytokines responsible for inflammatory reactions in the skin [85]. Free radicals trigger different biological responses via the activation of transcription factors as well, while lipid peroxidation induces the expression of vascular endothelial growth factors in human keratinocytes [85,86]. In the case of free radical-induced lipid oxidation, ferroptosis is a recognized form of programmed cell death different from apoptosis, necroptosis, and pyroptosis. According to the literature, ferroptosis is the basis of the pathogenesis of various skin diseases, including psoriasis, collagen diseases, and skin cancers [87]. In the previous paper, it was shown that UV-irradiated liposomes possessed Raman spectra bands with strong intensities located at 834 and 867 cm^{-1} as the most characteristic features of stearic acid [33]. In addition, the current study reported that FT-IR analysis confirmed the presence of bands in the spectra between 800 and 900 cm^{-1}, indicating the presence of hydroperoxide species for the UV-irradiated liposomes, a potentially oxidative derivative of stearic acid. In various papers, it was shown that stearic acid and its oxidative derivative are lipotoxic, decrease cell viability, and induce cell death [88,89]. This agrees with the observation related to the UV-irradiated liposomes in HaCaT cells, and it is plausible that an increase in stearic acid and its oxidative derivatives content confer their elevated cytotoxicity. The observed cytotoxic effect of empty liposomes can be explained by the excessive amount of phospholipids, which probably caused this cytotoxicity. It corresponds to what other authors observed, e.g., that cell death in HaCaT keratinocytes could be induced by the presence of large amounts of lecithin in the formulations [90]. In the study with the HEK-293 cells, the reduction in the cells' viability was perceived at the highest-used concentrations of lecithin-based systems: emulsions, liposomes, and aqueous lecithin dispersion (at 10% or 25%), while formulations diluted 10-fold (to a final phospholipid concentration of 0.12% and 0.5% in emulsions and other dispersions, respectively), did not cause any toxic effect on the cells [91]. According to the literature data, one of the main disadvantages of liposome usage is their degradation when the hydrocarbonate chains hydrolysate, the ester bond, to glycerol, and by the peroxidation of unsaturated chains, leading to short-chain lipids, which will form soluble derivatives, decreasing the quality of the liposomal system [29].

The cell treatment using liposomes with silibinin reduced ROS levels in comparison to cells exposed to H_2O_2 alone. The Li et al. study [92] showed that silibinin can decrease the mitochondrial ROS level. On the other hand, silibinin has been found to increase the ROS production involved in apoptosis and induce oxidative stress in cancer cell lines [93]. Since MLVs and all modified liposomal systems with silibinin showed a significant decrease in the ROS levels at the same concentration (0.1 μg/mL), it can be concluded that the modification technique did not have a significant influence on the antioxidant potential of the obtained liposomes. However, UV-irradiated liposomes and SUVs caused a significant decrease in ROS levels at the highest concentration. This was probably due to the smaller cell number producing ROS, considering that these concentrations of UV-irradiated liposomes and SUVs with silibinin reduced the cell viability as shown in MTT (Figure 7).

Namely, when unsaturated and other lipids are present in liposomal vesicles, photon energy emissions during UV irradiation can result in membrane disorders, due to the formation of free radicals through various processes, including one-electron redox reactions, thermal homolysis of the bonds, and high-energy radiation, as well as photolysis [69].

All developed liposomes with silibinin significantly reduced MIF expression in cells incubated for 24 h only with liposomes (without LPS). The results from the experiment where the cells were exposed to LPS confirmed the inhibitory effect on the MIF expression of all four liposomal forms. Namely, all tested liposomes with silibinin (non-modified and modified samples) significantly influenced the MIF expression, causing its inhibition. Thus, post-processing procedures for the liposomal modifications did not significantly affect the inhibitory capacity of the developed silibinin-loaded liposomes in terms of the MIF level. The Ramasamy et al. study [94] showed that silibinin decreased the level of MIF in tumor-associated macrophages. The pre-incubation of lyophilized liposomes significantly reduced the expression of IL-1β (in cells treated with LPS), whereas SUVs showed a reducing but not significant trend. In contrast, MLVs and UV-irradiated liposomes did not have a significant influence. Namely, the liposome size and its reduction (SUVs and lyophilized samples possessed a lower diameter, Table 1) play a significant role in terms of skin delivery because the mentioned parameter influences the penetration of encapsulated components through the skin to the deeper layers [29]. For example, the reduced particle size of liposomes was used to enhance their therapeutic efficacy in vitiligo [29]. The Peralta et al. study [95] has shown that liposomes with an average vesicle size of 100 nm function effectively as enhancers of skin penetration, consequently improving the efficiency of the applied preparation. Since silibinin has reduced the level of IL-1β in preeclamptic women, exhibiting potent anti-inflammatory activity [96], the reason for the absence of a significant down-modulation of inflammatory cytokine production, such as IL-1β, can be explained by its encapsulation in liposomal particles and potential prolonged or postponed release. In the case of lyophilized liposomes and SUVs with silibinin, the particle size was significantly lower in comparison to MLVs and UV-irradiated parallels; thus, a higher release of encapsulated silibinin due to a higher contact surface can be the reason for the better effect on the reduction of the IL-1β expression. The Yan et al. study [97] demonstrated that silibinin in liposomes had better effects on inflammation than silibinin alone in an in vivo model via modulating signaling pathways, but after oral and parenteral applications, due to excellent oral absorption and bioavailability.

5. Conclusions

Silibinin, as a potent antioxidant, antimicrobial, anti-inflammatory, and UV protective agent, was encapsulated in phospholipid liposomes to improve its stability and bioavailability. The liposomes obtained were further modified via UV irradiation, sonication, and lyophilization. The effect of UV irradiation, the ultrasound reduction of vesicle size, or freeze drying on the cytotoxic, antioxidant, and anti-inflammatory capacity of liposomes with encapsulated silibinin on keratinocytes, storage stability, and the FTIR and Raman fingerprint spectra were investigated for the first time in the present research. Different treatments of silibinin-loaded liposomes caused diverse effects on physicochemical properties and biological activities, depending on the type of the process. UV irradiation significantly changed the rheological characteristics of the liposomes and increased the cytotoxic effect on HaCaT cells due to chemical changes proven by FTIR and Raman spectroscopy. The freeze-drying process significantly affected the physical characteristics of liposomes, decreased their EE and ABTS and DPPH radical scavenging activity, and enhanced their anti-inflammatory potential (reduction of the expression of potent proinflammatory cytokine, IL-1β, in HaCaT cells treated with LPS). The sonication significantly decreased the EE and changed the physical and rheological characteristics of silibinin-liposomes, and slightly increased their cytotoxicity. On the other hand, the inhibitory effect on the expression of IL-1β and anti-ABTS and the anti-DPPH capacity of sonicated liposomes was significantly enhanced. All silibinin-loaded liposomes showed an increasing trend in particle size and a decreasing trend in zeta potential (absolute values) during storage. MLVs and lyophilized liposomes with silibinin showed promising antioxidant potential on ROS generated in HaCaT cells and anti-inflammatory activity via reducing MIF expression in HaCaT cells treated with LPS, and did not cause a cytotoxic effect. Due to the shown promising bioactivities related to skin cells and the possible synergistic beneficial effects of silibinin and phospholipids on human skin, the developed liposomal systems can find application in various cosmetic or pharmaceutical formulations. However, UV irradiation should not be used as a method for the sterilization of silibinin-loaded liposomes because of the shown cytotoxic potential of the obtained samples. Nevertheless, freeze drying can be employed as a technique for the prevention of hydrolytic and oxidative degradation in a final silibinin-liposome formulation due to preserved bioactivities (antioxidant and anti-inflammatory) and the absence of cytotoxic effect. Therefore, future perspectives will be focused on the optimization of the lyophilization process via varying the pressure, temperature, and time of the process, employing various types of cryoprotectants and their amounts, as well as on wound healing, anti-aging, and other potential effects of silibinin-loaded liposomes in sophisticated cell-based models of skin diseases, wounds, and aging.

Supplementary Materials: The following supporting information can be downloaded at: https://www.mdpi.com/article/10.3390/pharmaceutics16111476/s1, Figure S1: FT-IR spectra of Phospholipon (Ph), Phospholipon after UV irradiation (Ph UV), empty liposomes, and empty liposomes after UV irradiation (empty liposome UV); Figure S2: The structure of phosphatidylcholine (a) and silibinin A (b); Figure S3: FT-IR spectra of silibinin, empty liposomes, silibinin-loaded liposomes (MLVs), and UV-treated liposomes for different periods of 15–90 min of UV irradiation in the 1550–1800 cm^{-1} spectral region; Figure S4: The deconvolution of the 1550–1800 cm^{-1} spectral region before and after 30 min of UV irradiation of Phospolipon (Ph) and empty liposomes; Figure S5: The deconvolution of the 1550–1800 cm^{-1} spectral region of the silibinin-loaded liposomes (MLVs) and their UV-irradiated samples after 15, 30, 45, and 90 min; Figure S6: The UV-initiated time-dependent change of the peaks in the 600–1300 cm^{-1} region for Phospolipon (Ph) and empty liposomes; Table S1: The results of deconvolution of the Phospholipon (Ph), empty liposomes, and silibinin-loaded liposomes (MLVs) before and after the defined period of UV irradiation; Figure S7: Raman spectra of the initial components Phospholipon (A) and silibinin (B); Figure S8: Effect of 24 h pre-incubation with the empty liposomes in a range of phospholipid concentrations (1, 10, 100, 250, 500, and 1000 μg/mL) on the cell viability of HaCaT cells *versus* control (represented by dashed line); determined by MTT assay. Data are expressed as mean + SEM relative to the unexposed control (dashed line); * $p < 0.05$ by one-way analysis of variance (ANOVA) with Tukey's multiple comparison *post hoc* test; Figure S9: Effect of 24 h pre-incubation with the empty liposomes in a range of phospholipid concentrations (1, 10, 100, 250, 500, and 1000 μg/mL) on the production of reactive oxygen species in HaCaT cells *versus* control; determined by H2DCFDA assay. The data are expressed as mean + SEM; * $p < 0.05$ by one-way analysis of variance (ANOVA) with Tukey's multiple comparison *post hoc* test; Figure S10: Effect of 24 h pre-incubation with the empty liposomes at a concentration of 10 μg/mL on the protein expression of cyclooxygenase-2 (COX-2), interleukin 1 beta (IL-1β), and macrophage inhibitory factor (MIF) in HaCaT cells *versus* control; using the cELISA method. The data are expressed as mean + SEM.

Author Contributions: Conceptualization, A.A.K., M.M. and A.A.J.; Funding acquisition, A.M.; Investigation, A.A.K., B.S. and A.A.J.; Methodology, A.A.K., A.P., M.M., B.S. and A.A.J.; Resources, A.P., K.Š., A.M. and A.A.J.; Software, A.P., M.M. and B.S.; Supervision, K.Š., A.M. and A.A.J.; Writing—original draft, A.A.K.; Writing—review and editing, A.P., M.M., K.Š., A.M. and A.A.J. All authors have read and agreed to the published version of the manuscript.

Funding: Ministry of Science, Technological Development and Innovation of the Republic of Serbia, 451-03-65/2024-03/200135, 451-03-66/2024-03/200019, 451-03-66/2024-03/200026, and 451-03-47/2024-01/20003.

Institutional Review Board Statement: Not applicable.

Informed Consent Statement: Not applicable.

Data Availability Statement: The datasets generated during and/or analyzed during the current study are available from the corresponding author upon reasonable request.

Acknowledgments: The authors acknowledge their gratitude to the COST Action CA21108-European Network for Skin Engineering and Modeling (NETSKINMODELS) supported by European Cooperation in Science and Technology (COST).

Conflicts of Interest: The authors declare no conflicts of interest.

References

1. Michalak, M. Plant extracts as skin care and therapeutic agents. *Int. J. Mol. Sci.* **2023**, *24*, 15444. [CrossRef] [PubMed]
2. Ibrahim, N.'I.; Wong, S.K.; Mohamed, I.N.; Mohamed, N.; Chin, K.Y.; Ima-Nirwana, S.; Shuid, A.N. Wound healing properties of selected natural products. *Int. J. Environ. Res. Public Health* **2018**, *15*, 2360. [CrossRef] [PubMed]
3. Zhang, Z.; Li, X.; Sang, S.; McClements, D.J.; Chen, L.; Long, J.; Jiao, A.; Wang, J.; Jin, Z.; Qiu, C. A review of nanostructured delivery systems for the encapsulation, protection, and delivery of silymarin: An emerging nutraceutical. *Food Res. Int.* **2022**, *156*, 111314. [CrossRef] [PubMed]
4. Singh, R.P.; Agarwal, R. Flavonoid antioxidant silymarin and skin cancer. *Antioxid. Redox Signal.* **2002**, *4*, 655–663. [CrossRef]
5. Singh, R.P.; Agarwal, R. Cosmeceuticals and silibinin. *Clin. Dermatol.* **2009**, *27*, 479–484. [CrossRef]
6. Liu, C.H.; Jassey, A.; Hsu, H.Y.; Lin, L.T. Antiviral activities of silymarin and derivatives. *Molecules* **2019**, *24*, 1552. [CrossRef]
7. Zhao, F.; Li, X. Evaluation of immunomodulatory activity of silymarin extract from *Silybum marianum* in mice of health food. *Int. J. Food Process. Technol.* **2015**, *8*, 278–282. [CrossRef]
8. Ahmad, U.; Akhtar, J.; Singh, S.P.; Ahmad, F.J.; Siddiqui, S. Silymarin nanoemulsion against human hepatocellular carcinoma: Development and optimization. *Artif. Cells Nanomed. Biotechnol.* **2018**, *46*, 231–241. [CrossRef]
9. Verdura, S.; Cuyàs, E.; Ruiz-Torres, V.; Micol, V.; Joven, J.; Bosch-Barrera, J.; Menendez, J.A. Lung cancer management with silibinin: A historical and translational perspective. *Pharmaceuticals* **2021**, *14*, 559. [CrossRef]
10. Singh, R.P.; Dhanalakshmi, S.; Tyagi, A.K.; Chan, D.C.; Agarwal, C.; Agarwal, R. Dietary feeding of silibinin inhibits advance human prostate carcinoma growth in athymic nude mice and increases plasma insulin-like growth factor-binding protein-3 levels. *Cancer Res.* **2002**, *62*, 3063–3069.
11. Song, X.Y.; Liu, P.C.; Liu, W.W.; Hayashi, T.; Mizuno, K.; Hattori, S.; Fujisaki, H.; Ikejima, T. Protective effects of silibinin against ethanol- or acetaldehyde-caused damage in liver cell lines involve the repression of mitochondrial fission. *Toxicol. In Vitro* **2022**, *80*, 105330. [CrossRef] [PubMed]
12. García-Viñuales, S.; Ilie, I.M.; Santoro, A.M.; Romanucci, V.; Zarrelli, A.; Di Fabio, G.; Caflisch, A.; Milardi, D. Silybins inhibit human IAPP amyloid growth and toxicity through stereospecific interactions. *Biochim. Biophys. Acta Proteins Proteom.* **2022**, *1870*, 140772. [CrossRef] [PubMed]
13. Matsumura, Y.; Ananthaswamy, H.N. Toxic effects of ultraviolet radiation on the skin. *Toxicol. Appl. Pharmacol.* **2004**, *195*, 298–308. [CrossRef] [PubMed]
14. Mohammadi, M.; Ariafar, S.; Talebi-Ghane, E.; Afzali, S. Comparative efficacy of silibinin and nano-silibinin on lead poisoning in Male Wistar rats. *Toxicology* **2022**, *475*, 153242. [CrossRef] [PubMed]
15. Ephrem, E.; Najjar, A.; Charcosset, C.; Greige-Gerges, H. Encapsulation of natural active compounds, enzymes, and probiotics for fruit juice fortification, preservation, and processing: An overview. *J. Funct. Foods* **2018**, *48*, 65–84. [CrossRef]
16. Jovanović, A.; Balanč, B.; Djordjević, V.; Ota, A.; Skrt, M.; Šavikin, K.; Bugarski, B.; Nedović, V.; Poklar-Ulrih, N. Effect of gentisic acid on the structural-functional properties of liposomes incorporating β-sitosterol. *Colloids Surf. B Biointerfaces* **2019**, *183*, 110422. [CrossRef]
17. Kalušević, A.; Salević, A.; Jovanović, A.; Trifković, K.; Veljović, M.; Pravilović, R.; Nedović, V. Encapsulation of plant extracts in Encapsulation. In *Food Processing and Fermentation*; Lević, S., Nedović, V., Bugarski, B., Eds.; Taylor & Francis Group: London, UK, 2022; pp. 172–203. [CrossRef]
18. Desai, K.; Park, H. Recent developments in microencapsulation of food ingredients. *Dry. Technol.* **2005**, *23*, 1361–1394. [CrossRef]
19. Isailović, B.; Kostić, I.; Zvonar, A.; Đorđević, V.; Gašperlin, M.; Nedović, V.; Bugarski, B. Resveratrol loaded liposomes produced by different techniques. *Innov. Food Sci. Emerg. Technol.* **2013**, *19*, 181–189. [CrossRef]
20. Mozafari, M.; Johanson, C.; Hatziantoniou, S.; Demetzos, C. Nanoliposomes and their applications in food nanotechnology. *J. Liposome Res.* **2008**, *18*, 309–327. [CrossRef]
21. Taylor, T.; Davidson, P.; Bruce, D.; Weiss, J. Liposomal nanocapsules in food science and agriculture. *Crit. Rev. Food Sci. Nutr.* **2005**, *45*, 587–605. [CrossRef]
22. Jash, A.; Ubeyitogullari, A.; Rizvi, S. Liposomes for oral delivery of protein and peptide-based therapeutics: Challenges, formulation strategies, and advances. *J. Mater. Chem. B* **2021**, *9*, 4773–4792. [CrossRef] [PubMed]
23. Lee, M.-K. Liposomes for enhanced bioavailability of water-insoluble drugs: In vivo evidence and recent approaches. *Pharm.* **2020**, *12*, 264. [CrossRef] [PubMed]
24. Shade, C.W. Liposomes as advanced delivery systems for nutraceuticals. *Integr. Med.* **2016**, *15*, 33–36. [PubMed]
25. Srinivasan, V.; Chavan, S.; Jain, U.; Tarwadi, K. Liposomes for Nanodelivery Systems in Food Products. In *Nanoscience for Sustainable Agriculture*; Pudake, R., Chauhan, N., Kole, C., Eds.; Springer: Cham, Switzerland, 2019; pp. 627–638. [CrossRef]
26. Akbarzadeh, A.; Rezaei-Sadabady, R.; Davaran, S.; Joo, S.W.; Zarghami, N.; Hanifehpour, Y.; Samiei, M.; Kouhi, M.; Nejati-Koshki, K. Liposome: Classification, preparation, and applications. *Nanoscale Res. Lett.* **2013**, *8*, 102. [CrossRef]

27. Huang, X.; Caddell, R.; Yu, B.; Xu, S.; Theobald, B.; Lee, L.J.; Lee, R.J. Ultrasound-enhanced microfluidic synthesis of liposomes. *Anticancer Res.* **2010**, *30*, 463–466. [CrossRef]
28. Jovanović, A.; Balanč, B.; Ota, A.; Pegi, A.; Djordjević, V.; Šavikin, K.; Bugarski, B.; Nedović, V.; Poklar-Ulrih, N. Comparative effects of cholesterol and β-sitosterol on the liposome membrane characteristics. *Eur. J. Lipid Sci. Technol.* **2018**, *120*, 1–41. [CrossRef]
29. Castañeda-Reyes, E.D.; Perea-Flores, M.J.; Davila-Ortiz, G.; Lee, Y.; de Mejia, E.G. Development, characterization and use of liposomes as amphipathic transporters of bioactive compounds for melanoma treatment and reduction of skin inflammation: A review. *Int. J. Nanomed.* **2020**, *15*, 7627–7650. [CrossRef]
30. Yao, W.; Liu, C.; Wang, N.; Zhou, H.; Shafiq, F.; Yu, S.; Qiao, W. *O*-nitrobenzyl liposomes with dual-responsive release capabilities for drug delivery. *J. Mol. Liq.* **2021**, *334*, 116016. [CrossRef]
31. Munin, A.; Edwards-Lévy, F. Encapsulation of natural polyphenolic compounds; A review. *Pharmaceutics* **2011**, *3*, 793–829. [CrossRef]
32. Fang, Z.; Bhandari, B. Encapsulation of polyphenols—A review. *Trends Food Sci. Technol.* **2010**, *21*, 510–523. [CrossRef]
33. Jovanović, A.A.; Balanč, B.; Volić, M.; Pećinar, I.; Živković, J.; Šavikin, K.P. Rosehip extract-loaded liposomes for potential skin application: Physicochemical properties of non- and UV-irradiated liposomes. *Plants* **2023**, *12*, 3063. [CrossRef] [PubMed]
34. Petrović, S.; Taćić, A.; Savić, S.; Nikolić, V.; Nikolić, L.; Savić, S. Sulfanilamide in solution and liposome vesicles; *In vitro* release and UV-stability studies. *Saudi Pharm. J.* **2017**, *25*, 1194–1200. [CrossRef]
35. Zuhair, R.A.; Aminah, A.; Sahilah, A.M. Effect of extraction solvents on the phenolic content and antioxidant properties of two papaya cultivars. *J. Med. Plant Res.* **2013**, *7*, 3354–3359. [CrossRef]
36. Pirković, A.; Vilotić, A.; Borozan, S.; Nacka-Aleksić, M.; Bojić-Trbojević, Ž.; Krivokuća, M.J.; Battino, M.; Giampieri, F.; Dekanski, D. Oleuropein attenuates oxidative stress in human trophoblast cells. *Antioxidants* **2023**, *12*, 197. [CrossRef] [PubMed]
37. Bruić, M.; Pirković, A.; Borozan, S.; Nacka Aleksić, M.; Jovanović Krivokuća, M.; Spremo-Potparević, B. Antioxidative and anti-inflammatory effects of taxifolin in H_2O_2-induced oxidative stress in HTR-8/SVneo trophoblast cell line. *Reprod. Toxicol.* **2024**, *126*, 108585. [CrossRef]
38. Bojić-Trbojević, Ž.; Božić, M.; Vićovac, L. Steroid hormones modulate galectin-1 in the trophoblast HTR-8/SVneocell line. *Arch. Biol. Sci.* **2008**, *60*, 11–23. [CrossRef]
39. Tian, M.; Han, J.; Ye, A.; Liu, W.; Xu, X.; Yao, Y.; Li, K.; Kong, Y.; Wei, F.; Zhou, W. Structural characterization and biological fate of lactoferrin-loaded liposomes during simulated infant digestion. *J. Sci. Food Agric.* **2019**, *99*, 2677–2684. [CrossRef]
40. Nakhaei, P.; Margiana, R.; Bokov, D.O.; Abdelbasset, W.K.; Jadidi Kouhbanani, M.A.; Varma, R.S.; Marofi, F.; Jarahian, M.; Beheshtkhoo, N. Liposomes: Structure, biomedical applications, and stability parameters with emphasis on cholesterol. *Front. Bioeng. Biotechnol.* **2021**, *9*, 705886. [CrossRef]
41. Rahdar, A.; Sayyadi, K.; Sayyadi, J.; Yaghobi, Z. Nano-gels: A versatile nano-carrier platform for drug delivery systems: A mini review. *Nanomed. Res. J.* **2019**, *4*, 1–9. [CrossRef]
42. Chadorshabi, S.; Hallaj-Nezhadi, S.; Ghasempour, Z. Liposomal system based on lyophilization of a monophase solution for stabilization of bioactives from red onion skin. *LWT* **2022**, *172*, 114174. [CrossRef]
43. Hamadou, A.H.; Huang, W.C.; Xue, C.; Mao, X. Formulation of vitamin C encapsulation in marine phospholipids nanoliposomes: Characterization and stability evaluation during long term storage. *LWT Food Sci. Technol.* **2020**, *127*, 109439. [CrossRef]
44. Lewis, R.N.A.H.; McElhaney, R.N. Structures of the subgel phases of n-saturated diacyl phosphatidylcholine bilayers: FTIR spectroscopic studies of 13C=O and 2H labeled lipids. *Biophys. J.* **1992**, *61*, 63–77. [CrossRef] [PubMed]
45. Batinić, P.; Đorđević, V.; Stevanović, S.; Balanč, B.; Marković, S.; Luković, N.; Mijin, D.; Bugarski, B. Formulation and characterization of novel liposomes containing histidine for encapsulation of a poorly soluble vitamin. *J. Drug Deliv. Sci. Technol.* **2020**, *59*, 101920. [CrossRef]
46. Murru, C.; Badía-Laíño, R.; Díaz-García, M.E. Oxidative stability of vegetal oil-based lubricants. *ACS Sustain. Chem. Eng.* **2021**, *9*, 1459–1476. [CrossRef] [PubMed]
47. Lazzari, M.; Chiantore, O. Drying and oxidative degradation of linseed oil. *Polym. Degrad. Stab.* **1999**, *65*, 303–313. [CrossRef]
48. Sun, L.; Wang, H.; Du, J.; Wang, T.; Yu, D. Ultrasonic-assisted extraction of grape seed procyanidins, preparation of liposomes, and evaluation of their antioxidant capacity. *Ultrason. Sonochem.* **2024**, *105*, 106856. [CrossRef]
49. Narayanapillai, S.; Agarwal, C.; Tilley, C.; Agarwal, R. Silibinin is a potent sensitizer of UVA radiation-induced oxidative stress and apoptosis in human keratinocyte HaCaT cells. *Photochem. Photobiol.* **2012**, *88*, 1135–1140. [CrossRef]
50. Dhanalakshmi, S.; Mallikarjuna, G.U.; Singh, R.P.; Agarwal, R. Silibinin prevents ultraviolet radiation-caused skin damages in SKH-1 hairless mice via a decrease in thymine dimer positive cells and an up-regulation of p53-p21/Cip1 in epidermis. *Carcinogenesis* **2004**, *25*, 1459–1465. [CrossRef]
51. Medina-Torres, L.; Santiago-Adame, R.; Calderas, F.; Gallegos-Infante, J.A.; González-Laredo, R.F.; Rocha-Guzmán, N.E.; Núñez-Ramírez, D.M.; Bernad-Bernad, M.J.; Manero, O. Microencapsulation by spray drying of laurel infusions (*Litsea glaucescens*) with maltodextrin. *Ind. Crops Prod.* **2016**, *90*, 1–8. [CrossRef]
52. Czamara, K.; Majzner, K.; Pacia, M.Z.; Kochan, K.; Kaczor, A.; Baranska, M. Raman spectroscopy of lipids: A review. *J. Raman Spectrosc.* **2015**, *46*, 4–20. [CrossRef]
53. Jovanović, A.A.; Ćujić, D.; Stojadinović, B.; Čutović, N.; Živković, J.; Šavikin, K. Liposomal bilayer as a carrier of *Rosa canina* L. seed oil: Physicochemical characterization, stability, and biological potential. *Molecules* **2023**, *28*, 276. [CrossRef] [PubMed]

54. Šeremet, D.; Štefančić, M.; Petrović, P.; Kuzmić, S.; Doroci, S.; Mandura Jarić, A.; Vojvodić Cebin, A.; Pjanović, R.; Komes, D. Development, characterization and incorporation of alginate-plant protein covered liposomes containing ground ivy (*Glechoma hederacea* L.) extract into candies. *Foods* **2022**, *11*, 1816. [CrossRef] [PubMed]
55. Vasić, D.; Špirović Trifunović, B.; Pećinar, I.; Paunović, D.; Popović-Djordjević, J. Chemical characterization of *Rosa canina* L. rosehip seed: Application of Raman spectroscopy and gas chromatography. *Biol. Life Sci. Forum* **2021**, *3*, 50. [CrossRef]
56. Qiu, J.; Hou, H.-Y.; Yang, I.-S.; Chen, X.-B. Raman spectroscopy analysis of free fatty acid in olive oil. *Appl. Sci.* **2019**, *9*, 4510. [CrossRef]
57. Lee, C.; Bain, C.D. Raman spectra of planar supported lipid bilayers. *Biochim. Biophys. Acta Biomembr.* **2005**, *1711*, 59–71. [CrossRef]
58. Tan, J.M.; Karthivashan, G.; Arulselvan, P.; Fakurazi, S.; Hussein, M.Z. Characterization and *in vitro* sustained release of silibinin from pH responsive carbon nanotube-based drug delivery system. *J. Nanomater.* **2014**, *2014*, 439873. [CrossRef]
59. Solís-Gómez, A.; Sato-Berrú, R.Y.; Mata-Zamora, M.E.; Saniger, J.M.; Guirado-López, R.A. Characterizing the properties of anticancer silibinin and silybin B complexes with UV–Vis, FT-IR, and Raman spectroscopies: A combined experimental and theoretical study. *J. Mol. Struct.* **2019**, *1182*, 109–118. [CrossRef]
60. Chotphruethipong, L.; Hutamekalin, P.; Sukketsiri, W.; Benjakul, S. Effects of sonication and ultrasound on properties and bioactivities of liposomes loaded with hydrolyzed collagen from defatted sea bass skin conjugated with epigallocatechin gallate. *J. Food Biochem.* **2021**, *45*, e13809. [CrossRef]
61. Guldiken, B.; Gibis, M.; Boyacioglu, D.; Capanoglu, E.; Weiss, J. Physical and chemical stability of anthocyanin-rich black carrot extract-loaded liposomes during storage. *Int. Food Res. J.* **2018**, *108*, 491–497. [CrossRef]
62. Ghanbarzadeh, S.; Valizadeh, H.; Zakeri-Milani, P. The effects of lyophilization on the physico-chemical stability of sirolimus liposomes. *Adv. Pharm. Bull.* **2013**, *3*, 25–29. [CrossRef]
63. Sharma, K.; Nilsuwan, K.; Ma, L.; Benjakul, S. Effect of liposomal encapsulation and ultrasonication on debittering of protein hydrolysate and plastein from salmon frame. *Foods* **2023**, *12*, 761. [CrossRef] [PubMed]
64. Chen, C.; Han, D.; Cai, C.; Tang, X. An overview of liposome lyophilization and its future potential. *J. Control. Release* **2010**, *142*, 299–311. [CrossRef] [PubMed]
65. Chen, C.; Han, D.; Zhang, Y.; Yuan, Y.; Tang, X. The freeze-thawed and freeze-dried stability of cytarabine-encapsulated multivesicular liposomes. *Int. J. Pharm.* **2010**, *387*, 147–153. [CrossRef] [PubMed]
66. Morais, H.A.; da Silva Barbosa, C.M.; Delvivo, F.M.; Mansur, H.S.; de Oliveira, C.M.; Silvestre, M.P.C. Comparative study of microencapsulation of casein hydrolysates in lipospheres and liposomes. *J. Food Biochem.* **2004**, *28*, 21–41. [CrossRef]
67. Silva, R.; Ferreira, H.; Little, C.; Cavaco-Paulo, A. Effect of ultrasound parameters for unilamellar liposome preparation. *Ultrason. Sonochem.* **2010**, *17*, 628–632. [CrossRef]
68. Wong-Ekkabut, J.; Xu, Z.; Triampo, W.; Tang, I.M.; Tieleman, D.P.; Monticelli, L. Effect of lipid peroxidation on the properties of lipid bilayers: A molecular dynamics study. *Biophys. J.* **2007**, *93*, 4225–4236. [CrossRef]
69. Toopkanloo, S.P.; Tan, T.B.; Abas, F.; Azam, M.; Nehdi, I.A.; Tan, C.P. Improving vesicular integrity and antioxidant activity of novel mixed soy lecithin-based liposomes containing squalene and their stability against UV light. *Molecules* **2020**, *25*, 5873. [CrossRef]
70. Lopez-Polo, J.; Silva-Weiss, A.; Giménez, B.; Cantero-López, P.; Vega, R.; Osorio, F.A. Effect of lyophilization on the physicochemical and rheological properties of food grade liposomes that encapsulate rutin. *Food Res. Int.* **2020**, *130*, 108967. [CrossRef]
71. Arias-Alpizar, G.; Kong, L.; Vlieg, R.C.; Rabe, A.; Papadopoulou, P.; Meijer, M.S.; Bonnet, S.; Vogel, S.; van Noort, J.; Kros, A.; et al. Light-triggered switching of liposome surface charge directs delivery of membrane impermeable payloads *in vivo*. *Nat. Commun.* **2020**, *11*, 3638. [CrossRef]
72. Hosseini, S.F.; Ramezanzade, L.; Nikkhah, M. Nano-liposomal entrapment of bioactive peptidic fraction from fish gelatin hydrolysate. *Int. J. Biol. Macromol.* **2017**, *105*, 1455–1463. [CrossRef]
73. Bouarab, L.; Maherani, B.; Kheirolomoom, A.; Hasan, M.; Aliakbarian, B.; Linder, M.; Arab-Tehrany, E. Influence of lecithin–lipid composition on physico-chemical properties of nanoliposomes loaded with a hydrophobic molecule. *Colloids Surf. B Biointerfaces* **2014**, *115*, 197–204. [CrossRef] [PubMed]
74. Froude, V.E.; Zhu, Y. Dielectrophoresis of functionalized lipid unilamellar vesicles (liposomes) with contrasting surface constructs. *J. Phys. Chem. B* **2009**, *113*, 1552–1558. [CrossRef] [PubMed]
75. Duffy, C.; Gafoor, S.; Richards, D.; Admadzadeh, H.; O'Kennedy, R.; Arriaga, E. Determination of properties of individual liposomes by capillary electrophoresis with postcolumn laser-induced fluorescence detection. *Anal. Chem.* **2001**, *73*, 1855–1861. [CrossRef] [PubMed]
76. Yang, D.; Wang, X.; Gan, L.; Zhang, H.; Shin, J.; Lee, K.; Hong, S. Effects of flavonoid glycosides obtained from a *Ginkgo biloba* extract fraction on the physical and oxidative stabilities of oil-in-water emulsions prepared from a stripped structured lipid with a low omega-6 to omega-3 ratio. *Food Chem.* **2015**, *174*, 124–131. [CrossRef]
77. Yu, J.Y.; Chuesiang, P.; Shin, G.H.; Park, H.J. Post-processing techniques for the improvement of liposome stability. *Pharmaceutics* **2021**, *13*, 1023. [CrossRef]
78. Sebaaly, C.; Charcosset, C.; Stainmesse, S.; Fessi, H.; Greige-Gerges, H. Clove essential oil-in-cyclodextrin-in-liposomes in the aqueous and lyophilized states: From laboratory to large scale using a membrane contactor. *Carbohydr. Polym.* **2016**, *138*, 75–85. [CrossRef]

79. Lidgate, D.; Hegde, S.; Maskiewicz, R. Conductivity measurement as a convenient technique for determination of liposome capture volume. *Int. J. Pharm.* **1993**, *96*, 51–58. [CrossRef]
80. Yanagihara, S.; Kitayama, Y.; Yuba, E.; Harada, A. Preparing size-controlled liposomes modified with polysaccharide derivatives for pH-responsive drug delivery applications. *Life* **2023**, *13*, 2158. [CrossRef]
81. Narenji, M.; Talaee, M.R.; Moghimi, H.R. Investigating the effects of size, charge, viscosity and bilayer flexibility on liposomal delivery under convective flow. *Int. J. Pharm.* **2016**, *513*, 88–96. [CrossRef]
82. Zheng, L.; Li, B.; Lin, P.; Zhang, X.; Zhang, C.; Zhao, B.; Wang, T. Sedimentation and precipitation of nanoparticles in power-law fluids. *Microfluid. Nanofluidics* **2013**, *15*, 11–18. [CrossRef]
83. Čutović, N.; Marković, T.; Carević, T.; Stojković, D.; Bugarski, B.; Jovanović, A.A. Liposomal and liposomes-film systems as carriers for bioactives from *Paeonia tenuifolia* L. petals: Physicochemical characterization and biological potential. *Pharmaceutics* **2023**, *15*, 2742. [CrossRef] [PubMed]
84. Luo, Z.; Murray, B.S.; Yusoff, A.; Morgan, M.R.; Povey, M.J.; Day, A.J. Particle-stabilizing effects of flavonoids at the oil−water interface. *J. Agric. Food Chem.* **2011**, *59*, 2636–2645. [CrossRef] [PubMed]
85. Nakai, K.; Tsuruta, D. What Are Reactive Oxygen Species, Free Radicals, and Oxidative Stress in Skin Diseases? *Int. J. Mol. Sci.* **2021**, *22*, 10799. [CrossRef] [PubMed]
86. Nakai, K.; Yoneda, K.; Ishihara, Y.; Ohmori, K.; Moriue, T.; Igarashi, J.; Kohno, M.; Kosaka, H.; Kubota, Y. Lipid peroxidation-induced VEGF expression in the skin of KKAy obese mice. *Exp. Dermatol.* **2011**, *20*, 388–393. [CrossRef]
87. Dixon, S.J.; Lemberg, K.M.; Lamprecht, M.R.; Skouta, R.; Zaitsev, E.M.; Gleason, C.E.; Patel, D.N.; Bauer, A.J.; Cantley, A.M.; Yang, W.S.; et al. Ferroptosis: An iron-dependent form of nonapoptotic cell death. *Cell* **2012**, *149*, 1060–1072. [CrossRef]
88. Yang, Y.; Huang, J.; Li, J.; Yang, H.; Yin, Y. Effects of stearic acid on proliferation, differentiation, apoptosis, and autophagy in porcine intestinal epithelial cells. *Curr. Mol. Med.* **2020**, *20*, 157–166. [CrossRef]
89. Ying, L.; Yajun, C.; Jinwei, L.; Yuanpeng, W.; Yuanfa, L. Epoxy stearic acid, an oxidative product derived from oleic acid, induces cytotoxicity, oxidative stress, and apoptosis in HepG2 cells. *J. Agric. Food Chem.* **2018**, *66*, 5237–5246. [CrossRef]
90. Tran, H.-M.; Yang, C.-Y.; Wu, T.-H.; Yen, F.-L. Liposomes encapsulating morin: Investigation of physicochemical properties, dermal absorption improvement and anti-aging activity in pm-induced keratinocytes. *Antioxidants* **2022**, *11*, 1183. [CrossRef]
91. Płaczek, M.; Wątróbska-Świetlikowska, D.; Stefanowicz-Hajduk, J.; Drechsler, M.; Ochocka, J.R.; Sznitowska, M. Comparison of the *in vitro* cytotoxicity among phospholipid-based parenteral drug delivery systems: Emulsions, liposomes and aqueous lecithin dispersions (WLDs). *Eur. J. Pharm. Sci.* **2019**, *127*, 92–101. [CrossRef]
92. Li, W.; Qu, X.; Kang, X.; Zhang, H.; Zhang, X.; Hu, H.; Yao, L.; Zhang, L.; Zheng, J.; Zheng, Y.; et al. Silibinin eliminates mitochondrial ROS and restores autophagy through IL6ST/JAK2/STAT3 signaling pathway to protect cardiomyocytes from doxorubicin-induced injury. *Eur. J. Pharmacol.* **2022**, *929*, 175153. [CrossRef]
93. Zhang, H.; Kim, H.; Kim, S.Y.; Hai, H.; Kim, E.; Ma, L.; Kim, D.; Kim, C.Y.; Park, K.; Park, S.; et al. Silibinin induces oral cancer cell apoptosis and reactive oxygen species generation by activating the JNK/c-Jun pathway. *J. Cancer* **2023**, *14*, 1875–1887. [CrossRef] [PubMed]
94. Ramasamy, K.; Deep, G.; Tyagi, A.; Agarwal, C.; Agarwal, R. Silibinin inhibits tumor associated macrophages-induced lung cancer cell growth and invasiveness by down-regulating macrophage migration inhibitory factor. In Proceedings of the 104th Annual Meeting of the American Association for Cancer Research, Washington, DC, USA, 6–10 April 2013. [CrossRef]
95. Peralta, M.F.; Guzmán, M.L.; Pérez, A.P.; Apezteguia, G.A.; Fórmica, M.L.; Romero, E.L.; Olivera, M.E.; Carrer, D.C. Liposomes can both enhance or reduce drugs penetration through the skin. *Sci. Rep.* **2018**, *8*, 13253. [CrossRef] [PubMed]
96. Giorgi, V.S.; Peracoli, M.T.; Peracoli, J.C.; Witkin, S.S.; Bannwart-Castro, C.F. Silibinin modulates the NF-κb pathway and pro-inflammatory cytokine production by mononuclear cells from preeclamptic women. *J. Reprod. Immunol.* **2012**, *95*, 67–72. [CrossRef] [PubMed]
97. Yan, B.; Zheng, X.; Wang, Y.; Yang, J.; Zhu, X.; Qiu, M.; Xia, K.; Wang, Y.; Li, M.; Li, S.; et al. Liposome-based silibinin for mitigating nonalcoholic fatty liver disease: Dual effects *via* parenteral and intestinal routes. *ACS Pharmacol. Transl. Sci.* **2023**, *6*, 1909–1923. [CrossRef]

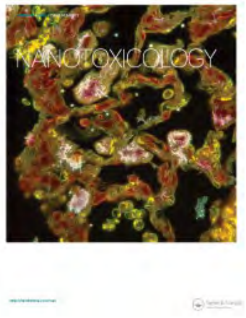

Nanotoxicology

ISSN: 1743-5390 (Print) 1743-5404 (Online) Journal homepage: www.tandfonline.com/journals/inan20

Probing the effects of dextran-coated CeO_2 nanoparticles on lung fibroblasts using multivariate single-cell Raman spectroscopy

Mirjana Mićević, Sonja Čalija, Lela Korićanac, Jelena Žakula, Aleksandra Vilotić, Marko Radović, Igor Golić, Aleksandra Korać, Mirjana Nacka-Aleksić, Bojan Stojadinović & Zorana Dohčević-Mitrović

To cite this article: Mirjana Mićević, Sonja Čalija, Lela Korićanac, Jelena Žakula, Aleksandra Vilotić, Marko Radović, Igor Golić, Aleksandra Korać, Mirjana Nacka-Aleksić, Bojan Stojadinović & Zorana Dohčević-Mitrović (2025) Probing the effects of dextran-coated CeO_2 nanoparticles on lung fibroblasts using multivariate single-cell Raman spectroscopy, Nanotoxicology, 19:1, 100-118, DOI: 10.1080/17435390.2025.2453576

To link to this article: https://doi.org/10.1080/17435390.2025.2453576

NANOTOXICOLOGY
2025, VOL. 19, NO. 1, 100–118
https://doi.org/10.1080/17435390.2025.2453576

Taylor & Francis
Taylor & Francis Group

RESEARCH ARTICLE

OPEN ACCESS

Probing the effects of dextran-coated CeO_2 nanoparticles on lung fibroblasts using multivariate single-cell Raman spectroscopy

Mirjana Mićević[a], Sonja Čalija[a], Lela Korićanac[b], Jelena Žakula[b], Aleksandra Vilotić[c], Marko Radović[d], Igor Golić[e], Aleksandra Korać[e], Mirjana Nacka-Aleksić[c], Bojan Stojadinović[a] and Zorana Dohčević-Mitrović[a]

[a]Institute of Physics Belgrade, University of Belgrade, Belgrade, Serbia; [b]Vinča Institute of Nuclear Sciences, National Institute of the Republic of Serbia, University of Belgrade, Belgrade, Serbia; [c]Institute for the Application of Nuclear Energy, Department for Biology of Reproduction, University of Belgrade, Belgrade, Serbia; [d]BioSense Institute, University of Novi Sad, Novi Sad, Serbia; [e]Center for Electron Microscopy, Faculty of Biology, University of Belgrade, Belgrade, Serbia

ABSTRACT

In this study, we investigated the cytotoxic effect of highly soluble dextran-coated CeO_2 nanoparticles on human fetal lung fibroblasts MRC-5. We examined individual nanoparticle-treated cells by Raman spectroscopy and analyzed Raman spectra using non-negative principal component analysis and k-means clustering. In this way, we determined dose-dependent differences between treated cells, which were reflected through the intensity change of lipid, phospholipid and RNA-related Raman modes. Performing standard biological tests for cell growth, viability and induction of apoptosis in parallel, these changes were correlated with nanoparticle-induced apoptotic processes. The cells with specific spectral characteristics, referring to non-apoptotic, but possibly autophagic cell death modality, were also detected. Additionally, Raman imaging combined with principal component and vertex component analysis was used to map the spatial distribution of biological molecules in treated and untreated cells. This work provided the description of different resulting states of the treated cells depending on the dextran-coated CeO_2 nanoparticles dose, which can be later used in the design of the nanoparticles for industrial or medical applications. The wide content of information resulting from single-cell Raman spectroscopy has the potential to detect biochemical changes caused by nanoparticles that would otherwise require a series of expensive and time-consuming standard biological techniques.

ARTICLE HISTORY
Received 17 July 2024
Revised 17 December 2024
Accepted 2 January 2025

KEYWORDS
CeO_2; MRC-5 fibroblasts; Raman spectroscopy; PCA; VCA

1. Introduction

Cerium oxide (CeO_2) is a rare earth metal oxide, characterized by a fluorite cristal structure with a significant concentration of oxygen vacancies (Campbell and Peden 2005). Cerium can exist in two oxidation forms, Ce^{3+} and Ce^{4+} (Reed et al. 2014). By receiving or releasing one or more oxygen atoms from crystal lattice and changing the Ce^{3+}/Ce^{4+} ratio at the same time, cerium oxide can easily cycle between CeO_2 and CeO_{2-x} states. Such characteristics provide CeO_2 with excellent redox and catalytic capabilities, used for industrial application (Ma et al. 2018), but also crucial for biological activities. Namely, CeO_2 nanoparticles (NPs) can mimic the activity of numerous cellular enzymes, like superoxide dismutase and catalase, but also oxidase and peroxidase (Walkey et al. 2015; Feng et al. 2022). This means that those NPs can act both as scavenger and generator of harmful reactive oxygen species (ROS) in the cell. The imbalance between the pro-oxidant and anti-oxidant activities of CeO_2 can lead to oxidative stress, resulting in apoptotic cell death, which is considered the main reason for the possible cytotoxicity of these NPs (Jana et al. 2014; Mittal and Pandey 2014; Nourmohammadi et al. 2019).

Nowadays, CeO_2 NPs are present in a large number of industrial products, such as fuel catalysts, polishing agents, gas sensors etc. (Reed et al. 2014; Zhou et al. 2021; Jung, Kittelson, and Zachariah 2005; Mangalaraja et al. 2010). Emitted into the air

CONTACT Mirjana Mićević mmicevic@institut-cacak.org; mileticjm@ipb.ac.rs Fruit Research Institute, Kralja Petra I 9, 32000 Čačak, Serbia.

Supplemental data for this article can be accessed online at https://doi.org/10.1080/17435390.2025.2453576.

from such sources, they can be inhaled and potentially affect the lungs and other internal organs. The toxicity of inhaled CeO_2 NPs, manifested by decreased viability of lung cells and induction of inflammation, has been demonstrated in some *in vivo* studies in rat and mouse model systems (Srinivas et al. 2011; Guo et al. 2019). It has also been shown that these NPs can cause pulmonary fibrosis, a very serious and progressive disease with fatal outcome (Annangi et al. 2021; Hill et al. 2019). Contrary to these studies, other *in vivo* and *in vitro* experiments showed that CeO_2 NPs can protect cells from the negative influence of free radicals, such as those from cigarette smoke (Niu, Wang, and Kolattukudy 2011; Chen et al. 2006). There is limited information about the mechanisms of CeO_2 NPs interactions with different bronchiolar and alveolar cell types and their interplay during lung tissue remodeling (Annangi et al. 2021; Ma et al. 2012).

MRC-5 is a cell line derived from human fetal lung fibroblasts, connective tissue cells that play a key role in the development of pulmonary fibrosis (Ortiz-Zapater et al. 2022). In the literature, only few data about the possible cytotoxic effect of CeO_2 NPs on these cells are available and the results of the performed studies are not clear and consistent, evidencing both weak and strong cytotoxicity (Pešić et al. 2015; Spezzati et al. 2017; Alghamdi 2023). Some studies have shown that the cytotoxic effect is highly dependent on the dimensions of NPs and the size of their agglomerates in dispersion, which are usually present due to CeO_2 poor solubility (Abdi Goushbolagh et al. 2018). In recent decades, researchers have investigated surface modifications that would address the solubility problem. One such modification concerns the coating of NPs with dextran. Dextran molecules have been shown to successfully stabilize the surface charge of CeO_2 NPs and prevent agglomeration, without affecting the redox properties and toxicity of CeO_2 *per se* (Naha et al. 2020; Perez et al. 2008; Yazici, Alpaslan, and Webster 2015; Karakoti et al. 2007).

The most common methods for screening the cytotoxicity of NPs are based on the loss of cell membrane integrity or mitochondrial membrane potential, demonstrating the physical state of the cells, with no insight into the underlying mechanisms. To detect more specific biochemical changes caused by NPs, e.g. DNA degradation or expression of a protein of interest, several standard methods that include labels, dyes or antibodies would be required (Drasler et al. 2017). With some of them NPs can interfere, which makes the result of the experiment irrelevant (Monteiro-Riviere, Inman, and Zhang 2009). On the other hand, Raman spectroscopy gives an insight into the entire chemical composition of the cell and the structures of present biomolecules (Ferraro, Nakamoto, and Brown 2003). Physiological or pathological changes in the cell that lead to a change in its biochemical composition are reflected in the cell's Raman spectrum (Brauchle et al. 2014; Shin et al. 2019; Wieland et al. 2021; Short et al. 2005; Lasalvia, Perna, and Capozzi 2019). Since the Raman spectrum of a NP-treated cell contains information about the effect of NPs on numerous cellular macromolecules, it can be used to simultaneously monitor several changes, for which several conventional biological methods are usually needed. Furthermore, Raman spectroscopy is a non-destructive, biocompatible method that does not require additional chemicals and labels. Consequently, Raman spectroscopy offers great possibilities in screening and studying the effects of NPs on human cells.

Raman measurements are most often performed on a single cell, which is another advantage compared to conventional methods for evaluating the effects of NPs on the cells (Brauchle et al. 2014; Ma et al. 2021; Pavillon and Smith 2023). Differences in the Raman spectra of NP-treated cells enable monitoring of different modalities of interactions between NPs and the cell and correlate spectroscopic with biochemical and morphological changes (Lasalvia, Perna, and Capozzi 2019; Fazio et al. 2020). For this purpose, Raman images, showing the spatial distribution of spectral information, are of great help (Harvanova et al. 2017; Ahlinder et al. 2013). To assess the effects of NPs on the cell culture as a whole, it is necessary to analyze the Raman spectra of a large number of cells using multivariate statistical methods. In this way, cells can be grouped and classified according to the effects of NPs and finally can be compared with each other. One of the common methods used for this application is principal component analysis (PCA) (Brauchle et al. 2014; Pavillon and Smith 2023; Schie et al. 2014; Crow et al. 2005). In a previous publication, we showed that the relatively new and non-standard method of non-negative PCA (nnPCA) is particularly suitable for the analysis of cells' spectra, since in the resulting components, which show the differences between the analyzed spectra, Raman spectral features of specific molecules are easily recognized (Miletić et al. 2023). Particular attention was paid to the lipid features of the Raman spectrum as potentially important for recognizing the degree of cell damage caused by NPs. Vertex component analysis (VCA) is another unsupervised method of multivariate statistics. While PCA components represent linear combinations of original variables that capture the variability of the data set in the best way, the VCA algorithm extracts pure components, so-called endpoints, which are differently abundant in each of the original variables (Nascimento and Dias 2005). If Raman spectra are collected at many points across the entire cell, the contribution of each VCA component can be quantified for each point and used to create a color image of the cell. This method is less frequently used than PCA (Mazur et al. 2013; Hedegaard et al. 2011; Krafft et al. 2011; Zuser et al. 2010; Liu et al. 2022) for the analysis of the cells' Raman spectra. There are only few published studies that used VCA for Raman imaging of NP-treated cells, and none of them addressed the cytotoxic effect of NPs (Chernenko et al. 2009; Chernenko et al. 2013; Tolstik et al. 2016).

In this work, the cytotoxic effect of dextran-coated CeO_2 NPs on MRC-5 cells was studied using vibrational Raman spectroscopy. To the best of our knowledge, there is no data in the available literature on the effect of dextran or similar material coated CeO_2 NPs on MRC-5 cells. Dose-dependent differences among cell spectra were analyzed primarily using nnPCA. Raman spectra combined with PCA and VCA were also used to obtain Raman-PCA/Raman-VCA images, showing the differences in the spatial distribution of biomolecules of control and treated cells. In addition to Raman spectroscopy, several conventional biological methods were employed to detect changes in cell growth, metabolic activity and induction of apoptosis in NP-treated MRC-5 cells. The performed experiments aimed to expand knowledge about safety issues related to the use of CeO_2 NPs in industry and medicine, applying for this purpose a comprehensive approach of Raman spectroscopy and at the same time examining the potential of the given methodology in this scientific field.

2. Materials and methods

2.1. Cell culture

MRC-5 cells (ATCC, USA), human fetal lung fibroblasts, were cultured in DMEM high glucose content medium (Sigma-Aldrich, USA) supplemented with 10 % fetal calf serum (FCS, Sigma-Aldrich) (v/v) and 1 % antibiotic/antimycotic solution (Sigma-Aldrich), in a humidified atmosphere with 5 % CO_2 at 37◦C.

MRC-5 is a normal diploid human cell line with a 46, XY karyotype, derived from normal lung tissue of a 14-week-old male embryo (Jacobs et al., 1970). The modal number of chromosomes is 46 and occurs in 70 % of cells, with the polyploidy rate of 3.6 %. Cells are capable of 42 to 46 population doublings before senescence begins. MRC-5 cells display a fibroblast-like morphology, with a diameter of approximately 18 µm. Doubling time can vary between 35 and 45 hours, depending on cultivation conditions. MRC-5 cells used in this study were between 25 and 30 population doublings (ATCC n.d.; Cytion n.d.).

2.2. NPs synthesis and cell treatment

Dextran-coated CeO_2 (CD) NPs were synthesized according to the synthesis procedure by Karakoti et al (Karakoti et al. 2007). Briefly, 0.5 g of cerium nitrate hexahydrate was added in 50 ml of 0.135 mM dextran T40 solution in deionized water. The resulting solution was oxidized with 0.05 ml of 30 % ammonia and stirred for 24 hours. 24 hours after cell seeding, the cell culturing medium is replaced with a fresh medium containing 100 µg/ml, 200 µg/ml or 400 µg/ml CD NPs and incubated for 48 hours. Synthesized NPs were stable in dispersion, with an average grain size of 3–4 nm and the hydrodynamic radius of 47 nm (Miletić et al. 2020).

2.3. NPs characterization

The grain size of NPs was estimated using transmission electron microscopy, while crystalline structure and average crystallite size was determined from X-ray diffraction (XRD) spectra, as described in our previous study (Miletić et al. 2020). The specific surface area and porosity of the nanoparticles were determined using a gas-adsorption analyzer, SURFER ANALYZER 11510300 (Thermo Fisher Scientific). Before measuring, the powder samples were degassed under vacuum ($10–^2$ Torr) at 150 °C for 2 hours to remove any adsorbed gases. The Brunauer-Emmett-Teller (BET) analysis method was employed to calculate the specific surface area. Average hydrodynamic radius of NP was determined by dynamic light scattering (DLS), also described earlier (Miletić et al. 2020).

2.4. SRB assay

Cells were cultured in 96-well plates with seeding density of 7000 cells/well. Next day the cells were treated with CD NPs, incubated for 48 h and then fixed with trichloroacetic acid. After fixation, the cells were stained for 15 min with 0.4 % (wt/vol) sulforhodamine B (SRB) (Sigma-Aldrich) dissolved in 1 % acetic acid. Washing with 1 % acetic acid repeated in four steps was applied to remove unbound dye. SRB which stayed bound was extracted with 10 mM unbuffered Tris base (Sigma-Aldrich). The absorbance of the extracted dye solution was measured at 550 nm in a microplate reader (Wallac, VICTOR2 1420 Multilabel counter, PerkinElmer, Finland). The absorbance values obtained for NPs without the cells (blank) was subtracted from the values obtained for samples. Results were presented as percent of the control, where the cell growth of control is set to 100 %, in the form of mean values ± standard error. The assay was performed three times in three replicates for every experimental group. Statistical significance of differences between treated and untreated cells was estimated by one-way analysis of variance (ANOVA) and *post-hoc* Tukey test, performed in R.

2.5. MTT assay

Cells were seeded in 96-well plates at density of 7000 cells/well and next day treated with CD NPs. After 48 h, the cell culture medium with NPs was discarded and 100 µl of fresh culture medium containing 0.5 mg/ml of MTT (Sigma-Aldrich) was added. Upon 2 h of incubation at 37 °C and 5 % CO_2, 100 µl of 10 % SDS (0.01 N HCl) was added to each well and the plate was incubated at 37 °C overnight. The absorbance was measured at 570 nm on a microplate reader (ELx800, BioTek). Results were calculated by subtracting absorbance values obtained for blank (NPs without the cells) from the values obtained for samples and the average value for the control cells (cells without NPs) was set to 100 %. Results were presented as percent of the control. Experiments were repeated three times in three replicates. The data are presented as mean ± standard error. One-way ANOVA with Tukey *post-hoc* test performed in R was used for statistical analyses since the data followed a normal distribution.

2.6. Apoptosis detection

For apoptosis detection, a commercial FITC Annexin V Apoptosis Detection Kit with PI (Biolegend, USA) was used. The protocol given by the manufacturer was adapted for staining on microscope slides. The cells were grown for 48 h on 20 × 20 mm glass slides in a cell culture medium, after which the medium was removed. The slides were rinsed twice with PBS and immersed in annexin-V binding buffer with annexin-V-FITC (5 µl/100 µl of buffer) and propidium iodide (PI; 10 µl/100 µl of buffer) added. After 15 min of incubation at room temperature in the dark, slides were rinsed twice in PBS and air dried. In the final step of sample preparation, microscope cover slips were mounted to slides with the aid of mounting medium Mowiol (Sigma-Aldrich). The samples were analyzed by Leica TCS SP5 II confocal microscope (Leica Microsystems, Germany), equipped with acusto-optic tunable filter and acusto-optic beam splitter for excitation-emission separation. The emitted radiation of various wavelengths is taken to two photomultiplier tubes for detection. Visualization was achieved by excitation of FITC with 488 nm Ar laser and PI with 543 nm HeNe laser. The emitted fluorescence was detected in sequential mode via the green (FITC) and red (PI) channels, to avoid signal overlap between the channels. Samples with untreated cells that underwent exactly the same staining and preparation procedure as treated cells were used as negative controls. At least six fields of view were recorded from each sample.

For assessing the frequency of apoptotic cells by flow cytometry, the same FITC Annexin V/PI kit was used, following the manufacturer's instructions for flow cytometry. In brief, untreated MRC-5 cells and cells incubated with NPs for 48 h were washed twice in PBS supplemented with 2 % FCS and 0.01 % NaN_3 (Sigma-Aldrich Chemie GmbH), and resuspended in Annexin V Binding Buffer. Next, 5 µL of FITC-conjugated annexin V and 10 µL of PI solution were added to the cells and incubated for 15 min at room temperature in the dark. For analysis, 50 000 events per sample were acquired on a flow cytometer (LSR II, Becton Dickinson, East Rutherford, NJ, USA). Data were analyzed using FlowJo v10 software (TreeStar Inc., Achland, OR, USA). One-way ANOVA with Tukey *post-hoc* test was used for statistical analyses.

2.7. Transmission electron microscopy (TEM)

NP-treated cells after 24 hours of incubation, as well as untreated controls were detached from the cell flask surface using trypsin/EDTA, washed twice with PBS and fixed in 2.5 % glutaraldehyde in 0.1 M cacodylate buffer. Cells were then post-fixed with 1 % osmium tetroxide in the same buffer, dehydrated in a series of ethanol and embedded in Epon (Agar Scientific, UK). The sections were cut with a diamond knife (Diatome, Switzerland), mounted on copper grids and counterstained with uranyl acetate and lead citrate on Leica EM STAIN (Leica Microsystems, Germany). Philips CM12 transmission electron microscope (Philips/FEI, The Netherlands) operated at 60 keV and equipped with a SIS MegaView III digital camera (Olympus Soft Imaging Solutions, Germany) was used for examination and images obtaining.

2.8. Raman spectroscopy

For the Raman experiments, three sample groups were prepared: cells treated with 200 µg/ml CD NPs, cells treated with 400 µg/ml CD NPs and control cells. Each group was grown in three T-25 cell culturing flasks in parallel, i.e. in three replicates. After incubation with NPs, treated cells, as well as untreated controls, were detached with trypsin/EDTA. During the step of inhibition of trypsin, cell suspensions from three cell flasks of the same sample group were collected into one common tube. After removing the trypsin, the cells were fixed in Roti-Histofix 4 % (Roth, Germany) for 20 min at room temperature and washed twice in PBS (2 × 5 ml per flask). The resulting pellets were resuspended in 1 ml of PBS and stored at 4 °C. Right before the measurement, PBS was discarded, the cells were washed in 1 ml of DI water and resuspended in 50 µl of DI water (100 µl for control sample, due to higher cell density). A drop of 20 µl was placed onto CaF_2 coverslip and air dried. Raman spectra were acquired with NT-MDT system NTEGRA Prima (NT-MDT, The Netherlands) using 600 g/mm grating. A laser excitation line of 532 nm with an incident power of ~0.5 mW was used and the exposure time was 180 s. Raman spectra were measured in the nuclear region of the cell, to avoid spectral differentiation based on different cell compartments. The cells chosen to be measured were not selected based on their morphology but randomly chosen.

2.9. Raman spectra preprocessing

The obtained spectra were calibrated using Raman spectra of paracetamol. The spectral region (700–1800) cm^{-1}, so called fingerprint region, was chosen for the analysis. The background was subtracted by first order polynomial fit. Finally, Raman spectra were normalized relative to the mean intensity calculated for entire spectrum. All spectral preprocessing steps were performed in R, using hyperSpec package (Beleites and Sergo 2024).

2.10. Raman data analysis

nnPCA was performed in R using *nsprcomp* package (Sigg 2018). The function of the same name, *nsprcomp*, computes components (nnPCs) by projecting the principal vectors onto the non-negative orthant. Each nnPC is calculated after the previous one so that it captures the maximum of variance not explained by the previous nnPCs. The procedure would be the same as standard PCA if the negativity restriction were not applied. The percentage of the explained additional variance of each nnPCA is calculated using function *peav*.

K-means clustering was performed using the function *kmeans* from the R package *stats*. The goal of this method is to group the data of the dataset into clusters, in such a way that the sum of squares from each data point (a spectrum) to the centroid of the cluster is minimized. The number of clusters should be predefined. Here, the grouping of all measured Raman spectra (control and treated cells' spectra) into four clusters was chosen. Clustering into three and five groups was also tried out but gave less valid physical meaning.

2.11. Raman imaging

Cell samples for Raman imaging were prepared in the same way as for previously described Raman measurements (Paragraph 2.8). Two sets of samples were prepared: cells treated with 200 µg/ml CD NPs and control (untreated) cells. Micro-Raman spectroscopy investigation of the individual cells was performed on confocal Horiba Xplora plus system equipped with 532 nm laser excitation source and Peltier cooled CCD detector. The Raman spectra were collected with low laser power, using 50x long working distance (LWD) objective and 600 g/mm grating.

To map single cells, we utilized a piezo-controlled sample stage, adjusting the grid raster to match the morphology of the cells under investigation. Data acquisition was performed within the spectral range of 500 cm^{-1} to 1800 cm^{-1}, with each acquisition lasting 30 seconds. Following the measurements, we applied a first order polynomial baseline fitting procedure to all collected spectra. This step was crucial for compensating for random spatial variations on the sample surface.

Subsequently, PCA analysis of measured spectra in the region 700 cm^{-1} to 1800 cm^{-1} was performed for each single cell (NP-treated and control), using R function *prcomp* from package *stats*. The resulting

PC1 was used for cell imaging: PC1 score values for each pixel were presented by color scale (from green to red). Similarly, the VCA imaging method was applied: based on the abundance of VC1, VC2 and VC3 components in the spectra of each pixel, color maps of both control and treated cells were created. This method was applied using R function *vca* from package *hyperSpec.utils*, with *ncomp* argument set to value 3 (for extraction of three pure components from the data set) (Mayer 2024). Spectra measured on the cell periphery were excluded from both PCA and VCA imaging, due to the significantly different background and signal-to-noise ratio. If they were included in the analysis, they would be separated into distinct group as outliers, masking the differences between the spectra measured on the central part of the cells. For that reason, we first did PCA to identify such outliers and then repeated PCA or performed VCA with the rest of the spectra. In that way we have imaged ~500–600 pixels for control and NP-treated cells, with a pixel size of 0.6 × 0.6 µm.

3. Results and discussion

MRC-5 cells grown in culture were treated with CD NPs synthesized and characterized in our previous study (Miletić et al. 2020). They proved to be very stable in dispersion, with a hydrodynamic radius of less than 50 nm, while the CeO_2 NPs used in previous studies on MRC-5 cells were very susceptible to agglomeration, with a hydrodynamic radius of at least 500 nm (Pešić et al. 2015; Spezzati et al. 2017; Alghamdi 2023; Abdi Goushbolagh et al. 2018). The average grain size, crystallite size, hydrodynamic radius and specific surface area (SBET) of CD NPs are summarized in Table 1 (more details are given in Supplementary material and Figure S1).

CD NPs were applied in the dose range of (100–400) µg/ml, also used in previous studies of CeO_2 NPs effect on MRC-5 cells (Pešić et al. 2015; Spezzati et al. 2017; Alghamdi 2023; Abdi Goushbolagh et al. 2018), with an altered incubation time of 48 hours. The effects of NPs were first evaluated by standard biological methods, in order to select the doses that will be used for Raman measurements based on their results and to assure more reliable interpretation of Raman spectra analysis.

Table 1. Characteristics of CD NPs: grain size estimated from TEM images; average crystallite size, determined from XRD using Scherrer formula; average hydrodynamic radius, determined by DLS; and BET specific surface area (S_{BET}).

Grain size (TEM)	Crystallite size (XRD)	Hydrodynamic radius (DLS)	Specific surface area (S_{BET})
≈ 4 nm	3.5 nm	46.5 nm	34.4 m^2/g

3.1. NPs effects on cell growth, metabolic activity and apoptosis induction

Effects of NPs on cell growth (SRB assay), metabolic activity (MTT) and induction of apoptosis (annexin-V-FITC) were examined. Changes in metabolic activity determined by MTT were more intense than the changes in cell growth detected by SRB assay for the same applied dose of NPs (Figure 1). While average cell growth decreased to 67 % and 29 % in average upon treatment with 200 µg/ml (CD-200 cells) and 400 µg/ml CD NPs (CD-400 cells), respectively, metabolic activity registered by MTT dropped sharply to 32 % and 10 % in average, relative to control. Considering that MTT assay detects the level of metabolic activity based on mitochondrial function preservation, it follows that mitochondrial function impairment is one of the first events in the cells treated with cytotoxic dose of CD NPs. Interestingly, at the lowest applied dose, 100 µg/ml, a slight increase (109 % in average) in metabolic activity is noticed, possibly through the stimulation of cell proliferation. At higher doses, CD NPs are undoubtedly cytotoxic. As previously stated, due to their physicochemical properties, CeO_2 NPs exert both pro-oxidative and anti-oxidative activity, which could result in different, sometimes opposite, effects on cells. Nevertheless, in order to trace the changes of the same parameters, we limited this study to cytotoxic doses of NPs.

Impairment of mitochondrial activity caused by CD NPs leads to induction of cell death, which is confirmed by staining the cells with fluorescently labeled annexin-V and PI. Annexin-V specifically binds to phosphatidylserine, while PI intercalates between the bases of nucleic acids and dyes them. In the confocal microscopy images shown in Figure 2a, left panel, cells stained by annexin-V-FITC only (annexin-V^+/PI^-, colored green) represent the cells with externalized phosphatidylserine, but still with the intact cell membrane, i.e. the cells in early apoptosis. The cells stained with both annexin-V-FITC and PI (annexin-V^+/PI^+, colored green and red) are the cells with damaged cell membrane, i.e. cells in necrosis or later phases of apoptosis. For quantifying cell frequencies in early and late apoptosis flow cytometry was used. The flow cytometry analysis confirmed that exposure to CD NPs induced apoptotic cell death of MRC cells. Namely, compared to the control cells, 48 h

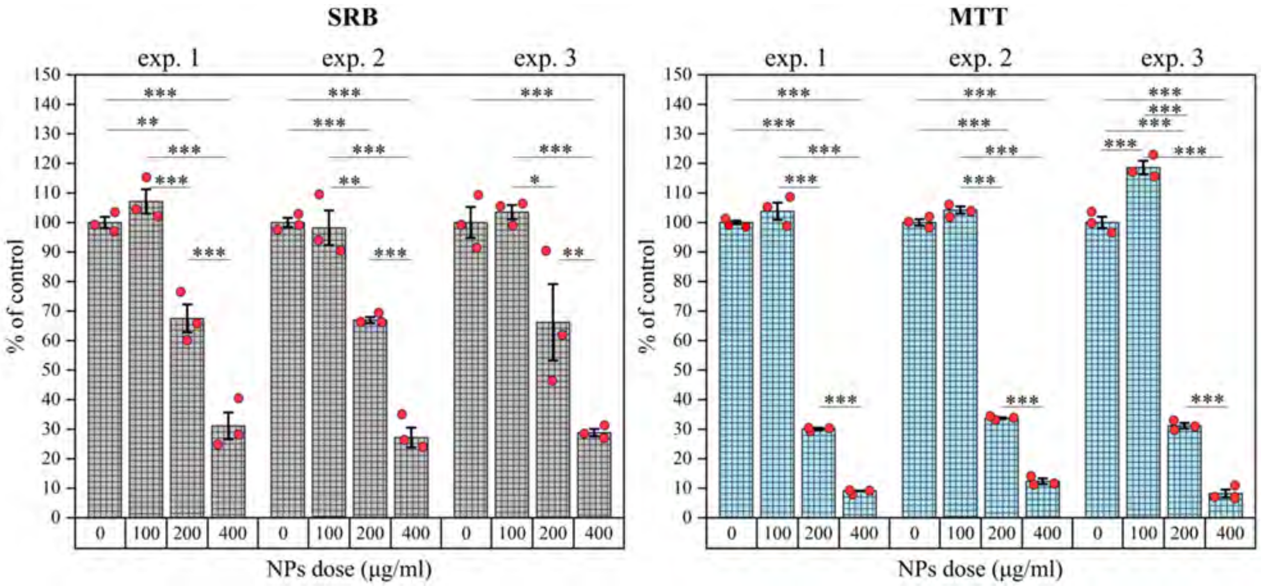

Figure 1. Changes in cell growth (left) and metabolic activity (right) induced by CD NPs, assessed by SRB and MTT assays, respectively. Standard error bars, $^*p < 0.05$, $^{**}p < 0.01$, $^{***}p < 0.001$.

exposure to both CD-200 and CD-400 NPs increased the frequency of early (annexin V^+/PI^-) and late (annexin V^+/PI^+) apoptotic cells in culture. Moreover, the frequency of late apoptotic cells increased in a concentration-dependent manner, whereas the frequency of early apoptotic/necrotic cells was similar among the cells exposed to either CD-200 or CD-400 (Figure 2a, right panel, and Figure 2b).

TEM imaging was performed on treated cells with lower dose of CD NPs, i.e. CD-200 cells, to confirm the uptake and intracellular presence of NPs. TEM images of both control and CD-200 cells are shown in Figure 3. Accumulations of NPs can be detected mostly in cytoplasmic endosome-like vesicles across the entire NP-treated cell, except within the nucleus.

3.2. Raman spectroscopy of NP-treated cells and spectral multivariate analysis

Since biological methods showed that doses of 200 μg/ml and 400 μg/ml CD NPs are both cytotoxic to MRC-5 cells but to a different extent, the Raman measurements were performed on both groups of MRC-5 treated cells, as well as on untreated cells as controls. Raman spectra of treated and untreated MRC-5 cells were comparatively analyzed. In Figure S3 (Supplementary material) mean Raman spectra of control and treated cells are presented. As can be seen, spectral differences between the three cell groups are very subtle and manifested by the changes of relative intensity, rather than by radical decrease/increase of particular Raman modes intensities. The standard deviation for CD-200 cells is the largest, suggesting the existence of different subpopulations of the cells, with unequal levels of damage.

To extract more precisely changes in the Raman modes in treated cells, nnPCA was applied. This non-conventional modification of standard PCA is useful in the analysis of cell spectra, resulting in PC loadings which could be interpreted more intuitively. nnPCA was performed in a pairwise manner, meaning that CD-200 and CD-400 cells spectra were analyzed separately, through direct comparison with the control. PC components that enable the greatest separation of cell groups, i.e. that best describe the differences between control and treated cells, were identified using PC scores plots. The relevant scores plots for CD-200 and CD-400 cells are shown in Figures 4 and 6, respectively. Corresponding PC loading vectors for CD-200 and CD-400 cells are shown together in Figure 5. The peaks contained by PC loading vectors indicate Raman modes whose intensity changes in the spectra of treated cells, while the sign of PC scores (PC^+ or PC^-) determines the direction of the change (increase or decrease of Raman mode intensity).

As can be seen from Figure 4, nnPCA of control and CD-200 cells abstracted two PCs which segregate control and treated cells: PC1 and PC2. Taken together, those two PCs encompass ~60 % of total variance among the cells spectra. On average, CD-200 cells have a positive PC1 score ($PC1^+$), hence PC1 presents Raman modes whose intensity increases after the treatment with NPs (Figure 5a). For PC2, the reverse is true: CD-200 cells on average

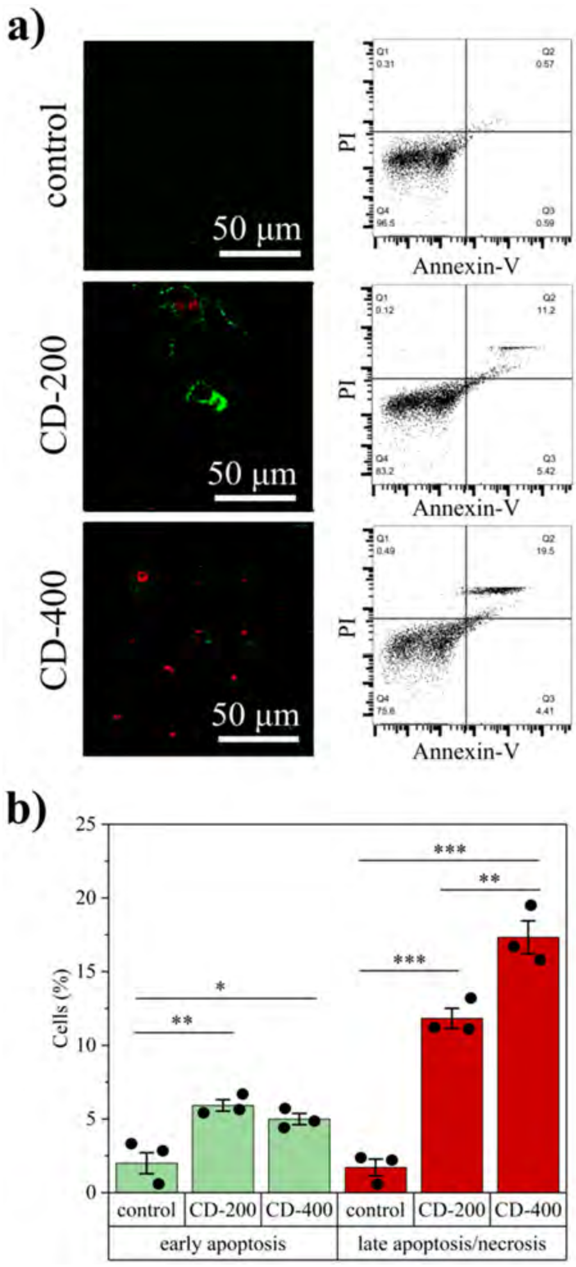

Figure 2. Induction of cell death caused by CD NPs. a) Left panel: fluorescence confocal microscopy images of cells dyed with annexin-V-FITC (green) and PI (red). Annexin-V^+/PI^- (colored only green) are cells in early apoptosis, while annexin-V^+/PI^+ (colored green and red) are in late apoptosis or necrosis. Right panel: the corresponding flow cytometry dot plots indicating annexin-V-FITC *vs* PI staining of MRC-5 cells are presented (control cells in the first row and CD-200 and CD-400 treated cells in the second and third rows, respectively). b) Distribution of early (quadrant Q3) and late (quadrant Q2) apoptotic cells, gated as indicated on the flow cytometry dot plots. Standard error bars, $^*p < 0.05$, $^{**}p < 0.01$, $^{***}p < 0.001$. The presented data are from one of two experiments with similar results performed in three technical replicates.

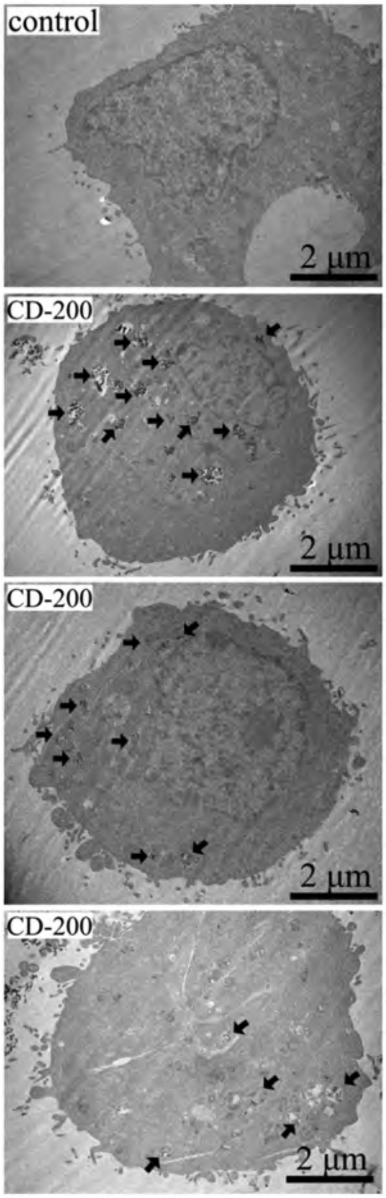

Figure 3. TEM images of the untreated cell (row 1) and the cells treated with CD-200 NPs (rows 2–4). Arrows point to NPs accumulations in the cell. For more images of control cells see Figure S2 in Supplementary material.

have a negative PC2 score sign ($PC2^-$), therefore PC2 presents the Raman modes with decreasing intensity in NP-treated cells (Figure 5d). Control cells on average have negative PC1 and positive PC2 scores ($PC1^-$/ $PC2^+$); the corresponding annotation will be used for the other PCs in the further text.

PC1 overall appearance from Figure 5a resembles the Raman spectrum of lipid molecules and almost all presented peaks can be assigned to different types of lipid modes, though other biomolecules cannot be strictly excluded. In Table S1 (Supplementary material) are presented cell Raman modes assignations. Furthermore, all peaks present in this component, except 1128 cm^{-1}, 1147 cm^{-1}, 1162 cm^{-1}, 1548 cm^{-1} and 1597 cm^{-1} peaks, are contained in the Raman spectrum of phosphatidylserine (Milligan et al. 2021).

PC2 resulting from the same analysis is shown in Figure 5d. Considering the negative PC2 score sign for CD-200 cells, all peaks that appear in this component indicate the decreasing intensity of corresponding Raman modes. PC2 is composed of typical nucleic acid modes: 786 cm^{-1}, 1099 cm^{-1}, 1182 cm^{-1}, 1375 cm^{-1}, 1485 cm^{-1} and 1576 cm^{-1}. The presence of a small shoulder at 814 cm^{-1}, as well as the position of the mode at 1099 cm^{-1} instead of 1095 cm^{-1}, suggest that RNA molecules are present among the nucleic acids which diminish in CD-200 treated cells. Also, for the peaks centered at 1237 cm^{-1} and 1337 cm^{-1}, the shoulders positioned at ~1245 cm^{-1} and 1322 cm^{-1}, which are particularly prominent in RNA (Samuel et al. 2022), are hinted. Beside nucleic acids modes, this PC2 contains a few peaks typical for protein Raman modes (1006 cm^{-1}, 1162 cm^{-1}, 1683 cm^{-1}). Modes at 1237 cm^{-1} and 1337 cm^{-1} could be from protein and nucleic acids both (see Table S1).

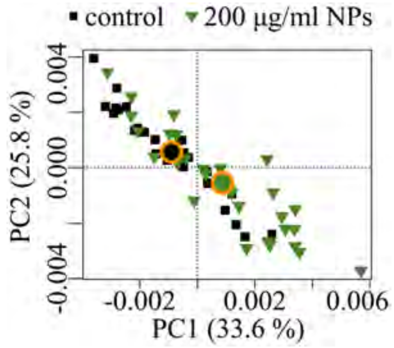

Figure 4. nnPCA of control (black squares) and CD-200 cells (green triangles): PC1:PC2 scores plot. Centroids of the groups are represented by a correspondingly colored circles with an orange border. Percentages in the brackets denote the amount of total variance encompassed by each PC.

Results of the Raman spectra analysis by nnPCA method can be explained in the light of the results given by standard biological experiments. A decrease in cellular metabolic activity, that is disordered mitochondrial function, could be caused by oxidative stress generated by CD NPs in the cell, which was reported in previous studies (Hussain et al. 2012; Park et al. 2008). Overproduced ROS induce mitochondrial membrane potential loss and impairment of the mitochondrial oxidative chain, leading to increased mitochondrial membrane permeability and loss of its function. At that step, MTT assay already detects the cytotoxic effect of NPs (Figure 1). Cytochrome C released from dysregulated mitochondria triggers the apoptosis pathway (Figure 2), while disruption of mitochondrial redox reactions leads to the enhancement of oxidative stress and deterioration of oxidative damage of other cell structures and molecules. Beside mitochondria, ROS damage DNA, causing breaks of its chains, which also triggers apoptosis. Therefore, decreased DNA Raman modes, especially those originating from phosphodiester bonds, could be expected as a consequence of oxidative DNA damage. RNA present in the cell is also damaged by ROS, while new RNA transcription is disabled by the degradation of DNA and overall metabolic dysregulation. When apoptosis is triggered in the cells, one of the first biochemical events is an externalization of phosphatidylserine to the outer leaflet of the cell

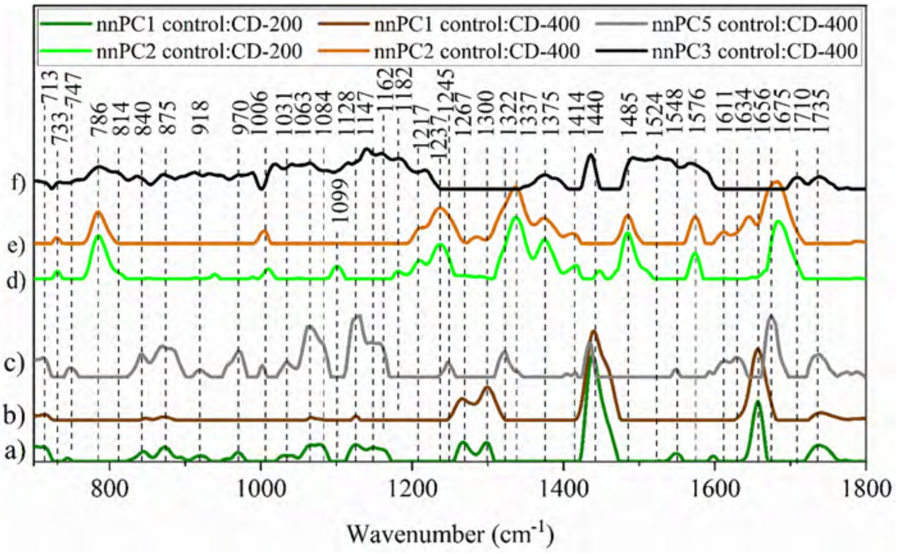

Figure 5. PC loading vectors showing the variations in lipid content among the cells: a) PC1 obtained from nnPCA of control and CD-200 cells, b) PC1 obtained from nnPCA of control and CD-400 cells, c) PC5 obtained from nnPCA of control and CD-400 cells. PC loading vectors showing the variations in nucleic acid content among the cells: d) PC2 obtained from nnPCA of control and CD-200 cells, e) PC2 obtained from nnPCA of control and CD-400 cells, f) PC3 obtained from nnPCA of control and CD-400 cells.

membrane. Externalized phosphatidylserine is therefore conventionally used as a marker for early apoptosis detection, usually by exposing the cells to labeled annexin-V (Figure 2). Detection of early apoptotic NP-treated cells correlates to increased phosphatydylserine Raman modes in treated cell spectra. Other lipid structures in treated cells which can be associated with increased lipid Raman modes, are different membranous organelles, such as endosomes or endolysosomes, generated by NPs intake, or lipid droplets, overaccumulated in cell death processes.

The changes in the Raman spectra of CD-200 cells (Figure 5a and d), correspond very well with the results obtained by standard biological assays. The resemblance of nnPC components to the Raman spectra of particular biomolecules (lipids and nucleic acids) makes spectral analysis of CD-200 cells relatively simple.

However, with the higher dose of NPs (CD-400), the analysis becomes slightly more complex. Figure 6a and b present PC scores obtained from nnPCA of control and CD-400 cells. The upper score plot shows that treated and untreated cells can be best distinguished by PC1 and PC5, though separation by PC1 is much greater: more than 90 % of analyzed treated cells differ from control. This component also encompasses much larger part of the total variance than PC5. Corresponding PC1 and PC5 loadings are shown in Figure 5b and c, respectively.

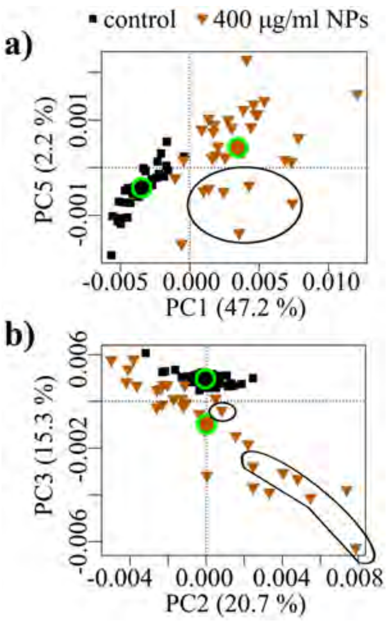

Figure 6. nnPCA scores plots of control (black squares) and CD-400 cells (brown triangles): PC1:PC5 (a) and PC2:PC3 (b). Centroids of the groups are represented by a correspondingly colored circles with a green border. Percentages in the brackets denote the amount of total variance encompassed by each PC. The cells with positive PC1 but negative PC5 score values (PC1$^+$/PC5$^-$ cells) are encircled by a black curve at the upper graph; the same cells at the bottom graph are encircled also with black curves.

Like PC1 from the analysis of cells treated with lower dose of NPs, this PC1 also shows an increase in lipid modes intensity in treated cells. The difference in lipid content between treated and control cells, based on PC1, is more emphasized for the higher than for the lower dose (compare Figures 4 and 6 a). This could be partially attributed to the increased level of endocytic vesicles, more present at higher doses. The appearance of PC1 difference among the two doses (Figure 5a and b) seems to be of particular interest. The most obvious difference is in the relative intensity of 1267 cm^{-1} and 1300 cm^{-1} peaks, I_{1267}/I_{1300}, which is significantly higher for the cells treated with the lower dose of NPs (Figure S4, Supplementary material). According to the literature, higher intensity ratio of these modes in the Raman spectra of cells indicates lower saturation of cellular lipids (Czamara et al. 2015). Our previous study pointed to this intensity ratio as a potential marker indicating the degree of NP-induced cell damage (Miletić et al. 2023). This study confirms that I_{1267}/I_{1300} has a higher value in early apoptotic cells, compared to the cells in late apoptosis or necrosis.

Furthermore, PC1 obtained from the analysis of higher dose (Figure 5b) is less rich in resolved peaks and almost without peaks in the region (800–1000) cm^{-1}, typical for phospholipids. Instead, phospholipid modes from this region appear in PC5 (Figure 5c), which also has positive score sign for treated cells (PC5$^+$). In PC1:PC5 score plot (Figure 6a) the following can be observed: while almost all treated cells differ from control by PC1, most of them, but not all, differ also by PC5. Those cells in which total lipid content is increasing (PC1$^+$), but markers of phosphatidylserine and other phospholipids are not expressed (PC5$^-$) are circled by a black curve in the score plot, in order to trace their behavior regarding PC2 and PC3 components. Besides lipid modes, PC5 contains some protein modes too.

PC2 component, bearing mostly DNA Raman modes (Figure 5e), does not separate control and CD-400 cells (Figure 6b). Still, it can be observed that the dispersion of DNA content among treated cells is wider than among control cells: there are cells having lower or higher DNA content than either control cells. It can be assumed that the intensity of DNA Raman signal is under the influence of DNA quantity, integrity and density;

therefore it can be diminished by DNA cleavage, but also enhanced by DNA condensation (Brauchle et al. 2014; Corfe, Dive, and Garrod 2000).

Unlike PC2, PC3 component from analysis of CD-400 cells separates treated from control cells (Figure 6b). This component also bears some of the nucleic acid modes (Figure 5f), but it indicates their decrease upon cell treatment. The most important modes are 786 cm^{-1}and 814 cm^{-1}, but also 733 cm^{-1}, 1182 cm^{-1}, 1237 cm^{-1}, 1337 cm^{-1}, 1375 cm^{-1}, 1485 cm^{-1} and 1576 cm^{-1}. Relative intensity I_{814}/I_{786} in this component is particularly high and indicates that the content of RNA rather than DNA diminishes in the cell. Considering that apoptotic nuclear content can be cleaved or highly condensed, while cytoplasmic RNA is degraded, such results of Raman spectra analysis, representing decrease of Raman RNA modes intensity, are in accordance with the previous conclusion.

Treated cells with high nucleic acid content in general (PC2$^+$), but with lower RNA content compared to control (PC3$^-$) are seen in the score plot in Figure 6b. All cells that have a higher lipid (PC1$^+$) but not phosphatidylserine content (PC5$^-$) also belong to this group of treated cells and are marked with the black curve in Figure 6b.

There is, therefore, a population of CD-400 cells in which the lipid content is increased compared to the control (PC2$^+$/PC3$^-$), but also the DNA content (PC1$^+$/PC5$^-$), which is an unusual phenomenon that did not occur with CD-200 cells, nor has it been described in previous studies on NP-treated cells by Raman spectroscopy. At the same time, lipids in the given CD-400 cells were not characterized by phospholipid features, and the content of RNA was reduced compared to the control cells. In order to examine whether PC2$^+$/PC3$^-$ and PC1$^+$/PC5$^-$ cells underwent specific changes induced only by the highest dose of NPs, the k-means clustering method was applied. This analysis included control, CD-200 and CD-400 cells altogether. The goal was to determine whether among all examined cells, PC2$^+$/PC3$^-$ and PC1$^+$/PC5$^-$ CD-400 cells would be segregated into a separate cluster. The k-means clustering method requires the number of resulting clusters to be set as an input parameter. Based on theoretical knowledge, it was assumed that cells can be divided into four clusters: unchanged (control) cells, cells in early apoptosis, cells in late apoptosis or necrosis, and cells in some other modality of cell death, characterized by very small reduction of DNA material and an increase in lipids without phosphatidylserine markers. As a result of this analysis, the examined cell spectra were divided into four clusters (Figure 7a), where indeed the spectra of PC2$^+$/PC3$^-$ and PC1$^+$/PC5$^-$ cells belonged exclusively to one cluster, i.e. cluster 4 (Figure 7a, brown stars). Bar plots in Figure 7b show the composition of each cluster. Most of the control cells belonged to the cluster 3 and a smaller part to the cluster 1. Approximately half of the CD-200 cells belonged to the cluster 3 and half to the cluster 1. Therefore, it was assumed that the cluster 3 contains unchanged cells, while the cluster 1 contains cells in early apoptosis. Cluster 2 contains only two CD-200 cells and more than half of CD-400 cells, therefore it can be assumed that it represents cells in late apoptosis or necrosis. Cluster 4 consists exclusively of a certain number of CD-400 cells. Spectra that correspond to the centroid of each cluster are provided in Supplementary material (Figure S5), along with optical images of the cells positioned closest to each centroid (Figure S6). To analyze spectral differences among the clusters, intensities of typical lipid (I_{1300}) and typical DNA (I_{786}) Raman modes in four centroid spectra were compared. The values are shown in Figure 7c. The cells of cluster 4 have nucleic acids content slightly lower than the control but higher than the cells assumed to be in early and late apoptosis. The lipid content of the cells in cluster 4 is very high, approximately equal to the cells in late apoptosis (Figure 7c). Therefore, it seems more likely that these cells are in some alternative modality of cell death, rather than in the furthest stages of apoptosis or necrosis.

There is a study which showed that at high doses of CeO_2 NPs, in addition to the increased level of apoptosis, the percentage of autophagic cells also increases (Hussain et al. 2012). At low, non-cytotoxic doses, autophagy was not detected. On the other hand, another study shows that autophagic cells are hardly distinguishable from control cells by Raman spectra (Rangan et al. 2018). In the case of cells treated with CD NPs, a large difference in the amount of lipids compared to the control can certainly come from a large number of endocytic vesicles by which the NPs were introduced into the cell, but also from a large number of resulted autophagosomes. Unlike apoptotic cells, autophagic cells are not characterized by externalized phosphatidylserine. In accordance with the above stated, the assumption that CD-400 cells with increased lipid content and not highly reduced nucleic acid content (compared to the control) can represent cells in autophagy is not unfounded. High concentration of NPs could activate autophagy as a protective mechanism, which in the

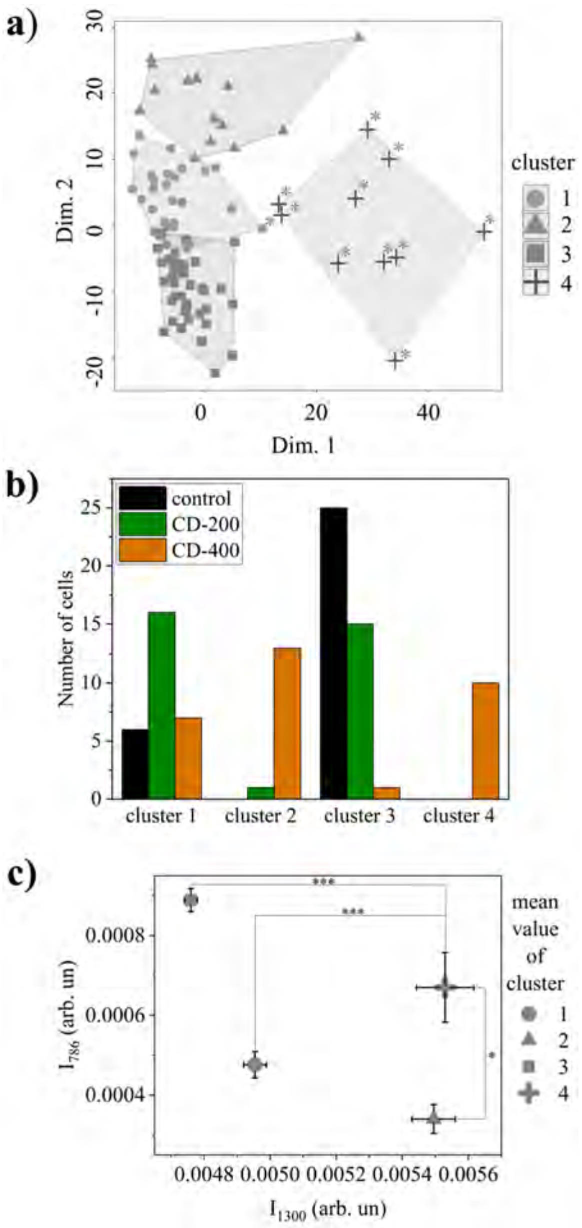

Figure 7. K-means clustering of control and treated cells Raman spectra. a) Four clusters with belonging cell spectra. PC1$^+$/PC5$^-$ and PC2$^+$/PC3$^-$ cells are marked with brown stars. b) The composition of each cluster. c) Plot showing Raman intensities I_{1300} (lipids) and I_{786} (nucleic acids) for each cluster and standard error bars. Lines parallel with x-axis and y-axis present statistical significance of differences between the clusters in x (I_{1300}) and y (I_{786}) values, respectively (nonparametric ANOVA, ***$p < 0.001$, *$p < 0.05$).

final outcome can lead to cell death. It is known that the mechanisms of apoptosis and autophagy communicate in the cell in a complex manner (Hussain et al. 2012; Mariño et al. 2014). Cells detected by Raman spectroscopy as members of a separate cluster may therefore be cells that managed to survive the impact of NPs thanks to autophagy, at least until the moment of examination.

It should be noted that proposed distribution of cells in different phases or modalities of cell death, based on the k-mean clustering of cells' Raman spectra, is not entirely consistent with the frequency of apoptosis detected by flow cytometry, though NP dose-dependent increase of late apoptosis frequency is indicated by both methods. Moreover, the percent of NP-treated cells in which changes were detected by Raman spectroscopy is significantly higher than the frequency of apoptosis detected by flow cytometry. Raman spectroscopy certainly captures a wider spectrum of changes in the cells caused by NPs than the externalization of phosphatidylserine and the appearance of cell membrane permeability. Some of them are related to the entry and transport of NPs in the cell and to the direct and indirect interactions of NPs with cellular molecules, which do not necessarily result in apoptosis. On the other hand, MTT assay showed a very large decrease of viability of NP-treated cells, consistent with Raman spectroscopy. Markers of various biochemical changes are intertwined in the Raman spectrum of the NP-treated cell and provide a unique representation of its physiological state. The possibility that Raman fingerprint can indicate lethal changes caused by NPs earlier or more completely than some of the conventional methods used for this purpose should not be overlooked.

3.3. Raman imaging

Raman imaging is usually performed using the intensity of one or more Raman modes in a certain number of locations on the sample to generate an image or map of the sample, where the intensity of the color corresponds to the intensity of a given Raman mode. In this work, instead of classical methodology, the imaging based on multivariate (PCA or VCA) analysis of Raman spectra was used. The goal of combining statistical methods with Raman imaging was to distinguish spectral characteristics across the analyzed cells more clearly. For this reason, we labeled the applied methods as PCA-Raman imaging and VCA-Raman imaging.

The imaging experiments aimed to show NP-induced changes in the spatial arrangement of cell molecules. For this purpose, CD-200 cells were selected, as moderately damaged NP-treated cells which largely kept their integrity, so their maps are more comparable to those of control cells. Raman spectra were measured in each pixel of three control and three CD-200 cells and PCA was applied to all measured spectra of six cells together. The resulting

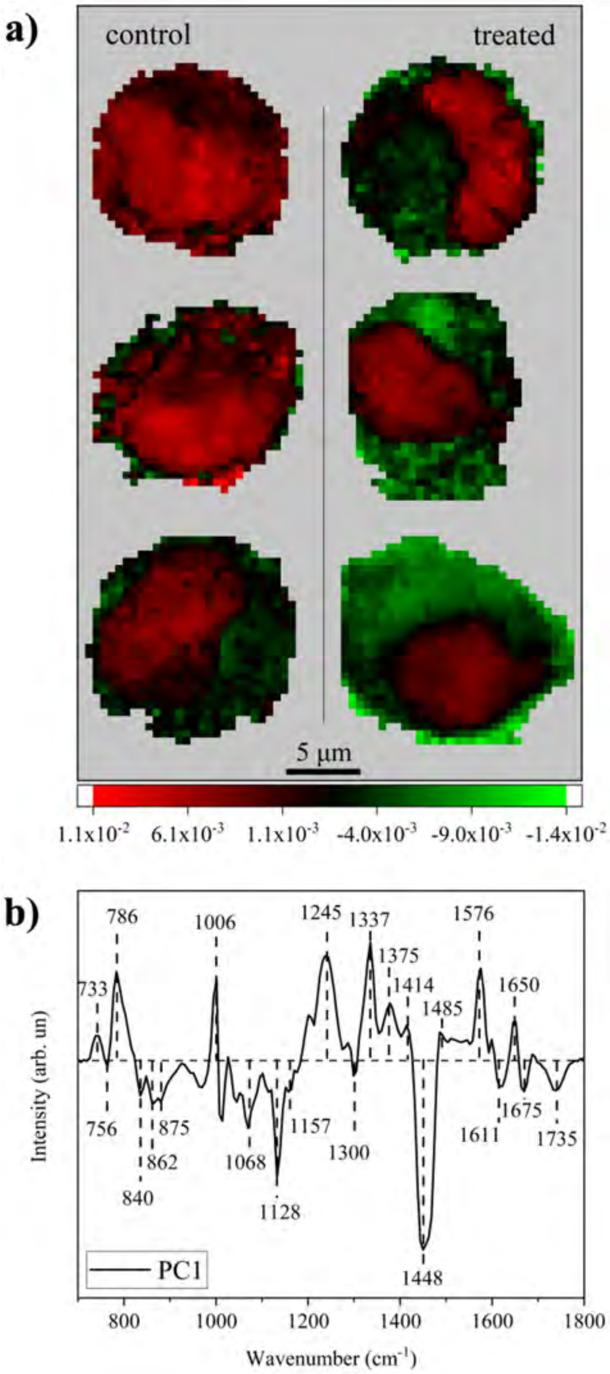

Figure 8. PCA-Raman imaging of control and CD-200 treated cells a) PCA-Raman images of analyzed cells, based on PC1 score values in each pixel (left column – control cells, right column – NP-treated cells); b) PC1 loading spectrum. Local maxima of PC1 are assigned to nucleic acids' and proteins' Raman modes while local minima are assigned to lipid Raman modes, which imply that positive score values at images characterize pixels with high nucleic acids but low lipid content (red) and negative score values characterize pixels with low nucleic acids but high lipid content (green).

PC1 was used to create PCA-Raman images of the cells. Results of this experiment are presented in Figure 8. PCA-Raman images are shown in Figure 8a. PC1 loading spectrum, used for imaging, is shown in Figure 8b. It reflects Raman modes of nucleic acids and proteins as local maxima and lipid modes as local minima (Table S1, Supplementary material). It should be noted that, in this case, standard PCA was used instead of nnPCA, in order to simplify the presentation of both lipid and nucleic acid changes in the same image. PCA-Raman images are generated based on PC1 score value for each pixel on the image, in the way that the highest positive score is represented by light red and the highest negative by light green color (color scale in Figure 8a). Hence, light red pixels denote Raman spectra with high intensity of nucleic acid and protein modes (maxima) but low intensity of lipid modes (minima), while light green represents the opposite: Raman spectra with high intensity of lipid and low intensity of nucleic acid and protein modes. It is interesting that Raman mode at 1006 cm^{-1}, assigned to phenylalanine, which is probably the most typical Raman mode of proteins, shares trend in spatial distribution with nucleic acids and not with lipids, although proteins are present together with lipids in the membranes of endocytic vesicles and definitely the smaller portion of total cell proteins is localized in nucleus (Itzhak et al. 2016).

By observing obtained PCA-Raman maps, it can be seen that in control cells, Raman modes of nucleic acids and proteins dominate, occupying the majority of the cell area (Figure 8a, left). They should be most intense in the nuclear region, the edges of which are not clearly defined in the first two control cells. Outside the nucleus, the presence of Raman modes with positive intensity in PC1 may originate from RNA molecules or possibly from mitochondrial DNA. In the third control cell (Figure 8a, third row left), the nucleus is more clearly distinguished, but the intensity of lipid Raman modes, i.e. the lipid content of the cell, is still low. On the other hand, in treated cells, lipids are significantly abundant, as evidenced by the presence of light green dots on the map, while the nuclear region is clearly limited to a smaller area than in control cells (Figure 8a, right). Since these cells, according to the MTT test, are metabolically less active than control cells, reduced transcriptional activity, and thus the amount of RNA and protein in the cytoplasm is expected for them. Also, the increase in the amount of lipids is consistent with endocytosis and demonstrated induction of apoptosis in the treated cells.

In addition to PCA, the VCA method is also applied for Raman imaging. The aim of this method is to extract spectra of pure components from the mixture of components constituting the sample. Biomolecules that are contained in a cell have many common Raman modes and most often together form different supra-molecular structures. Thus, it is likely that there are no points in the cell that contain perfectly pure components. However, it is expected to obtain components in which the spectral characteristics of certain molecules are more prevalent than others. It was reasonable to expect that components representing lipids, nucleic acids and proteins, as the three main groups of biomolecules in the cell, could be extracted. For that reason, VCA algorithm is designed to calculate three VCA components (VC1, VC2, VC3). VCA is applied to spectra/pixels of each control or CD-200 cell separately. This analysis is performed on the same cells used for PCA-Raman imaging. Results for one control and one treated cell (cells whose PCA-Raman images are shown in the first row in Figure 8a) are presented in Figure 9. Extracted VCA ('pure') components are given in the first row for control cell (Figure 9a–c) and in the fourth row for CD-200 cell (Figure 9j–l), while corresponding VCA-Raman images are given in the second row for the control (Figure 9d–f) and in the third row for the CD-200 cell (Figure 9g–i). For components representing mostly DNA (VC1) and lipid (VC3) Raman modes, red and green colors are used, respectively. Other two colors are used for VCA components proposed to be dominantly RNA (blue) and dominantly cytochrome c (apricot orange). The intensity scale is denoted on the right side of each image and refers exclusively to a given image.

As expected, in both control and CD-200 treated cell, two VCA components with pronounced nucleic acid (VC1, Figure 9a and j) and lipid Raman markers (VC3, Figure 9c and l) were extracted. In this case, nuclear area in control cell is equally well defined

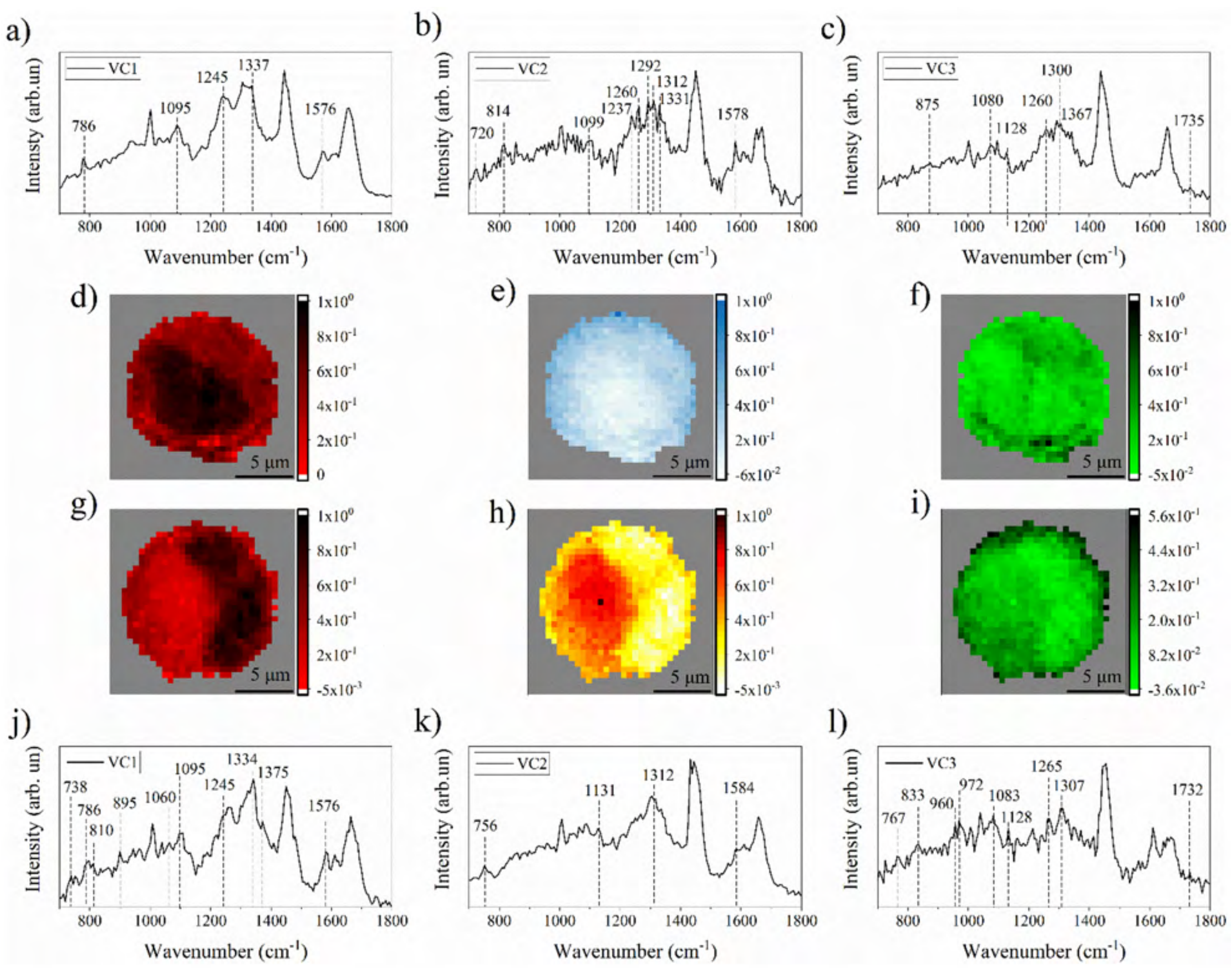

Figure 9. VCA-Raman imaging of control and CD-200 cells. a), b), c) VCA components of the control cell, used for imaging; d), e), f) corresponding images of the control cell. j), k), l) VCA components of the treated cell, used for imaging; g), h), i) corresponding images of the treated cell. Red is used for imaging based on nuclear acid component, green for lipid component, blue for RNA and orange for cytochrome c component.

as in treated cell, presumably due to the fact that RNA content of control cell is represented by VC2. Also, since this analysis is performed on each cell separately, it should be more successful in distinguishing intracellular spectral differences. On the contrary, described PCA-Raman imaging (Figure 8) captured both intracellular and intercellular differences, but their intensity range is mutually dependent: if the differences between cells are greater than the differences within cells, the image contrast of some cells may be insufficiently pronounced. Contrary to expected, in VC2 component, protein Raman markers were not distinctly distinguished. Instead of that, VC2 component of the control cell bears Raman markers which could be assigned to RNA. This component is slightly less intensively distributed in the nuclear than in cytoplasmic region. In the case of the treated cell, in VC2 component, peaks corresponding to resonance Raman markers of cytochrome c (marked with corresponding wavenumbers in Figure 9k) are distinguished. This component is pronounced in the cytoplasm and very weakly in the nuclear region of treated cell. Cytochrome c is pro-apoptotic factor, released from mitochondria to the cytoplasm in the early stages of apoptosis, whereas nuclear accumulation of cytochrome c starts later (Nur et al. 2004). The images obtained by VC3 are characterized by lower contrast, hence the differences between different compartments of the cells are hardly noticeable. In addition, the VC3 component differs between control and treated cells - it probably describes a presence of different set of lipids, combined with other classes of molecules. Similarly, in dominantly lipid VC components obtained from the analysis of other four cells (Figure S7, Supplementary material), the influence of different cellular molecules is visible. Extensive imaging of a large number of control and treated cells would be required to clarify which types of molecules are involved and to what extent each component is useful in describing the NP-induced state of the cell. With the current instrumentation, there are severe limitations for imaging large number of cells.

To summarize, standard biological tests showed the cytotoxic effect of CD NPs on MRC-5 cells starting from a dose of 200 μg/ml, which is accompanied by differences in Raman spectra, both between control and treated cells, and also between cells treated with different doses of NPs. The common general changes are an increase in the intensity of lipid modes and a decrease in the intensity of nucleic acid modes, detected by nnPCA. However, Raman modes that make the difference between the treated and the control cells are not the same for the two doses of NPs, indicating changes in different members of the lipid or nucleic acids class. Cells treated with a lower dose of NPs (200 μg/ml) are characterized by a marked increase in unsaturated fatty acids and phospholipid markers, especially phosphatidylserine, a marker of early apoptosis. After treatment with a high dose of NPs (400 μg/ml), cells with an increased intensity of lipid modes, but without phosphatidylserine markers can be clearly distinguished. At the same time, these cells are the ones in which there is no decrease in the content of nucleic acids in general, but only a decrease in the intensity of the RNA markers. The k-means clustering confirmed that these cells stand out as a distinct group, most likely as a group of autophagic cells characterized by a specific effect of CD NPs on them. It was proposed that most of the other CD-400 treated cells analyzed by Raman spectroscopy have undergone late apoptosis or necrosis. Raman images created based on score values for PCA components illustrated higher lipid content and reduced nuclear acids' area in CD-200 cells. Furthermore, Raman images based on VCA components abundance indicated that the amount of nucleic acids in the cytoplasm rather than in the nucleus is what distinguishes treated from untreated cells. Additionally, with the Raman-VCA method, it was possible to obtain an image of the treated cell based on the intensity of the Raman modes of cytochrome c, which indicated the presence of this apoptotic marker in the cytoplasm of the treated cell.

4. Conclusion

This study, based on multivariate single-cell Raman spectroscopy complemented by standard cytotoxicity assays and flow cytometry, unequivocally indicates the toxic effect of CD NPs on MRC-5 lung fibroblasts in culture, starting from the concentration of 200 μg/ml NPs. An early indicator of CD NPs' cytotoxicity is the deprivation of mitochondrial activity, which leads to cell death in a certain proportion of MRC-5 cells. Depending on the NPs dose, early or late apoptosis/necrosis is registered and related changes in biochemical composition are described. The most pronounced are the quantitative and qualitative changes in cellular lipid and nucleic acid content, which differentiate the NP-treated cells from the untreated ones, but also the cells treated with different doses of NPs from each other. Nevertheless, the other modality of cell death, possibly autophagy, caused by interaction with NPs in dose higher than 200 µg/ml, is also indicated. Considering the small dimensions of the NPs and the hydrodynamic stability provided by the dextran coating, cytotoxic effect of CD NPs could have been expected. The absence of formation of CeO_2 NPs agglomerates, otherwise problematic in studies of their cytotoxicity, makes the results of this study particularly reliable.

The obtained results confirmed the usefulness of phospholipid-related Raman modes in assessing the effects of NPs and especially the importance of the Raman intensity ratio I_{1267}/I_{1300} as a parameter for assessing the degree of cell damage or the phase of cell death. In addition, it was demonstrated that the intensities of nucleic acids Raman markers vary with the degree of cell damage and can be associated with changes in RNA composition, hence used also for evaluating the effects of NPs. In a cell, RNA is difficult to distinguish from DNA by Raman spectra; therefore the insight provided by this study is significant. Moreover, integrating the PCA and VCA methods into Raman imaging, we were able to depict changes in the spatial distribution of RNA, but also the spatial arrangements of lipids, DNA and cytochrome c in treated cells through a single experiment. Finally, yet importantly, with the single-cell approach enabled by Raman spectroscopy, we were able to separate cell populations with different types of NP-induced biochemical changes and subsequently cross-analyze them using several parameters and statistical methods. In this way, we detected individual cells that underwent a specific effect of CD NPs, not registered by applied standard biological methods. Combining different, both standard and unconventional methods for Raman spectra analysis reveals the wealth of information about cell-NP interactions accessible by Raman spectroscopy.

Disclosure statement

No potential competing interest was reported by the authors.

Funding

MM, SČ, BS and ZDM acknowledge funding provided by the Institute of Physics Belgrade, through the grant of the Ministry of Science, Technological Development and Innovation of the Republic of Serbia. LK and JZ acknowledge financial support provided by the Vinča Institute of Nuclear Sciences, through the Grant No: 451-03-66/2024-03/ 200017 of the Ministry of Science, Technological Development and Innovation of the Republic of Serbia. AV and MNA acknowledge financial support provided by the Institute for the Application of Nuclear Energy, through the Grant No: 451-03-66/2024-03/200019 of the Ministry of Science, Technological Development and Innovation of the Republic of Serbia. MR acknowledges financial support provided by ANTARES project that has received funding from the European Union's Horizon 2020 research and innovation programme under grant agreement SGA-CSA No. 739570 under FPA No. 664387. IG and AK acknowledge financial support provided by Faculty of Biology, through the Grants No: 451-03-65/2024-03/ 200178 and No. 451-03-66/2024-03/ 200178 of the Ministry of Science, Technological Development and Innovation of the Republic of Serbia.

Data availability statement

The data that support the findings of this study are available from the corresponding author, MM, upon reasonable request.

References

Abdi Goushbolagh, N., B. Farhood, A. Astani, A. Nikfarjam, M. Kalantari, and M. H. Zare. 2018. "Quantitative Cytotoxicity, Cellular Uptake and Radioprotection Effect of Cerium Oxide Nanoparticles in MRC-5 Normal Cells and MCF-7 Cancerous Cells." *BioNanoScience* 8 (3): 769–777. https://doi.org/10.1007/s12668-018-0538-z.

Ahlinder, L., B. Ekstrand-Hammarström, P. Geladi, and L. Osterlund. 2013. "Large Uptake of Titania and Iron Oxide Nanoparticles in the Nucleus of Lung Epithelial Cells as Measured by Raman Imaging and Multivariate Classification." *Biophysical Journal* 105 (2): 310–319. https://doi.org/10.1016/j.bpj.2013.06.017.

Alghamdi, A. A. A. 2023. "Biogenic Mg Doped CeO2 Nanoparticles via Hibiscus Sabdariffa and Its Potential Biological Applications." *Journal of Umm Al-Qura University for Applied Sciences* 9 (2): 132–141. https://doi.org/10.1007/s43994-023-00030-z.

Annangi, B., Z. Lu, J. Bruniaux, A. Ridoux, V. M. da Silva, D. Vantelon, J. Boczkowski, and S. Lanone. 2021. "Macrophage Autophagy Protects Mice from Cerium Oxide Nanoparticle-Induced Lung Fibrosis." *Particle and Fibre Toxicology* 18 (1): 6. https://doi.org/10.1186/s12989-021-00398-y.

ATCC. n.d. "CCL-171 MRC-5," ATCC (American Type Culture Collection) https://www.atcc.org/products/ccl-171.

Beleites, C., and V. Sergo. 2024. "hyperSpec: A Package to Handle Hyperspectral Data Sets in R," 0.100.0.

Brauchle, E., S. Thude, S. Y. Brucker, and K. Schenke-Layland. 2014. "Cell Death Stages in Single Apoptotic and Necrotic Cells Monitored by Raman Microspectroscopy." *Scientific Reports* 4 (1): 4698. https://doi.org/10.1038/srep04698.

Campbell, C. T., and C. H. F. Peden. 2005. "Oxygen Vacancies and Catalysis on Ceria Surfaces." *Science (New York, N.Y.)* 309 (5735): 713–714. https://doi.org/10.1126/science.1113955.

Chen, J., S. Patil, S. Seal, and J. F. McGinnis. 2006. "Rare Earth Nanoparticles Prevent Retinal Degeneration Induced by Intracellular Peroxides." *Nature Nanotechnology* 1 (2): 142–150. https://doi.org/10.1038/nnano.2006.91.

Chernenko, T., C. Matthäus, L. Milane, L. Quintero, M. Amiji, and M. Diem. 2009. "Label-Free Raman Spectral Imaging of Intracellular Delivery and Degradation of Polymeric Nanoparticle Systems." *ACS Nano* 3 (11): 3552–3559. https://doi.org/10.1021/nn9010973.

Chernenko, T., L. Milane, C. Matthäus, M. Diem, and M. Amiji. 2013. "Raman Microspectral Imaging for Label-Free Detection of Nanoparticle-Mediated Cellular and Subcellular Drug Delivery." In *Drug Delivery Applications of Noninvasive Imaging*, pp. 70–90. John Wiley & Sons, Inc., Hoboken, New Jersey.

Corfe, B. M., C. Dive, and D. R. Garrod. 2000. "Changes in Intercellular Junctions during Apoptosis Precede Nuclear Condensation or Phosphatidylserine Exposure on the Cell Surface." *Cell Death and Differentiation* 7 (2): 234–235. https://doi.org/10.1038/sj.cdd.4400634.

Crow, P., B. Barrass, C. Kendall, M. Hart-Prieto, M. Wright, R. Persad, and N. Stone. 2005. "The Use of Raman Spectroscopy to Differentiate between Different Prostatic Adenocarcinoma Cell Lines." *British Journal of Cancer* 92 (12): 2166–2170. https://doi.org/10.1038/sj.bjc.6602638.

Cytion. n.d. "MRC-5 Cell Line: Human Fetal Lung Fibroblasts in Viral Research," Cytion. https://www.cytion.com/.

Czamara, K., K. Majzner, M. Z. Pacia, K. Kochan, A. Kaczor, and M. Baranska. 2015. "Raman Spectroscopy of Lipids: A Review." *Journal of Raman Spectroscopy* 46 (1): 4–20. https://doi.org/10.1002/jrs.4607.

Drasler, B., P. Sayre, K. G. Steinhäuser, A. Petri-Fink, and B. Rothen-Rutishauser. 2017. "In Vitro Approaches to Assess the Hazard of Nanomaterials." *NanoImpact* 8: 99–116. https://doi.org/10.1016/j.impact.2017.08.002.

Fazio, E., B. Gökce, A. De Giacomo, M. Meneghetti, G. Compagnini, M. Tommasini, F. Waag, et al. 2020. "Nanoparticles Engineering by Pulsed Laser Ablation in Liquids: Concepts and Applications." *Nanomaterials (Basel, Switzerland)* 10 (11): 2317. https://doi.org/10.3390/nano10112317.

Feng, N., Y. Liu, X. Dai, Y. Wang, Q. Guo, and Q. Li. 2022. "Advanced Applications of Cerium Oxide Based Nanozymes in Cancer." *RSC Advances* 12 (3): 1486–1493. https://doi.org/10.1039/d1ra05407d.

Ferraro, J. R., K. Nakamoto, and C. W. Brown. 2003. "Chapter 1 - Basic Theory." in: *Introductory Raman Spectroscopy*, 2nd ed., eds. J.R. Ferraro, K. Nakamoto, C.W. Brown, pp. 1–94. Academic Press, San Diego.

Guo, C., S. Robertson, R. J. M. Weber, A. Buckley, J. Warren, A. Hodgson, J. Z. Rappoport, et al. 2019. "Pulmonary Toxicity of Inhaled Nano-Sized Cerium Oxide Aerosols in Sprague–Dawley Rats." *Nanotoxicology* 13 (6): 733–750. https://doi.org/10.1080/17435390.2018.1554751.

Harvanova, M. P., J. Jiravova, J. Malohlava, K. B. Tomankova, D. Jirova, and H. Kolarova. 2017. "Raman Imaging of Cellular Uptake and Studies of Silver Nanoparticles Effect in BJ Human Fibroblasts Cell Lines." *International Journal of Pharmaceutics* 528 (1-2): 280–286. https://doi.org/10.1016/j.ijpharm.2017.05.076.

Hedegaard, M., C. Matthäus, S. Hassing, C. Krafft, M. Diem, and J. Popp. 2011. "Spectral Unmixing and Clustering Algorithms for Assessment of Single Cells by Raman Microscopic Imaging." *Theoretical Chemistry Accounts* 130 (4-6): 1249–1260. https://doi.org/10.1007/s00214-011-0957-1.

Hill, C., J. Li, D. Liu, F. Conforti, C. J. Brereton, L. Yao, Y. Zhou, et al. 2019. "Autophagy Inhibition-Mediated Epithelial–Mesenchymal Transition Augments Local Myofibroblast Differentiation in Pulmonary Fibrosis." *Cell Death & Disease* 10 (8): 591. https://doi.org/10.1038/s41419-019-1820-x.

Hussain, S., F. Al-Nsour, A. B. Rice, J. Marshburn, B. Yingling, Z. Ji, J. I. Zink, N. J. Walker, and S. Garantziotis. 2012. "Cerium Dioxide Nanoparticles Induce Apoptosis and Autophagy in Human Peripheral Blood Monocytes." *ACS Nano* 6 (7): 5820–5829. https://doi.org/10.1021/nn302235u.

Itzhak, D. N., S. Tyanova, J. Cox, and G. H. H. Borner. 2016. "Global, Quantitative and Dynamic Mapping of Protein Subcellular Localization." *eLife* 5: e16950. https://doi.org/10.7554/eLife.16950.

Jacobs, J. P., C. M. Jones, and J. P. Baille. 1970. "Characteristics of a Human Diploid Cell Designated MRC-5." *Nature* 227 (5254): 168–170. https://doi.org/10.1038/227168a0.4316953

Jana, S. K., P. Banerjee, S. Das, S. Seal, and K. Chaudhury. 2014. "Redox-Active Nanoceria Depolarize Mitochondrial Membrane of Human Colon Cancer Cells." *Journal of Nanoparticle Research* 16 (6): 2441. https://doi.org/10.1007/s11051-014-2441-z.

Jung, H., D. B. Kittelson, and M. R. Zachariah. 2005. "The Influence of a Cerium Additive on Ultrafine Diesel Particle Emissions and Kinetics of Oxidation." *Combustion and Flame* 142 (3): 276–288. https://doi.org/10.1016/j.combustflame.2004.11.015.

Karakoti, A. S., S. V. N. T. Kuchibhatla, K. S. Babu, and S. Seal. 2007. "Direct Synthesis of Nanoceria in Aqueous Polyhydroxyl Solutions." *The Journal of Physical Chemistry C* 111 (46): 17232–17240. https://doi.org/10.1021/jp076164k.

Krafft, C., M. A. Diderhoshan, P. Recknagel, M. Miljkovic, M. Bauer, and J. Popp. 2011. "Crisp and Soft Multivariate Methods Visualize Individual Cell Nuclei in Raman Images of Liver Tissue Sections." *Vibrational Spectroscopy* 55 (1): 90–100. https://doi.org/10.1016/j.vibspec.2010.09.003.

Lasalvia, M., G. Perna, and V. Capozzi. 2019. "Biochemical Changes in Human Cells Exposed to Low Concentrations of Gold Nanoparticles Detected by Raman Microspectroscopy." *Sensors* 19 (10): 2418. https://doi.org/10.3390/s19102418.

Liu, Y.-J., M. Kyne, S. Wang, S. Wang, X.-Y. Yu, and C. Wang. 2022. "A User-Friendly Platform for Single-Cell Raman Spectroscopy Analysis." *Spectrochimica Acta Part A: Molecular and Biomolecular Spectroscopy* 282: 121686. https://doi.org/10.1016/j.saa.2022.121686.

Ma, Y., W. Gao, Z. Zhang, S. Zhang, Z. Tian, Y. Liu, J. C. Ho, and Y. Qu. 2018. "Regulating the Surface of Nanoceria and Its Applications in Heterogeneous Catalysis." *Surface Science Reports* 73 (1): 1–36. https://doi.org/10.1016/j.surfrep.2018.02.001.

Ma, J. Y., R. R. Mercer, M. Barger, D. Schwegler-Berry, J. Scabilloni, J. K. Ma, and V. Castranova. 2012. "Induction of Pulmonary Fibrosis by Cerium Oxide Nanoparticles." *Toxicology and Applied Pharmacology* 262 (3): 255–264. https://doi.org/10.1016/j.taap.2012.05.005.

Mangalaraja, R. V., S. Ananthakumar, A. Schachtsiek, M. López, C. P. Camurri, and R. E. Avila. 2010. "Synthesis and Mechanical Properties of Low Temperature Sintered, Sm3+ Doped Nanoceria Electrolyte Membranes for IT-SOFC Applications." *Materials Science and Engineering: A* 527 (16-17): 3645–3650. https://doi.org/10.1016/j.msea.2010.01.025.

Mariño, G., M. Niso-Santano, E. H. Baehrecke, and G. Kroemer. 2014. "Self-Consumption: The Interplay of Autophagy and Apoptosis." *Nature Reviews. Molecular Cell Biology* 15 (2): 81–94. https://doi.org/10.1038/nrm3735.

Mayer, K. 2024. "hyperSpec.utils: Utility Functions to Work with Objects of the hyperSpec Class," 0.0.0.9002.

Ma, C., L. Zhang, T. He, H. Cao, X. Ren, C. Ma, J. Yang, R. Huang, and G. Pan. 2021. "Single Cell Raman Spectroscopy to Identify Different Stages of Proliferating Human Hepatocytes for Cell Therapy." *Stem Cell Research & Therapy* 12 (1): 555. https://doi.org/10.1186/s13287-021-02619-9.

Mazur, A. I., J. L. Monahan, M. Miljković, N. Laver, M. Diem, and B. Bird. 2013. "Vibrational Spectroscopic Changes of B-Lymphocytes upon Activation." *Journal of Biophotonics* 6 (1): 101–109. https://doi.org/10.1002/jbio.201200136.

Miletić, M., S. Aškrabić, J. Rüger, B. Vasić, L. Korićanac, A. S. Mondol, J. Dellith, J. Popp, I. W. Schie, and Z. Dohčević-Mitrović. 2020. "Combined Raman and AFM Detection of Changes in HeLa Cervical Cancer Cells Induced by CeO2 Nanoparticles – Molecular and Morphological Perspectives." *The Analyst* 145 (11): 3983–3995. https://doi.org/10.1039/c9an02518a.

Miletić, M., A. Vilotić, L. Korićanac, J. Žakula, M. J. Krivokuća, Z. Dohčević-Mitrović, and S. Aškrabić. 2023. "Spectroscopic Signature of ZnO NP-Induced Cell Death Modalities Assessed by Non-Negative PCA." *Spectrochimica Acta. Part A, Molecular and Biomolecular Spectroscopy* 288: 122180. https://doi.org/10.1016/j.saa.2022.122180.

Milligan, K., X. Deng, P. Shreeves, R. Ali-Adeeb, Q. Matthews, A. Brolo, J. J. Lum, J. L. Andrews, and A. Jirasek. 2021. "Raman Spectroscopy and Group and Basis-Restricted Non Negative Matrix Factorisation Identifies Radiation Induced Metabolic Changes in Human Cancer Cells." *Scientific Reports* 11 (1): 3853. https://doi.org/10.1038/s41598-021-83343-5.

Mittal, S., and A. K. Pandey. 2014. "Cerium Oxide Nanoparticles Induced Toxicity in Human Lung Cells: role of ROS Mediated DNA Damage and Apoptosis." *Biomed Research International*. 2014: 1–14. https://doi.org/10.1155/2014/891934.

Monteiro-Riviere, N. A., A. O. Inman, and L. W. Zhang. 2009. "Limitations and Relative Utility of Screening Assays to Assess Engineered Nanoparticle Toxicity in a Human Cell Line." *Toxicology and Applied Pharmacology* 234 (2): 222–235. https://doi.org/10.1016/j.taap.2008.09.030.

Naha, P. C., J. C. Hsu, J. Kim, S. Shah, M. Bouché, S. Si-Mohamed, D. N. Rosario-Berrios, et al. 2020. "Dextran-Coated Cerium Oxide Nanoparticles: A Computed Tomography Contrast Agent for Imaging the Gastrointestinal Tract and Inflammatory Bowel Disease." *ACS Nano* 14 (8): 10187–10197. https://doi.org/10.1021/acsnano.0c03457.

Nascimento, J. M. P., and J. M. B. Dias. 2005. "Vertex Component Analysis: A Fast Algorithm to Unmix Hyperspectral Data." *IEEE Transactions on Geoscience and Remote Sensing* 43 (4): 898–910. https://doi.org/10.1109/TGRS.2005.844293.

Niu, J., K. Wang, and P. E. Kolattukudy. 2011. "Cerium Oxide Nanoparticles Inhibit Oxidative Stress and Nuclear Factor-κB Activation in H9c2 Cardiomyocytes Exposed to Cigarette Smoke Extract." *The Journal of Pharmacology and Experimental Therapeutics* 338 (1): 53–61. https://doi.org/10.1124/jpet.111.179978.

Nourmohammadi, E., H. Khoshdel-Sarkarizi, R. Nedaeinia, H. R. Sadeghnia, L. Hasanzadeh, M. Darroudi, and R. Kazemi Oskuee. 2019. "Evaluation of Anticancer Effects of Cerium Oxide Nanoparticles on Mouse Fibrosarcoma Cell Line." *Journal of Cellular Physiology* 234 (4): 4987–4996. https://doi.org/10.1002/jcp.27303.

Nur, E. K. A., S. R. Gross, Z. Pan, Z. Balklava, J. Ma, and L. F. Liu. 2004. "Nuclear Translocation of Cytochrome c during Apoptosis." *The Journal of Biological Chemistry* 279 (24): 24911–24914. https://doi.org/10.1074/jbc.C400051200.

Ortiz-Zapater, E., J. Signes-Costa, P. Montero, and I. Roger. 2022. "Lung Fibrosis and Fibrosis in the Lungs: Is It All about Myofibroblasts?" *Biomedicines* 10 (6): 1423. https://doi.org/10.3390/biomedicines10061423.

Park, E. J., J. Choi, Y. K. Park, and K. Park. 2008. "Oxidative Stress Induced by Cerium Oxide Nanoparticles in Cultured BEAS-2B Cells." *Toxicology* 245 (1-2): 90–100. https://doi.org/10.1016/j.tox.2007.12.022.

Pavillon, N., and N. I. Smith. 2023. "Non-Invasive Monitoring of T Cell Differentiation through Raman Spectroscopy." *Scientific Reports* 13 (1): 3129. https://doi.org/10.1038/s41598-023-29259-8.

Perez, J. M., A. Asati, S. Nath, and C. Kaittanis. 2008. "Synthesis of Biocompatible Dextran-Coated Nanoceria with pH-Dependent Antioxidant Properties." *Small (Weinheim an Der Bergstrasse, Germany)* 4 (5): 552–556. https://doi.org/10.1002/smll.200700824.

Pešić, M., A. Podolski-Renić, S. Stojković, B. Matović, D. Zmejkoski, V. Kojić, G. Bogdanović, et al. 2015. "Anti-Cancer Effects of Cerium Oxide Nanoparticles and Its Intracellular Redox Activity." *Chemico-Biological Interactions* 232: 85–93. https://doi.org/10.1016/j.cbi.2015.03.013.

Rangan, S., S. Kamal, S. O. Konorov, H. G. Schulze, M. W. Blades, R. F. B. Turner, and J. M. Piret. 2018. "Types of Cell Death and Apoptotic Stages in Chinese Hamster Ovary Cells Distinguished by Raman Spectroscopy." *Biotechnology and Bioengineering* 115 (2): 401–412. https://doi.org/10.1002/bit.26476.

Reed, K., A. Cormack, A. Kulkarni, M. Mayton, D. Sayle, F. Klaessig, and B. Stadler. 2014. "Exploring the Properties and Applications of Nanoceria: Is There Still Plenty of Room at the Bottom?" *Environmental Science: Nano* 1 (5): 390–405. https://doi.org/10.1039/C4EN00079J.

Samuel, A. Z., K. Sugiyama, M. Ando, and H. Takeyama. 2022. "Direct Imaging of Intracellular RNA, DNA, and Liquid–Liquid Phase Separated Membraneless Organelles with Raman Microspectroscopy." *Communications Biology* 5 (1): 1383. https://doi.org/10.1038/s42003-022-04342-4.

Schie, I. W., L. Alber, A. L. Gryshuk, and J. W. Chan. 2014. "Investigating Drug Induced Changes in Single, Living Lymphocytes Based on Raman Micro-Spectroscopy." *The Analyst* 139 (11): 2726–2733. https://doi.org/10.1039/c4an00250d.

Shin, H. J., J. H. Lee, Y. D. Kim, I. Shin, T. Sim, and D.-K. Lim. 2019. "Raman-Based in Situ Monitoring of Changes in Molecular Signatures during Mitochondrially Mediated Apoptosis." *ACS Omega* 4 (5): 8188–8195. https://doi.org/10.1021/acsomega.9b00629.

Short, K. W., S. Carpenter, J. P. Freyer, and J. R. Mourant. 2005. "Raman Spectroscopy Detects Biochemical Changes Due to Proliferation in Mammalian Cell Cultures." *Biophysical Journal* 88 (6): 4274–4288. https://doi.org/10.1529/biophysj.103.038604.

Sigg, C. 2018. "nsprcomp: Non-Negative and Sparse PCA." https://cran.r-project.org/web/packages/nsprcomp/index.html.

Spezzati, G., K. Fant, A. Ahniyaz, M. Lundin-Johnson, E. J. M. Hensen, H. Langermans, and J. P. Hofmann. 2017. "Synthesis, Physicochemical Characterization, and Cytotoxicity Assessment of CeO2 Nanoparticles with Different Morphologies." *European Journal of Inorganic Chemistry* 2017 (25): 3184–3190. https://doi.org/10.1002/ejic.201700248.

Srinivas, A., P. J. Rao, G. Selvam, P. B. Murthy, and P. N. Reddy. 2011. “Acute Inhalation Toxicity of Cerium Oxide Nanoparticles in Rats.” *Toxicology Letters* 205 (2): 105–115. https://doi.org/10.1016/j.toxlet.2011.05.1027.

Tolstik, E., L. A. Osminkina, C. Matthäus, M. Burkhardt, K. E. Tsurikov, U. A. Natashina, V. Y. Timoshenko, R. Heintzmann, J. Popp, and V. Sivakov. 2016. “Studies of Silicon Nanoparticles Uptake and Biodegradation in Cancer Cells by Raman Spectroscopy.” *Nanomedicine: nanotechnology, Biology, and Medicine* 12 (7): 1931–1940. https://doi.org/10.1016/j.nano.2016.04.004.

Walkey, C., S. Das, S. Seal, J. Erlichman, K. Heckman, L. Ghibelli, E. Traversa, J. F. McGinnis, and W. T. Self. 2015. “Catalytic Properties and Biomedical Applications of Cerium Oxide Nanoparticles.” *Environmental Science. Nano* 2 (1): 33–53. https://doi.org/10.1039/C4EN00138A.

Wieland, K., M. Masri, J. von Poschinger, T. Brück, and C. Haisch. 2021. “Non-Invasive Raman Spectroscopy for Time-Resolved in-Line Lipidomics.” *RSC Advances* 11 (46): 28565–28572. https://doi.org/10.1039/d1ra04254h.

Yazici, H., E. Alpaslan, and T. J. Webster. 2015. “The Role of Dextran Coatings on the Cytotoxicity Properties of Ceria Nanoparticles Toward Bone Cancer Cells.” *JOM Journal of the Minerals Metals and Materials Society*. 67 (4): 804–810. https://doi.org/10.1007/s11837-015-1336-5.

Zhou, C., X. Xu, L. Dai, H. Gong, and S. Lin. 2021. “Chemical-Mechanical Polishing Performance of Core-Shell Structured Polystyrene@Ceria/Nanodiamond Ternary Abrasives on Sapphire Wafer.” *Ceramics International* 47 (22): 31691–31701. https://doi.org/10.1016/j.ceramint.2021.08.048.

Zuser, E., T. Chernenko, J. Newmark, M. Miljković, and M. Diem. 2010. “Confocal Raman Microspectral Imaging (CRMI) of Murine Stem Cell Colonies.” *The Analyst* 135 (12): 3030–3033. https://doi.org/10.1039/c0an00546k.

Applied Surface Science 710 (2025) 163753

Contents lists available at ScienceDirect

Applied Surface Science

journal homepage: www.elsevier.com/locate/apsusc

Unraveling the effects of terbium doping on the electronic structure and conductivity of $BiFeO_3$ thin films

Bojan Stojadinović [a],[*], Igor Popov [b], Borislav Vasić [a], Dejan Pjević [c], Milena Rosić [c], Nenad Tadić [d], Zorana Dohčević-Mitrović [a]

[a] Institute of Physics Belgrade, University of Belgrade, Pregrevica 118, 11080 Belgrade, Serbia
[b] Institute for Multidisciplinary Research, University of Belgrade, Kneza Višeslava 1, 11000 Belgrade, Serbia
[c] "Vinča" Institute of Nuclear Sciences, National Institute of the Republic of Serbia, University of Belgrade, Mike Petrovića Alasa 12-14, 11351 Belgrade, Serbia
[d] Faculty of Physics, University of Belgrade, Studentski trg 12-16, 11000 Belgrade, Serbia

ARTICLE INFO

Keywords:
$BiFeO_3$ thin films
Tb doping
Oxygen vacancies
Conductivity
Electronic structure
Density functional theory (DFT)

ABSTRACT

The structural and electrical properties of sol–gel synthetized $Bi_{1-x}Tb_xFeO_3$ films (x = 0, 0.05, 0.1, 0.2) were analyzed combining experimental observations and density functional theory, with an aim to elucidate the influence of Tb dopant on conduction properties of the films. $Bi_{1-x}Tb_xFeO_3$ films have a rhombohedral crystal structure, as identified from X-ray diffraction and Raman spectroscopy. Raman and X-ray photoelectron spectroscopy revealed that 10% Tb-doped film had significantly lower concentration of oxygen vacancies. This sample showed notably lower leakage current compared to other ones. Conductive atomic force microscopy measurements confirmed the lowest conductivity of 10% Tb-doped film. Density functional theory calculations provide atomic-level insights into the electronic structure and are consistent with experimental findings. Undoped and ~5% doped films are conductive due to high density of surface oxygen vacancy conducting states, whereas the conductivity of ~20% Tb-doped film originates from increased density of Tb conductive states near the Fermi level. In contrast, in ~10% Tb-doped film, lack of states responsible for electronic transport was found. These results highlight the necessity of judicious selection of doping concentrations to suppress vacancy-assisted as well as dopant-induced conduction paths and provide valuable guidelines for designing future $BiFeO_3$-based multiferroic materials with high resistivity.

Contents

---

[*] Corresponding author.
E-mail address: bojans@ipb.ac.rs (B. Stojadinović).

https://doi.org/10.1016/j.apsusc.2025.163753
Received 10 April 2025; Received in revised form 22 May 2025; Accepted 5 June 2025

1. Introduction

Bismuth ferrite ($BiFeO_3$) is a notable room temperature multiferroic material, exhibiting both ferroelectricity and G-type antiferromagnetism, as well as, weak ferromagnetism and coupling between ferroelectricity and ferro/antiferromagnetism [1–3]. With high Curie and Néel temperatures ($T_C \approx 830$ °C and $T_N \approx 370$ °C), it is highly suitable for the applications in next generation of ferroelectric random access memory (FeRAMs) and magnetoresistive random-access memory (MRAM) devices, but can also be a promising material for spintronic devices such as novel types of magnetoelectric sensors and magnetoelectric random access memories (MERAM) [2–6].

However, the major issue for the practical application of $BiFeO_3$ is large leakage current density which mainly originates from Bi volatility and formation of oxygen vacancies or presence of impurity phases, responsible for the deterioration of multiferroic features of $BiFeO_3$ [7–9]. An effective way to suppress the high leakage current and improve the multifunctional properties of $BiFeO_3$ is the partial substitution of rare-earth ions at Bi sites. It is documented that rare-earth ion doping prevents the volatilization of Bi atoms and creation of oxygen vacancies and other impurity phases, enhancing the resistive properties of $BiFeO_3$ [9–15]. Nevertheless, some authors have shown that doping with rare earth elements more than 20% can deteriorate the electric properties of $BiFeO_3$ [16]. Among the rare-earth elements, terbium (Tb) doping has gained attention for its ability to suppress the formation of oxygen vacancies and impurity phases, thereby enhancing ferroelectric or ferromagnetic characteristics of $BiFeO_3$ thin films and nanostructures [8,17–20]. However, higher Tb doping (≥ 10%) causes structural phase transition, when improved ferroelectric characteristics weaken [20,21].

The conductivity properties of Tb-doped $BiFeO_3$ are controversial. Some authors stated that for $BiFeO_3$ nanowires [8] and thin films [20], leakage current continuously decreases with increasing of Tb content up to 15%. When the substitution exceeds 15% of Tb, the leakage current increases approaching the value of undoped $BiFeO_3$ [20]. The other authors claimed that only 5 or 10 (11)% of Tb doping of $BiFeO_3$ thin films led to the reduction of leakage current [19,22,23]. These findings suggest that Tb doping of $BiFeO_3$ can mitigate defect-related conduction, but the conductivity is strongly dependent on dopant concentration and structural modifications and therefore warrants further investigation.

Previous conductivity measurements were mostly performed on a macroscopic scale. However, these measurements often fail to reveal important local variations in conductivity. Such local conductivity measurements can be performed using conductive atomic force microscopy (C-AFM), but its application to $BiFeO_3$ films has been scant [24,25]. In above mentioned papers structural, electrical, magnetic and ferroelectric properties of Tb-doped $BiFeO_3$ have been widely studied, but to the best of our knowledge the density functional theory (DFT) calculations of Tb influence on electronic structure of $BiFeO_3$ have not been performed. These calculations are useful to predict the role of dopant and defects i.e. how their position within the crystal lattice and concentration will play on conductivity.

This study investigates the effect of Tb doping on structural, morphological and conductivity properties of $BiFeO_3$ thin films, combining several experimental techniques and DFT calculations of electronic structure. We discussed the relations between dopant and vacancy concentrations on one hand and electronic properties on the other hand, which gave us an in-depth understanding of our experimental results. By correlating the above-mentioned findings, we aim to clarify the mechanisms responsible for the significant improvement in electrical performance of the 10% Tb-doped $BiFeO_3$ film, in order to optimize $BiFeO_3$-based materials for advanced multiferroic applications.

2. Methods

2.1. Materials synthesis

$Bi_{1-x}Tb_xFeO_3$ thin films were prepared using the sol–gel spin coating process. Knowing from the literature that the solubility limit of Tb is between 15 and 20% [8,26], $BiFeO_3$ films were doped with 5, 10 and 20% of Tb. The following reagents were used: bismuth nitrate pentahydrate ($Bi(NO_3)_3\cdot 5H_2O$, Sigma-Aldrich), terbium nitrate hexahydrate ($Tb(NO_3)_3\cdot 6H_2O$, Sigma-Aldrich), iron nitrate nonahydrate ($Fe(NO_3)_3\cdot 9H_2O$, Sigma-Aldrich), and glacial acetic acid (CH_3COOH, Merck Millipore). The reagents were dissolved in acetic acid and mixed under constant magnetic stirring for 30 min. Films were deposited onto FTO glass (Fluorine doped Tin Oxide coated glass slide). substrates from the prepared solution using sol–gel spin coating. Depositions were carried out at 1000 rpm for 30 seconds using a Laurell WS-650-23 Spin Coater. The films were dried for 40 min at 150 °C, followed by heat treatment at 550 °C for 2 h.

2.2. Structural and morphological characterization

The crystalline structure of $Bi_{1-x}Tb_xFeO_3$ thin films has been investigated using a Rigaku Ultima IV diffractometer, equipped with Cu $K\alpha_{1,2}$ radiations and operating at 40 kV and 40 mA in the 2θ range of 20° to 80° in a continuous scan mode with a scanning step size of 0.05° and a scan rate of 1°/min. Thin films were analyzed using X-ray diffraction at a grazing incidence angle of 0.5°, a technique known as Grazing Incidence X-ray Diffraction (GIXRD). This method was chosen to improve the signal quality. By using a small angle, we get better X-ray penetration into the film, which enhances the resolution of the diffraction pattern and gives us clearer details about the film's structure and crystallinity. The PDXL2 (Ver. 2.8.4.0) software was used to evaluate the phase composition and identification [27]. All obtained thin films were identified using the ICDD database [28] and the ICSD database [29]. GIXRD pattern analysis was performed using the software package Powder Cell [30,31]. The TCH pseudo-Voigt profile function gave the best fit to the experimental X-ray data. Crystallite sizes and microstrain were estimated from the GIXRD data using the Williamson-Hall method [32]. Micro-Raman spectra of thin films of $Bi_{1-x}Tb_xFeO_3$ were collected in a backscattering configuration using a Jobin Yvon T64000 triple spectrometer, with the spectral resolution of 2 cm^{-1}. The argon/krypton ion laser with an emitting line at $\lambda = 514.5$ nm was used as an excitation source, with the output laser power less than 2 mW to avoid the heating effects and/or sample degradation.

All atomic force microscopy measurements were done using Ntegra Prima system from NT-MDT. Topographic imaging of samples was done in tapping mode using SCOUT 350 RAI probes from NUNANO. Based on these images, we calculated surface roughness (from the images with 30×30 μm^2 scan size), and grain size distributions (from the images with 2×2 μm^2 scan size).

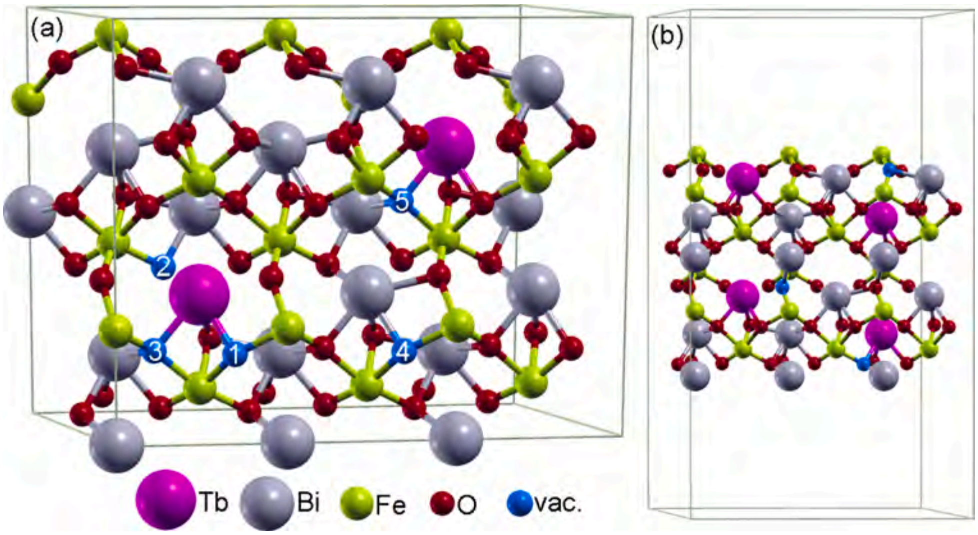

Fig. 1. (a) Perspective view of the conventional unit cell with considered positions of terbium dopants (pink spheres) and oxygen vacancies (blue spheres). (b) The surface supercell. Green lines indicate the boundaries of the bulk and surface supercells.

2.3. *Macroscopic and microscopic leakage current measurements*

The leakage current of $Bi_{1-x}Tb_xFeO_3$ films was measured by macroscopic, as well as microscopic electrical measurements. Macroscopic I–V curves were measured using a Keithley 2450 Source Meter, with the voltage varied from −3 V to 3 V, providing leakage current density as a function of voltage.

Local electrical currents (microscopic measurements) of investigated samples were measured using C-AFM and platinum coated AFM probes CSG10/Pt. The measurements were done by recording the electrical current through the conductive probes during scanning in contact mode, while a DC bias voltage was applied to the conductive FTO glass substrate (conductive AFM probe was virtually grounded). In order to get statistical information about conductivity from two dimensional current maps, we determined a conductive surface in percents in the following way. For each current map, we first calculated a bearing ratio curve which corresponds to the cumulative probability density function. Each point on this curve gives the percentage of points (y-axis) in the considered current map with a current below the value specified on the x-axis. The current map is taken as conductive if the current measured at this point is above the threshold defined as 10 pA or 50 pA. Therefore, the conductive surface in percents was obtained from bearing ratio curves by calculating percents of points with the current above the specified threshold current.

2.4. *X-ray photoelectron spectroscopy*

Chemical analysis of the $Bi_{1-x}Tb_xFeO_3$ thin films was performed by X-ray photoelectron spectroscopy (XPS). SPECS System with XP50M X-ray source for Focus 500 and PHOIBOS 100/150 analyzer was employed, operating at 12.5 kV and 250 W. Excitation of the spectra was performed with monochromatic Al Kα radiation (1486.7 eV). Survey spectra were recorded in the range of 800-0 eV, with constant pass energy of 40 eV, step size 0.5 eV and dwell time of 0.2 s in the fixed analyzer transmission (FAT) mode. High resolution spectra of Fe 2p, O 1s and C 1s peaks were recorded with constant pass energy of 20 eV, step size of 0.1 eV and dwell time of 2 s in the FAT mode. Instrument base pressure was $\sim 10^{-9}$ mbar during the experiments. To minimize the effect of charging at samples, electron flood gun (SPECS FG15/40) was used for charge neutralization, and all peak positions were referenced to C 1s at 284.8 eV. The data was analyzed after Shirley-type background subtraction, and by using CasaXPS software package. The fitting of high-resolution spectra was conducted with a Gaussian/Lorentzian (70/30) product formula for peak shapes. For the Fe 2p spectra, area constraints were applied to ensure a 2:1 ratio between the 2p3/2 and 2p1/2 peaks.

2.5. *Theoretical calculations*

2.5.1. *Parameters used in DFT calculations*

Density functional theory calculations were performed using SIESTA software [33] with the Perdew–Burke–Ernzerhof (PBE) form of the generalized gradient approximation (GGA) of exchange–correlation functional [34], norm-conserving Troullier–Martins pseudopotentials [35], and a double-ζ basis including polarization orbitals. Since GGA does not always describe well transition metals and lanthanoids, we employed GGA+U functionals [36–38], which proved efficient in our previous studies [39,40]. We used a Hubbard parameter $U_{eff} = 3.8$ eV for the Fe 3d orbital, $U_{eff} = 0.95$ eV for the Fe 4s orbital, and $U_{eff} = 2.5$ eV for Tb 4f orbital. The reciprocal space was sampled with a $2 \times 8 \times 2$ k-point mesh for geometry optimizations and refined to $10 \times 16 \times 10$ for calculations of electronic properties. A real-space sampling cut-off energy of 350 Ry was used. To achieve atomic geometries where maximum atomic forces do not exceed 0.05 uniteV/Å, we integrated several optimization methods: conjugate gradient, FIRE [41], L-BFGS [42], and a modified Broyden algorithm [43]. Each method was allowed to proceed up to 600 steps; if convergence failed, the structure with minimal atomic forces served as the initial point for subsequent method. Due to difficulties to achieve convergence of atomic forces, we applied constrained optimization on some structures containing vacancies, allowing only atoms adjacent or second-nearest neighbors to vacancies and dopants to move while other atoms remained fixed. Moreover, since a lattice parameter change of 0.33% between crystals with 0% and 10% doping levels was experimentally observed, close to the accuracy limit of our DFT method with pseudopotentials, we fixed the lattice parameters in our calculations to their experimental values. We investigated the type G antiferromagnetic (AFMG) ordering, which is the most prevalent in $BiFeO_3$ crystal.

2.5.2. *Model of atomic structure and structural relaxation*

Studying both bulk and surface structures in materials like $BiFeO_3$ doped with terbium is essential for a comprehensive understanding of their properties and behavior. The bulk structure provides fundamental information about the intrinsic material properties. However, surfaces and interfaces can exhibit distinct behaviors due to altered coordination environments. These effects are critical for understanding phenomena like charge transport, which is often dominated by surface states.

To simulate materials approximating experimental doping levels of 5%, 10%, and 20%, we used a supercell containing 18 Bi atoms, with one, two, or four Tb atoms substituted for Bi atoms at respective concentrations of 5.5%, 11.1%, and 22.2%. A larger supercell would more accurately match the desired doping levels but at the expense of significantly increased DFT computational time. The conventional unit cell of terbium-doped $BiFeO_3$ is depicted in Fig. 1(a). It was formed by $3 \times 1 \times 1$ replication of the hexagonal unit cell. The supercell has lattice parameters a = 16.65 Å, b = 5.55 Å, and c = 13.84 Å. For relatively small b lattice parameter, terbium dopants form chains; however, the dispersion of terbium electronic bands is minimal, as discussed later, indicating negligible Tb–Tb coupling in these chains.

In addition to terbium doping, we introduced oxygen vacancies in $BiFeO_3$. We analyzed combinations of 0.0%, 5.5% (1 Tb dopant per supercell), and 11.1% (2 Tb dopants per supercell) doping levels in conjunction with 0.0%, 1.9% (one vacancy per supercell), and 3.8% O vacancies (two vacancies per supercell). Bulk crystals with 20% doping level are not presented since structural relaxation could not drop atomic forces below the desired threshold of 0.05 eV/Å. Given the computational complexity, we could not calculate all possible combinations using an ab initio method. For instance, for 11.1% Tb doping and 3.7% vacancies, there are $\binom{54}{2} \times \binom{18}{2} = 218943$ possible arrangements to choose two Bi atoms from the supercell for substitution by two Tb atoms and two O atoms for vacancies. Therefore, we selected a representative subset of combinations. Particularly, we focused on positions of O vacancies, indicated as blue spheres in Fig. 1, that were either adjacent to or separated from Tb dopants by several intervening atoms. The locations of these Tb atoms are also shown in the same figure. Calculated configurations are labeled accordingly; for instance, v1 configuration is vacancy at position 1, whereas v12 is the configuration with two vacancies at positions 1 and 2. v4 is a vacancy separated from nearest Tb atom by several intervening atoms. Besides bulk we also considered a (0001) surface atomic structure, which model is shown in Fig. 1(b). It is constructed from the bulk supercell with lattice parameter c extended to 29 Å, which presents a 15 Å thick vacuum layer between the periodic replicas.

3. Results and discussions

3.1. Structural and morphological properties

Fig. 2 shows the diffraction patterns of $Bi_{1-x}Tb_xFeO_3$ thin films on FTO glass substrate. Based on the results of GIXRD analysis, it was determined that the rhombohedrally distorted $R3c$ (S.G. N° 161) perovskite structure is present in all samples. The corresponding Miller indices of the $R3c$ phase are indicated, whereas all other peaks can be indexed to tetragonal $P4_2/mnm$ (S.G. N° 136) cassiterite SnO_2 (ICSD # 56671) originating from the FTO glass substrate, without the presence of impurities.

The broad peaks of low intensity indicate the nanocrystalline nature of the thin films. With an increase of terbium content, a minimal changes of peak intensities are observed, but not their shift towards larger or smaller angles. Good agreement was obtained (based on data from the database, card number ICSD # 168740) between the experimental and calculated diffractograms.

The values of the lattice parameters and the unit cell volume are presented in Table 1, whereas the crystallite size and microstrain as a function of Tb doping are presented in the inset of Fig. 2. The lattice parameters a and c show a slight decrease up to 10% Tb doping, accompanied by a shrinkage of the unit cell volume. This behavior is consistent with the substitution of Bi^{3+} (~1.03 Å) by smaller Tb^{3+} ions (~0.92 Å) [19,20]. At 20% doping, a slight increase in both lattice parameters and unit cell volume is observed. The changes of the lattice parameters and unit cell volume correlate well with the evolution of crystalite size and microstrain with Tb doping, as shown in the inset of Fig. 2. As can be seen, the crystallite size increases with Tb doping, whereas the microstrain values decrease. The presence of higher microstrain in $Bi_{1-x}Tb_xFeO_3$ samples with smaller crystallite size can lead to the shrinkage of the unit cell, particularly along the c-axis [44]. The microstrain decreases as the crystallite size increases [45], causing the lattice to slightly expand, which is reflected in the moderate increase of the a and c parameters, as observed in the case of 20% Tb-doped sample.

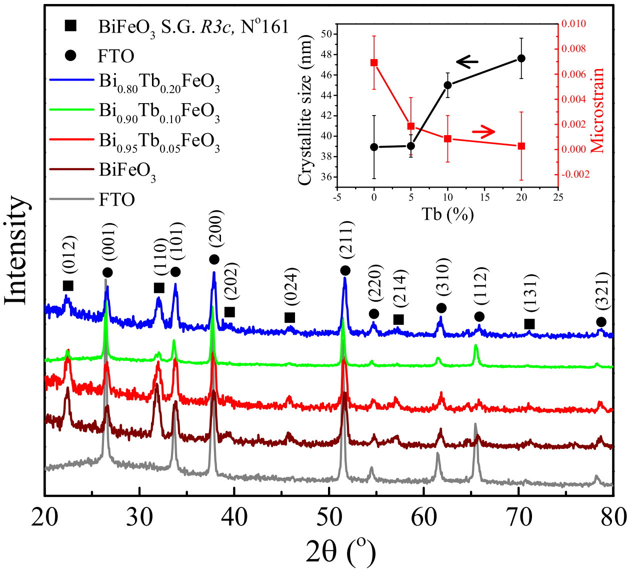

Fig. 2. GIXRD pattern of the $Bi_{1-x}Tb_xFeO_3$ thin films fabricated by the sol–gel spin coating process. The inset illustrates the average crystallite size and microstrain as a function of Tb doping.

In order to investigate the surface morphology and grain size distribution of the samples, AFM topographic images and corresponding height histograms are presented in Fig. 3. This figure includes 30 × 30 μm^2 and 2 × 2 μm^2 AFM images for $Bi_{1-x}Tb_xFeO_3$ samples at various doping levels (images (a), (d), (g), and (j) for 30 × 30 μm^2 and (b), (e), (h), and (k) for 2 × 2 μm^2). The topographic images show that all films have a flat surface, without visible cracks and holes, and with a well defined grain structure. The histograms (images (c), (f), (i), and (l)) depict an average grain size, showing values of 180, 187, 200, and 224 nm for $BiFeO_3$, $Bi_{0.95}Tb_{0.05}FeO_3$, $Bi_{0.90}Tb_{0.10}FeO_3$ and $Bi_{0.80}Tb_{0.20}FeO_3$, respectively.

Using these topographic images, we calculated the surface roughness and the grain size distribution. The corresponding results are presented in Fig. 4. The grain size increases with Tb doping, in agreement with XRD crystallite size. The grain sizes are several times larger than the crystallites, indicating that each grain consists of multiple

Table 1
The lattice parameters and the volume of the unit cell.

Phase	$BiFeO_3$	$Bi_{0.95}Tb_{0.05}FeO_3$	$Bi_{0.90}Tb_{0.10}FeO_3$	$Bi_{0.80}Tb_{0.20}FeO_3$
$BiFeO_3$ ICSD #168740 rhombohedral S. G. $R3c$ N°(161)	a = 5.58 Å c = 13.87 Å V = 374.25 Å^3	a = 5.57 Å c = 13.87 Å V = 373.10 Å^3	a = 5.56 Å c = 13.82 Å V = 371.07 Å^3	a = 5.57 Å c = 13.85 Å V = 372.67 Å^3

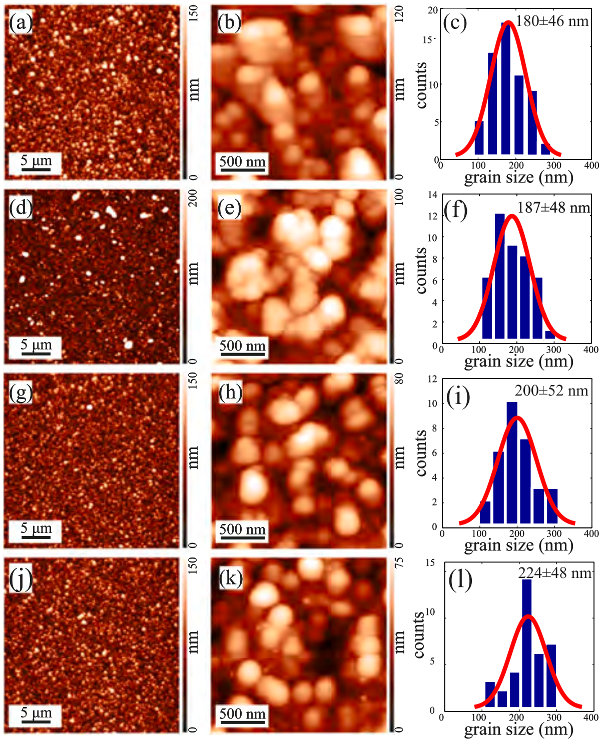

Fig. 3. The left column (images (a), (d), (g), (j)) presents 30 × 30 µm^2 AFM images, whereas the middle column (images (b), (e), (h), (k)) shows 2 × 2 µm^2 AFM images of $BiFeO_3$, $Bi_{0.95}Tb_{0.05}FeO_3$, $Bi_{0.90}Tb_{0.10}FeO_3$ and $Bi_{0.80}Tb_{0.20}FeO_3$ thin films, respectively. The right column (images (c), (f), (i), (l)) displays the corresponding histograms of average grain size derived from the 2 × 2 µm^2 AFM images. The red lines stand for Gaussian fits.

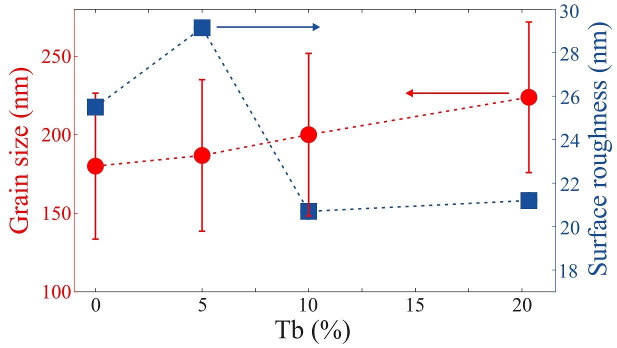

Fig. 4. Grain size (left axis) and surface roughness (right axis) data obtained from AFM measurements of $Bi_{1-x}Tb_xFeO_3$ thin films.

crystallites. The surface roughness of investigated films is low, in the range 20–30 nm.

Fig. 5(a) presents the room-temperature Raman spectra of $Bi_{1-x}Tb_xFeO_3$ thin films, deconvoluted using a Lorentzian type profiles. According to the factor group analysis, rhombohedral structure of $BiFeO_3$ exhibits 13 Raman-active modes, classified as 4 A_1 and 9E, all of which are observed in the spectrum of $BiFeO_3$ at room temperature and marked in Fig. 5(a). The low frequency, intense A_1 and E modes, are associated with Bi–O vibrations. The weaker E modes at higher frequencies, mainly correspond to Fe–O vibrations.

Tb doping induces noticeable changes in the Raman spectrum. At lower Tb concentrations, slight peak shifts to higher wavenumbers and a reduction of the intensity of low-frequency A_1 modes are observed. As the Tb content increases, the blueshift and broadening of the Raman modes become more pronounced [46]. These changes of the A_1 modes suggest structural distortion due to the substitution of Bi^{3+} ions with the smaller Tb^{3+} ones and higher electronegativity of the Tb–O bonds which strengthen the Bi(Tb)–O covalent bonds [23]. The rest of the E and A_1 modes at higher frequencies show minor shifts and intensity changes, except the E mode at 471 cm^{-1}. This mode undergoes a pronounced blue shift and intensity increase in all doped samples except for $Bi_{0.90}Tb_{0.10}FeO_3$, suggesting the modifications in Fe–O bonding interactions with Tb incorporation.

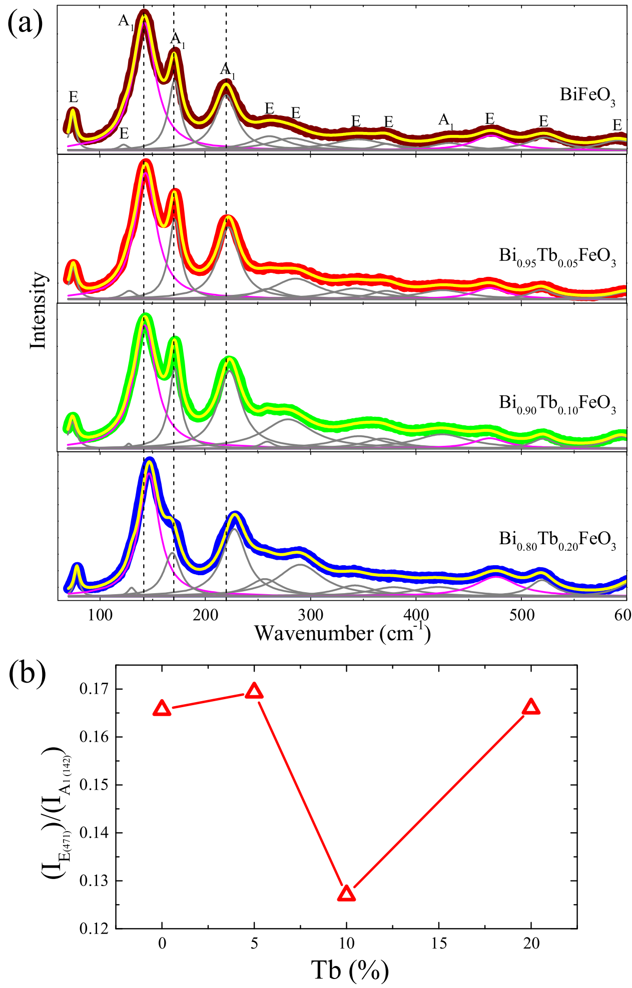

Fig. 5. (a) Raman spectra of $Bi_{1-x}Tb_xFeO_3$ thin films (thick colored lines), along with cumulative fits (yellow lines). Individual Lorentzian peaks are presented with thin lines. Vertical dashed lines represent the guide to the eye in tracking the shift of specific modes. (b) Intensity ratio of the $E_{(471)}$ and $A_{1(142)}$ Raman modes, as a function of Tb doping.

It is well known that the volatility of Bi^{3+} during synthesis process promotes the formation of oxygen vacancies, which significantly influence the structural and vibrational properties of $BiFeO_3$. These defects predominantly affect Fe–O bond dynamics within the FeO_6 octahedra, altering specific Raman modes. Notably, the E mode located around 471 cm^{-1}, associated with Fe–O–Fe bending vibrations, exhibits a distinct blue shift and intensity change with Tb doping.

As suggested by Gupta et al. [47], the E mod at 471 cm^{-1} is affected by oxygen vacancies. They found that relative intensity ratio of E and A_1 modes at 471 and 142 cm^{-1} ($E_{(471)}/A_{1(142)}$) increases with increased disorder, i.e increased concentration of oxygen vacancies. In Fig. 5(b) is presented the $E_{(471)}/A_{1(142)}$ ratio as a function of Tb doping. As can be seen, the lowest $E_{(471)}/A_{1(142)}$ ratio is found in 10% Tb-doped sample, indicating that this sample has the lowest oxygen vacancy concentration. In undoped, 5% and 20% Tb–doped samples

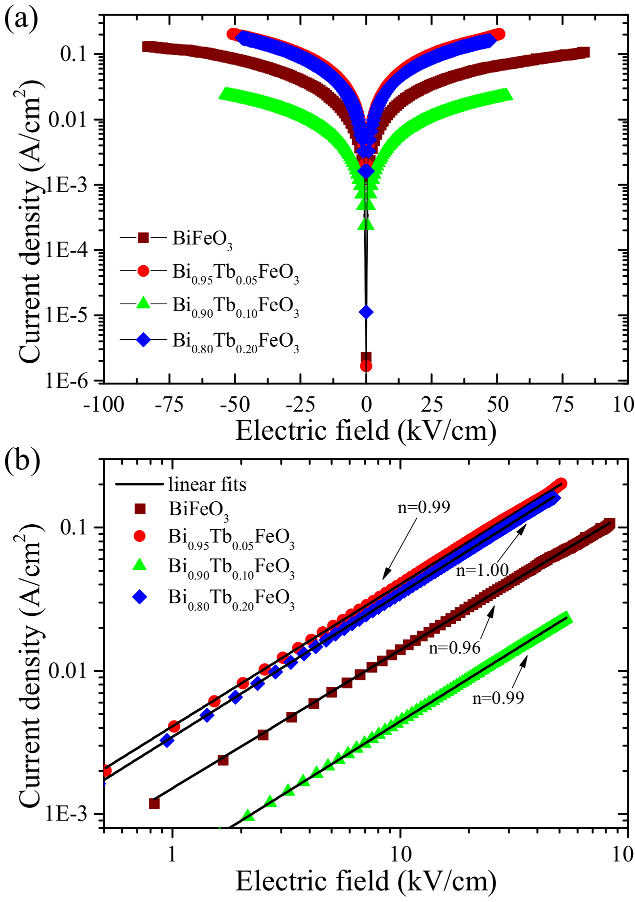

Fig. 6. (a) Semilogarithmic representation of current density (J) versus electric field (E) for $Bi_{1-x}Tb_xFeO_3$ thin films. (b) Log–log representation of current density versus electric field, including linear fits with corresponding slope coefficients.

this intensity ratio is higher implying that these samples have higher concentration of oxygen vacancies.

3.2. Leakage current

Fig. 6(a) presents the current density (J) versus electric field (E) curves for $Bi_{1-x}Tb_xFeO_3$ thin films, while Fig. 6(b) displays the same data in a logarithmic scale. The data in Fig. 6(a) show that the 10% Tb-doped sample exhibits a current density an order of magnitude lower compared to other doping levels. In Fig. 6(b), the measured data were fitted with linear functions, yielding slopes approximately equal to 1, indicating that the Ohmic conduction is dominant [23].

Our results indicate that the most significant reduction in leakage current occurs at 10% Tb doping. Further doping does not proportionally enhance resistive properties; instead, the $Bi_{0.80}Tb_{0.20}FeO_3$ sample becomes more conductive. A similar non-monotonic dependence of conductivity on Tb content has been observed in previous studies, where intermediate doping levels led to minimized leakage current, while higher doping concentrations resulted in increased conductivity [22].

Although the previous results of the macroscopic measurements revealed how electrical conductivity change with Tb-doing, we employed C-AFM in order to measure local currents at the micro-scale and to get further insights into conduction mechanisms. Typical current maps measured on the surface of the $Bi_{0.90}Tb_{0.10}FeO_3$ film using C-AFM at different bias voltages ((a) 1 V, (b) 2 V, (c) 3 V, and (d) 4 V) are displayed in Fig. 7. As can be seen, the maps exhibit very low currents for low bias voltages (1 V and 2 V, Figs. 7(a) and 7(b), respectively). At the same time, conductive paths represented by a bright contrast and associated with a more pronounced current are very narrow and localized. On the other hand, at higher bias voltages (3 V and 4 V, Figs. 7(c) and 7(d), respectively), the current is significantly enhanced while conductive paths become extended. Therefore, one of the main features of the presented current maps is their spatial inhomogeneity. This implies that the film surface is associated with an analogous spatial inhomogeneity of the conductivity.

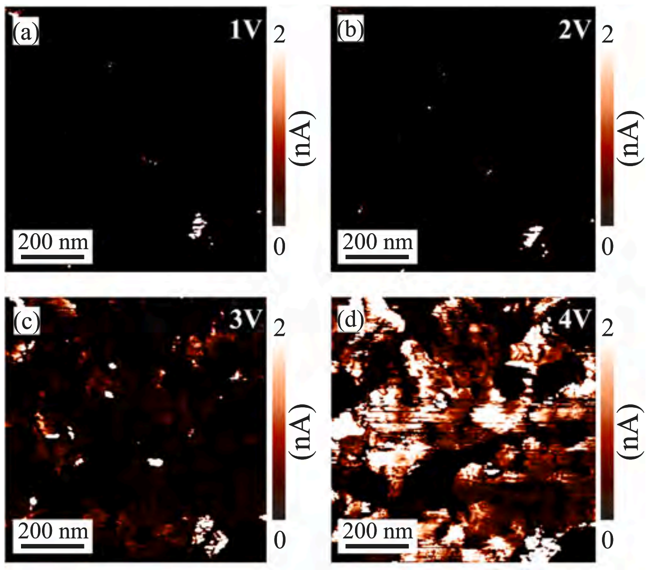

Fig. 7. Current maps of the $Bi_{0.90}Tb_{0.10}FeO_3$ sample measured by C-AFM at different bias voltages: (a) 1 V, (b) 2 V, (c) 3 V, and (d) 4 V. The color scales for all maps were adjusted to the same range 0-2 nA (they were saturated at 2 nA) in order to highlight lower (leakage) currents and at the same time, to facilitate the comparison of all current maps.

The current maps from Fig. 7 show that the conduction starts from very small and localized domains, which are spatially separated. With increasing bias voltage, these domains spatially extend. Finally, for high voltages they start to merge into large conductive domains.

As we have already demonstrated for similar $BiFeO_3$ samples, there is a significant difference in electrical properties among the grains and grain boundaries [24]. The most obvious difference is that the grain boundaries are much more conductive. Since the grain boundaries present a certain discontinuity in a crystal structure of single grain, they are always associated with an increased concentrations of various defects which facilitate conduction. Oxygen vacancies are the most frequent defects in $BiFeO_3$ films. Therefore, bright contrast in the current maps in Fig. 7 measured at lower voltages, most probably corresponds to a network of grain boundaries with enhanced concentration of oxygen vacancies resulting in increased conductivity. Current maps like in Fig. 7 (recorded at increasing bias voltage) were measured on all investigated films. The current maps of all samples, measured at 1 V, are presented in Figs. 8(a–d) for comparison. The color scales in all maps are saturated at 100 nA for better visibility and easier comparison. Since absolute current value is, in principle, not relevant for our study, the presented current maps exhibit a nearly black-and-white color contrast. They are practically binary images, where dark areas (zero current) indicate insulating domains, and bright areas represent conductive domains. As can be seen, the dark contrast dominates in all maps indicating a near-zero current, while bright spots mark narrow conductive paths. Based on the visual comparison, the area of the conductive paths is the smallest for the film with 10% Tb doping (Fig. 8(c)) implying the lowest conductivity. On the other hand, the film with 5% Tb doping (Fig. 8(b)) exhibits a dense network of bright domains indicating a pronounced leakage current.

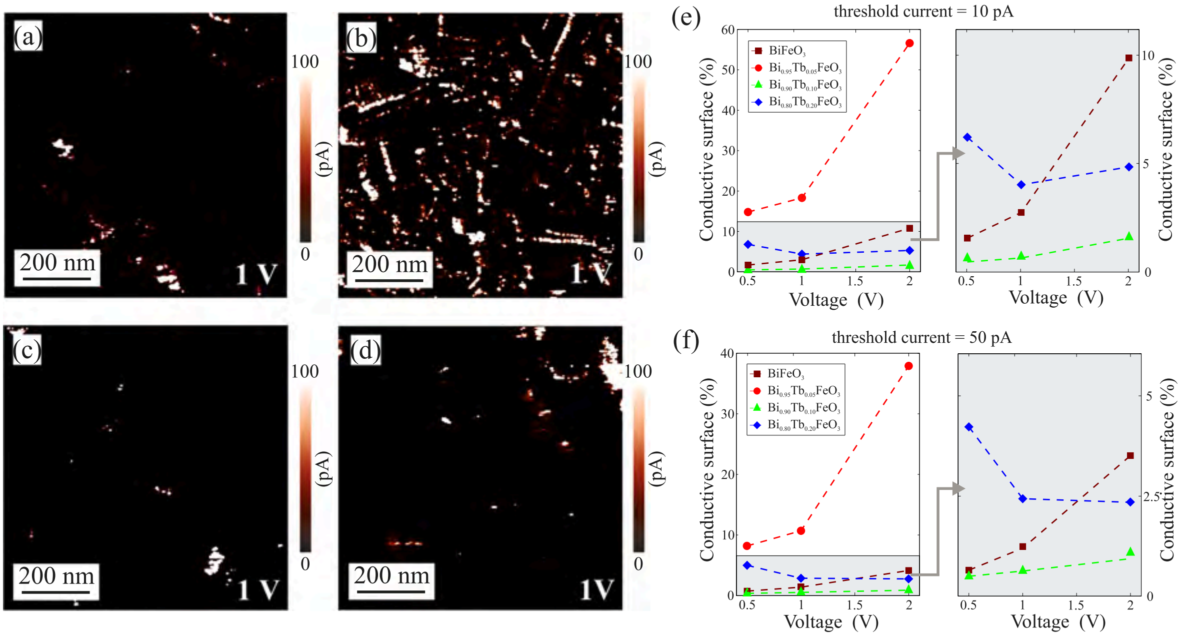

Fig. 8. Current maps measured at 1 V for (a) BiFeO$_3$, (b) Bi$_{0.95}$Tb$_{0.05}$FeO$_3$, (c) Bi$_{0.90}$Tb$_{0.10}$FeO$_3$ and (d) Bi$_{0.80}$Tb$_{0.20}$FeO$_3$ thin films. The color bar is saturated at 100 pA in all current maps in order to emphasize the contrast on conductive paths representing leakage currents. Conductive surface of investigated films expressed in percents as a function of applied voltage and for two current thresholds: (e) 10 pA and (f) 50 pA. To better illustrate the evolution of the conductive surface in the approximate range of 0%–10%, the gray regions marked on the main graphs are enlarged and shown on the right-hand side.

In order to compare the presented current maps, each of them was associated with a corresponding conductive surface expressed in percents. Briefly, each point on a measured current map (each map consists of 256 × 256 pixels) was counted as a conductive if the measured current at the considered point was larger than the predefined threshold current. The conductive surface in percents was then obtained as a ratio between a number of conductive and total number of points for one map. Two selected threshold currents were set at 10 pA and 50 pA. The comparison of conductive surfaces for all considered samples as a function of the applied bias voltage is given in Figs. 8(e) and 8(f). As can be seen, the Bi$_{0.90}$Tb$_{0.10}$FeO$_3$ film exhibits the smallest conductive surface for both threshold currents. This observation is in accordance with the results of the macroscopic I–V measurements and it confirms that the Bi$_{0.90}$Tb$_{0.10}$FeO$_3$ film has the smallest conductivity.

While moderate doping (around 10%) effectively reduces leakage current, higher doping levels (20%) lead to an increase in leakage current. Therefore, a delicate balance between Tb dopant concentration and defect control is essential to optimize the electrical performance of BiFeO$_3$ thin films.

3.3. *X-ray photoelectron spectroscopy (XPS)*

The survey XPS spectra of Bi$_{1-x}$Tb$_x$FeO$_3$ thin films, as shown in Fig. 9, provide insights into the chemical composition, oxidation states and the presence of defects.

These survey spectra confirm the presence of all major elements in the films: Fe, Bi, Tb, and O, whose most prominent lines are clearly marked. One can also see signals from the Sn substrate and adventitious carbon (C 1s) contamination at 284.8 eV, reflecting the sensitivity of the XPS technique in capturing both intrinsic and extrinsic elements. Furthermore, the changes in the O 1s and Fe 2p spectra can provide insight into defect structure of Bi$_{1-x}$Tb$_x$FeO$_3$ thin films.

The oxidation states of Fe in Bi$_{1-x}$Tb$_x$FeO$_3$ thin films, analyzed by XPS, are shown in Fig. 10 (right panel). The Fe 2p$_{3/2}$ peak is deconvoluted into two components corresponding to Fe^{2+} at 709.6(2) eV and Fe^{3+} at 711.1(2) eV. Their coexistence indicates charge compensation mechanisms mediated by oxygen vacancies. The splitting between Fe 2p$_{3/2}$ and Fe 2p$_{1/2}$ components is consistently 13.6 eV for all samples, confirming the expected multiplet structure. Additionally, a noticeable Sn 3p contribution, present in all samples, overlaps with the Fe 2p region, preventing us to perform more precise quantitative estimation of Fe^{2+}/Fe^{3+} fraction. Since XPS only probes the surface to a few nanometers, the Sn signal is more prominent in the undoped sample and decreases with the increased thickness of the doped films. The presence of Sn in the spectra can also be attributed to thermal treatment, which has caused Sn to diffuse towards the film's surface.

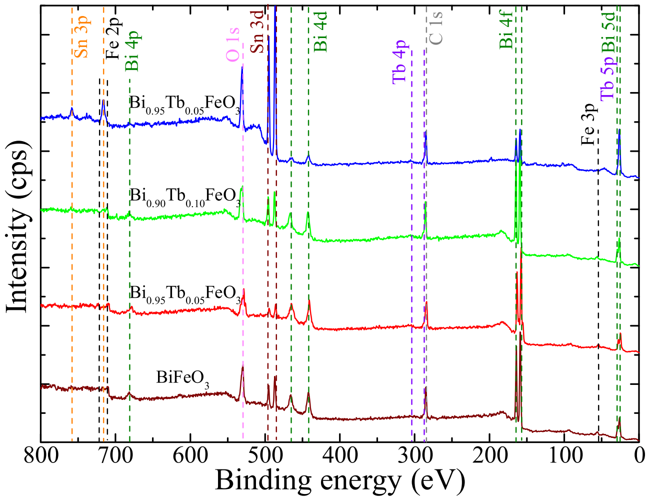

Fig. 9. XPS survey spectra of Bi$_{1-x}$Tb$_x$FeO$_3$ thin film.

The O 1s spectra of Bi$_{1-x}$Tb$_x$FeO$_3$ samples, presented in Fig. 10 (left panel), were deconvoluted into multiple peaks. The binding energies of lattice oxygen bonded to Fe and Sn are 529.4(1) eV and 530.5(1) eV, respectively, while the peak centered at 531.4(2) eV corresponds to oxygen vacancy-related species and hydroxides [48,49]. To quantitatively investigate the effect of Tb doping on oxygen vacancies, atomic percentages of oxygen vacancies (V$_O$) for each sample were extracted

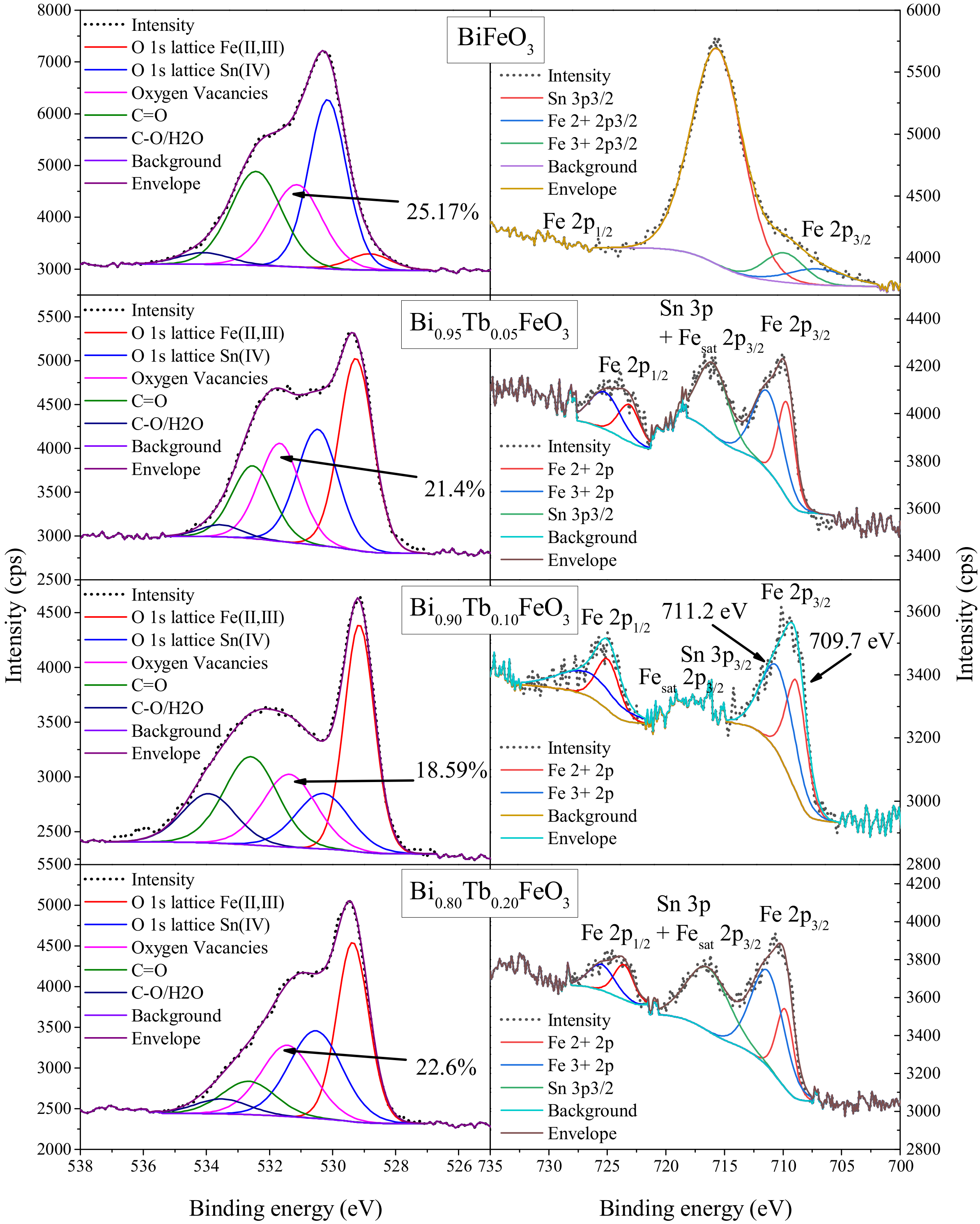

Fig. 10. High-resolution XPS spectra of O 1s (left) and Fe 2p (right) regions for $Bi_{1-x}Tb_xFeO_3$ thin films, including experimental data (dots) and fitted peaks (solid lines).

from deconvoluted high-resolution XPS spectra of O 1s spectrum and are summarized in Table 2.

The concentration of oxygen vacancies is the highest in the undoped $BiFeO_3$ film and decreases a bit for $Bi_{0.95}Tb_{0.05}FeO_3$ sample, reaching a minimum for the $Bi_{0.90}Tb_{0.10}FeO_3$ sample. However, at higher doping levels, a slight increase is observed, suggesting a complex relationship between defect concentration and dopant incorporation. The XPS results are in fairly good agreement with the conductivity measurements, showing that among all samples the $Bi_{0.90}Tb_{0.10}FeO_3$ has the lowest

Table 2
Atomic percentage of oxygen vacancies (V_O) for $Bi_{1-x}Tb_xFeO_3$ thin films.

Sample	V_O [at%]
$BiFeO_3$	25.2
$Bi_{0.95}Tb_{0.05}FeO_3$	21.4
$Bi_{0.90}Tb_{0.10}FeO_3$	18.6
$Bi_{0.80}Tb_{0.20}FeO_3$	22.6

Table 3
Relaxation energies and vacancy formation energies. Configuration labels correspond to the positions of vacancies marked in Fig. 1.

Configuration	E_{rel} (eV/atom)	E_{form} (eV/atom)
undoped		
no vac.	−0.020	
v1	−0.008	0.061
v2	−0.006	0.057
v12	−0.013	0.119
1 Tb (5.5%)		
no vac.	−0.015	
v4	−0.049	0.026
v5	−0.040	0.037
v1	−0.034	0.043
v2	−0.030	0.034
v45	−0.051	0.067
v13	−0.003	0.097
2 Tb (11.1%)		
no vac.	−0.024	
v4	−0.012	0.031
v1	−0.009	0.042
v13	−0.001	0.063
v14	−0.001	0.030

concentration of oxygen vacancies which makes this sample the least conductive.

3.4. Theoretical calculations

3.4.1. Bulk atomic structure and relaxation energies

The favorable vacancy concentration can typically be derived from the formation energy associated with specific chemical reactions used in sample fabrication. However, the fabrication conditions employed in this study introduce uncertainties that complicate precise theoretical calculations. For instance, the exact atomic structures of nitrates involved in the fabrication process cannot be definitively determined. To circumvent these limitations, we compared relaxation energies upon introducing vacancies into bulk structures for various atomic configurations and also evaluated vacancy formation energies. While this approach does not yield an exact vacancy concentration for our experimental samples, it provides qualitative insights into doping level versus vacancy concentration dependencies.

The relaxation energies from structural optimization are detailed in Table 3. When oxygen vacancies are introduced near the Tb dopant sites (designated as v1 and v2) within a 5.5%-doped crystal, the relaxation energies decrease to −0.034 eV and −0.030 eV from their respective values of −0.008 eV and −0.006 eV in undoped sample. This observation indicates a strong interaction between Tb doping and nearby oxygen vacancies, enhancing structural stability. Interestingly, when the vacancies are located farther away from the Tb dopant (designated as v4 and v5), their presence leads to even lower relaxation energies of −0.049 eV and −0.040 eV. This suggests that while local interactions between Tb doping and oxygen vacancies contribute significantly to stability, long-range effects also play an important role in lowering the overall energy of the doped system. For structures with two Tb dopants (11.1% doping concentration), the presence of vacancies results in relaxation energies higher than those without any vacancy. This indicates that at 11.1% doping level, the system is less prone to incorporating oxygen vacancies.

Vacancy formation energies are also presented in Table 3. These energies are defined as:

$$E_{\text{form}} = \frac{E_t\ (\text{vacant str.}) + N_{\text{O}}\frac{E_t(\text{O}_2)}{2} - E_t\ (\text{pristine})}{N},$$

where E_t (vacant str.) and E_t (pristine) are the total DFT energies of relaxed structures with vacants and pristine structures respectively, $E_t(\text{O}_2)$ is the energy of an oxygen molecule, N_{O} is the number of oxygen vacancies and N is the number of atoms in the structure. Similar to the trend observed for relaxation energies, vacancy formation energies are consistently lower in lattices with 5.5% doping compared to undoped structures. However, at an 11.1% doping concentration, these energies do not significantly differ from those at a 5.5% doping level.

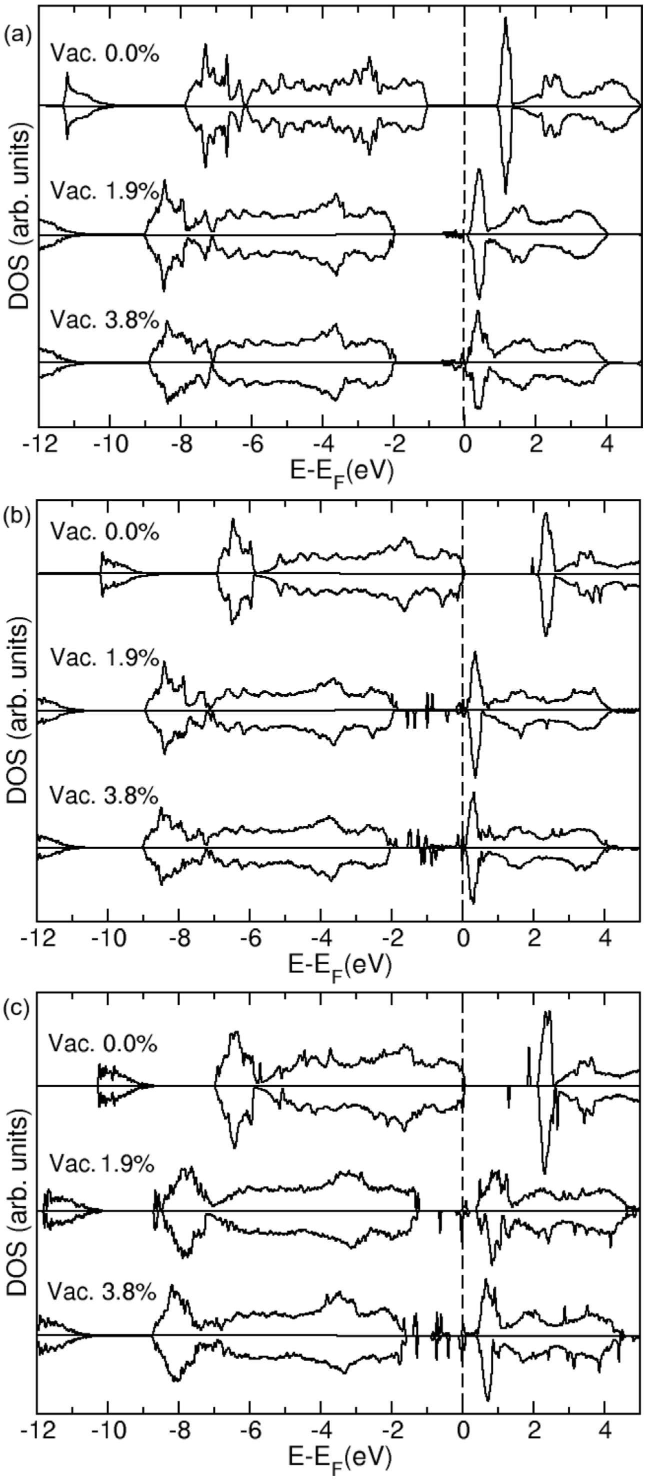

Fig. 11. DOS of (a) undoped, (b) 5.5% doped and (c) 11.1% Tb doped $BiFeO_3$. In each panel the top, middle and bottom graphs correspond to 0.0%, 1.9% and 3.8% oxygen vacancies. Each graph depicts DOS for majority/minority spins above/below local horizontal axes. Vertical dashed line marks the Fermi level.

3.4.2. Analysis of bulk electronic properties

In Fig. 11, we present a comparative analysis of the electronic density of states (DOS) of $BiFeO_3$ with varying concentrations of terbium dopants and oxygen vacancies. We examined three doping levels: 0%, 5.5%, and 11.1% terbium, alongside three vacancy concentrations: 0%, 1.9%, and 3.8%.

The Fermi level of the undoped vacant-free $BiFeO_3$ is positioned at the center of the band gap, as expected for the semiconducting pristine bismuth ferrite. Introducing the oxygen vacancies into an undoped crystal shifts the Fermi level towards the bottom of the conduction band due to excess electrons from vacant oxygen sites (Fig. 11(a)). In contrast, the Fermi level for 5.5% and 11.1% doped $BiFeO_3$ with no oxygen vacancies (0.0%) is positioned at the top of the valence band, evident from the top graphs in panels b and c of Fig. 11. In $BiFeO_3$ crystals doped at 5.5%of Tb (Fig. 11(b)), oxygen vacancies cause a significant upward shift in the Fermi level, placing it near or within the conduction band. At higher terbium doping levels (11.1%, Fig. 11(c)), an equilibrium between vacancy-induced n-type doping and dopant-induced p-type behavior results in the Fermi level returning to the bandgap. Our DFT calculations encountered convergence issues for terbium concentrations above 11.1% in bulk structures, preventing theoretical DOS graphs for these conditions. However, further doping would likely exacerbate p-type behavior, shifting the Fermi level towards or within the valence band. Both terbium doping and oxygen vacancies introduce states within the bandgap of $BiFeO_3$. In vacancy-free crystals, dopants at 5.5% and 11.1% concentrations generate one and two distinct bandgap states, respectively. Conversely, systems with oxygen vacancies exhibit a proliferation of bandgap states due to the presence of numerous dangling bonds. These additional states are characterized by minimal dispersion, indicating strong localization. The localized nature of these bandgap states plays a crucial role in modulating charge transport properties. In vacancy-free crystals, excess electrons would naturally fill the conduction band upon increasing vacancy concentration, potentially rendering the material conductive. However, the presence of localized bandgap states necessitates sequential filling according to Fermi-Dirac statistics and Pauli exclusion principle, thereby impeding easy movement of the Fermi level within the bandgap.

3.4.3. Local density of states

Local density of states (LDOS) integrated ±0.05 eV around the Fermi level is presented for three atomic configurations in Fig. 12: an undoped supercell with 2 vacancies (Fig. 12(a)), a supercell with 1 Tb atom and two neighboring vacancies (Fig. 12(b)), and a supercell with 2 Tb atoms, each with one neighboring vacancy (Fig. 12(c)). Graphical representation of LDOS can vary with isosurface values; from our careful analysis of LDOS for a range of isovalues we found that isovalue of 0.0003 states/eV/$Å^3$ captures the most important details of investigated supercells' electronic structures.

Fig. 12 reveals two key observations: 1. In the undoped configuration (a), significant LDOS contributions are not localized around both vacancies, contrary to expectations, but rather LDOS is relatively delocalized through the supercell. 2. For doped configurations (b) and (c), LDOS is concentrated around Tb dopants and their neighboring vacancies, with a decaying distribution further away. These findings suggest that in doped systems, electronic states become more localized near the dopant sites, potentially leading to delocalization at higher doping concentrations as the wavefunctions overlap increasingly with dopant concentration (conversely the Tb–Tb distance decreases). This could result in percolation effects and an increase in electrical conductivity as dopant concentration increases. The states around the Fermi level in undoped structure are delocalized, which is one of the key conditions for high electric conductivity.

Table 4
Vacancy formation energies.

Configuration	E_{form} (eV/atom)
undoped	
one vac. in bulk	0.039
one vac. on Bi surf.	0.034
one vac. on Fe surf.	0.036
1 Tb (5.5% doping)	
one vac. in bulk	0.016
one vac. on Bi surf.	0.003
one vac. on Fe surf.	0.055
2 Tb (11.1% doping)	
one vac. in bulk	0.042
one vac. on Bi surf.	0.210
one vac. on Fe surf.	0.060
4 Tb (22.2% doping)	
one vac. in bulk	0.102
one vac. on Bi surf.	0.049
one vac. on Fe surf.	0.121

3.4.4. Vacancy formation energies in surfaces

The infinite periodic structures we considered above are representative of doping and vacancy effects in bulk. However, experimental samples are rather polycrystalline in which surfaces and grain boundaries may affect the electronic and transport properties. The lower coordination of oxygen atoms at surfaces can significantly alter their binding energies and consequently affect the distribution of vacancies. To bridge this gap between theoretical models and experimental observations, we extended our investigation to incorporate surface phenomena. Specifically, we introduced a single vacancy into either the Bi or Fe layer at the surface or within deeper layers of the structure. We utilized the supercell from our bulk studies but modified it by extending the c lattice vector to 29 Å to ensure an adequate vacuum layer between periodic replicas, i.e. negligible interaction between them. While we aimed to optimize these surface structures, atomic forces could not be reduced below a tolerance level of 0.05 ev/Å for some structures. In order to have fair comparison among all configurations, we present data only for unoptimized structures. The Table 4 presents calculated values of vacancy formation energy for various configurations, including undoped and doped structures with one, two or four Tb atoms per supercell. These calculations are performed to determine the most favorable positions for oxygen vacancies within these structures. Undoped $BiFeO_3$ exhibits similar vacancy formation energies regardless of the surface type, indicating minimal intrinsic anisotropy in oxygen vacancies under pristine conditions. When one Tb atom is introduced per supercell (corresponding to 5.5% doping level), vacancy formation energies change significantly. The energy in bulk (0.016 eV/atom) and Fe surface (0.055 eV/atom) decrease compared to the undoped structure, suggesting that Tb doping facilitates oxygen vacancy formation in these configurations. However, the most striking change is observed at the Bi surface: 0.003 eV/atom. This suggests that Tb doping strongly facilitates vacancy formation on the Bi-terminated surface even at the room temperature. Introducing two Tb atoms per supercell (corresponding to 11.1% doping level) alters these trends. The vacancy energy increases for all studied configurations, indicating a less favorable environment for vacancies in these configurations. This is in agreement with our analysis of vacancies using XPS (Section 3.4), while the doping level also corresponds well to the doping level for which the reduced leakage current was observed (Section 3.2). Interestingly, the most significant increase of vacancy formation energy is for Bi-terminated surface, which is the most favorable place for less doped level. This implies that with two Tb atoms per supercell, oxygen vacancies are least favorable to form at either surfaces or in bulk. At four Tb atoms per supercell (corresponding to 22.2% doping level), vacancies become significantly least favorable in bulk and Fe-terminated surfaces. Vacancy formation energy on Bi-terminated surface decreases to 0.049 eV/atom from

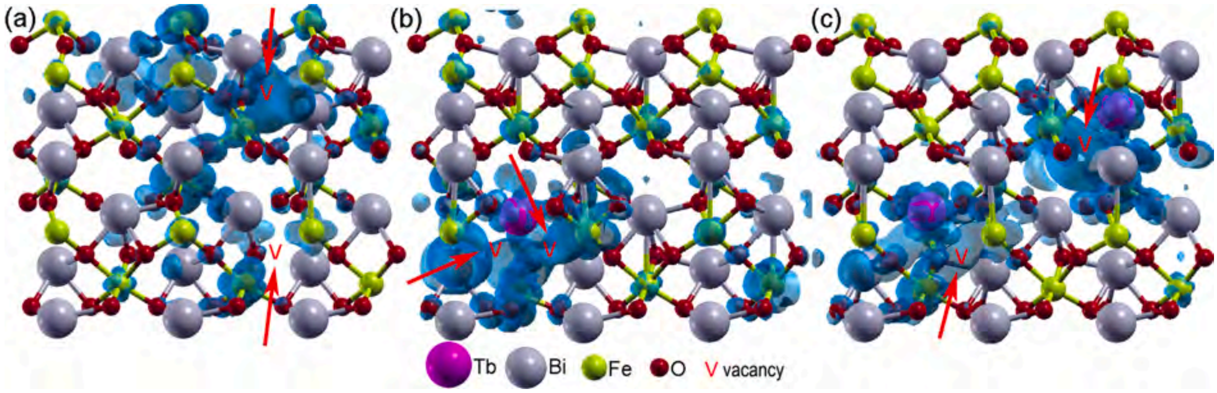

Fig. 12. Local density of states integrated within ±0.05 eV around the Fermi level for three different supercell configurations: (a) an undoped supercell with two vacancies, a supercell containing one Tb atom, (b) with two neighboring vacancies to the Tb atom, and (c) a supercell with two Tb atoms each having a neighboring vacancy. Elemental spheres are color-coded as indicated in the legend at the bottom. Vacancies are marked by red 'V' labels. An isosurface value of 0.0003 states/eVÅ^3 is depicted for all configurations.

0.210 eV/atom in structure with 2 Tb atoms per supercell; however this is still significantly larger than the values obtained for 5.5%-doped structures. Interesting, the trend of DFT-predicted change of vacancy concentrations corresponds to the dependence of grain sizes and surface roughness obtained with our AFM measurements. Particularly, DFT calculations indicate that vacancy concentration rises for undoped to 5.5%-doped structures, whereas the vacancy concentration decreases for 11.1% and 22.2% Tb doping levels. Less vacancies, i.e. defects can naturally result in larger grains and smoother surfaces, as observed experimentally. At room temperature, which corresponds to approximately 0.025 eV/atom, we can infer that vacancies would be most favorable in structures with a single Tb dopant per super cell and vacancy located on the Bi surface (formation energy 0.003 eV/atom). This is because this vacancy formation energy is well below the room temperature and represents the lowest activation barrier for vacancy formation. It is important to note that these energies are calculated for non-optimized structures. Optimization would likely decrease all vacancy formation energies, potentially bringing them closer to the room temperature value and enhancing the stability of vacancies at certain positions. Note that vacancy formation energies obtained for unrelaxed surfaces are consistently lower than those for relaxed bulk structures (Table 3), further signifying the possibility for vacancy formation in the former configurations.

3.4.5. Electronic structure of surfaces with vacancies

The DOS profiles for surface energetically favorable structures of $BiFeO_3$, doped with 0%, 5.5%, 11.1%, and 22.2% terbium, and containing vacancy concentrations of either 0% or 1.9%, are depicted in Fig. 13. Fig. 13(a) illustrates the DOS for energetically favorable atomic configurations of Tb-doped $BiFeO_3$ with and without oxygen vacancies. Notably, there are both qualitative and quantitative differences between undoped and 5.5% doped materials compared to those with higher doping concentrations (11.1% and 22.2%). The total DOS for these structures indicates electronic bandgaps of approximately 0.2 eV for the former two configurations and around 0.3 eV and 0.4 eV for the latter two.

A critical factor influencing electric conductivity is the position of the Fermi level relative to the available energy states. In undoped and 5.5% doped structures, the Fermi level resides at the bottom of dispersive bands, providing numerous accessible electronic states that enhance electrical conductivity. Conversely, in both 11.1% and 22.2% doped structures, the Fermi level is positioned at the top of filled bands separated from unfilled bands by a sizable bandgap. The similar DOS characteristics of 11.1% and 22.2% doped structures seemingly contradicts our experimental finding, which shows an increase in current when doping level increases from 10% to 20%. To address this disagreement we have to inspect the projected density-of-states (PDOS).

Fig. 13 (panels (b), (c) and (d)) provide PDOS for analyses of 5.5%, 11.1%, and 22.2% doping levels, respectively. These figures illustrate that the electronic states around the Fermi level predominantly originate from the first atomic surface layers, mainly Fe-terminated surfaces, with less influence from Bi-terminated surface and minor contributions from bulk Bi and Fe layers. In all cases, a narrow Tb state is present at the Fermi level. However, contribution to PDOS from Tb dopants varies with dopant concentration. In the energy range ±2 eV around Fermi level the Tb states are sparse and non-dispersive for 5.5% and 11.1% doping levels. Importantly, as the doping concentration increases from 11.1% to 22.2%, there is a significant increase in the number of available Tb states, as evidenced by comparing PDOS profiles for these concentrations. The physical origin of the experimentally observed variation in electric conductivity with Tb doping level can be summarized as follows:

1. Effects of doping and vacancies are mutually opposite; while vacancies shift Fermi level up towards the conduction band, doping pulls the Fermi level towards the valence band.
2. Undoped and weakly doped bismuth ferrites are conducting materials, with transport channels localized primarily on surfaces and eventually grain boundaries in experimental samples. The oxygen vacancies present at this doping level n-type doped material, bringing its Fermi level to the region with high density of dispersive well-conducting states.
3. Samples with the approximately 10% doping level lack states responsible for electronic transport; the Fermi level is shifted below a bandgap, making unoccupied states that provide conducting channels in undoped and lower-doped materials unreachable at low bias voltages in the intermediately doped structure. Additionally, dopant states around Fermi level are dispersionless, which do not contribute to efficient charge transport.
4. Increased conductivity in highly doped (approximately 20%) samples can be attributed to a significantly denser population of Tb states around the Fermi level. With a sufficient dopant concentration these states can overlap, delocalize and present dispersive, hence conducting states.

The results of DFT calculation are in accordance with our experimental findings. Undoped and weakly Tb-doped (~5%) $BiFeO_3$ thin films are conductive due to the formation of oxygen vacancies primarily on the surface and grain boundaries. For much higher Tb doping (~20%) DFT calculations indicate a significant increase of Tb conducting states around the Fermi level and less formation of oxygen vacancies. Therefore, experimentally obtained high conductivity of $Bi_{0.80}Tb_{0.20}FeO_3$ sample originates from the increased number of Tb conductive states. In the case of intermediate Tb doping (~10%) DFT calculations showed that the formation of oxygen vacancies is the

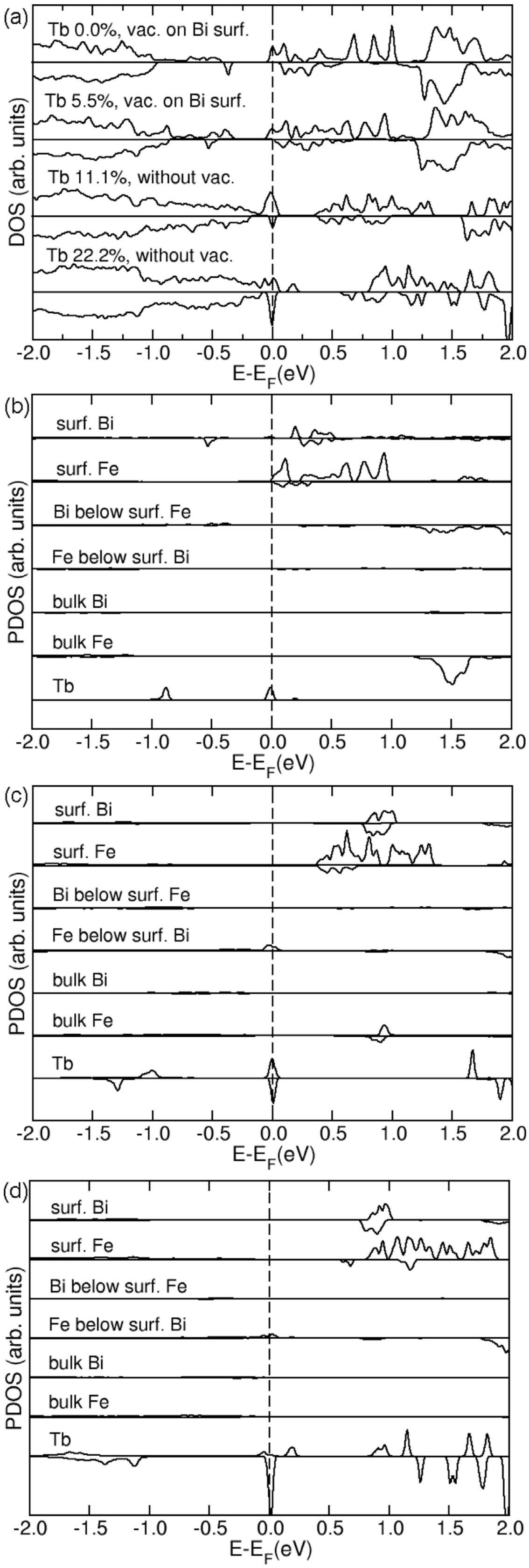

Fig. 13. Electronic structure of Tb-doped $BiFeO_3$ surfaces. (a) DOS of favorable vacancy configurations for different doping levels. Partial contributions to DOS from surface Bi layer, surface Fe layer, Bi layer below Fe surface, Fe layer below Bi surface, a bulk Bi layer, a bulk Fe layer and Tb dopants for (b) 5.5% doped structure with a vacancy on Bi surface, (c) 11.1% doped structure without vacancies, and (d) 22.2% doped vacant-free structure. Each graph shows DOS for majority/minority spins above/below local horizontal axes. Vertical dashed line marks the Fermi level.

least favorable, whereas sparse and non-dispersive Tb states do not contribute to efficient charge transport. It can be concluded that the balance between dopant concentration and defect formation is a key factor in achieving the much higher resistivity of the $Bi_{0.90}Tb_{0.10}FeO_3$ sample compared to the other samples. The findings presented above give a meaningful insight into how the Tb doping concentration influences the defect formation and thus the electrical properties of $BiFeO_3$ thin-films.

4. Concluding remarks

In summary, this study revealed that Tb doping has a great and non uniform influence on the formation of oxygen vacancy defects and electronic structure of $BiFeO_3$ thin films. The noticeable decrease of the intensity of 471 cm^{-1} Raman mode, seen in 10% Tb-doped film, indicates that 10% Tb doping leads to a decrease in the oxygen vacancy concentration. XPS analysis confirmed that 10% Tb-doped film has the lowest concentration of oxygen vacancies. Macroscopic I–V measurements showed that this sample has significantly reduced leakage current i.e the smallest conductivity. C-AFM measurements at the micro-scale provided additional insights into the conduction processes of Tb-doped $BiFeO_3$ thin films. These measurements confirmed that among all films, 10% Tb-doped film is the least conductive. At low voltages, the conduction is confined to localized, spatially inhomogeneous domains and takes place across grain boundaries with enhanced concentration of defects. As the voltage increases, the localized domains merge into larger conductive domains. From ab initio calculations, atomistic insight into such phenomena was gained. Undoped and ~5% doped samples are conductive due to high density of dispersive well-conducting oxygen vacancy states. For much higher Tb dopant concentration (~20%), DFT calculations indicate that less oxygen vacancies are formed, whereas the high conductivity originates from increased density of Tb conductive states near the Fermi level. An intermediate Tb doping concentration of ~10% causes a lack of states responsible for electronic transport, i.e. the concentration of oxygen vacancies is significantly lower, whereas the dopant non-dispersive states near the Fermi level are sparse and insufficient for the efficient charge transport. It is exactly this balance between the dopant and oxygen vacancy concentrations that ensures the best electrical performances of 10% Tb-doped film. These investigations pave the way for designing advanced multiferroic materials with thoroughly controlled structural and electrical properties.

CRediT authorship contribution statement

Bojan Stojadinović: Writing – original draft, Visualization, Investigation, Formal analysis, Data curation, Conceptualization. **Igor Popov:** Writing – original draft, Supervision, Methodology, Investigation, Formal analysis. **Borislav Vasić:** Writing – original draft, Methodology, Investigation, Formal analysis. **Dejan Pjević:** Writing – original draft, Methodology. **Milena Rosić:** Software, Methodology. **Nenad Tadić:** Investigation, Data curation. **Zorana Dohčević-Mitrović:** Writing – review & editing, Supervision, Formal analysis.

Declaration of competing interest

The authors declare that they have no known competing financial interests or personal relationships that could have appeared to influence the work reported in this paper.

Acknowledgments

B. S., B. V. and Z. D. M. acknowledge funding provided by the Institute of Physics Belgrade, through the grant by the Ministry of Science, Technological Development and Innovation of the Republic of Serbia. I. P. acknowledges financial support from the Ministry of Science, Technological Development and Innovation of the Republic of Serbia (Contract No. 451-03-66/2024-03/200053, Institute for Multidisciplinary Research, University of Belgrade), while M. R. and D. P. acknowledges financial support from the same ministry under Contract No. 451-03-136/2025-03/200017 (“Vinča” Institute of Nuclear Sciences–National Institute of the Republic of Serbia, University of Belgrade). DFT calculations were performed using computational resources at the Center of Surface and Nanoanalytics, Johannes Kepler University, Linz, Austria. We are grateful to Prof. Kurt Hingerl for providing the necessary computational resources at JKU.

Data availability

Data will be made available on request.

References

[1] T. Zhao, A. Scholl, F. Zavaliche, K. Lee, M. Barry, A. Doran, M.P. Cruz, Y.H. Chu, C. Ederer, N.A. Spaldin, R.R. Das, D.M. Kim, S.H. Baek, C.B. Eom, R. Ramesh, Electrical control of antiferromagnetic domains in multiferroic BiFeO$_3$ film at room temperature, Nat. Mater. 5 (2006) 823–829.

[2] C.H. Yang, D. Kan, I. Takeuchi, V. Nagarajan, J. Seidel, Doping BiFeO$_3$: Approaches and enhanced functionality, Phys. Chem. Chem. Phys. 14 (2012) 15953–15962.

[3] G. Catalan, J. Scott, Physics and applications of bismuth ferrite, Adv. Mater. 21 (2009) 2463–2485.

[4] R. Ramesh, N. Spaldin, Multiferroics: Progress and prospects in thin films, Nat. Mater. 6 (2007) 21–29.

[5] N. Spaldin, Multiferroics: Past, present, and future, Phys. Today 63 (2010) 38–43.

[6] J. Ma, J. Hu, Z. Li, C.W. Nan, Recent progress in multiferroic magnetoelectric composites: From bulk to thin films, Adv. Mater. 23 (2011) 1062–1087.

[7] S. Iakovlev, C.-H. Solterbeck, M. Kuhnke, M. Es-Souni, Multiferroic BiFeO$_3$ thin films processed via chemical solution deposition: Structural and electrical characterization, J. Appl. Phys. 97 (2005) 094901.

[8] G. Lotey, N. Verma, Multiferroic properties of Tb-doped BiFeO$_3$ nanowires, J. Nanopart. Res. 15 (2013) 1553.

[9] Y.-J. Kim, J.W. Kim, C.M. Raghavan, J.-J. Oak, H.J. Kim, W.-J. Kim, M.H. Kim, T.K. Song, S.S. Kim, Enhancement of electrical properties of (Gd, V) co-doped BiFeO$_3$ thin films prepared by chemical solution deposition, Ceram. Int. 39 (2013) S195–S199.

[10] S.K. Pradhan, B.K. Roul, Effect of gd doping on structural, electrical and magnetic properties of BiFeO$_3$ electroceramic, J. Phys. Chem. Solids 72 (2011) 1180–1187.

[11] B. Yu, M. Li, Z. Hu, L. Pei, D. Guo, X. Zhao, S. Dong, Enhanced multiferroic properties of the high-valence Pr doped BiFeO$_3$ thin film, Appl. Phys. Lett. 93 (2008) 182909.

[12] N. Kumar, N. Panwar, B. Gahtori, N. Singh, H. Kishan, V.P.S. Awana, Structural, dielectric and magnetic properties of Pr substituted Bi$_{1-x}$Pr$_x$FeO$_3$ ($0 \leq x \leq 0.15$) multiferroic compounds, J. Alloy. Compd. 501 (2010) L29–L32.

[13] Y. Wang, R.Y. Zheng, C.H. Sim, J. Wang, Charged defects and their effects on electrical behavior in Bi$_{1-x}$La$_x$FeO$_3$ thin films, J. Appl. Phys. 105 (2009) 016106.

[14] J. Liu, M. Li, L. Pei, J. Wang, B. Yu, X. Wang, X. Zhao, Structural and multiferroic properties of the Ce-doped BiFeO$_3$ thin films, J. Alloy. Compd. 493 (2010) 544–548.

[15] B. Stojadinović, Z. Dohčević-Mitrović, D. Stepanenko, M. Rosić, I. Petronijević, N. Tasić, N. Ilić, B. Matović B. Stojanović, Dielectric and ferroelectric properties of Ho-doped BiFeO$_3$ nanopowders across the structural phase transition, Ceram. Int. 43 (2017) 16531–16538.

[16] P. Sharma, D. Varshney, S. Satapathy, P.K. Gupta, Effect of Pr substitution on structural and electrical properties of BiFeO$_3$ ceramics, Mater. Chem. Phys. 143 (2014) 629–636.

[17] G. Dhir, G.S. Lotey, P. Uniyal, P.N.K. Verna, Size-dependent magnetic and dielectric properties of Tb-doped BiFeO$_3$ nanoparticles, J. Mater. Sci.: Mater. Electron. 24 (2013) 4386–4392.

[18] Q.X. Xing, Z. Han, S. Zhao, Crystal structure and magnetism of BiFeO$_3$ nanoparticles regulated by rare-earth Tb substitution, J. Mater. Sci.: Mater. Electron. 28 (2017) 295–303.

[19] M.L. Yi, C.B. Wang, L. Li, J.M. Wang, Q. Shen, L.M. Zhang, Influence of tb doping on structure and multiferroic properties of BiFeO$_3$ films prepared by pulsed laser deposition, Appl. Surf. Sci. 344 (2015) 47–51.

[20] Y. Wang, C.W. Nan, Effect of Tb doping on electric and magnetic behavior of BiFeO$_3$ thin films, J. Appl. Phys. 103 (2008) 024103.

[21] M. Muneeswaran, R. Dhanalakshmi, N. Giridharan, Effect of Tb substitution on structural, optical, electrical and magnetic properties of BiFeO$_3$, J. Mater. Sci.: Mater. Electron. 26 (2015) 3827–3839.

[22] G. Dong, G. Tan, W. Liu, A. Xia, H. Ren, Effect of Tb doping on structural and electrical properties of BiFeO$_3$ thin films prepared by Sol-Gel technique, J. Mater. Sci. Technol. 30 (2014) 365–370.

[23] G. Dong, G. Tan, Y. Luo, W. Liu, H. Ren, A. Xia, Investigation of Tb-doping on structural transition and multiferroic properties of BiFeO$_3$ thin films, Ceram. Int. 40 (2014) 6413–6419.

[24] B. Stojadinović, B. Vasić, D. Stepanenko, N. Tadić, R. Gajić, Z. Dohčević-Mitrović, Variation of electric properties across the grain boundaries in BiFeO$_3$ film, J. Phys. D Appl. Phys. 49 (2015) 045309.

[25] Y. Wang, P. Zhou, L. Fetisov, Y. Fetisov, Y. Qi, T. Zhang, Phase conductance of BiFeO$_3$ film, Sensors 23 (2023) 9123.

[26] S. Saxin, C.S. Knee, Crystal structure of Bi$_{1-x}$Tb$_x$FeO$_3$ from high-resolution neutron diffraction, J. Solid State Chem. 184 (2011) 1576–1579.

[27] Rigaku, PDXL Integrated X-Ray Powder Diffraction Software, Rigaku, Tokyo, Japan, 2011.

[28] PDF-2, International Crystallographical Database (ICDD). N.S. 12 Campus Blvd, PA 19073, USA, Editor. 2012: USA (2023).

[29] https://icsd.products.fiz-karlsruhe.de/.

[30] W. Kraus, G. Nolze, POWDER CELL — A program for the representation and manipulation of crystal structures and calculation of the resulting X-ray powder patterns, J. Appl. Crystallogr. 29 (1996) 301–303.

[31] PowderCell for Windows 2.4, software available at http://powdercell-for-windows.software.informer.com/2.4/. (Accessed 15 February 2019).

[32] G.K. Williamson, W.H. Hall, X-ray line broadening from filed aluminium and wolfram, Acta Metall. Mater. 1 (1) (1953) 22–31.

[33] E. Artacho, E. Anglada, O. Diéguez, J.D. Gale, A. García, J. Junquera, R.M. Martin, P. Ordejón, J.M. Pruneda, D. Sánchez-Portal, J.M. Soler, The SIESTA method; developments and applicability, J. Phys.: Condens. Matter. 20 (2008) 064208.

[34] J. Perdew, K. Burke, M. Ernzerhof, Generalized gradient approximation made simple, Phys. Rev. Lett. 77 (1996) 3865–3868.

[35] N. Troullier, J. Martins, Efficient pseudopotentials for plane-wave calculations, Phys. Rev. B 43 (1991) 1993–2006.

[36] A. Liechtenstein, V. Anisimov, J. Zaanen, Density-functional theory and strong interactions: Orbital ordering in Mott–Hubbard insulators, Phys. Rev. B 52 (1995) R5467–R5470.

[37] V. Anisimov, J. Zaanen, O. Andersen, Band theory and mott insulators: Hubbard U instead of stoner I, Phys. Rev. B 44 (1991) 943–954.

[38] V.I. Anisimov, F. Aryasetiawan, A.I. Lichtenstein, First-principles calculations of the electronic structure and spectra of strongly correlated systems: The LDA+ U method, J. Phys.: Condens. Matter. 9 (1997) 767.

[39] M. Čebela, D. Zagorac, K. Batalović, J. Radaković, B. Stojadinović, V. Spasojević, R. Hercigonja, BiFeO$_3$ perovskites: A multidisciplinary approach to multiferroics, Ceram. Int. 43 (2017) 1256–1264.

[40] M. Čebela, D. Zagorac, I. Popov, F. Torić, T. Klaser, Ž. Skoko, D. Pajić, Enhancement of weak ferromagnetism, exotic structure prediction and diverse electronic properties in holmium substituted multiferroic bismuth ferrite, Phys. Chem. Chem. Phys. 25 (2023) 22345–22358.

[41] E. Bitzek, P. Koskinen, F. Gähler, M. Moseler, P. Gumbsch, Structural relaxation made simple, Phys. Rev. Lett. 97 (2006) 170201.

[42] D. Liu, J. Nocedal, On the limited memory BFGS method for large scale optimization, Math. Program. 45 (1989) 503–528.

[43] D. Johnson, Modified Broyden’s method for accelerating convergence in self-consistent calculations, Phys. Rev. B 38 (1988) 12807–12813.

[44] S. Nandy, P. Mocherla, C. Sudakar, Temperature-dependent Raman spectral evidence of local structural changes in BiFeO$_3$ thin films: Influence of substrate and oxygen vacancies, J. Appl. Phys. 135 (2024) 024101.

[45] P. Mocherla, C. Karthik, R. Ubic, M. Rao, C. Sudakar, Effect of microstrain on the magnetic properties of BiFeO$_3$ nanoparticles, Appl. Phys. Lett. 105 (2014) 132409.

[46] J. Zhang, Y.J. Wu, X.K. Chen, X.J. Chen, Structural evolution and magnetization enhancement of Bi$_{1-x}$Tb$_x$FeO$_3$, J. Phys. Chem. Solids 74 (2013) 849–853.

[47] S. Gupta, M. Tomar, V. Gupta, A. James, M. Pal, R. Guo, A. Bhalla, Optimization of excess Bi doping to enhance ferroic orders of spin casted BiFeO$_3$ thin film, J. Appl. Phys. 115 (23) (2014) 234105.

[48] G. Gomez-Iriarte, A. Pentón-Madrigal, L. Oliveira, J. Sinnecker, XPS study in BiFeO$_3$ surface modified by argon etching, Materials 15 (2022) 4285(1–13).

[49] Y. Zhang, Y. Wang, J. Qi, Y. Tian, J. Zhang, M. Wei, Y. Liu, J. Yang, Structural, magnetic and impedance spectroscopy properties of Ho^{3+} modified BiFeO$_3$ multiferroic thin film, J. Mater. Sci.: Mater. Electron. 30 (2019) 2942–2952.

processes

Article

Development of a Chestnut Shell Bio-Adsorbent for Cationic Pollutants: Encapsulation in an Alginate Carrier for Application in a Flow System

Atef Aljnin [1], Gorica Cvijanović [1], Bojan Stojadinović [2], Milutin Milosavljević [3], Katarina Simić [4], Aleksandar D. Marinković [5] and Nataša Đ. Knežević [6,*]

[1] Faculty of Biofarming, Megatrend University, Maršala Tita 39, 24300 Bačka Topola, Serbia; atefaljnin@gmail.com (A.A.); cvijagor@yahoo.com (G.C.)
[2] Institute of Physics Belgrade, University of Belgrade, Pregrevica 118, 11000 Belgrade, Serbia; bojans@ipb.ac.rs
[3] Faculty of Technical Science, University of Priština, Knjaza Miloša 7, 38220 Kosovska Mitrovica, Serbia; milutin.milosavljevic@pr.ac.rs
[4] Institute of Chemistry, Technology and Metallurgy—National Institute of the Republic of Serbia, University of Belgrade, Technology and Metallurgy, Njegoševa 12, 11000 Belgrade, Serbia; katarina.simic@ihtm.bg.ac.rs
[5] Faculty of Technology and Metallurgy, University of Belgrade, Karnegijeva 4, 11000 Belgrade, Serbia; marinko@tmf.bg.ac.rs
[6] "VINČA" Institute of Nuclear Sciences—National Institute of the Republic of Serbia, University of Belgrade, Mike Petrovića Alasa 12-14, 11351 Belgrade, Serbia
* Correspondence: natasa.knezevic@vin.bg.ac.rs; Tel.: +381-63-717-3172

Abstract

Melanin-based biosorbents (MiCS), derived from chestnut shells, were encapsulated in sodium alginate to obtain MiCS@Alg, useful in a column adsorption study. MiCS contains various acidic surface groups able to participate in the removal of cationic pollutants from aqueous solutions. The MiCS and MiCS@Alg were characterized by Fourier-transform Infrared Spectroscopy (FTIR), Scanning Electron Microscopy (SEM), and Dynamic Light Scattering (DLS), while zeta potential and particle size analyses were performed to gain deeper insight into surface charge behavior. Batch adsorption experiments were carried out at three different temperatures, demonstrating that the adsorption kinetics followed a pseudo-second-order (PSO) model and that the Freundlich model best described the equilibrium data. The process was found to be endothermic and spontaneous, with maximum adsorption capacities of 300.2 mg g^{-1} (BR2), 201.5 mg g^{-1} (BY28) and 73.08 mg g^{-1} (NH_3) on MiCS, and 189.3 mg g^{-1} (BR2), 117.1 mg g^{-1} (BY28) and 50.06 mg g^{-1} (NH_3) on MiCS@Alg at 45 °C and compared with the unmodified chestnut shell. The MiCS and MiCS@Alg exhibited good adsorption performance, improved environmental compatibility, and greater reusability. Overall, these results highlight MiCS@Alg as a cost-effective, sustainable, and highly promising novel biosorbent for the removal of cationic pollutants (BR2, BY28, and NH_3) from water.

Keywords: melanin; sodium alginate; adsorption; textile dyes; ammonia; environmental protection

check for updates

Academic Editors: Alejandro Regalado-Méndez, Reyna Natividad and Rubi Romero

Received: 22 September 2025
Revised: 10 October 2025
Accepted: 13 October 2025
Published: 16 October 2025

Citation: Aljnin, A.; Cvijanović, G.; Stojadinović, B.; Milosavljević, M.; Simić, K.; Marinković, A.D.; Knežević, N.Đ. Development of a Chestnut Shell Bio-Adsorbent for Cationic Pollutants: Encapsulation in an Alginate Carrier for Application in a Flow System. *Processes* **2025**, *13*, 3314. https://doi.org/10.3390/pr13103314

1. Introduction

Water pollution by synthetic compounds, particularly pharmaceutical pollutants and dyes containing amine functional groups, represents one of the most significant challenges in environmental protection. These compounds, including antidepressants (e.g., amitriptyline [1]), beta-blockers (e.g., atenolol), antibiotics (e.g., amoxicillin), and various cationic dyes (such as methylene blue [2]), are often not effectively removed by conventional wastewater treatment methods, leading to their accumulation in aquatic ecosystems and threatening human health and biodiversity. According to data from UNICEF and the World Health Organization (WHO), in 2020, two billion people lacked access to safe drinking water (WHO and UNICEF 2021) [3]. Yaseen and Scholz (2019) [4] report that dye concentrations in textile wastewater can range from 10 to 7000 mg L^{-1}, depending on the type of fabric and dye used during the manufacturing process. Consequently, the efficient treatment of dye-containing wastewater is essential before its discharge into aquatic environments [5]. Colored effluents are released by numerous industries, including textile, dyeing, food, pharmaceutical, paper, leather, and cosmetics sectors [6]. Among these pollutants, Safranin T (BR2) is a widely used azine dye. In addition to its application in the textile and leather industries, BR2 also finds use as a photosensitizer, biological stain, and fluorescent probe [7]. However, exposure to BR2 poses serious health risks, such as eye irritation, skin inflammation, and respiratory tract disorders. Owing to its extensive industrial use in textiles, plastics, paper, and cosmetics, the removal of BR2 from industrial effluents and wastewater is of urgent importance for ensuring a safer and healthier environment. Alongside dyes, ammonia (NH_3/NH_4^+) represents another major contaminant in municipal and industrial wastewaters, originating from agriculture, fertilizer production, and domestic effluents. High concentrations of ammonia can cause eutrophication, oxygen depletion, and toxicity to aquatic organisms, thereby creating significant ecological and regulatory concerns.

Conventional biological treatments, such as nitrification–denitrification, are commonly employed but are often limited by high operational costs, long retention times, and sensitivity to pH and temperature fluctuations. In this regard, adsorption has emerged as a particularly attractive alternative due to its simplicity, efficiency, and potential for adsorbent regeneration. A wide variety of adsorbents [8] have been investigated for dye and ammonia removal, including zeolites, activated carbon [9], and biochar [10,11]. Among them, bio-based materials stand out as sustainable and cost-effective options. Within this category, melanin-based sorbents derived from chestnut shells (MiCS) and their alginate-modified derivatives (MiCS@Alg) show considerable potential, offering abundant functional groups and environmentally friendly synthesis routes. In the search for efficient, environmentally friendly, and cost-effective wastewater treatment solutions, the application of adsorption processes using biosorbents made from plant waste materials is gaining increasing importance. One such material is chestnut shell, an agro-industrial waste generated in large quantities during the peeling process, accounting for 10% of the total mass. In 2020, global chestnut production reached 2.322 million tons, distributed across many countries worldwide [12]. Chestnut shells are rich in lignocellulosic components and contain various functional groups (–OH, –COOH), enabling interaction with water contaminants. Like other agricultural wastes, chestnut shells have been evaluated for the adsorption of dye molecules and metal ions, either in their natural form or after carbonization and activation, with quite satisfactory results [13]. Their natural adsorption properties are often insufficient for the efficient removal of pollutants, especially those with specific functional groups such as amines. Main compounds in chestnut shell were found to be holocellulose 42.4 wt.% (27.8 wt.% of α-cellulose), 39.8 wt.% lignin, and extractive content was 3.2 wt.% [extraction agent MeOH/Water (95:5 v/v)] [14]. Therefore, chemical modification of natural biosorbents is necessary, offering an effective approach to enhancing their adsorption capacity. In this study, sodium alginate was used as a surface-modifying agent for melanin isolated from chestnut shells. By cross-linking with melanin particles, a higher number of functional groups (e.g., carboxyl and hydroxyl groups) was introduced, enabling the formation of microbeads with stronger and more selective interactions with cationic pollutants. Moreover, sodium alginate (Na-alg) is rich in carboxylate groups (–COOH), which facilitate chelation with a wide range of multivalent metal ions, forming stable "egg-box" structures [15,16]. This property makes it particularly suitable for the removal of heavy metals and cationic pollutants from water, such as dyes Astrazon Yellow 7GLL (BY28) and Safranin T (BR2). To improve its mechanical stability and adsorption efficiency, sodium alginate is frequently modified into various composite forms. For example, Na-alg has been successfully combined with chitin, humic acid, polyaniline, cellulose, and even carbon nanotubes, significantly enhancing its adsorption capacity and applicability in wastewater treatment. Recent studies have increasingly focused on the development of sorbents designed for the removal of carbon dioxide (CO_2), one of the major air pollutants that significantly affects climate change and human health. In this study [17], a mesoporous silica foam (MSF) was used as a support, prepared from coal fly ash (CFA), providing a cost-effective porous material while simultaneously enabling the recycling of silicoaluminate solid waste.

This research aimed to develop and characterize a new biosorbent derived from raw chestnut shell, initially in the form of isolated melanin, and subsequently encapsulated in alginate beads to obtain spherical microstructures to serve as a carrier material for the removal of cationic dyes from aqueous solutions. Adsorption capacity, sorption mechanisms, as well as the stability and reusability of the material, were examined through a series of experiments, with a particular focus on its potential application in the treatment of textile wastewater. In addition to its chemical advantages, the particle shape in the form of microgranules helps to overcome common issues associated with powdered biosorbents, such as small particle size, difficulty in separating the sorbent from the solution after adsorption, and limited potential for reuse. The prepared composites exhibited good stability in aqueous environments and a structure suitable for continuous pollutant removal processes. The materials characterization was performed to confirm the success of material purification and morphological changes. The adsorption performance of the new sorbent was evaluated through a series of batch experiments, including adsorption isotherm and kinetic analyses under varying temperature and pH conditions, with particular emphasis on interactions with cationic pollutants in aqueous systems.

2. Materials and Methods

2.1. Chemicals and Materials

Chestnut shells (*Castanea mollissima*) [15] were collected in Vršac, Serbia (Supplementary Materials S2.1), and the pericarp (outer shell) was separated and used in this study. Sodium alginate (Na-alg), copper sulfate ($CuSO_4$), calcium chloride ($CaCl_2$), Folin–Ciocalteu's phenol reagent (2N, ACS), potassium hexacyanoferrate(III) (≥99%, ACS), ammonium hydroxide (~25%), gallic acid ($C_7H_6O_5$, 97.5–102.5%, p.a.), iron(III) sulfate pentahydrate (99.9%, trace metals), butyl alcohol ($CH_3(CH_2)_3OH$, ≥99.5%), potassium hydroxide (KOH, 90%, flakes), sodium hydrogen carbonate ($NaHCO_3$, ≥99.7%, ACS), sodium chloride (≥99%), sodium sulphate (≥99%), magnesium sulphate (≥99%), aluminium sulphate (99.99%), methylene blue (≥97%), and sodium benzoate (99%) were purchased from Sigma-Aldrich (Merck), Darmstadt, Germany. Ethanol, hydrochloric acid (HCl, 38% *w*/*w*, AG), and sodium hydroxide (NaOH) were obtained from Alkaloid, Skopje, Macedonia. Nitric acid (65% HNO_3) was purchased from Zorka Pharma a.d., Šabac, Serbia. Tannic acid (99%, ACS), potassium nitrate (KNO_3, ≥99.0%), and bovine serum albumin (≥98%, p.a.) were obtained from Merck, Darmstadt, Germany. All chemicals were of analytical grade and used without further purification. All solutions were prepared with distilled water purified using a Simplicity® UV water purification system (Merck Millipore, Darmstadt, Germany). Dye solutions with different concentrations were prepared in deionized water.

Astrazon Yellow 7GLL (C.I. Basic Yellow 28, BY28) and Safranin T (C.I. Basic Red 2, BR2) were purchased from Sigma-Aldrich, Darmstadt, Germany.

2.2. Extraction of Melanin from Integument Chestnut Shell (MiCS)

Pulverized chestnut shell (iCS, 70 g) was subjected to alkaline extraction using 0.5 M NaOH at a solid-to-liquid ratio of 1:1.15 (w/v), in a 1 L glass beaker with continuous stirring for 12 h. The mixture was then treated in an ultrasonic bath at 40 °C for 2 h. The resulting suspension was centrifuged for 15 min at 5000 rpm to separate the phases. The supernatant was further purified from proteins using the Sevag method. The obtained effluent was acidified to pH 2.5 using 2 M HCl and left to stand for 12 h. The precipitated melanin was then left at room temperature to dry for three days and subsequently used in the following experimental procedures. Following drying, the melanin precipitate was dissolved in an appropriate volume of 1.25% NaOH solution (200 mL) to attain a final pH < 8 [18]. The obtained alkaline extract was then treated with an equal volume of 8 wt.% $CuSO_4 \cdot 5H_2O$ solution [19] with continuous stirring for 30 min at room temperature. The resulting dark melanin precipitate was separated by centrifugation, thoroughly washed with distilled water, and treated with 200 mL 2.5% HCl, filtered, and washed with 250 mL deionized water (DW). The re-dispersion of wet products in 200 mL of DW using ultrasound for 10 min, and filtration with 250 mL of DW (two cycles applied), and freeze-dried (frozen at −50 °C for 2 h and lyophilized overnight at −70 °C) gave 15.6 g of product (yield 22.3 wt.%). All operation was performed in an inert atmosphere. The final water-insoluble melanin brown powder was used for further characterization and evaluation of its adsorptive properties. Residual Cu^{2+} ion was determined first by microwave digestion and atomic absorption spectroscopy (residual Cu^{2+} ion was found to be less than 0.01%).

2.3. Preparation of MiCS Encapsulated in Alginate Particles (MiCS@Alg)

The melanin obtained in powder form was used for the synthesis of MiCS@Alg, as illustrated in Scheme 1. Dissolution of sodium alginate (2.0 g) in 100 mL of deionized water was followed by the addition of 2.0 g MiCS, and stirring until a homogeneous dispersion was obtained [20]. Na-alg hydrogel beads were formed by dropping the produced dispersion into a $CaCl_2$ solution (2%, w/v). The resulting Na-alg beads were further immersed in the $CaCl_2$ solution for an additional 30 min to ensure complete cross-linking. After cross-linking, the beads were frozen at −50 °C for 2 h and lyophilized overnight at −70 °C. The resulting lyophilized beads were used for further characterization and adsorption experiments. The yield of MiCS@Alg was 33%. The results show that 77% of the free volume of MiCS@Alg was available for the filling/wetting with adsorption medium, providing a large free volume available for pollutant transport.

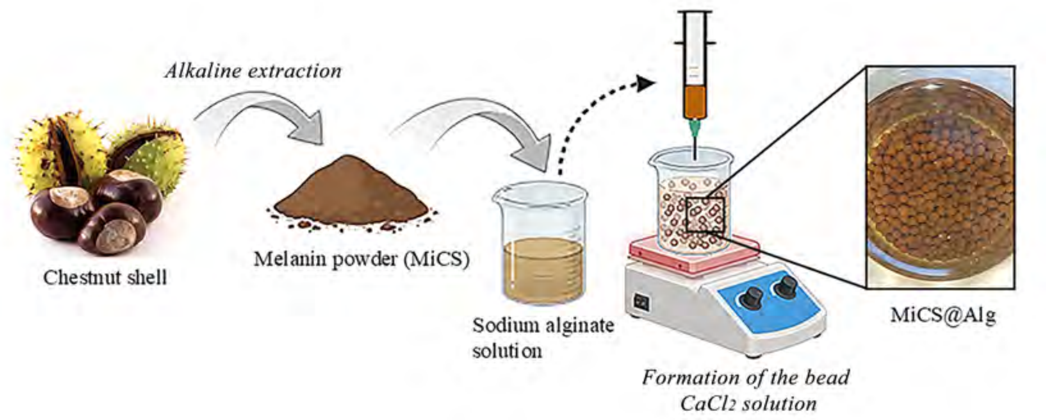

Scheme 1. Graphical presentation of sodium alginate treatment of extracted melanin.

2.4. Characterization and Analysis

The structural and physicochemical properties of all samples were characterized using scanning electron microscopy (SEM), Fourier-transform infrared spectroscopy (FTIR), UV–Vis spectrophotometry, dynamic light scattering (DLS), and laser Doppler electrophoresis (LDE) with a Zetasizer Nano ZS and a Multi-Purpose Titrator MPT-2, as well as elemental analysis. Detailed results are provided in Supplementary Material S2.4.

Other characterization and analytical methods, such as the determination of specific density, total polyphenol content (TPC) in chestnut shells, total tannin content (TTC), protein analysis, Bradford assay, enzymatic deproteinization, and "dry-wet mass" method for porosity, are presented in the Supplementary Materials S2.4. The methods for determining total basic, total acidic, and carboxyl groups are provided in Supplementary Materials S2.4.1.

The collected filtrate, after iCS purification (Section 2.2. Extraction of melanin from integument chestnut shell (MiCS)), was analyzed for copper presence using atomic absorption spectrometry (AAS), Perkin Elmer PinAAcle 900T, PerkinElmer, Inc., Shelton, CT, USA.

Determination of chemical oxygen demand (COD) value: to assess adsorption success, the study referred to Serbian national emission limit values: COD = 200 mg O_2 L^{-1} (satisfies the criteria prescribed by the Official Gazette of the Republic of Serbia, No. 67/2011, 48/2012, and 1/2016) [21]. The ISO 6060 method determined chemical oxygen demand (COD) using a Lovibond MD 600 spectrophotometer and Lovibond RD 125 sample heating apparatus [22]. Spectrophotometric tests, with mercury(II) sulfate masking chloride, were conducted for COD determination.

2.5. Adsorption Experiments

The adsorption behavior of the new materials was investigated using the batch and column methods (MiCS@Alg). Briefly, varying masses of the adsorbent (1, 2.5, 5, 7.5, and 10 mg) were added into 10 mL glass conical flasks containing 8 mL of dye solution with an initial concentration of 30 mg L^{-1}. The flasks were then placed on a digitally heated magnetic stirrer (Thermo Scientific, Waltham, MA, USA) and stirred at a constant rate for 90 min to reach equilibrium. In an experiment of ammonia removal, plastic centrifuge tubes of 50 mL and varying masses of the adsorbent (5, 12.5, 25, 37.5, and 50 mg) were used. The shaking was provided using the Thermo Scientific Thermal mixer and Blocks. The temperature was maintained at 25 °C, 35 °C, or 45 °C, depending on the experimental condition, while the pH was adjusted to the optimal value of 7.5 for dyes removal and pH 4 for ammonia (Section 3.3.1 Adsorption isotherm study). pH was adjusted using either 1 mol L^{-1} HCl or 1 mol L^{-1} NaOH solution. After equilibrium was reached, the MiCS@Alg and MiCS adsorbents were separated either by filtration through quantitative Whatman filter paper or centrifugation for 15 min at 11,000 rpm, respectively. The residual concentration of pollutants in the filtrate was determined using a UV–Vis spectrophotometer in absorption peak intensity at 518 nm and 435 nm (λmax of BR2 and BY28, respectively), as shown in Scheme 2. The residual ammonia concentration in aqueous samples was determined using the standard boric acid absorption–titration method following alkaline distillation (modified Kjeldahl procedure) [23]. To describe the experimental data and determine the nature of the adsorption process, commonly used isotherm models, as well as various kinetic models adopted from relevant literature, were employed [2]. Ionic strength influences on adsorption efficiency were performed in the presence of KNO_3 (0.01, 0.05, and 0.1 mol dm^{-3}). Each experiment was run in triplicate, and mean values were calculated. The chemical structure of the dyes is presented in Figure 1.

The design of adsorption experiments is presented in the Supplementary Information, in the section on Supplementary Materials S2.7. Response Surface Methodology (RSM).

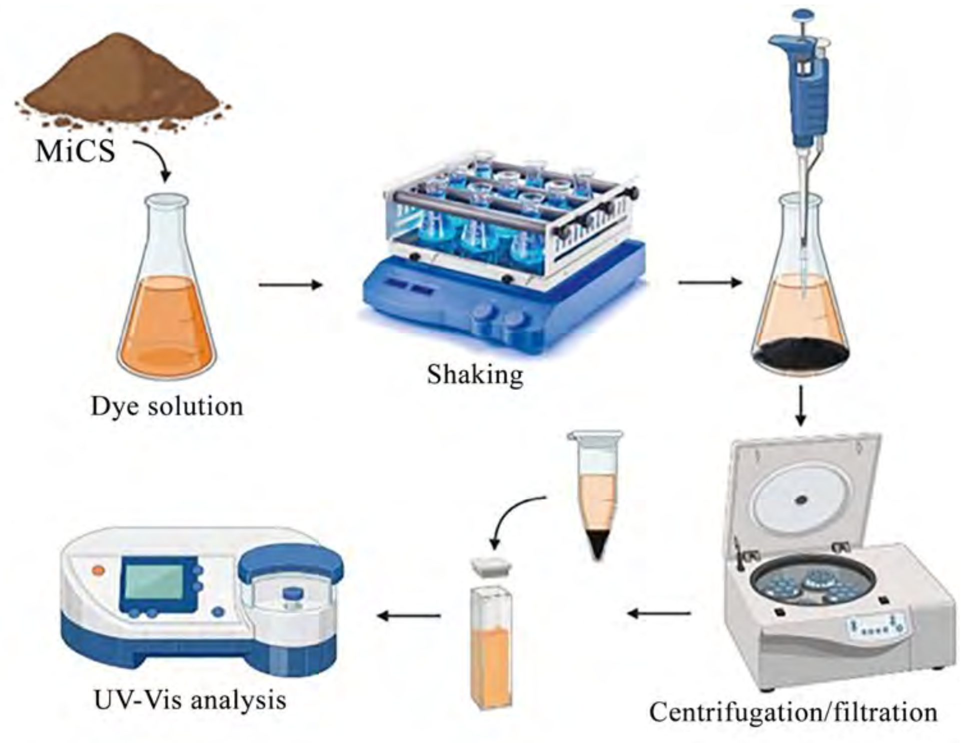

Scheme 2. Schematic representation of the adsorption procedure.

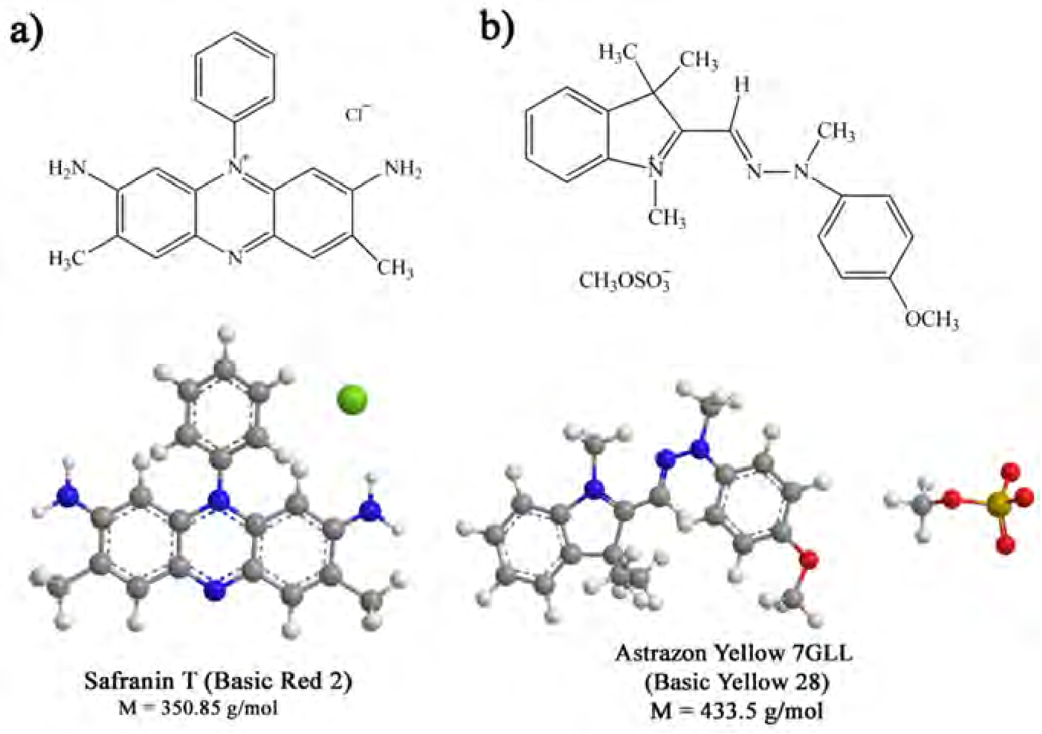

Figure 1. Chemical structures of the dyes. (**a**) 2D model. (**b**) 3D model.

In order to test the applicability of MiCS and MiCS@Alg adsorbents, a higher pollutant concentration—e.g., C_i of 200 mg dm^{-3}—of the dyes and ammonia was used, and adsorption experiments were performed at the following conditions: C_i = 30 mg L^{-1}, m = 1 mg, V = 8 mL, T = 25 °C, and t = 90 min.

Competitive adsorption experiments were performed in a two-component system using Ca^{2+}, Al^{3+}, Cl^{-}, $SO_4{}^{2-}$, methylene blue (MB), and sodium benzoate at 30 mg dm^{-3} of initial concentration.

For column adsorption (Supplementary Materials S2.5), data analysis was simplified using the Bohart–Adams and Yoon–Nelson models. The test solution was prepared by passing BR2 and BY28 dyes or ammonia (5 mg L^{-1}) through model water adjusted to pH 7.5 for the dyes and pH 4 for ammonia, at controlled flow rates of 0.5, 1.0, and 1.5 mL min^{-1}.

2.6. Desorption Experiments

Desorption and reuse of adsorbents were examined using a batch method to evaluate their efficiency in repeated adsorption of BY28, BR2 dyes, and NH_3 from wastewater. The experiments were performed according to the procedure described in [24]. Each test was carried out separately using 0.1 M HCl as the desorption agent for 3 h under agitation at 150 rpm to regenerate the surface of MiCS and MiCS@Alg adsorbents loaded with pollutants. Before reuse, each adsorbent was thoroughly rinsed with distilled water. This procedure was repeated for five consecutive cycles.

3. Results

3.1. Characterization of Materials

In this work, an attempt is made to isolate melanin and encapsulate it into Na-alg matrix to obtain applicable adsorbents in both batch and flow systems. Chemical and elemental analysis (Table S2) of pulverized chestnut shell (iCS) showed the presence of holocellulose, mainly α-cellulose, and klason lignin. After chestnut shell purification—i.e., melanin isolation from cellulose and lignin—significant increases in the total basic group, from 0.28 to 0.71 mmol g^{-1}, the total acidic group, from 1.32 to 3.06 mmol g^{-1}, and the carboxyl group, from 0.89 to 2.14 mmol g^{-1}, indicate high potential of MiCS for cationic pollutants removal. Recording of the NMR spectra of the MiCS material (dissolved in DMSO-d6) was not possible, since melanin possesses a stable population of free radicals distributed across its aromatic structures, as confirmed by the Electron Spin Resonance (ESR) spectrum [25].

3.1.1. SEM Analysis

SEM micrographs of iCS, MiCS, and the surface of MiCS@Alg are given in Figure 2.

SEM was employed to investigate the surface morphology of raw chestnut fruit shells, the isolated melanin, and the Na-alg-based formed beads. As shown in Figure 2a, irregularly shaped and sized fragments with a rough and porous surface were observed. The particles exhibited a layered and heterogeneous texture, which is characteristic of lignocellulosic plant residues rich in lignin, cellulose, and hemicellulose, as presented in the study [13]. The pronounced surface damage can be attributed to the mechanical grinding applied as part of the pretreatment using a laboratory mill. In Figure 2b, the surface of the MiCS displays narrowed slits and a wavy, layered structure with an amorphous appearance [12]. At higher magnifications, a compact amorphous morphology with low porosity becomes evident, which is typical of melanin derived from plant-based materials [26]. Figure 2c presents a cross-section of the formed beads MiCS@Alg, showing a homogeneous and smooth surface, indicating successful alginate cross-linking. Similar to the melanin sample, the internal structure appears dense and non-porous, with no pronounced cavities, suggesting uniform distribution within the gel matrix. At higher magnification, traces of dispersed particles, most likely melanin, can be observed in the central region of the bead. Figure 3 presents SEM micrographs of bead cross-sections, along with their morphological characteristics and diameters. The bead diameters were determined using a digital optical microscope (Delta Optical Smart 5.0 MP PRO) equipped with HiView (HiRISE) software, version 1.5.0.

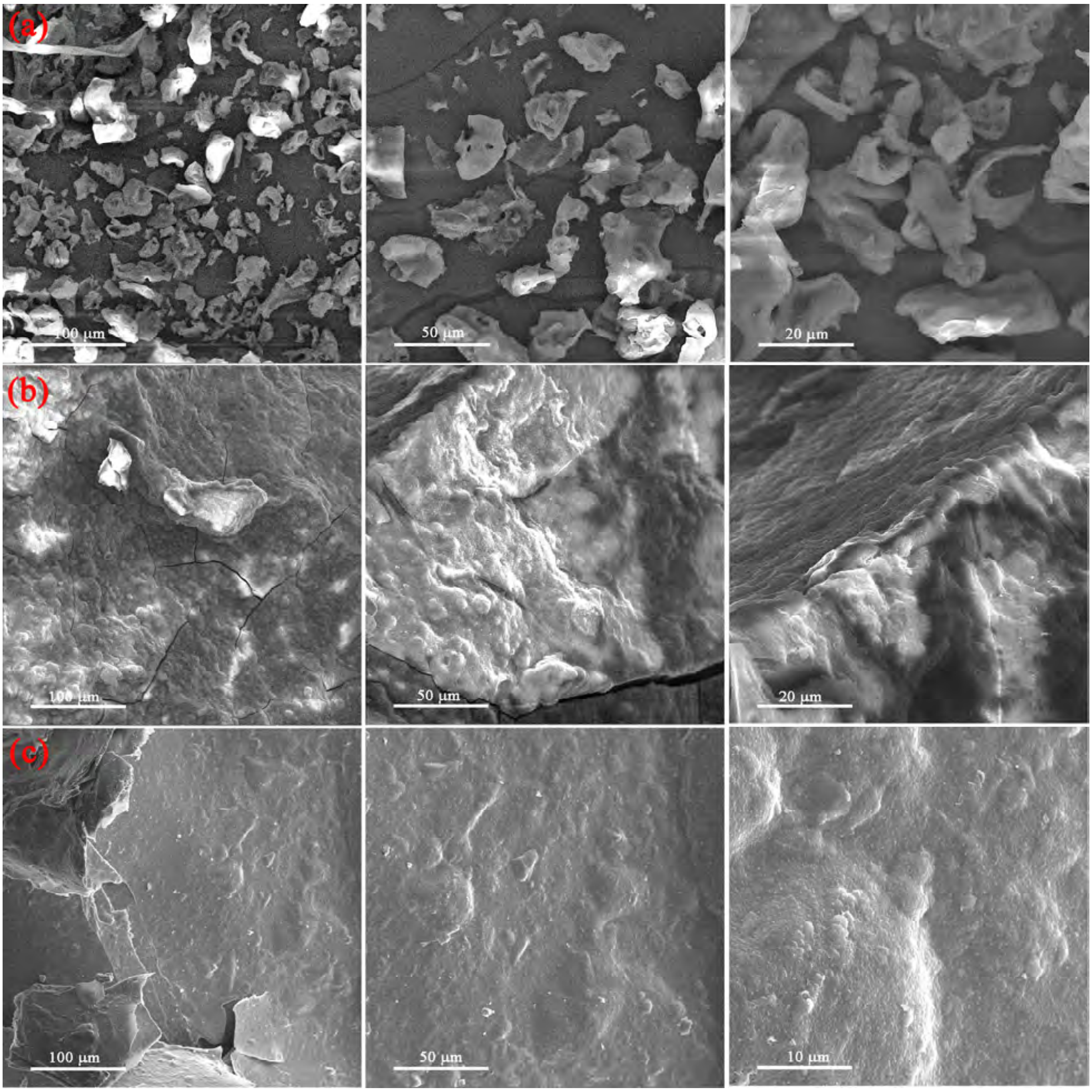

Figure 2. SEM micrographs of (**a**) pulverized chestnut shell (iCS), (**b**) MiCS, and (**c**) external surface of MiCS@Alg at a magnification of 500, 1000, 2000/5000×.

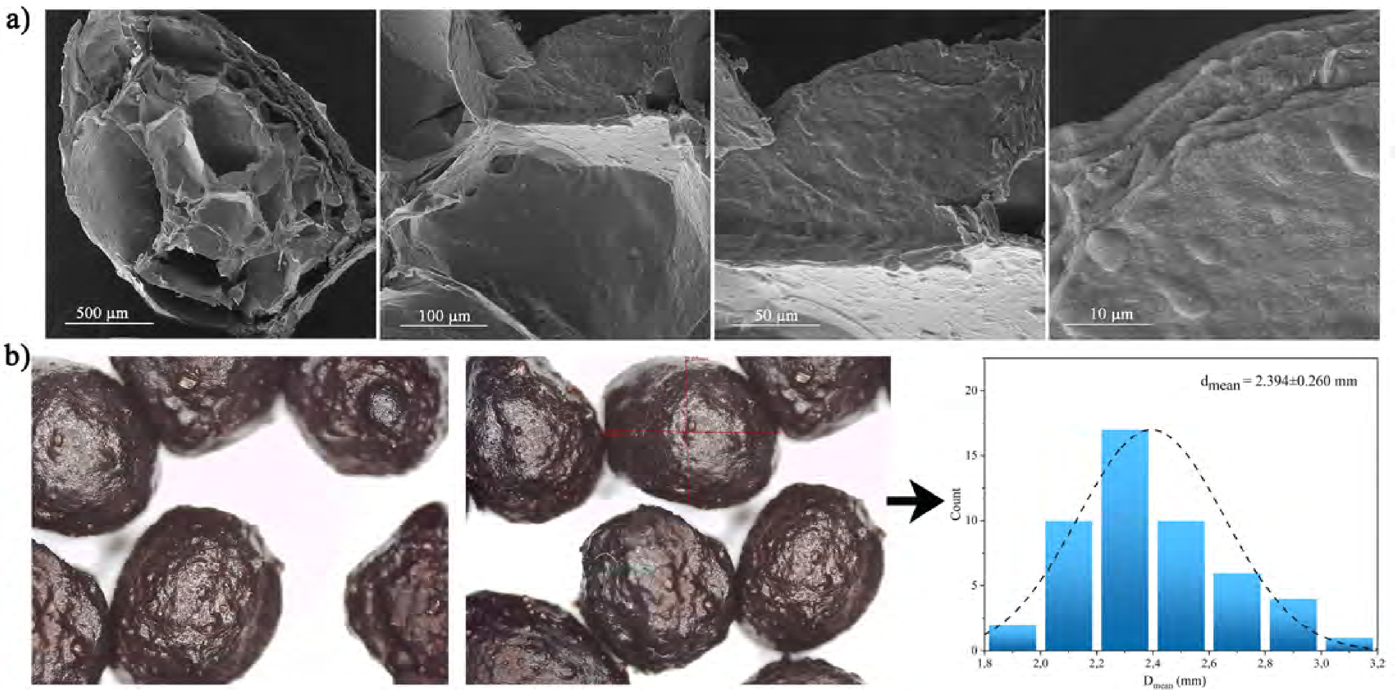

Figure 3. (**a**) SEM micrographs of cross-sections of beads and (**b**) the morphology and average diameter of MiCS@Alg beads.

SEM micrographs (Figure 3a), taken at magnifications from 500 µm down to 10 µm, reveal the highly porous internal architecture of the MiCS@Alg beads. The cross-sections reveal interconnected macropores with irregular walls, while higher magnifications reveal a rough, layered morphology with micro-fissures, indicating an enhanced surface area that is favorable for adsorption. A complementary analysis (Figure 3b) was performed on a large number of beads to obtain accurate size measurements, and the size-distribution characteristics were determined by processing digital images of the samples. The synthesized composites appeared as small black beads, forming nearly monodisperse spheres of varying diameters. SEM observations confirmed that the lyophilized beads retained a spherical shape with a rough surface and no visible signs of collapse, with an average diameter of 2.394 ± 0.260 mm. Volume shrinkage caused by water evaporation during lyophilization inevitably led to slight shape deformation, and the observed irregularities in sphericity can be attributed to this effect. Similar findings have been reported for Argan-nutshell-based beads used for methylene-blue removal [6]. The result of the "dry-wet mass" method revealed that the determined bead porosity was about 76.2%. The density, determined to be 0.19 g mL^{-1}, was calculated following the procedure reported by Popovic et al. [27].

3.1.2. FTIR Analysis

FTIR spectra of the iCS, MiCS, Na-alg, and MiCS@Alg are given in Figure 4.

The broad absorption band at 3255 cm^{-1} indicates the presence of O–H groups, characteristic of hydroxyl moieties in cellulose, hemicellulose, and lignin. The bands in the region between 2929 and 2850 cm^{-1} correspond to symmetric and asymmetric C–H stretching vibrations of methyl and methylene groups, commonly found in lignocellulosic structures. A moderate peak at 1734 cm^{-1}, observed in the spectrum of the raw sample (iCS), is assigned to ester and carbonyl (C=O) groups, which are mainly associated with hemicellulose and/or pectin [28]. The disappearance of this peak in the MiCS sample after melanin extraction suggests the removal or hydrolysis of the ester group in the course of melanin isolation. In any case, a significant number of carboxylic groups are still present in MiCS (Table S3). The iCS spectrum also displays a prominent band at 1014 cm^{-1}, which can be attributed to C–O stretching vibrations of phenolic compounds, indicating the presence of natural pigments. Similar melanin spectra have been reported in a study comparing standard and extracted pigments [29]. In addition, bending vibrations of aliphatic groups and aromatic ring deformations were observed at 1435 and 1281 cm^{-1}, respectively, confirming the presence of lignin-related structures. In the MiCS sample (blue line), the O–H stretching band shifts and decreases in intensity (from 3255 to 2929 cm^{-1}), indicating chemical modification of the material and a reduction in free hydroxyl groups. The transmission at 1605 cm^{-1} represents aromatic C=C stretching vibrations (skeletal stretching), suggesting an increased content of aromatic structure after treatment. The band at 1435 cm^{-1} is also related to deformation vibrations of aliphatic moieties. Following acid extraction, the intensity of the peak at 1085 cm^{-1}, associated with cellulosic material, is significantly reduced in the MiCS@Alg spectrum, confirming successful cellulose removal from the matrix. The Na-alg spectrum showed characteristic asymmetric and symmetric vibrations of the carboxylate anion at 1605 and 1405 cm^{-1}, respectively.

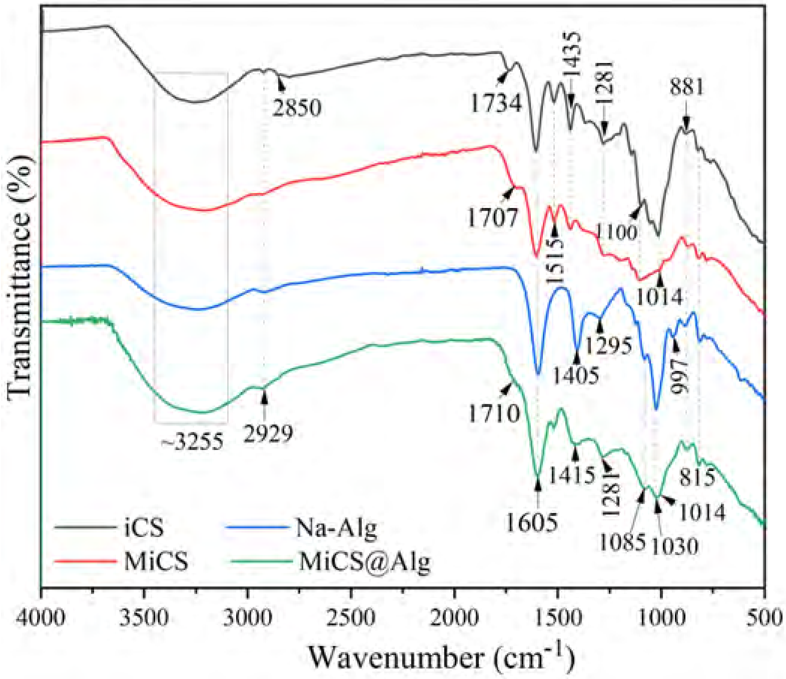

Figure 4. FTIR spectrum of raw chestnut shell (iCS), Na-alginate and isolated melanin (MiCS), and Na-alg beads (MiCS@Alg).

The spectrum of MiCS@Alg shows multiple absorption peaks, including a broad band around 3255 cm^{-1}, assigned to O–H stretching vibrations of hydroxyl groups in the alginate and melanine structure [30]. The peak at 1710 cm^{-1}, resulting from C=O stretching, is related to the carboxyl groups of the melamine structure. An additional intense peak at 1605 and 1415 cm^{-1} further confirms the presence of carboxylate anion. The bands at 1281, 1085, and 1014 cm^{-1} correspond to C-H and C-O deformation vibrations, characteristic of polysaccharide structures. Finally, the peaks at 997 and 815 cm^{-1} can be attributed to C–O–C vibrations and glycosidic linkages in the ring structures of alginate.

Natural materials MiCS showed structural complexity of constituent material, which indicates that the adsorption mechanisms are very demanding. From that point of view, it is of utmost importance to quantify surface functionalities to discuss the relation between adsorption performance versus adsorbent properties. Melanin, lignin, and tannins, present in the chestnut shell and MiCS, contain an appropriate number and type of functional groups as potential binding sites for specific pollutants. The establishment of a relationship between adsorbent properties/functionalities versus adsorption performance can be based on the quantitative determination of surface functionalities. The results from total basic and acidic groups, and carboxyl groups content determination using standard volumetric methods are given in Table S3.

3.1.3. UV-Vis Analysis

UV-Vis spectra of iCS and MiCS are given in Figure 5.

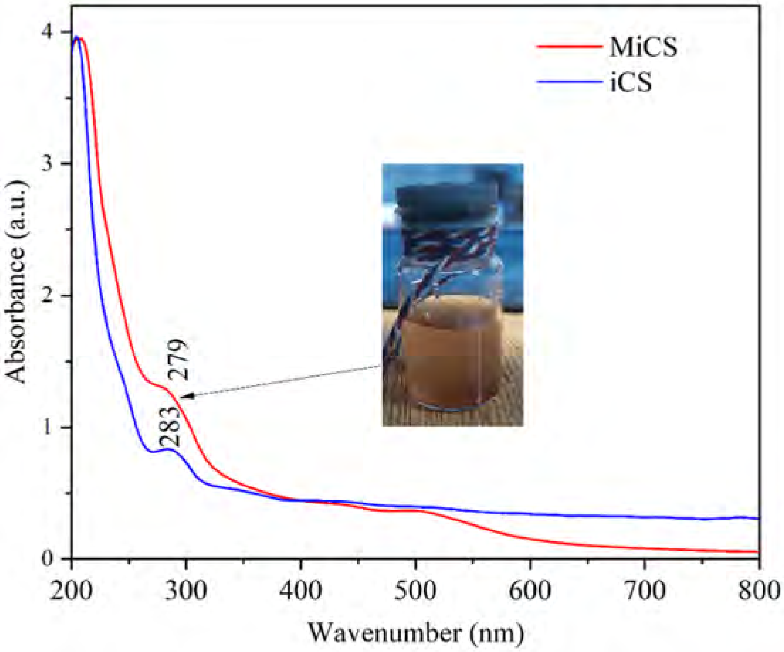

Figure 5. UV—Vis absorbance spectra of iCS and MiCS in aqueous NaOH solutions.

On the basis of the obtained UV–Vis spectra, an intense absorption in the UV region can be observed with maxima at 279 nm (iCS) and 283 nm (MiCS), corresponding to π–π* transitions of aromatic chromophores present in the melanin structure. Following these maxima, the absorbance gradually decreases toward longer wavelengths, displaying a continuous "tail" up to 800 nm without distinct peaks, which represents a typical characteristic of melanin and melanin-like materials known for their so-called "featureless broadband absorption" profile [31,32]. A comparison of the samples shows that MiCS exhibits slightly more pronounced absorption in the UV region, indicating a higher concentration or better dispersion of melanin pigments compared to the iCS sample. The obtained results clearly confirm that the analyzed samples exhibit the spectral characteristics of melanin, with the identification of this pigment further corroborated by its distinctive continuous absorption behavior in the visible region. A similar spectrum was reported in the study [32], where melanin was extracted from the marine sponge-associated actinomycete *Micromonospora fulva* HV6.

3.1.4. DLS and ZETA Analysis

The zeta potential and average particle radius were determined to better understand surface electrostatics as a function of pH. The zeta potential of the isolated melanin is −36.6 ± 2.9 mV at a pH of 10.5, while the untreated chestnut bark exhibits a value of −25.9 ± 1.04 mV at a pH of 12.8 (Figure 6). These results indicate a pronounced negative surface charge of both materials, which can significantly influence their ability to interact with cations in solution, specifically Astrazon Yellow 7GLL and Safranin T dyes. In relation to these results, a series of preliminary adsorption experiments at initial pH 6, 7, and 8 were performed, and the optimal results were obtained at pH 7.5. Higher pH affects the increase in solubility of MiCS.

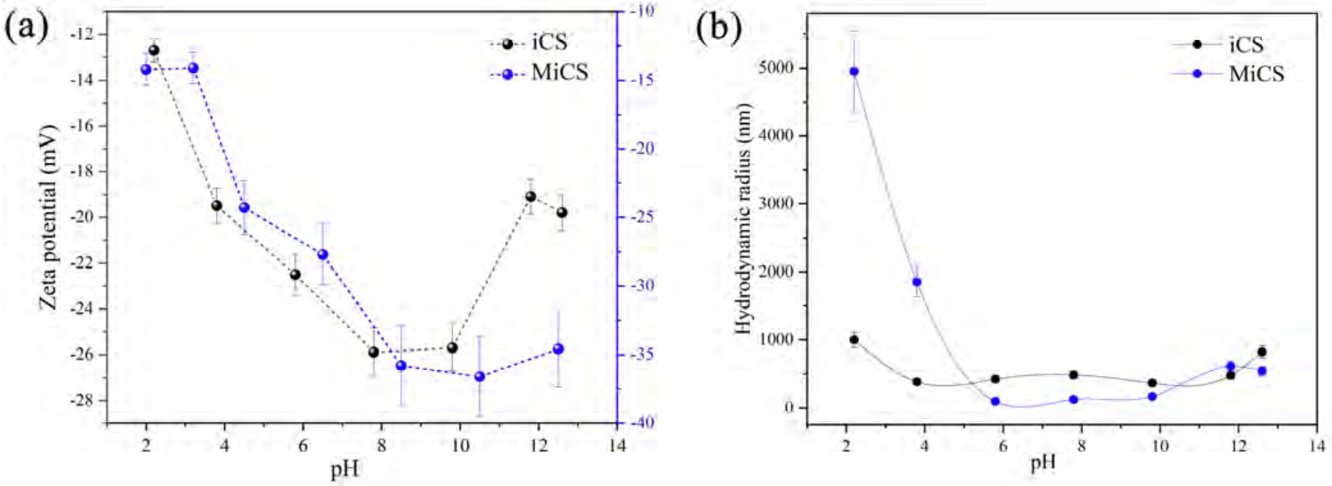

Figure 6. Effect of pH on (**a**) zeta potential and (**b**) hydrodynamic radius of nontreated chestnut shell (iCS) and MiCS.

The stability of the colloidal dispersions of the iCS and MiCS samples was investigated as a function of pH by determining their hydrodynamic radius using DLS analysis (Figure 6). The results clearly indicate that the aggregation behavior of the particles depends on the pH of the medium. At pH 2, the MiCS sample exhibited a huge hydrodynamic radius (4952 nm), suggesting strong particle aggregation in the acidic environment due to reduced zeta potential and destabilization of interparticle repulsion. In contrast, the iCS sample showed a significantly smaller radius at the same pH (997 nm), indicating somewhat better dispersibility.

As the pH increased to 4, a decrease in the hydrodynamic radius was observed for both samples. Although MiCS still exhibited a larger radius compared to iCS (1852 nm versus 384 nm), a significant reduction in aggregation relative to pH 2 was evident. The lowest values of hydrodynamic radius were recorded in the pH range of 6 to 10, where both samples displayed relatively small dimensions (below 500 nm), indicating the highest colloidal stability. Within this pH range, MiCS exhibited a slightly smaller radius compared to iCS, suggesting that melanin extraction contributes to enhanced dispersion stability, likely through the reduction in interparticle interactions caused by changes in surface functional groups. At higher pH values (12 and 13), a slight increase in hydrodynamic radius was observed for both samples, with aggregation more pronounced in iCS (821 nm at pH 12.6). In contrast, MiCS maintained a moderate size (612 nm), further confirming the stabilizing effect of melanin extraction. As shown in Figure 6, MiCS exhibits better dispersibility and a lower degree of aggregation across a broad pH range. The most favorable pH for stable dispersion of both samples lies within the 6–10 range, which is particularly important for potential applications in aqueous systems, including wastewater treatment. In this range, the average particle size of iCS was 786 nm at pH 5.8, while MiCS measured 612 nm at pH 10.5.

3.2. Elemental Analysis

The elemental composition of the pulverized chestnut shells and MiCS is presented in Supplementary Table S2. Compared to the raw chestnut shells, MiCS exhibited a slightly increased carbon content (49.7 wt.%) and decreased hydrogen (3.90 wt.%) and oxygen

(43.21 wt.% vs. 41.83 wt.%) contents, indicating a mild concentration of organic components and partial removal of oxygen- and hydrogen-containing functional groups during the preparation process. The nitrogen content remained essentially unchanged, suggesting the preservation of proteinaceous or nitrogen-containing constituents. Overall, these changes reflect subtle modifications in the chemical composition of the material resulting from the MiCS preparation process.

3.3. Batch Adsorption Experiments

3.3.1. Adsorption Isotherm Study

Analysis of adsorption equilibrium data provides valuable information about the interaction mechanisms between the adsorbent and adsorbate. Analyzing the zeta potential measurement at different pH (Figure 6a) and the results from the study of the pH influences on dyes and ammonia adsorption efficiencies onto MiCS and MiCS@Alg (Figure S1), it was deduced that pH 7 was optimal for dyes removal, while pH 4 was optimal for ammonia removal. Low decrease in adsorption capacity of both MiCS and MiCS@Alg adsorbent indicates the significance of deprotonated phenol groups in dyes removal. Moreover, a wider pH range, from 6 to 8, could be used in processes of dye removal, while a narrower pH range, from 4 to 5, could be applied for ammonia removal without a significant decline in adsorption efficiency. This pH range can possibly be used in processes of dye removal, which falls in the range of most natural water, while one that could be applied in processes of ammonia removal could be found in wastewater from the mining industry.

In this study, adsorption experiments were conducted at three different temperatures to determine the adsorption capacity of MiCS and MiCS@Alg. The experimental data were fitted to both the Langmuir and the Freundlich isotherm models [33], which describe monolayer and multilayer adsorption on surfaces with a defined number of active sites, respectively. The corresponding model nonlinear parameters and correlation results are presented in Table 1. The results of nonlinear modelling using Langmuir and the Freundlich isotherms are presented in the Supplementary, in Figure S2. Data fitting with other adsorption isotherms (Dubinin-Radushkevich, Tempkin, Sips, Toth, etc.) [34] provides modelling data at lower statistical validity.

The equilibrium adsorption data were analyzed using both the Langmuir and the Freundlich isotherm models (Table 1). The Langmuir model assumes monolayer adsorption on a homogeneous surface, whereas the Freundlich model accounts for adsorption on heterogeneous surfaces with the possibility of multilayer formation. In this study, the Freundlich model exhibited a superior fit, with R^2 values ranging from 0.752 to 0.997, confirming that adsorption predominantly occurs on heterogeneous surfaces, consistent with the structural complexity of the synthesized adsorbents. The Langmuir equilibrium constants (K_L) also supported these trends. For BR2, MiCS exhibited values up to 0.2471 L mg^{-1}, whereas BY28 showed moderately lower constants (0.2154 L mg^{-1}). For NH_3, however, K_L values were much higher (2.21 L mg^{-1} for MiCS and 4.79 L mg^{-1} for MiCS@Alg at 45 °C), suggesting a strong affinity of NH_3 molecules for active sites despite the lower q_m values, which may reflect steric limitations and weaker multilayer formation compared to dye molecules. The Freundlich constants (K_F) confirmed these observations. The highest K_F was obtained for BR2 adsorption on MiCS (62.73 mg g^{-1} (L mg^{-1})$^{1/n}$ at 45 °C), confirming its strong adsorption capacity. For NH_3, K_F values were also substantial (40.28 mg g^{-1} (L mg^{-1})$^{1/n}$ for MiCS and 35.13 mg g^{-1} (L mg^{-1})$^{1/n}$ for MiCS@Alg at 45 °C), indicating favorable adsorption but less pronounced than for dyes. The Freundlich intensity factor (n) ranged from 1.70 to 5.80 across all systems, confirming favorable adsorption conditions, with NH_3 on MiCS@Alg showing the highest intensity (n = 5.81) (Table 1). Overall, the Freundlich model provided a more accurate description of the adsorption behavior, highlighting the heterogeneous surface nature of both adsorbents and the potential for multilayer adsorption, as also in the work [35]. Comparable adsorption capacities have been reported in the literature, such as the removal of BR2 using bentonite (269 mg g^{-1}) and the removal of BY28 with zinc oxide-chitosan composites [36,37]. Similarly, adsorption of ammonium ions has been extensively studied, with related findings reported in recent works [10] further validating the observed trends in this study. In order to test the applicability of both MiCS and MiCS@Alg adsorbents at higher initial pollutant concentrations at 200 mg L^{-1} of dye and ammonia pollutants, adsorption experiments in a batch system were performed. The preliminary results confirmed the high potential of produced adsorbents, and the following adsorption capacities were obtained: 954.4 mg g^{-1} for BR2, 686.2 mg g^{-1} for BY28, and 176.4 mg g^{-1} for NH_3 on MiCS; 628.4 mg g^{-1} for BR2, 445.8 mg g^{-1} for BY28, and 116.2 mg g^{-1} for NH_3 on MiCS@Alg at 25 °C. In the case of BY28 dye, methyl groups contribute to the steric inhibition of both the approach and the establishment of electrostatic interactions. On the other hand, BR2 dye, with its higher aromatization and charge dispersibility in the phenazine ring, helps in adaptable access to the carboxylate anion. Without exception, the contribution of amino to the establishment of hydrogen bonding with carboxylate anions must not be neglected.

Table 1. Results of nonlinear Langmuir and Freundlich model for pollutant adsorption (Ci = 30 mg L^{-1}, m_a = 1–10 mg, V = 8 mL, T = 25–45 °C, t = 90 min).

Sample			**Langmuir**			**Freundlich**		
	Pollutant	**T (°C)**	q_m **(mg g^{-1})**	K_L **(L mg^{-1})**	R^2	K_F **(mg g^{-1}) (L $mg^{-1})^{1/n}$**	**n**	R^2
MiCS	BR2	25	291.1 ± 21.5	0.2166 ± 0.061	0.9635	56.21 ± 2.47	1.714 ± 0.08	0.9912
		35	295.7 ± 22.2	0.2247 ± 0.064	0.9632	58.36 ± 2.62	1.715 ± 0.08	0.9905
		45	300.2 ± 22.6	0.2471 ± 0.075	0.9601	62.73 ± 2.98	1.709 ± 0.08	0.9912
	BY28	25	192.5 ± 13.4	0.1864 ± 0.03	0.9829	35.67 ± 0.96	1.873 ± 0.045	0.9974
		35	198.2 ± 13.8	0.1942 ± 0.03	0.9827	37.65 ± 1.36	1.882 ± 0.074	0.9933
		45	201.5 ± 14.3	0.2154 ± 0.03	0.9857	40.40 ± 1.26	1.895 ± 0.056	0.9960
	NH_3	25	71.26 ± 5.46	1.9554 ± 1.15	0.7565	38.35 ± 3.04	3.563 ± 0.501	0.9354
		35	71.94 ± 5.52	2.0242 ± 1.19	0.7558	38.98 ± 3.06	3.569 ± 0.503	0.9361
		45	73.08 ± 5.85	2.2128 ± 1.32	0.7519	40.28 ± 3.13	3.596 ± 0.504	0.9361
MiCS@Alg	BR2	25	180.5 ± 9.40	0.2351 ± 0.106	0.8829	43.09 ± 3.14	2.175 ± 0.17	0.9757
		35	184.3 ± 10.5	0.2338 ± 0.116	0.8654	44.37 ± 3.71	2.193 ± 0.205	0.9674
		45	189.3 ± 10.8	0.2853 ± 0.141	0.8741	48.91 ± 3.68	2.141 ± 0.187	0.9755
	BY28	25	109.3 ± 8.96	0.4981 ± 0.28	0.7919	39.28 ± 3.33	2.736 ± 0.301	0.9564
		35	115.2 ± 9.45	0.4566 ± 0.27	0.7872	40.24 ± 3.51	2.706 ± 0.304	0.9545
		45	117.1 ± 9.60	0.4873 ± 0.30	0.7775	42.20 ± 3.67	2.747 ± 0.316	0.9529
	NH_3	25	49.78 ± 5.15	4.1601 ± 2.78	0.7809	34.24 ± 2.28	5.622 ± 1.00	0.9309
		35	49.65 ± 5.14	4.5621 ± 3.17	0.7762	34.62 ± 2.24	5.726 ± 1.01	0.9333
		45	50.06 ± 4.99	4.7934 ± 3.17	0.7882	35.13 ± 2.23	5.807 ± 1.02	0.9338

In summary, the produced adsorbents MiCS and MiCS@Alg showed significantly higher adsorption capacities in relation to iCS (preliminary results indicated between 32 and 36% of those obtained for MiCS and MiCS@Alg, as shown in Table 1). Use of MiCS as an ammonia adsorbent provides additional benefits, as the enriched materials contain approximately 10 wt.% nitrogen, which could be used in agriculture as fertilizer. Also, the obtained results refer to the possibility of MiCS use as adsorbents for removing unpleasant odors in toilets. Moreover, the production of MiCS@Alg beads opens a new path for their potential applicability in a flow system, verifying the concept of melanin isolation and encapsulation in Na-alg carriers.

3.3.2. Adsorption Kinetics

Adsorption kinetics represents one of the key practical aspects in the application of environmentally friendly adsorptive materials. To demonstrate this effect, the influence of contact time on dye adsorption onto MiCS and MiCS@Alg sorbents was investigated at an initial dye concentration of 30 mg L^{-1}, using 0.001 g of adsorbent. The experiments were performed at three different temperatures (including 25 °C), under constant magnetic stirring. Adsorption equilibrium was monitored over 24 h, with maximum adsorption achieved after 90 min. The parameters obtained from nonlinear fitting are presented in the table for 25 °C, while the results for other temperatures are shown in Figure 7. To gain a deeper understanding of the adsorption kinetics, the experimental data were analyzed using pseudo-first-order (PFO) and pseudo-second-order (PSO) kinetic models [38]. The results are presented in Table 2. The kinetic results fitting, obtained by using the Weber–Morris (W–M) diffusion model [33], are presented in Table 2.

Table 2. Results of the nonlinear PFO and PSO models for pollutants adsorption (Ci = 30 mg L^{-1}, m_a = 1 mg, V = 8 mL, T = 25 °C, t = 90 min).

Adsorbent	Pollutant	Model Parameters	Pseudo-First	Pseudo-Second
MiCS	BR2	q_e (mg g^{-1}) k_1 (min^{-1})/k_2 (g mg^{-1} min^{-1}) R^2	165.7 ± 6.00 0.7401 ± 0.196 0.956	175.3 ± 5.58 0.0031 ± 0.001 0.979
	BY28	q_e (mg g^{-1}) k_1 (min^{-1})/k_2 (g mg^{-1} min^{-1}) R^2	125.5 ± 1.33 36.38 ± 0.00 0.995	127.9 ± 0.88 2.4812 ± 0.006 0.999
	NH_3	q_e (mg g^{-1}) k_1 (min^{-1})/k_2 (g mg^{-1} min^{-1}) R^2	54.90 ± 1.71 0.135 ± 0.02 0.975	60.97 ± 0.855 0.0031 ± 0.0003 0.997
MiCS@Alg	BR2	q_e (mg g^{-1}) k_1 (min^{-1})/k_2 (g mg^{-1} min^{-1}) R^2	117.3 ± 6.61 0.1565 ± 0.043 0.921	138.9 ± 8.6 5.7928 ± 2.077 0.962
	BY28	q_e (mg g^{-1}) k_1 (min^{-1})/k_2 (g mg^{-1} min^{-1}) R^2	78.45 ± 1.75 10.07 ± 8.38 0.982	80.23 ± 1.18 0.0198 ± 0.0065 0.995
	NH_3	q_e (mg g^{-1}) k_1 (min^{-1})/k_2 (g mg^{-1} min^{-1}) R^2	31.70 ± 1.24 0.0906 ± 0.015 0.969	36.35 ± 0.984 0.0032 ± 0.0004 0.993

The adsorption kinetics of BR2, BY28, and NH_3 onto MiCS and MiCS@Alg adsorbents were evaluated using pseudo-first-order (PFO) and pseudo-second-order (PSO) kinetic models (Table 2). In all cases, the equilibrium adsorption capacities (qe) calculated from the nonlinear PSO model were closer to the experimental values than those obtained from the PFO model. Moreover, the correlation coefficients (R^2) were consistently higher for the PSO model (0.962–0.999) compared to the PFO model (0.921–0.995), confirming its superior fitting. Similar results were reported for chestnut shell-derived activated carbon (CNS-AC) in the removal of quinary heavy metal ions [13]. For BR2 adsorption, MiCS exhibited a higher qe value (175.3 mg g^{-1}) compared to MiCS@Alg (138.9 mg g^{-1}). Similarly, for BY28, MiCS demonstrated a slightly higher adsorption capacity (127.9 mg g^{-1}) than MiCS@Alg (80.23 mg g^{-1}). A comparable trend was observed for NH_3, where MiCS reached qe = 60.97 mg g^{-1}, while MiCS@Alg achieved a lower value of 36.35 mg g^{-1}. Interestingly, although the incorporation of alginate slightly reduced the overall adsorption capacities of the sorbent, it led to an increase in the kinetic rate constants in some cases. For instance, in BR2 removal, MiCS@Alg displayed a significantly higher k_2 value compared to MiCS, indicating that surface modification improved the accessibility and reactivity of the binding sites. For BY28 and NH_3, the differences in k_2 values between the two sorbents were less pronounced, but MiCS still generally outperformed MiCS@Alg in terms of adsorption capacity. Kinetic analysis confirmed that the adsorption of dyes (BR2 and BY28) and ammonia (NH_3) onto both sorbents is more accurately described by the pseudo-second-order model. This highlights the predominance of chemisorption, involving electron sharing or exchange between the sorbent surface and pollutant molecules, as the dominant adsorption mechanism.

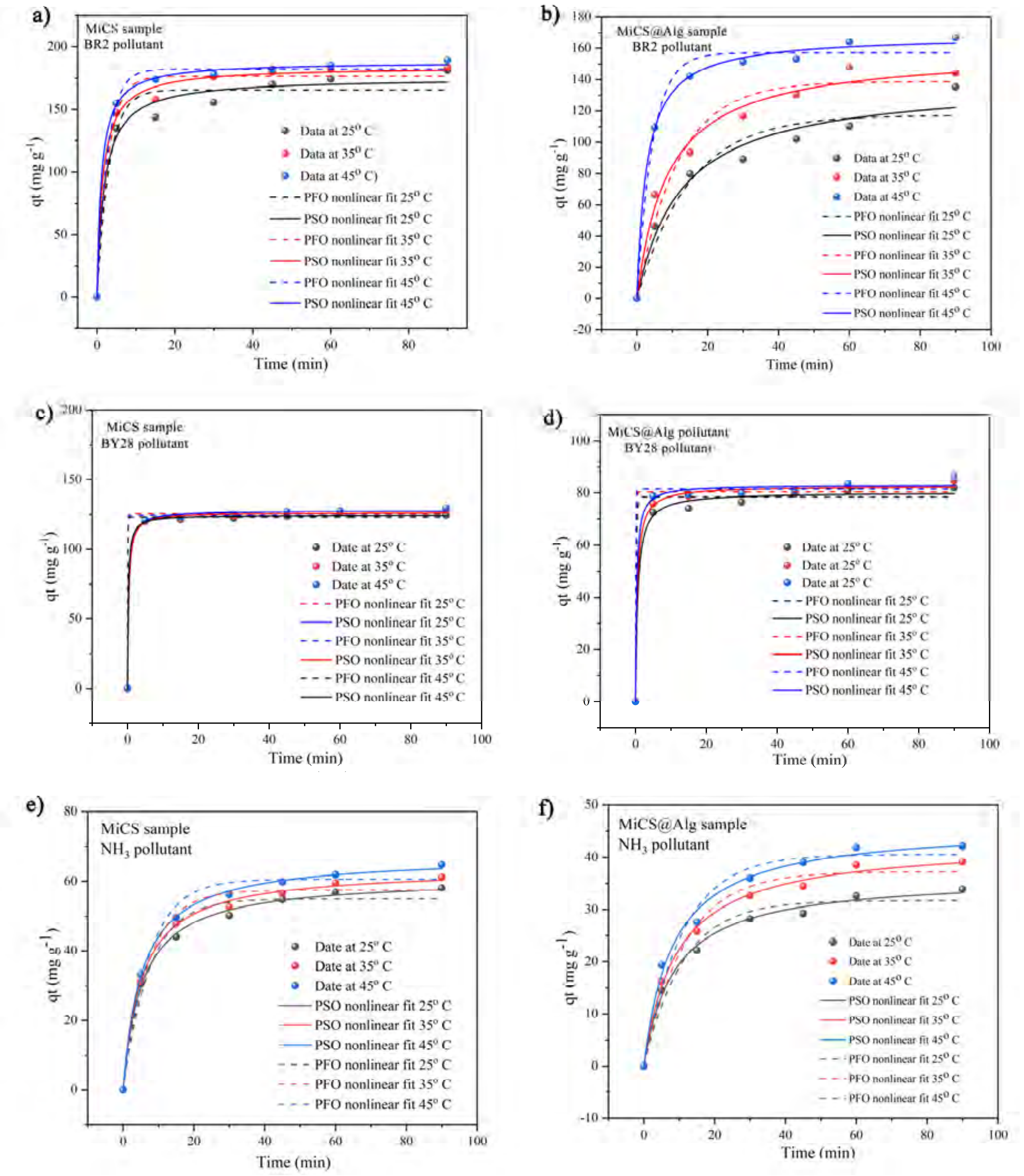

Figure 7. Results of PFO and PSO nonlinear model calculation for adsorption of dyes on (**a**,**c**,**e**) MiCS and (**b**,**d**,**f**) MiCS@Alg at three temperatures (Ci = 30 mg L^{-1}, m_a = 1 mg, V = 8 mL, T = 25 °C, t = 90 min).

The results of the Weber–Morris model in Table 3 confirmed that the adsorption of BR2, BY28, and NH_3 on MiCS and MiCS@Alg proceeds in two distinct steps. In Step 1, the diffusion rate constants (k_{id1}) for BR2 were the highest among all systems, reaching 6.385 mg g^{-1} $min^{-0.5}$ for MiCS and 13.25 mg g^{-1} $min^{-0.5}$ for MiCS@Alg. These values indicate a rapid and intense initial uptake of BR2, consistent with a strong surface affinity. For BY28, significantly lower kid1 values were observed (1.400 for MiCS and 0.935 for MiCS@Alg), indicating slower diffusion in the early stage. Similarly, NH_3 showed modest initial diffusion rates, reflecting weaker interaction in the initial surface-controlled phase compared to BR2. In Step 2, the process slowed down, as demonstrated by reduced k_{id2} values. For BR2, the diffusion rate constants decreased to 4.015 (MiCS) and 12.25 (MiCS@Alg), while for BY28, they were 1.219 (MiCS) and 0.8248 (MiCS@Alg). For NH_3, the kid2 values further decreased to 0.6746 (MiCS) and 0.9287 (MiCS@Alg), confirming that its adsorption is strongly controlled by intraparticle diffusion.

Table 3. Results of the intraparticle diffusion model (Weber–Morris) for BR2, BY28, and ammonia adsorption (Ci = 30 mg L^{-1}, m_a = 1 mg, V = 8 mL, T = 25 °C, t = 90 min).

Kinetic Model	**Model Parameters**	**MiCS**			**MiCS@Alg**		
		BR2	**BY28**	**NH_3**	**BR2**	**BY28**	**NH_3**
Weber–Morris (Step 1)	k_{id1} (mg g^{-1} $min^{-0.5}$)	6.385 ± 0.224	1.400 ± 0.050	1.078 ± 0.038	13.25 ± 0.517	0.935 ± 0.033	1.200 ± 0.042
	C_{BL} (mg g^{-1})	120.2	118.3	83.41	20.64	71.10	43.78
	R^2	0.992	0.997	0.879	0.909	0.865	0.982
Weber–Morris (Step 2)	k_{id2} (mg g^{-1} $min^{-0.5}$)	4.015 ± 0.141	1.219 ± 0.043	0.6746 ± 0.024	12.25 ± 0.480	0.8248 ± 0.029	0.9287 ± 0.035
	C_{BL} (mg g^{-1})	143.2	115.9	87.66	18.17	74.08	45.15
	R^2	0.999	0.887	0.879	0.982	0.992	0.973

The intercept values (C_{BL}) were consistently high for dyes on MiCS, indicating that intraparticle diffusion is not the sole rate-limiting mechanism, but rather that film diffusion and surface interactions also play significant roles. For NH_3, the C_{BL} values were notably lower, suggesting that the adsorption of ammonia is less affected by surface diffusion resistance and relies more on gradual penetration into the pores. Interestingly, the incorporation of alginate significantly reduced the intercept values for dyes, which indicates that Na-alginate modification weakens the external film diffusion resistance and alters the adsorption pathway.

The correlation coefficients (R^2) further supported these findings. For MiCS, the Weber–Morris model provided excellent fits, with R^2 values up to 0.999 (BR2, Step 2). For NH_3, the model also showed a good correlation (R^2 = 0.879–0.982), though slightly lower compared to dyes. In contrast, for MiCS@Alg, the model agreement was generally lower, with R^2 values ranging from 0.8649 to 0.9924, suggesting that alginate incorporation modifies the pore structure and sorption kinetics, thereby reducing the predictability of the intraparticle diffusion model. Overall, the Weber–Morris analysis demonstrates that BR2 exhibits the fastest sorption dynamics due to strong interactions with the sorbent surface, while BY28 shows slower kinetics but a significant contribution from intraparticle diffusion. In contrast, NH_3 adsorption is more strongly governed by diffusion within the sorbent pores. Alginate modification enhances the initial uptake rate of BR2 but reduces boundary layer effects, leading to altered adsorption kinetics compared to pristine MiCS.

The 25, 35, and 45 °C confirm that the PSO model provides a consistently better fit to the experimental data compared to the PFO model for all studied systems. This indicates that the adsorption rate is not solely governed by physical diffusion, but also involves chemisorptive interactions between the active sites of the sorbent and the adsorbate molecules. The adsorption process in all cases (Figure 7) exhibited a very fast initial phase, with most of the equilibrium uptake reached within the first 20–30 min, followed by a gradual plateau due to surface saturation. Temperature was found to influence adsorption differently depending on the pollutant and sorbent. For BR2 dye, increasing the temperature enhanced adsorption, confirming the endothermic nature of the process, whereas for BY28 dye and NH_3 pollutant, the adsorption capacity remained nearly unchanged with temperature. When comparing the two sorbents, MiCS@Alg generally showed a slower approach to equilibrium than MiCS, which can be attributed to the presence of alginate that modifies diffusion pathways and the accessibility of active sites. The compatibility between the experimental data and the kinetic models was evaluated based on the determination coefficient (R^2) and the amount of adsorbed pollutants (q_e). Since the calculated q_e value for the pseudo-first-order model was significantly lower than the experimental value, it can be concluded that this model does not provide adequate results for either sorbent. The pseudo-first-order equation fails to accurately describe the experimental data for both sorbents in the removal of the investigated pollutants. Similar results to those presented in the table were reported for biochar-alginate in MB removal [6].

3.3.3. Thermodynamic Study and Adsorption Mechanism

Gibbs free energy ($\Delta G^{\ominus}$), enthalpy ($\Delta H^{\ominus}$), and entropy ($\Delta S^{\ominus}$) were calculated using Van't Hoff equations to analyze the thermodynamic aspect of the adsorption process [38]. The calculated parameters are presented in Table 4. A better agreement with the experimental values (R^2) in the calculation of thermodynamic parameters was achieved by using the Langmuir constant obtained from the linear form of the Langmuir model. Larger deviations were obtained when applying the nonlinear form, as shown in Table 4.

Table 4. Thermodynamic parameters for BR2, BY28 and ammonia removal using MiCS and MiCS@Alg (Ci =30 mg L^{-1}, m_a = 1–10 mg, V = 8 mL, T = 25 °C, 35 °C and 45 °C, t = 90 min.

Adsorbent	**Pollutants**	**$\Delta G^{\ominus}$ (kJ mol^{-1})**			**$\Delta H^{\ominus}$ (kJ mol^{-1})**	**$\Delta S^{\ominus}$ (J mol^{-1} K^{-1})**	**R^2**
		25 °C	**35 °C**	**45 °C**			
MiCS	BR2	−39.33	−40.78	−42.43	6.78	154.5	0.941
	BY28	−38.58	−40.01	−41.50	4.91	145.8	0.988
	NH_3	−32.59	−33.74	−34.95	2.63	118.1	0.959
MiCS@Alg	BR2	−39.37	−40.82	−42.54	7.77	157.9	0.915
	BY28	−40.14	−41.52	−43.05	3.23	145.4	0.869
	NH_3	−33.83	−35.05	−36.29	2.87	123.1	0.997

The thermodynamic parameters obtained for the adsorption of BR2 and BY28 dyes and NH_3 on MiCS and MiCS@Alg provide clear insights into the nature of the process. The negative $\Delta G^{\ominus}$ values, ranging from −32.59 to −43.05 kJ mol^{-1}, confirm that adsorption is spontaneous within the investigated temperature range, with spontaneity generally increasing as the temperature rises. The positive $\Delta H^{\ominus}$ values (2.63–7.77 kJ mol^{-1}) indicate that the adsorption process is slightly endothermic, while the positive $\Delta S^{\ominus}$ values (118.1–157.9 J mol^{-1} K^{-1}) suggest an increase in randomness at the solid–solution interface, likely associated with the release of solvent molecules and structural rearrangements during adsorption. The most favorable adsorption was observed for BR2 on MiCS, with $\Delta G^{\ominus}$ values between −39.33 and −42.43 kJ mol^{-1} and $\Delta S^{\ominus}$ = 154.5 J mol^{-1} K^{-1}, reflecting the most potent driving force and a high entropic contribution. By contrast, the lowest spontaneity was recorded for NH_3 on MiCS, where $\Delta G^{\ominus}$ values ranged from −32.59 to −34.95 kJ mol^{-1} and $\Delta S^{\ominus}$ was 118.1 J mol^{-1} K^{-1}. Interestingly, although adsorption of BY28 on MiCS also showed relatively high spontaneity ($\Delta G^{\ominus}$ = −38.58 to −41.50 kJ mol^{-1}; $\Delta S^{\ominus}$ = 145.8 J mol^{-1} K^{-1}), this system exhibited the best agreement with the Van't Hoff model (R^2 = 0.9877), indicating strong consistency with the linear thermodynamic approach. Similar values of the thermodynamic parameters $\Delta H^{\ominus}$ and $\Delta S^{\ominus}$ were obtained for the removal of TC, as presented in the study [39].

For the alginate-modified material, MiCS@Alg, BR2 adsorption remained highly favorable, with $\Delta G^{\ominus}$ values between -39.37 and -42.54 kJ mol^{-1}, $\Delta H^{\ominus}$ = 7.77 kJ mol^{-1}, and $\Delta S^{\ominus}$ = 157.9 J mol^{-1} K^{-1}. This system showed a slightly higher enthalpic contribution compared to pristine MiCS ($\Delta H^{\ominus}$ = 6.78 kJ mol^{-1}), while maintaining a strong entropic effect. Adsorption of NH_3 on MiCS@Alg was characterized by $\Delta G^{\ominus}$ values of -33.83 to -36.29 kJ mol^{-1}, ΔH° = 2.87 kJ mol^{-1}, and $\Delta S^{\ominus}$ = 123.1 J mol^{-1} K^{-1}, showing improved spontaneity relative to NH_3 on MiCS, with excellent model agreement (R^2 = 0.997). On the other hand, BY28 on MiCS@Alg demonstrated the lowest fit to the Van't Hoff model (R^2 = 0.869), with $\Delta G^{\ominus}$ values ranging from -40.14 to -43.05 kJ mol^{-1}, $\Delta H^{\ominus}$ = 3.23 kJ mol^{-1}, and $\Delta S^{\ominus}$ = 145.4 J mol^{-1} K^{-1}, suggesting that alginate modification alters the thermodynamic profile by slightly reducing the entropic contribution compared to MiCS.

Overall, the results from Table 4 indicate that alginate modification modulates the balance between enthalpic and entropic contributions, strengthening spontaneity for NH3 adsorption while slightly decreasing the model's applicability for BY28.

Adsorption and thermodynamic results indicate that the ion-exchange is an operative mechanism with participation of electrostatic and π–π stacking interactions. Additional proof of the adsorption mechanism was accessed through supplementary experiments. In the course of the adsorption experiments, using BR2 and BY28 dyes, the initial and final pH, as well as the time-dependent changes, were followed. It was found that pHi was decreased by 0.58 and 0.74 units for MiCS, respectively. Even lower change was recorded for MiCS@Alg adsorbent. Thus, the most plausible mechanism can be described by the sodium exchange, due to pH adjustment with NaOH, with cationic dyes and nucleophilic ammonia (Figure S3). The selection of operative pH (Section 2.5. Adsorption experiments) was based on the availability of the most natural and polluted water and deprotonation of MiCS surface functionalities (mainly carboxylic group: pKa of carboxylic acid varies in the range 3.6–4.5). In that manner, effective deprotonation of carboxylic acid groups creates an anionic structure able to participate in an ion-exchange process with cation dyes. Otherwise, the use of lower pH in the course of ammonia adsorption is in favor of a simple neutralization reaction producing ammonium salt. Also, the study of ionic strength (IS) (0.01, 0.05, and 0.1 mol dm^{-3} KNO_3) showed a low effect on the change in adsorption efficiency (less than 10% adsorbent capacity decrease). It primarily affects adsorbent/adsorbate electrostatic interactions at the adsorbent surface, ion diffusivity, and hydration shell stability.

These phenomena were reflected through adsorption efficiency due to the same/opposite charge sign repulsion/attraction, causing higher deterioration in the adsorption efficiency of weakly bonded pollutants. Thus, MiCS could be effectively used at increased concentrations of anionic competing ions if we consider selective removal, considering organic pollutant sodium benzoate or Cl^- and $SO_4{}^2$ (less than 5% of adsorption capacities decrease, given in Table 1, was found). Otherwise, use of cationic pollutants, e.g., calcium or magnesia, and especially Al^{3+}, causes a significant decrease in dyes adsorption capacity. A large decrease in adsorption efficiency (higher than 70%) indicates the predominance of an electrostatic interaction between carboxylate anion and cation (e.g., Ca^{2+} and Mg^{2+}), i.e., higher affinity to ion-exchange with calcium cation, forming preferably calcium–carboxylate salt. Ca^{2+} and Mg^{2+} ions show a high affinity with respect to carboxylate ions, interacting through multiple binding modes by forming monodentate and bidentate metal complexes. The extent and type of metal/carboxylate ion binding are influenced by the number and orientation of neighboring carboxylate groups. The strength of these bindings can be affected by the presence of other carboxylic groups in close proximity, which help in the formation of bidentate complexes (cooperative mechanism). At a higher presence of negatively charged functionalities with diverse structural arrangements, they can participate in forming different binding structures on the adsorbent surface. Strong affinity of hard metal cation Al^{3+} to carboxylate ion, i.e., oxygen as electron donor, provides effective formation of stable complexes, even higher stability than those obtained with Ca^{2+} and Mg^{2+} cations (adsorption efficiency drop for more than 87% with respect to BY28). In general, MiCS and MiCS@Alg can effectively remove cationic species in the presence of anionic species, as they have a higher affinity for metal cations compared to textile dyes.

These results indicate the potential of the produced MiCS adsorbent to be applicable in the process of natural water softening. High influences on dye removal arise from their structural complexity, hydration, and steric hindrance to the attainment of multiple adsorbent/adsorbate interactions. The moderate effect of methylene blue on BY28 dye removal indicates that similar competitive potential (somewhat higher for methylene blue, 62% adsorption capacity decrease was found for BY28). It indicates the significance of structural limitation and charge concentration/availability for interaction with the carboxylate ion. On the contrary, the low competitive effect of the cationic pollutants (Ca^{2+}, Mg^{2+}, and Al^{3+}) with ammonia removal at pH 4 was observed. In this case, a neutralization reaction takes place freely with no competition from the side processes.

3.4. Desorption Study

Desorption studies play a key role in understanding the nature of the adsorption process and evaluating the regeneration of adsorbents [40] and were therefore conducted to investigate their reusability. The sorbent recycling study was performed over five cycles using 0.1 M HCl as the desorbing agent. The obtained results are presented in Figure 8 and summarized in Table S4.

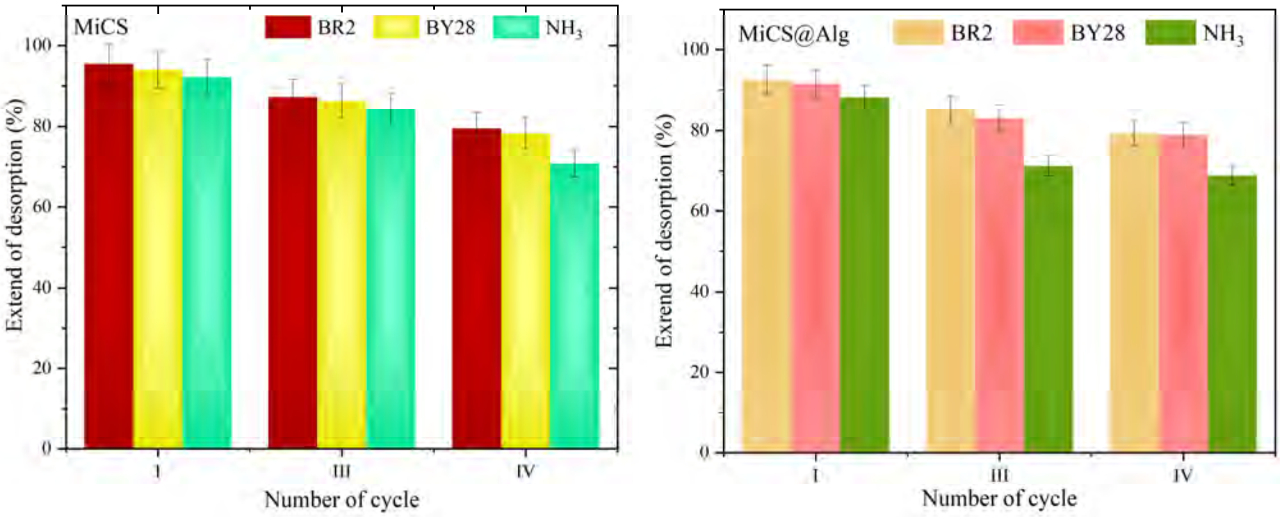

Figure 8. Reusability study of MiCS and MiCS@Alg in five adsorption/desorption cycles (Ci = 30 mg L^{-1}, m = 0.1 g, T = 25 °C, desorption time: 3 h) using 0.1 M HCl.

By comparing the performance of the MiCS and MiCS@Alg sorbents, it is evident that MiCS exhibits higher adsorption capacities and slightly better regenerability than the alginate-modified sorbent, which is consistent with the trend obtained from the Langmuir adsorption model. The maximum adsorption capacity for BR2 on MiCS reached 291.1 mg g^{-1}, whereas for MiCS@Alg it was significantly lower (180.5 mg g^{-1}). A similar trend was observed for BY28 and NH_3, where MiCS demonstrated higher adsorption capacities across all five cycles. The desorption efficiency of both materials was high in the first cycle (>90%) (Figure 8). However, MiCS@Alg showed a more pronounced decline in subsequent cycles, particularly for NH_3 (92.2% → 70.8% for MiCS vs. 88.2% → 68.8% for MiCS@Alg), corresponding to an overall capacity loss of 30–40% after five cycles, which indicates limited long-term regenerability, especially for MiCS@Alg. These results suggest that, although alginate contributes to forming a more mechanically stable composite, it may restrict the accessibility of active sites and reduce the overall efficiency of the adsorption–desorption process. MiCS, in contrast, retained a more stable capacity in the initial cycles, highlighting the advantage of the unmodified sorbent in maintaining accessible active sites. Comparable desorption values for BY28 dye from a natural-origin sorbent were reported in the study by [23], where desorption efficiencies of about 98–99% were achieved after the first and second cycles.

3.5. Bed Column Study

To evaluate the adsorption performance of MiCS@Alg in a flow system, it is essential to conduct adsorption experiments beyond batch tests. The maximum adsorption capacity (q_{exp}, mg g^{-1}) for each pollutant was calculated based on the number of bed volumes processed until the concentration in the effluent exceeded the maximum permissible concentration (MPC), which is controlled by COD determination (Section 2.4. Characterization and analysis). Data analysis was simplified by applying the Bohart–Adams and Yoon–Nelson models [33], which assume that adsorption kinetics control the rate-limiting step and are valid only for single-component systems. The test solution was prepared by passing either BR2 and BY28 dyes, or ammonia at a concentration of 5 mg L^{-1} to model water, adjusted to pH 7.5 for the dyes and pH 4 for ammonia. This solution was then passed through the column at controlled flow rates of 0.5, 1.0, and 1.5 mL min^{-1}. Effluent samples were collected at set intervals to measure the concentration of dyes and NH_3. The obtained results are presented in Table 5 and Figure S4.

The results obtained from the fixed-bed column tests (Table 5) indicate that MiCS@Alg performs effectively across all the pollutants studied. In similar tests carried out with a flow rate of 3 mL min^{-1} and an initial contaminant concentration of 5 mg L^{-1} (yielding an EBCT of 1.66 min), the observed adsorption capacities were 88.3 mg g^{-1} for BR2, 49.4 mg g^{-1} for BY28, and 33.2 mg g^{-1} for ammonia. These findings demonstrate that shorter residence times within the column result in lower adsorption capacities for each of the tested substances. The concentration of pollutants in the influent also plays a critical role in adsorption efficiency; lower feed concentrations were associated with increased adsorption capacities, improving by roughly 7–16%. This behavior underscores the potential of MiCS@Alg in treating drinking water, particularly at lower contaminant levels where the system operates on the initial, more efficient portion of the adsorption isotherm. The material’s high porosity and favorable surface properties contribute to reduced internal mass transfer resistance, making adsorption sites more readily accessible.

Table 5. B-A and Y–N fitting for BR2, BY28, and NH_3 adsorption onto MiCS@Alg ($Ci_{[BR2]}$ = $Ci_{[BY28]}$ = $Ci_{[NH3]}$ = 5.0 mg dm^{-3}, m_{ads} = 570 mg, T = 25 °C).

Model and Parameters		Pollutant	Q (cm^3 min^{-1})		
			0.5	1.0	1.5
B-A	K_{BA} (dm^3 mg^{-1} min^{-1})	BR2	0.0360 ± 0.0002	0.0703 ± 0.0006	0.109 ± 0.0012
	q_o (mg g^{-1})		147.6 ± 0.19	122.8 ± 0.25	100.1 ± 0.30
	R^2		0.999	0.999	0.993
	K_{BA} (dm^3 mg^{-1} min^{-1})	BY28	0.0409 ± 0.0005	0.0949 ± 0.0023	0.138 ± 0.0017
	q_o (mg g^{-1})		94.71 ± 0.32	77.02 ± 0.44	61.58 ± 0.26
	R^2		0.998	0.998	0.998
	K_{BA} (dm^3 mg^{-1} min^{-1})	NH_3	0.0665 ± 0.0008	0.130 ± 0.0024	0.216 ± 0.0047
	q_o (mg g^{-1})		47.28 ± 0.18	43.19 ± 0.28	37.51 ± 0.29
	R^2		0.999	0.999	0.998
Y-N	k_{YN} (min^{-1})	BR2	0.360 ± 0.0025	0.351 ± 0.0032	0.344 ± 0.0040
	θ (min)		16.83 ± 0.022	13.99 ± 0.050	11.42 ± 0.034
	R^2		0.999	0.999	0.999
	k_{YN} (min^{-1})	BY28	0.409 ± 0.0054	0.475 ± 0.0099	0.480 ± 0.0001
	θ (min)		10.80 ± 0.036	8.78 ± 0.069	7.02 ± 0.0003
	R^2		0.999	0.999	0.999
	k_{YN} (min^{-1})	NH_3	0.665 ± 0.00001	0.668 ± 0.012	0.719 ± 0.0056
	θ (min)		5.39 ± 0.00001	4.92 ± 0.031	4.27 ± 0.032
	R^2		0.999	0.998	0.998

3.6. Comparative Overview of Adsorption Data

Based on the data in Table S5 and previously reported studies, the adsorbents investigated in this work can be classified among materials with relatively high adsorption capacities. Notably, isolated melanin and sodium–alginate beads containing melanin (MiCS and MiCS@Alg) have not, to the best of our knowledge, been reported in the available literature for the removal of such cationic pollutants. These materials are particularly attractive because of their low cost, ready availability, and inherent biodegradability. MiCS exhibits a higher adsorption capacity than conventional activated carbon derived from horse chestnut (≈169 mg g^{-1}; [41]) and citric-acid-modified corn stalk (~200 mg g^{-1}; [42]) but lower than the highest values reported for $ZnCl_2$-activated chestnut shell [43] (≈1.1–1.4 g g^{-1}) and for the chestnut–snail shell composite MCS3-1 (up to 1.6 g g^{-1}; [44]). For ammonia (NH_3), MiCS shows a markedly lower capacity (≈73 mg g^{-1}), as expected from the different binding mechanism compared with cationic dyes. The encapsulation of melanin in sodium–alginate beads further decreases the adsorption capacity (e.g., from 300 to 189 mg g^{-1} for BR2) but produces a striking enhancement in adsorption kinetics. The pseudo-second-order rate constant (k_2) for BR2 increases from 0.0031 g mg^{-1} min^{-1} for MiCS to as high as 5.79 g mg^{-1} min^{-1} for MiCS@Alg-several orders of magnitude faster than most reported sorbents, including citric-acid-modified corn stalk (maximum 8.7 g mg^{-1} min^{-1} at elevated temperatures). Typical k_2 values for comparable sorbents fall in the 10^{-4}–10^{-3} g mg^{-1} min^{-1} range (e.g., chestnut–snail composite 1.25×10^{-4} [40]; almond–walnut 9.16×10^{-4}, [45]; Elaeagnus 1.26×10^{-4}, [46]). Within Table S5, the highest adsorption capacity is again observed for the chestnut–snail composite (MCS3-1), reaching ~1.6 g g^{-1} for cationic dye removal, followed by $ZnCl_2$-activated chestnut (1.1–1.4 g g^{-1}). The lowest value is recorded for MiCS toward ammonia, at ~73 mg g^{-1}. This range highlights both the exceptional performance of the chestnut snail composite and the expected limitation of MiCS when targeting non-aromatic, anionic pollutants, such as ammonia.

Regarding selectivity, MiCS exhibits excellent affinity for cationic dyes but lower affinity for ammonia, indicating that adsorption is primarily governed by electrostatic interactions and π–π stacking between the aromatic dye rings and the melanin structure. A slight increase in qmax with temperature (25–45 °C) follows the trend reported for $ZnCl_2$-activated chestnut and other carbonized materials.

Overall, the results summarized in Table S5 demonstrate that MiCS@Alg, particularly in the form of alginate beads, offers a competitive, rapid, and environmentally friendly approach for treating dye-contaminated and ammonium-rich wastewaters, even though its maximum capacity is lower than commercial activated carbons having high surface areas.

4. Conclusions

In this study, produced MiCS and MiCS@Alg, derived from chestnut shells, were successfully used as efficient adsorbents for the cationic dyes BR2 and BY28 and NH_3. Utilizing waste chestnut shells treated with environmentally friendly extraction and modification procedures, the melanin-based materials exhibited functional groups capable of removing cationic pollutants from aqueous solutions. Characterization results revealed significant changes in the structure and morphology of MiCS during the purification and encapsulation process in MiCS@Alg. The isolated melanin particles demonstrated improved adsorption efficiency compared to raw chestnut shell particles, which can be attributed to their smaller size and higher negative zeta potential (−36.6 ± 2.9 mV at pH 10.5). DLS measurements showed that the average particle size of iCS was 786 nm at pH 5.8, whereas MiCS measured 612 nm at pH 10.5. The process was found to be low endothermic and spontaneous, with maximum adsorption capacities of 300.2 mg g^{-1} (BR2), 201.5 mg g^{-1} (BY28) and 73.08 mg g^{-1} (NH_3) on MiCS, and 189.3 mg g^{-1} (BR2), 117.1 mg g^{-1} (BY28) and 50.06 mg g^{-1} (NH_3) on MiCS@Alg at 45 °C, as determined using the Langmuir model. Thermodynamic, kinetic, and mechanistic studies indicated a complex adsorption process, primarily governed by electrostatic interactions between the negatively charged functional groups of melanin and the cationic dyes. Positive enthalpy values (ΔH^{Θ} = 2.50–7.77 kJ mol^{-1}) suggest that adsorption is mildly endothermic, while negative Gibbs free energy values (ΔG^{Θ} from −33 to −43 kJ mol^{-1}) confirm that the process is spontaneous and feasible, with spontaneity generally increasing with temperature. Additionally, positive entropy values (ΔS^{Θ} = 119.3–157.9 J mol^{-1} K^{-1}) indicate an increase in randomness at the solid–solution interface, likely due to structural rearrangements and solvent molecule release during adsorption. The results obtained from the fixed-bed column tests indicate that MiCS@Alg performs effectively across all the pollutants studied. The materials also demonstrated good reusability over multiple adsorption–desorption cycles, maintaining significant adsorption efficiency, highlighting their potential for sustainable water treatment applications.

Supplementary Materials: The following supporting information can be downloaded at: https://www.mdpi.com/article/10.3390/pr13103314/s1. Table S1. Adsorption experiments template; Table S2. Elemental data of chestnut shell and MiCS; Table S3. Total basic, total acidic, and carboxyl groups content in iMC and MiCS; Table S4. The results from five adsorption–desorption cycles for BR2, BY28 and NH3 (Ci = 30 mg L^{-1}, m = 0.1 g, Q = 1.0 mL min^{-1}, T = 25 °C); Table S5. Overview of adsorption performance of literature data related to bio-based adsorbents; Figure S1. Influences of pH on dyes and ammonia removal using MiCS and MiCS@Alg adsorbents (Ci = 30 mg L^{-1}, m = 1 mg, V = 8 mL, T = 25 °C, t = 90 min); Figure S2. Langmuir and Freundlich model fitting for the removal of pollutants onto both sorbents at different temperatures (Ci = 30 mg L^{-1}, m = 1–10 mg, V = 8 mL, T = 25 °C, 35 °C, and 45 °C, t = 90 min); Figure S3. The schematic presentation of the most plausible adsorption mechanism; Figure S4. B-A and Y–N fitting for BR2, BY28, and

NH_3 adsorption onto MiCS@Alg (Ci[BR2)] = Ci[BY28] = Ci[NH3] = 5.0 mg dm^{-3}, mads = 570 mg, T = 25 °C). References [14,25,27,41–67] are cited in the supplementary materials.

Author Contributions: Conceptualization, A.A., M.M. and A.D.M.; methodology, A.D.M., N.Đ.K. and G.C.; software, N.Đ.K. and B.S.; validation, A.D.M. and M.M.; formal analysis, K.S. and N.Đ.K.; investigation, A.A. and N.Đ.K.; resources, A.D.M. and M.M.; data curation, N.Đ.K., B.S. and K.S.; writing—original draft preparation, A.A., N.Đ.K., A.D.M., K.S. and M.M.; writing—review and editing, all authors; visualization, N.Đ.K. and B.S.; supervision, A.D.M., M.M. and N.Đ.K.; project administration, A.D.M.; funding acquisition, A.D.M. and M.M. All authors have read and agreed to the published version of the manuscript.

Funding: This work was supported by the Ministry of Science, Technological Development and Innovation of the Republic of Serbia (Contract No. 451-03-136/2025-03/200026, 451-03-136/2025-03/200135, 451-03-136/2025-03/200017), and the Institute of Physics Belgrade. This research aligns with the Agenda 2030—United Nations Sustainable Development Goal 6, promoting clean water and sanitation (Ensure availability and sustainable management of water and sanitation for all).

Data Availability Statement: The original contributions presented in this study are included in the article/Supplementary Materials. Further inquiries can be directed to the corresponding author.

Conflicts of Interest: The authors declare no conflicts of interest.

References

1. Chang, P.-H.; Liu, P.; Sarkar, B.; Mukhopadhyay, R.; Yang, Q.-Y.; Tzou, Y.-M.; Zhong, B.; Li, X.; Owens, G. Unravelling the Mechanism of Amitriptyline Removal from Water by Natural Montmorillonite through Batch Adsorption, Molecular Simulation and Adsorbent Characterization Studies. *J. Colloid Interface Sci.* **2021**, *598*, 379–387. [CrossRef]
2. Knežević, N.; Milanović, J.; Veličković, Z.; Milošević, M.; Vuksanović, M.M.; Onjia, A.; Marinković, A. A Closed Cycle of Sustainable Development: Effective Removal and Desorption of Lead and Dyes Using an Oxidized Cellulose Membrane. *J. Ind. Eng. Chem.* **2023**, *126*, 520–536. [CrossRef]
3. United Nations Children's Fund (UNICEF); World Health Organization (WHO). *Joint Monitoring Programme for Water Supply, Sanitation and Hygiene*; WHO: Geneva, Switzerland; UNICEF: New York, NY, USA, 2023; ISBN 9789280654769.
4. Yaseen, D.A.; Scholz, M. Textile Dye Wastewater Characteristics and Constituents of Synthetic Effluents: A Critical Review. *Int. J. Environ. Sci. Technol.* **2019**, *16*, 1193–1226. [CrossRef]
5. da Gama, B.M.V.; Silanpää, M.; Selvasembian, R.; de Farias Silva, C.E.; Meili, L. Effective Adsorptive Removal of a Cationic Dye from Aqueous Solutions Using a Biosorbent Derived from *Sargassum* sp. *Water Pract. Technol.* **2024**, *19*, 263–280. [CrossRef]
6. Bahsaine, K.; Benzeid, H.; Zari, N.; Qaiss, A.e.K.; Bouhfid, R. Biochar-Alginate Beads Derived from Argan Nutshells for Effective Methylene Blue Removal: A Sustainable Approach to Wastewater Treatment. *Int. J. Biol. Macromol.* **2024**, *282*, 136853. [CrossRef]
7. Sadiq, M.U.; Shah, A.; Nisar, J.; Shah, I. Photoelectrocatalytic Detection and Degradation Studies of a Hazardous Textile Dye Safranin T. *Nanomaterials* **2023**, *13*, 2218. [CrossRef] [PubMed]
8. Budak, T.B. Adsorption of Basic Yellow 28 and Basic Blue 3 Dyes from Aqueous Solution Using Silybum Marianum Stem as a Low-Cost Adsorbent. *Molecules* **2023**, *28*, 6639. [CrossRef] [PubMed]
9. Boopathy, R.; Karthikeyan, S.; Mandal, A.B.; Sekaran, G. Adsorption of Ammonium Ion by Coconut Shell-Activated Carbon from Aqueous Solution: Kinetic, Isotherm, and Thermodynamic Studies. *Environ. Sci. Pollut. Res.* **2013**, *20*, 533–542. [CrossRef]
10. Han, B.; Butterly, C.; Zhang, W.; He, J.; Chen, D. Adsorbent Materials for Ammonium and Ammonia Removal: A Review. *J. Clean. Prod.* **2021**, *283*, 124611. [CrossRef]
11. Chen, Y.; Xiong, C.; Nie, J. Removal of Ammonia Nitrogen from Wastewater Using Modified Activated Sludge. *Pol. J. Environ. Stud.* **2016**, *25*, 419–425. [CrossRef]
12. Liu, Z.-F.; Liu, Z.-J.; Qie, L.-M.; Yao, Z.-Y. Effects of Melanin Extraction on Biosorption Behavior of Chestnut Shells Towards Methylene Blue. *Water Conserv. Sci. Eng.* **2021**, *6*, 163–173. [CrossRef]
13. Khalla, D.; Belguidoum, K.; Nacef, M.; Boukour, M.; Chelaghmia, M.L.; Khelifi, O.; Selaimia, R.; Bengourna, N.; Affoune, A.M.; Amira-Guebailia, H. Competitive Adsorption of Quinary Heavy Metal Ions onto Chestnut Shell Activated Carbon. *Mater. Chem. Phys.* **2024**, *323*, 129646. [CrossRef]
14. Çitlacifci, H.; Pekgözlü, A.K.; Gülsoy, S.K. Characterization of Cheestnut Shell. *Bartın Univ. Int. J. Nat. Appl. Sci.* **2022**, *5*, 145–150. [CrossRef]

15. Paudyal, H.; Pangeni, B.; Inoue, K.; Kawakita, H.; Ohto, K.; Ghimire, K.N.; Alam, S. Preparation of Novel Alginate Based Anion Exchanger from Ulva Japonica and Its Application for the Removal of Trace Concentrations of Fluoride from Water. *Bioresour. Technol.* **2013**, *148*, 221–227. [CrossRef]
16. Cao, L.; Lu, W.; Mata, A.; Nishinari, K.; Fang, Y. Egg-Box Model-Based Gelation of Alginate and Pectin: A Review. *Carbohydr. Polym.* **2020**, *242*, 116389. [CrossRef] [PubMed]
17. Yan, F.; Chen, H.; Chi, T.; Lu, J.; Shen, X.; Xie, F.; Wang, P.; Zhang, Z. Highly Efficient and Regenerable Amine-Impregnated Adsorbents: Mechanistic Insights into Glycerol Modification for Enhanced Direct Air Capture. *Chem. Eng. J.* **2025**, *520*, 166450. [CrossRef]
18. Filatova, A.V.; Azimova, L.B.; Djurabaev, D.T.; Radjabov, O.I.; Otajonov, A.Y.; Yakubova, R.A. Technology for Obtaining Melanin from the Shells of Horse Chestnut (*Aesculus hippocastanum* L.), Studying Its Composition. *BIO Web Conf.* **2024**, *113*, 03001. [CrossRef]
19. Zou, Y.; Hu, W.; Ma, K.; Tian, M. Fermentative Production of Melanin by the Fungus *Auricularia auricula* Using Wheat Bran Extract as Major Nutrient Source. *Food Sci. Technol. Res.* **2017**, *23*, 23–29. [CrossRef]
20. Yan, Y.; An, Q.; Xiao, Z.; Zheng, W.; Zhai, S. Flexible Core-Shell/Bead-like Alginate@PEI with Exceptional Adsorption Capacity, Recycling Performance toward Batch and Column Sorption of Cr(VI). *Chem. Eng. J.* **2017**, *313*, 475–486. [CrossRef]
21. Jovanović, A.; Stevanović, M.; Barudžija, T.; Cvijetić, I.; Lazarević, S.; Tomašević, A.; Marinković, A. Advanced Technology for Photocatalytic Degradation of Thiophanate-Methyl: Degradation Pathways, DFT Calculations and Embryotoxic Potential. *Process Saf. Environ. Prot.* **2023**, *178*, 423–443. [CrossRef]
22. Mahvi, H.; Bazrafshan, E.; Jahed, G.R. Evaluation of COD Determination by ISO, 6060 Method, Comparing with Standard Method (5220, B). *Pak. J. Biol. Sci.* **2005**, *8*, 892–894. [CrossRef]
23. Bradstreet, R.B. Kjeldahl Method for Organic Nitrogen. *Anal. Chem.* **1954**, *26*, 185–187. [CrossRef]
24. Hardieka, A.M.; Budak, T.B. Investigation of Removing Basic Yellow 28 and Basic Blue 3 Dyes from Water Using Mulberry Leaves (*Morus nigra* L.) and Assessment of Ultrasonic Effects. *Molecules* **2025**, *30*, 3539. [CrossRef]
25. Yao, Z.; Qi, J.; Wang, L. Isolation, Fractionation and Characterization of Melanin-like Pigments from Chestnut (*Castanea mollissima*) Shells. *J. Food Sci.* **2012**, *77*, C671–C676. [CrossRef] [PubMed]
26. Costa, T.G.; Younger, R.; Poe, C.; Farmer, P.J.; Szpoganicz, B. Studies on Synthetic and Natural Melanin and Its Affinity for Fe(III) Ion. *Bioinorg. Chem. Appl.* **2012**, *2012*, 712840. [CrossRef]
27. Popovic, A.L.; Rusmirovic, J.D.; Velickovic, Z.; Kovacevic, T.; Jovanovic, A.; Cvijetic, I.; Marinkovic, A.D. Kinetics and Column Adsorption Study of Diclofenac and Heavy-Metal Ions Removal by Amino-Functionalized Lignin Microspheres. *J. Ind. Eng. Chem.* **2021**, *93*, 302–314. [CrossRef]
28. Sun, X.-F.; Sun, R.; Sun, J.-X. Acetylation of Rice Straw with or without Catalysts and Its Characterization as a Natural Sorbent in Oil Spill Cleanup. *J. Agric. Food Chem.* **2002**, *50*, 6428–6433. [CrossRef] [PubMed]
29. Kocer, S.; Utku Copur, O.; Ece Tamer, C.; Suna, S.; Kayahan, S.; Uysal, E.; Cavus, S.; Akman, O. Optimization and Characterization of Chestnut Shell Pigment Extract Obtained Microwave Assisted Extraction by Response Surface Methodology. *Food Chem.* **2024**, *443*, 138424. [CrossRef]
30. Chkirida, S.; Zari, N.; Achour, R.; Hassoune, H.; Lachehab, A.; Qaiss, A.e.K.; Bouhfid, R. Highly Synergic Adsorption/Photocatalytic Efficiency of Alginate/Bentonite Impregnated TiO2 Beads for Wastewater Treatment. *J. Photochem. Photobiol. A Chem.* **2021**, *412*, 113215. [CrossRef]
31. Ballard, M.; Shafiee, A.; Grage, E.; DeMarco, M.; Atala, A.; Ghadiri, E. Inkjet Printing of Synthesized Melanin Nanoparticles as a Biocompatible Matrix for Pharmacologic Agents. *Nanomaterials* **2020**, *10*, 1840. [CrossRef]
32. Rajagopal, K.; Kathiravan, G.; Karthikeyan, S. Extraction and Characterization of Melanin from Phomopsis: A Phellophytic Fungi Isolated from Azadirachta Indica A. *Juss. Afr. J. Microbiol. Res.* **2011**, *5*, 762–766. [CrossRef]
33. Aqlinia, M.; Astuti, R.I.; Prastya, M.E.; Wahyudi, A.T. Antioxidant Potential of Melanin Pigment from Marine Sponge-Associated Actinomycete *Micromonospora* sp. *J. Appl. Pharm. Sci.* **2025**, *15*, 212–224. [CrossRef]
34. Foo, K.Y.; Hameed, B.H. Insights into the Modeling of Adsorption Isotherm Systems. *Chem. Eng. J.* **2010**, *156*, 2–10. [CrossRef]
35. Filipkowska, U.; Kuczajowska-Zadrożna, M.; Jóźwiak, T.; Szymczyk, P.; Kaczyński, A. Adsorption of Basic Yellow 28 (BY 28) and Acid Yellow 23 (AY 23) Dyes onto Chitin. *Prog. Chem. Appl. Chitin Deriv.* **2015**, *XX*, 34–42. [CrossRef]
36. Hu, Q.H.; Qiao, S.Z.; Haghseresht, F.; Wilson, M.A.; Lu, G.Q. Adsorption Study for Removal of Basic Red Dye Using Bentonite. *Ind. Eng. Chem. Res.* **2006**, *45*, 733–738. [CrossRef]
37. Gubitosa, J.; Cignolo, D.; Lotito, S.; Fini, P.; Milella, A.; Perrotta, A.; Cosma, P.; Rizzi, V. Physical and Chemical Parameters Driving the Direct Blue-78 Adsorption from Water Using Chitosan/ZnO Hybrid Sponges Engineered via Atomic Layer Deposition. *ACS Omega* **2025**, *10*, 33897–33909. [CrossRef]
38. Bugarčić, M.; Lopičić, Z.; Šoštarić, T.; Marinković, A.; Rusmirovic, J.D.; Milošević, D.; Milivojević, M. Vermiculite Enriched by Fe(III) Oxides as a Novel Adsorbent for Toxic Metals Removal. *J. Environ. Chem. Eng.* **2021**, *9*, 106020. [CrossRef]

39. Rahimi, S.M.; Ramavandi, B.; Moslehi, M.H.; Rahiminia, M.; Nasseh, N. Application of $CuFe_2O_4$/CuS as a New Green Magnetic Nanocomposite in Adsorption of Tetracycline from Aqueous Solutions: Mathematical Models of Thermodynamics, Isotherms, and Kinetics. *Appl. Water Sci.* **2025**, *15*, 6. [CrossRef]
40. Knežević, N.; Vuksanović, M.M.; Banjanac, K.; Pantić, K.; Veličković, Z.; Cvijetić, I.; Marinković, A.; Milošević, M. Cationic Waste Hemp Fibers-Based Membrane: Case Study of Anionic Pollutants Removal through Environmentally Friendly Processes. *J. Environ. Manag.* **2024**, *371*, 123174. [CrossRef]
41. Momcilovic, M.; Purenovic, M.; Miljkovic, M.; Bojic, A.; Randjelovic, M. Adsorption of Cationic Dye Methylene Blue onto Activated Carbon Obtained from Horse Chestnut Kernel. *Hem. Ind.* **2011**, *65*, 123–129. [CrossRef]
42. Soldatkina, L.; Yanar, M. Equilibrium, Kinetic, and Thermodynamic Studies of Cationic Dyes Adsorption on Corn Stalks Modified by Citric Acid. *Colloids Interfaces* **2021**, *5*, 52. [CrossRef]
43. Kong, L.; Zhang, M. Adsorption of Methylene Blue on Chestnut Shell-Based Activated Carbon: Calculation of Thermodynamic Parameters for Solid–Liquid Interface Adsorption. *Catalysts* **2022**, *12*, 813. [CrossRef]
44. An, J.; Nhung, N.T.H.; Ding, Y.; Chen, H.; He, C.; Wang, X.; Fujita, T. Chestnut Shell-Activated Carbon Mixed with Pyrolytic Snail Shells for Methylene Blue Adsorption. *Materials* **2022**, *15*, 8227. [CrossRef]
45. Rial, A.; Pimentel, C.H.; Gómez-Díaz, D.; Freire, M.S.; González-Álvarez, J. Evaluation of Almond Shell Activated Carbon for Dye (Methylene Blue and Malachite Green) Removal by Experimental and Simulation Studies. *Materials* **2024**, *17*, 6077. [CrossRef]
46. Geçgel, Ü.; Üner, O.; Gökara, G.; Bayrak, Y. Adsorption of Cationic Dyes on Activated Carbon Obtained from Waste *Elaeagnus* Stone. *Adsorpt. Sci. Technol.* **2016**, *34*, 512–525. [CrossRef]
47. Koromilas, N.D.; Anastasopoulos, C.; Oikonomou, E.K.; Kallitsis, J.K. Preparation of Porous Polymeric Membranes Based on a Pyridine Containing Aromatic Polyether Sulfone. *Polymers* **2019**, *11*, 59. [CrossRef] [PubMed]
48. Batinić, P.; Jovanović, A.; Stojković, D.; Čutović, N.; Cvijetić, I.; Gašić, U.; Carević, T.; Zengin, G.; Marinković, A.; Marković, T. A Novel Source of Biologically Active Compounds—The Leaves of Serbian Herbaceous Peonies. *Saudi Pharm. J.* **2024**, *32*, 102090. [CrossRef]
49. FAO/IAEA. 2000. Available online: https://www.scienceopen.com/book?vid=e26b5125-3459-484c-bda9-fe5fa58477e2 (accessed on 1 October 2025).
50. Durán-Lara, E.F.; López-Cortés, X.A.; Castro, R.I.; Avila-Salas, F.; González-Nilo, F.D.; Laurie, V.F.; Santos, L.S. Experimental and Theoretical Binding Affinity between Polyvinylpolypyrrolidone and Selected Phenolic Compounds from Food Matrices. *Food Chem.* **2015**, *168*, 464–470. [CrossRef] [PubMed]
51. Mertoglu Elmas, G.; Yilgor, N. Chemical and Thermal Characterizations of Pinus Sylvestris and Pinus Pinaster. *BioResources* **2020**, *15*, 3604–3620. [CrossRef]
52. Rowell, R.M. *Handbook of Wood Chemistry and Wood Composites*, 2nd ed.; CRC Press: Boca Raton, FL, USA, 2012; ISBN 9781439853818.
53. TAPPI. **T 222 om-06: Acid-Insoluble Lignin in Wood and Pulp**; TAPPI Press: Atlanta, GA, USA, 2006.
54. Sluiter, A.; Hames, B.; Ruiz, R.; Scarlata, C.; Sluiter, J.; Templeton, D.; Crocker, D. Determination of Structural Carbohydrates and Lignin in Biomass. *Lab. Anal. Proced.* **2008**, *1617*, 1–6.
55. *ASTM D-1166–84*; American Society for Testing and Materials (ASTM). Standard Test Method for Methoxyl Groups in Wood and Related Materials. American Society for Testing and Materials (ASTM): West Conshohocken, PA, USA, 2013.
56. Milošević, D.L.; Tomić, N.Z.; Đokić, V.R.; Vidović, M.M.; Veličković, Z.S.; Jančić-Heinemann, R.; Marinković, A.D. Structural and Surface Modification of Highly Ordered Alumina for Enhanced Removal of Pb^{2+}, Cd^{2+} and Ni^{2+} from Aqueous Solution. *Desalination Water Treat.* **2020**, *178*, 220–239. [CrossRef]
57. Serrano, L.; Esakkimuthu, E.S.; Marlin, N.; Brochier-Salon, M.C.; Mortha, G.; Bertaud, F. Fast, Easy, and Economical Quantification of Lignin Phenolic Hydroxyl Groups: Comparison with Classical Techniques. *Energy Fuels* **2018**, *32*, 5969–5977. [CrossRef]
58. Guo, L.; Li, W.; Gu, Z.; Wang, L.; Guo, L.; Ma, S.; Li, C.; Sun, J.; Han, B.; Chang, J. Recent Advances and Progress on Melanin: From Source to Application. *Int. J. Mol. Sci.* **2023**, *24*, 4360. [CrossRef] [PubMed]
59. Sansinenea, E.; Ortiz, A. Melanin: A Photoprotection for Bacillus Thuringiensis Based Biopesticides. *Biotechnol. Lett.* **2015**, *37*, 483–490. [CrossRef]
60. Zhang, H.; Liu, Y.; Wu, X.; Jin, X.; Zhang, Z.; Zhao, H.; Liu, J.; Huang, Z.; Fang, M.; Min, X. Kinetics and Equilibrium Studies of the Adsorption of Methylene Blue on Euryale Ferox Shell-based Activated Carbon. *Micro Nano Lett.* **2018**, *13*, 552–557. [CrossRef]
61. Doğan, M.; Abak, H.; Alkan, M. Adsorption of Methylene Blue onto Hazelnut Shell: Kinetics, Mechanism and Activation Parameters. *J. Hazard. Mater.* **2009**, *164*, 172–181. [CrossRef]
62. Selengil, U.; Yildiz, D.; Tan, B. Adsorption of deep red on ac prepared from chestnut shell. *Bartın Univ. Int. J. Nat. Appl. Sci.* **2023**, *6*, 189–205. [CrossRef]
63. Hoc Thang, N.; Sy Khang, D.; Duy Hai, T.; Thi Nga, D.; Dinh Tuan, P. Methylene Blue Adsorption Mechanism of Activated Carbon Synthesised from Cashew Nut Shells. *RSC Adv.* **2021**, *11*, 26563–26570. [CrossRef]

64. Alkhabbas, M.; Al-Ma'abreh, A.M.; Edris, G.; Saleh, T.; Alhmood, H. Adsorption of Anionic and Cationic Dyes on Activated Carbon Prepared from Oak Cupules: Kinetics and Thermodynamics Studies. *Int. J. Environ. Res. Public Health* **2023**, *20*, 3280. [CrossRef]
65. Küçük, İ.; Önal, Y.; Başar, C. Ceviz Kabuğundan Karbon Dioksit Kullanılarak Aktif Karbon Üretimi ve Metilen Mavisi Adsorpsiyonu. *DÜMF Mühendislik Derg.* **2020**. [CrossRef]
66. Lv, X.; Zhou, X.; Yang, R.; Cai, D.; Ren, W. Enzymatic Modification of Walnut Shell for High-Efficiency Adsorptive Methylene Blue Removal. *Materials* **2025**, *18*, 3434. [CrossRef] [PubMed]
67. Hameed, B.H.; Krishni, R.R.; Sata, S.A. A Novel Agricultural Waste Adsorbent for the Removal of Cationic Dye from Aqueous Solutions. *J. Hazard. Mater.* **2009**, *162*, 305–311. [CrossRef] [PubMed]

Effect of gadolinium substitution on layer-structured Aurivillius $Bi_5Ti_3FeO_{15}$ ceramics

Jelena Bobić, Nikola Ilić, Robertas Grigalaitis, Aleksandar Radojković, Mirjana Vijatović Petrović, Saso Gyergyek, Ivan Stijepović, Bojan Stojadinović, Adis Dzunuzović, Algimantas Kežionis, Tomas Šalkus, Juras Banys

PII: S1002-0721(25)00265-0

DOI: https://doi.org/10.1016/j.jre.2025.07.017

Reference: JRE 2086

To appear in: *Journal of Rare Earths*

Received Date: 11 February 2025

Revised Date: 10 July 2025

Accepted Date: 17 July 2025

Please cite this article as: Bobić J, Ilić N, Grigalaitis R, Radojković A, Petrović MV, Gyergyek S, Stijepović I, Stojadinović B, Dzunuzović A, Kežionis A, Šalkus T, Banys J, Effect of gadolinium substitution on layer-structured Aurivillius $Bi_5Ti_3FeO_{15}$ ceramics, *Journal of Rare Earths*, https://doi.org/10.1016/j.jre.2025.07.017.

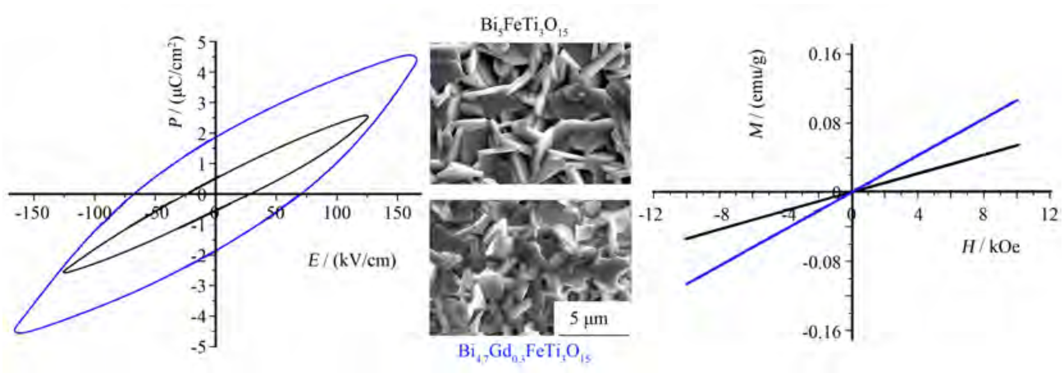
P / (μC/cm²)
5
4
3
2
1
0
-1
-2
-3
-4
-5
-150
-100
-50
0
50
100
150
E / (kV/cm)
Bi5FeTi3O15
5 μm
Bi4.7Gd0.3FeTi3O15
M / (emu/g)
0.16
0.08
0
-0.08
-0.16
-12
-8
-4
0
4
8
12
H / kOe

Effect of gadolinium substitution on layer-structured Aurivillius $Bi_5Ti_3FeO_{15}$ ceramics

Jelena Bobić[a], Nikola Ilić[b], Robertas Grigalaitis[c], Aleksandar Radojković[a], Mirjana Vijatović Petrović[a], Saso Gyergyek[d], Ivan Stijepović[e], Bojan Stojadinović[f], Adis Dzunuzović[a], Algimantas Kežionis[c], Tomas Šalkus[c], Juras Banys[c]

[a]*University of Belgrade, Institute for Multidisciplinary Research, 11000 Belgrade, Serbia*
[b]*Department of Atomic Physics, Vinca Institute of Nuclear Sciences, National Institute of the Republic of Serbia, University of Belgrade, 11000 Belgrade, Serbia*
[c]*Faculty of Physics, Institute of Applied Electrodynamics and Telecommunication, Vilnius University, LT-10257 Vilnius, Lithuania*
[d]*Department for Synthesis of Materials, Jožef Stefan Institute, SI-1000 Ljubljana, Slovenia*
[e]*Department of Materials Engineering, Faculty of Technology, University of Novi Sad, 21000 Novi Sad, Serbia*
[f]*Institute of Physics Belgrade, University of Belgrade, 11080 Belgrade, Serbia*

Abstract

Lately, considerable attention has been given to developing magnetoelectric-active materials in microelectronics and spintronics. Motivated by that, the influence of partial substitution of isovalent rare-earth gadolinium ions for bismuth in multiferroic four-layered Aurivillius $Bi_5FeTi_3O_{15}$ (BFT) compounds to improve magnetic and electric properties is reported in this work. Polycrystalline ceramics of Gd-doped BFT according to formula $Bi_{5-x}Gd_xFeTi_3O_{15}$ (x = 0, 0.1, 0.2, 0.3, 0.5, 1.0) were prepared by conventional solid-state reaction. Crystal structure, phase purity, and structural evaluation were investigated via X-ray diffraction, Rietveld refinement, and Raman spectroscopy. Scanning electron microscopy (SEM) images show a significant influence of Gd content on microstructure, and it is found that x=0.3 is a critical amount of Gd that affects the grain growth dynamics. Ferroelectric measurements show unsaturated leaky hysteresis loops in all samples, still showing a slight improvement of ferroelectric properties by low-level Gd substitution and their breakdown strength is enhanced. Magnetic measurements confirm the paramagnetic nature of BFT ceramics with the nonlinear, hysteretic behavior at 5 K in the sample with the highest Gd substitution level. Dielectric properties were investigated in various temperatures (300–1000 K) and frequencies (1 Hz–1 MHz). At temperatures above 990 K, a jump in the real part of the dielectric permittivity, related to the ferroelectric phase transition, appears and moves slightly toward higher temperatures with the increase of Gd content.

Keywords: Aurivillius structure, Gd^{3+} doping, Ferroelectrics, Magnetic properties, Dielectrics, Rare earths

☆ **Foundation item:** Project supported by the Ministry of Science, Technological Development and Innovation Republic of Serbia (451-03-136/2025-03/200053) and the Science Fund of the Republic of Serbia (PRIZMA, Grant No. 7383).

***Corresponding author.** E-mail address: jelena@imsi.rs (J.D. Bobic)

1. Introduction

Multiferroic materials are still attracting extensive attention because they offer prospective opportunities for multifunctional applications in modern technology, such as high-energy density capacitors, spintronic devices, and gas sensing applications [1, 2]. The coupling between ferromagnetism and ferroelectricity in multiferroics can produce attractive phenomena, such as the magnetodielectric (MD) and magnetoelectric (ME) effects.

$BiFeO_3$ is a unique single-phase multiferroic material due to its simultaneous ferroelectric (with a Curie temperature of 825 °C) and magnetic (with a Néel temperature of 370 °C) properties at or above room temperature that could be utilized for information storage, processing and transmission [3]. On the other side, compounds based on the Aurivillius ferroelectric $Bi_4Ti_3O_{12}$ have been investigated as potential options for non-volatile ferroelectric random access memory (FRAM). This interest arises from their excellent fatigue resistance and significant ferroelectric spontaneous polarizations along the *a*-axis, with a Curie temperature of 675 °C [4, 5]. By integrating $BiFeO_3$ with $Bi_4Ti_3O_{12}$, a typical Aurivillius phase known as $Bi_5FeTi_3O_{15}$ (BFT) can be formed characterized by its four-layered structure and general formula $(Bi_2O_2)^{2+}(A_{m-1}B_mO_{3m+1})^{2-}$ (m is the number of octahedral layers in the perovskite slab). BFT structural transition at 730 °C from orthorhombic $A2_1am$ to tetragonal $I4/mmm$ without any intermediate state was reported in the literature [6, 7]. It possesses the ferroelectric transition temperature and antiferromagnetic (AFM) ordering with its Neel temperature (T_N) at –180 °C [8, 9].

Many papers deal with the magnetic properties of BFT, but their origin is still under debate. They are highly dependent on sample preparation conditions, such as synthesis method, starting materials and, sintering temperature [10], as well as on the presence of secondary phases that are usually hard to detect by a laboratory X-ray diffractometer [11, 12]. Some earlier reports suggest superparamagnetic (SPM) behaviors for BFT with local antiferromagnetic (AFM) interaction [13, 14], while Mao et al. [15] and Liu et al. [16] confirmed weak ferromagnetism (WFM) in the paramagnetic background. Weak ferromagnetism appears because of insufficient magnetic ordering of Fe ions and the short-range exchange interaction in the perovskite block, probably also due to the presence of non-magnetic $(Bi_2O_2)^{2+}$ layers [2, 12]. On the other hand, more recent studies reported paramagnetic behavior with no magnetic long-range ordering at very low temperatures [17, 18].

BFT allows different site substitutions that enable the development of ferroelectricity and magnetism, leading to improved material properties. The most commonly-used structural modifications to improve magnetic properties are B-site (Fe ions) substitutions with other magnetic elements such as Co, Mn, Ni, and Cr [11, 16, 19-21]. In most cases, the magnetic properties were improved, but electrical properties were compromised due to the multivalent nature of the transition metals.

The incorporation of rare-earth ions with numerous oxidation states at the A-site can introduce a degree of disorder within the crystal lattice, leading to distortions in the lattice structure and resulting in modifications in ferroelectric and magnetic properties [22-26]. The

Gd^{3+} ion is recognized for its highly localized f-electrons and possesses a considerable magnetic moment, in contrast to the diamagnetic Bi^{3+} ion [27]. Furthermore, the smaller ionic radius of Gd^{3+} compared to Bi^{3+} could lead to structural distortions within the Aurivillius lattice structure. To our knowledge, very few papers deal with the structural and magnetic properties of Gd-doped $Bi_5FeTi_3O_{15}$ ceramics [28, 29]. Still, not such attention has been given to the ferroelectric and dielectric properties. Koval et al. [28] claimed that substitution of Bi^{3+} ions by Gd^{3+} ions on A-sites of the perovskite-like slabs is not capable of inducing any magnetic ordering in the four-layer Aurivillius-type $Bi_{5-x}Gd_xFeTi_3O_{15}$, while Zuo et al. [29] confirmed that the substitution of Gd ions can effectively enhance the room-temperature ferromagnetism.

This work presents a comprehensive study of the influence of different concentrations of Gd on $Bi_{5-x}Gd_xFeTi_3O_{15}$ (x=0.0–1.0) structure, microstructure, dielectric, and magnetic properties. The optimal content of gadolinium that affected those properties was determined.

2. Experimental

The pure and doped BFT polycrystalline ceramics were synthesized using the conventional solid-state reaction method. Appropriate analytically pure oxide precursors TiO_2, Fe_2O_3, Bi_2O_3, and Gd_2O_3 (Alfa Aesar, 99% pure) were used. The initial components were measured in stoichiometric ratios based on the subsequent chemical equation: $Bi_{5-x}Gd_xFeTi_3O_{15}$, x = 0.1, 0.2, 0.3, 0.5, and 1, denoted as BFTG1, BFTG2, BFTG3, BFTG5, and BFTG10.Details about the procedure used for obtaining the final undoped and doped ceramic samples can be found in the previous publication of the authors [20]. The relative density of the fabricated ceramics was calculated geometrically.

The phase structure of the prepared ceramics was determined via a conventional X-ray diffractometer (Model XRD D5000, Siemens, Germany) with Cu Kα radiation, 2θ range between 20° and 70°, step size of 0.02° (2θ), divergence slit = 0.5 mm, receiving slit = 0.3 mm. The Rietveld refinement was performed using the FullProf Suite toolbar. The micro-Raman spectra were measured at room temperature using a Jobin Yvon T64000 spectrometer with a nitrogen-cooled CCD detector. The λ = 514.5 nm line of Ar^+/Kr^+ mixed laser was used as an excitation source, with the output laser power kept at less than 2 mW to avoid the heating effects and/or sample degradation. The Bose-Einstein thermal occupation factor corrected the Raman spectra. Natural surface micrographs were examined using a scanning electron microscope (Model Vega TS5130MM, Tescan, Czech Republic) and the images were analyzed by the ImageJ software. The electrodes were deposited by painting the appropriate pastes onto the ceramic samples, silver paste (7095 Silver conductor paste, DuPont, USA) for polarization measurements and platinum paste (71% Pt, Gwent Electronics Materials Ltd.) for dielectric measurements. The dielectric measurements were performed using a custom-made impedance spectrometer, in which the sample under investigation is a part of the coaxial line [30] in the 1 kHz–7.8 GHz frequency range and between 300 and 1070 K with 1 K accuracy. The precision multiferroic test system measured the polarization-electric field curves with High Voltage Interface-Radiant Technologies, Inc., applying up to 4000 V at room temperature and at different external electric fields. The remnant hysteresis technique was applied to measure the real ferroelectric contribution to the total polarization at zero electric field. Magnetic measurements of materials were carried out using a vibrating-sample magnetometer (7307 Series VSM, Lake Shore Cryotronics, USA).

3. Results and discussion

3.1. XRD analysis

As can be seen in Fig. 1, all diffraction peaks of the $Bi_{5-x}Gd_xFeTi_3O_{15}$ ceramic samples matched the diffraction data for the orthorhombic structure according to the JCPDS database (No. 89–8545) with space group of $A21am$. The small impurity peak at $2\theta = 27.8°$ (marked by an asterisk) was found in undoped BFT and the samples with less Gd (BFTG1, BGTG2, and BFTG3). Secondary phase formation may be linked to the development of intermediate compounds of the sillenite type ($Bi_{12}TiO_{20}$), which are crystalographically related to cubic γ-Bi_2O_3 [20]. With Gd concentration increasing above x=0.2, the impurity peak disappears, confirming the reduction of the secondary phase in the structure. The amount of secondary phase is estimated to be from 5.9 wt% to 8.0 wt% in the undoped sample and the samples with less amount of Gd.

Fig 1. XRD patterns of unmodified and Gd^{3+}-doped BFT ceramics with different substitution concentrations. The impurity peak was marked by an asterisk (*)

The lattice parameters for all samples are presented in Table 1. The cell parameter a decreases almost linearly with increasing content of Gd in the structure, while parameter b varies but still has a partially decreasing trend (Fig. 2). Along the c direction, the structure expands with increasing Gd content while both the unit cell volume (V) and orthorhombic distortion ($\delta = 2(a-b)/(a+b)$) are progressively reduced. Obviously, regarding the partial replacement of larger Bi^{3+} ions (0.117 nm) with smaller Gd^{3+} ions (0.105 nm), the increase in Gd content caused the shrinkage of the crystal lattice and a gradual reduction of orthorhombic distortion of the unit cell. The anomalous increase in unit cell volume for BFTG3 can be attributed to a combination of improved phase purity, more homogeneous Gd incorporation, reduced internal strain, and grain size effects. The transition from a more defective structure (with secondary phases) at lower doping levels to a purer phase for BFTG3 likely allows a temporary expansion of the unit cell before contraction resumes at higher Gd concentrations.

Table 1 Refined structural parameters (a, b, c), unit cell volume (V), density (D), orthorhombic distortion (δ), phase composition and number of grain per μm^2 of all samples.

Samples	a (nm)	b (nm)	c (nm)	V (nm^3)	D (%)	δ (10^{-3})	Phase fraction (wt%)	BFT Sec. phase	No. of grains/μm^2
BFT	0.5479	0.5452	4.1256	1.2325	91.4	6.0	91.4	5.9	1.106

BFTG1	0.5474	0.5444	4.1277	1.2301	94.5	5.4	93.4	6.6	0.961
BFTG2	0.5463	0.5439	4.1304	1.2274	97.6	4.4	92.0	8.0	0.950
BFTG3	0.5463	0.5444	4.1328	1.2292	97.5	3.5	97.3	2.7	1.300
BFTG5	0.5437	0.5451	4.1337	1.2252	95.7	2.4	97.9	2.1	0.883
BFTG10	0.5428	0.5443	4.1416	1.2236	93.6	2.9	97.4	2.6	1.040

Fig 2. (a) Rietveld plots for refinement of undoped BFT ceramics; (b) Gd-substitution-induced change of the structural parameters in $Bi_{5-x}Gd_xFeTi_3O_{15}$ ceramics.

3.2 Raman scattering

The Raman spectra of all prepared ceramic samples recorded at RT for a wavenumber from 30 to 1000 cm^{-1} are shown in Fig. 3. All peak positions are generally consistent with the spectra reported in the literature. The Raman studies of bismuth-based layered materials distinguished two parts in the vibrational spectra, below 200 cm^{-1}, which can be ascribed to the motions of heavy Bi ions at the A-site, while those above 200 cm^{-1} result from the torsion, bending, and stretching of the oxygen octahedra [31, 32]. It is well known that the bismuth layer-structured ferroelectrics (BLSFs) have two sites containing Bi^{3+}, with different coordination surroundings; the [Bi_2O_2] layer site is an 8-coordinate position, while the perovskite A-site adopts 12-coordination [33, 34]. The lowest frequency peak at about 57 cm^{-1} results from the vibrations of Bi^{3+} ions in $(Bi_2O_2)^{2-}$ layers. At the same time, modes between 90 and 150 cm^{-1} are closely associated with the vibrations of the Bi^{3+} ions on the A-site positions of the perovskite-like slabs [28].

Fig 3. Raman spectra collected from $Bi_{5-x}Gd_xFeTi_3O_{15}$ ceramics at room temperature

As shown in Fig. 3, the soft Raman modes 1 and 2 at 51.9 and 62.8 cm^{-1} in the BFT spectra change with Gd substitution, merging into a single mode at 58.7 cm^{-1} above x=0.3. However, these modes match the Raman modes of $Bi_{12}TiO_{20}$, which is a secondary phase detected in neat BFT and samples doped with Gd up to x=0.3 [35, 36]. In BFTG5 and BFTG10, the presence of one mode at 57 cm^{-1} confirms that the $Bi_{12}TiO_{20}$ phase is almost absent, following XRD data. These observations confirm that Gd substitution in the BFT lattice does not affect the fluorite-like Bi_2O_2 layers for all investigated concentrations of Gd and that this mode is associated with the vibrations of Bi^{3+} ions in $(Bi_2O_2)^{2-}$ layers. Similar results were obtained by Koval and co-authors [28].

Through the Raman spectra, it can be further noticed that the intensities of triplet modes 3, 4, and 5 that are closely linked with the vibrations of the Bi^{3+} ions on the A-site positions of the perovskite-like slabs [32] progressively decrease by Gd doping compared to neat BFT. This suggests that Gd^{3+} ions are replacing Bi^{3+} ions at the A-sites of the pseudo-perovskite layers. Having in mind that ferroelectricity in Aurivillius $Bi_5Ti_3FeO_{15}$ compounds originates, among others, from the stereochemical activity of lone pair electrons of Bi^{3+} ions [35], the most prominent Bi-site vibration mode nearly disappears, indicating that the suppression of the ferroelectric long-range ordering in BFT ceramics might occur with high-level doping with Gd.

The spectral modes 6 and 7 (223 and 264 cm^{-1}) are related to the Ti−O/Fe−O bending vibrations. Generally, mode 6 should be inactive if no distortion occurs in the TiO_6 octahedron [34]. However, it can be noticed that these phonon modes are slightly suppressed with increasing gadolinium content. This kind of change can be attributed to the decreasing tilting distortion of the $[Ti/Fe]O_6$ octahedra and, hence, the decrease of the orthorhombic distortion δ, confirmed by presented XRD data. The low-intensity modes around 332 and 461 cm^{-1} (referred to as modes 8 and 9) are assigned to the oscillations related to the ferroelectricity, movement, or vibration of Bi atoms on the A site in the pseudo-perovskite layers and the $(Bi_2O_2)^{2+}$ layers [28]. The intensities of these modes decrease upon Gd substitution, which indicates that substitution affects the bending of $(Ti/Fe)O_6$ octahedra.

Modes 10 and 11, appearing at 542 and 569 cm^{-1}, showed interesting changes with varying Gd^{3+} concentrations. Gd^{3+} substitution on the A-site leads to structural disorder, which results in progressive shifting and merging of these two modes in one at 562 cm^{-1} (as marked by the box). These results indicated that the increase of Gd^{3+} content in the perovskite layer reduced the Bi cation interactions with the TiO_6 octahedron unit, consequently affecting the local structure surroundings around $[Ti/Fe]O_6$ octahedron [37]. It has been noted that the doublet of peaks observed in Raman spectra that tends to merge into a single mode is often observed when the Bi ion is replaced by rare earth elements [38]. Modes 12 and 13, which correspond to the stretching of the FeO_6 and TiO_6 octahedra, respectively, are unaffected by the Gd^{3+} modification as expected.

Generally, Raman scattering is used to investigate the intrinsic physical behavior of materials. Specifically, many papers used Raman analysis to investigate complex Aurivillius structures. Chen and co-authors [39] investigated the La-doping on Bi^{3+} site in four- and five-BLSFs, namely $SrBi_4Ti_4O_{15}$, $Sr_2Bi_4Ti_5O_{18}$, and $Bi_4Ti_3O_{12}$-$SrBi_4Ti_4O_{15}$. They claimed, by Raman analysis, that the influence of La dopant on the Bi_2O_2 layers is negligible. In contrast, the influence on pseudoperovskite layers is significant when the dopant content is relatively low. Further, Osada and co-authors [40] reported that La occupies the perovskite A site of three-BLSFs $Bi_{4-x}La_xTi_3O_{12}$ samples with x less than 0.75. They claimed that La was incorporated in both the perovskite and Bi_2O_2 layers above this value. These reports witness the complexity of the structural changes induced by doping in a wide range of dopant concentrations that might reflect on the functional properties of this type of material.

3.3 Microstructure and morphology evaluation

Fig. 4 shows SEM images of free surfaces of all investigated compositions. Evidently, the ceramics are dense and show well-grown laminar grains with random orientations, which are unique microstructural features of Aurivillius compounds [41]. The density of neat BFT ceramic is 91.5% of the theoretical value. At the same time, Gd substitution improved the sintering behavior and, therefore, the relative densities of the samples are up to ~98% of the theoretical value for BFTG2 and BFTG3 samples (Table 1). SEM micrograph confirms that improvement. A particular lamellar morphology was formed due to the structurally highly anisotropic grain growth of the Aurivillius type of crystal structure, which had a much higher grain growth rate in the direction perpendicular to the *c*-axis than the *a*-*b* direction [5]. The micrographs of all samples revealed the dimensions of the grains up to 3–5 μm in width and 0.1 μm in thicknesses with the exception of the BFGT3 sample, which possessed significantly shorter grains up to 1 μm in length. This was confirmed by the ImageJ software by calculations of number of grains per μm^2 (presented in Table 1). This parameter was convenient to study since the shape of the grains significantly deviates from the spherical, and one can assess the grain boundary abundance per surface area that can influence the electrical properties. The BFTG3 sample contained obviously the largest number of grains/grain boundaries per surface area, while the other samples' grain number density follows no specific trend yielding around 1 grain per μm^2.

Fig 4. SEM images of the free surface of BFT (a), BFTG1 (b), BFTG2 (c), BFTG3 (d), BFTG5 (e) and BFTG10 (f) samples.

3.4 Ferroelectric properties

Generally, ferroelectricity in Aurivillius $Bi_5Ti_3FeO_{15}$ compounds originates from the rotation and tilting of TiO_6/FeO_6 octahedra, the stereochemical activity of lone pair electrons of Bi^{3+} ions and distorted $(Bi_2O_2)^{2+}$ layers [20]. As for the ferroelectric properties, the role of the Gd^{3+} differs at lower (up to *x*=0.3) and higher concentrations (over *x*=0.5), in general. It is more comprehensive by comparison of the hysteresis loops measured at the highest electric field for each sample (Fig. 5(a) and (b)). The light-doped samples (BFTG1, BFTG2, and BFTG3) could sustain higher electric fields than the undoped sample (130 kV/cm). Specifically, the BFTG1 and BFTG3 samples withstood the highest electric field (170 kV/cm). At that field, the hysteresis loops appeared wider, whereby the sample BFTG3 exhibited the optimal ferroelectric potential. On the other hand, the samples with higher amount of Gd^{3+} (the samples BFTG5 and BFTG10) showed no significant improvement of the ferroelectric properties, judging by their narrower hysteresis loops even at somewhat higher electric fields than that for the undoped sample.

In Fig. 5(c), by observing the leakage current profiles of all the samples expressed as a log*j*–log*E* plot, one can conclude that Gd^{3+} was ineffective in reducing leakage currents as assumed by replacing highly volatile Bi^{3+}, responsible for the occurrence of structural defects such as bismuth and oxygen ion vacancies. Again, the divide between the light and heavily doped samples concerning leakage properties is evident. The undoped sample exhibited the lowest conductivity, although within the same order of magnitude as the BFTG1, BFTG2, and BFTG3 samples. A significant increase in conductivity is yet present for the samples with higher Gd content (BFTG5 and BFTG10). Besides, we can see that all log*j*–log*E* plots follow the same pattern with the slope values (*m*) between 1 and 2 up to 100 kV/cm that are related to the space-charge-limited conduction (SCLC) mechanism [42]. At high fields (above 100 kV/cm), the log*j* values start to exhibit a non-linear relationship with the log*E* values, and this indicates a shift from bulk-dominated conduction to grain boundary-limited conduction (GBLC) [43, 44]. It is a consequence of accumulation of space charge at the grain boundaries that decreases the mobility of the charge carriers. The anisotropic grain structure can influence the conduction process by directing the current along the planes of the grains. As a result, it may restrict conduction more significantly at higher electric fields if the mobility of charge carriers is affected by resistivity at the grain boundaries. Even though the BFT sample exhibited the lowest conductivity within the SCLC region, it became more vulnerable after the transition to GBLC, which resulted in the lowest breakdown voltage (130 kV) compared to the Gd-doped samples. Apart from other reasons, it can be due to the highest porosity of this sample (~9%).

There are typically two primary reasons for breakdown when a high electric field is applied. The first one relates to intrinsic dielectric breakdown, a property of the material itself. The second factor is influenced by defects and imperfections, likely due to randomly distributed open pores, voids, inclusions, and other irregularities [45]. In practice, the breakdown strength of even high-density good-prepared ceramics is mainly affected by the presence of defects formed inside the ceramics. In this investigation, gadolinium improved the sinterability of BFT by reducing porosity (below 3% for BFTG3). These doped ceramics were more resistant to the dielectric breakdown under the stress [46]. While the leakage current in the doped samples was higher than that of pure BFT, their breakdown strength was improved, particularly at low levels of Gd. Therefore, understanding the ferroelectric properties of BFTG materials is complicated by the interplay of various factors such as dealing with the complex four-layered Aurivilius structure, change in symmetry and microstructure by Gd doping, porosity, anisotropic grain growth, and the presence of secondary phases.

Fig. 5. (a, b) Ferroelectric loops of the maximum field that all sample has withstood; (c) Leakage current measurements presented in the form of log*j*–log*E*; (d) Remnant polarizations for pure BFT and light-doped samples at 130 and 140 kV/cm; (e) Hysteresis loop (with RMH loop) for BFTG3 at 50 °C; (f) Current loop for BFTG3 sample at 50 °C.

The beneficial method for detecting the pure ferroelectric response is the remnant hysteresis (RMH) loop measurement. The rationale of this method is explained in detail elsewhere [47]. Thus, the measured remnant polarization (RMP) is free from electric and dielectric contributions that can often lead to misinterpretation of ferroelectric properties. The RMP values at 130 kV/cm (Fig. 5(d)) reveal that the ferroelectric potential decreases as Gd^{3+} concentration increases. It can be due to the inability of the spheric Gd^{3+} cations to polarize like Bi^{3+}, which contains the lone $6s^2$ electron pair. Furthermore, these values comply with the change in structural symmetry expressed by a decrease in the orthorhombic distortion (δ) with an increase in Gd content. At 140 kV/cm, the results are more dependent on microstructure-driven factors as explained in the previous paragraph. The BFTG3 sample reached the highest RMP value of 0.65 μC/cm^2 at room temperature, which is probably due to its less anisotropic grain structure, the highest density and the least amount of secondary phases compared to BFTG1 (0.42 μC/cm^2), and BFTG2 (0.41 μC/cm^2) that also exhibit higher remnant polarizations than the undoped sample at 130 kV/cm (0.30 μC/cm^2).

In the end, we tried to enhance the ferroelectric properties of BCTG3 sample by increasing its temperature to 50 °C, but not at fields above 140 kV/cm due to the immediate breakdown of the sample. As can be seen from Fig. 5(e), the RMP value at 140 KV/cm increased from 0.65 to 1.2 μC/cm^2 when the sample tamperature increased from room temperature to 50 °C, which indicates that ferroelectric properties of BFT are highly temperature-sensitive. Also, as the evidence of ferroelectric switching, two characteristic peaks around 100 kV, and –100 kV/cm were present in the current loop measured up to 140 kV/cm at 50 °C (Fig. 5(f)). Thus, light-doping up to x=0.3(BFTG3) can be beneficial to ferroelectric properties of BFT, first of all by allowing the application of higher electric fields that can initiate dipole switching in the material. At x=0.3 (BFTG3), Gd^{3+} doping enhances the sinterability and reduces the porosity, allowing for a more dense material. A dense material generally exhibits better ferroelectric properties because there are fewer structural defects and more uniform polarization switching within the grains. The XRD analysis indicates that the structural symmetry decreases (i.e., the orthorhombic distortion diminishes) as Gd content increases. This suggests that at BFTG3, the material may achieve a structure that is still conducive to ferroelectric switching. The decrease in symmetry could reduce energy barriers for domain switching, allowing for more efficient polarization at higher electric fields. Besides, the structure of BFTG3 is less anisotropic, meaning that the grains are more uniformly oriented and the grain boundaries are better aligned. This could help the material switch polarization more effectively, contributing to the highest Pr value observed. Anisotropic grains can sometimes create resistance to ferroelectric switching, as polarization would prefer to switching along certain crystallographic directions [48]. Higher Gd^{3+} concentrations, on the contrary, cause an increase in conductivity and change in the structural symmetry as demonstrated by XRD analysis and Raman spectroscopy, all of which deteriorated the ferroelectric properties of BFT. Also, inability of Gd^{3+} to polarize in the same manner as Bi^{3+}, which has a lone 6s^2 electron pair that contributes to polarization, is one more reason that negatively impacts the ferroelectric properties [35]. As shown in many investigations on ferroelectric properties of $Bi_5Ti_3FeO_{15}$ ceramics influenced by various dopants, it is hard to obtain a saturated hysteresis loop at room temperature [20-25, 37, 49-50]. The ferroelectric hysteresis loops, very close to saturation, were obtained only in $Bi_5Ti_3FeO_{15}$ thin films [51], where, due to a different domain structure, smaller volume and thickness, much higher electric fields can be applied. These changes allow for faster and easier formation of saturated hysteresis loops than in thicker materials, where the breakdown occurs regularly at lower electric fields.

3.5 Magnetic measurements

Magnetic measurements for neat and Gd-doped ($Bi_{5-x}Gd_xFeTi_3O_{15}$) samples at room temperature are shown in Fig. 6(a). The maximum magnetic field of ±10 kOe is applied to explore the magnetic nature of the samples. The relationship between magnetization and magnetic field for both pure BFT and all doped samples exhibited a linear behavior at room temperature, which is characteristic of paramagnetic materials. The magnetization gradually increased with the increase in Gd content, which can be explained by the highly magnetic nature of Gd^{3+} ions due to the electron configuration with 7 unpaired electrons, more than that in most other ions. However, the concentration of Fe^{3+} ions is relatively low in the BFT structure. It consists of 25% magnetic Fe ion and 75% non-magnetic Ti ion in the B-site of the perovskite slab. So, the presence of non-magnetic ions within the same site of the octahedral unit results in a weakened magnetic super-exchange interaction. Also, the long order of magnetic interaction is restricted because of barrier of the non-magnetic [Bi_2O_2] layer sandwiched between the perovskite layers [13]. For this specific concentration of magnetic ions, the limited range of the superexchange interaction poses a significant obstacle to achieving long-range magnetic order at elevated temperatures [2].

Fig 6. Magnetic hysteresis loops of all samples at room temperature (a) and BFTG10 at 5 K (b); (c) Temperature dependences of the magnetization for BFTG10 sample at $H = 100$ Oe (The inset demonstrates Curie−Weiss law fitting of the reciprocal susceptibility for BFTG10 sample).

Generally, the magnetic order in doped structures depends on the ionic radius and electronic structure of substituting ions. As was already confirmed by Rietveld analysis, doping on the A-site of BFT with Gd^{3+} introduces distortion in the perovskite lattice because of a significant difference between the ionic radii (the ionic radius of Gd^{3+} is smaller than that of Bi^{3+}). Related to that, and considering the effective magnetic moment of rare earth Gd^{3+} ions of 6.9 μ_B (that is higher than the magnetic moment of 5.9 μ_B for Fe^{3+}), it is anticipated that gadolinium will induce considerable alterations in magnetic behavior [38]. Although the magnetization at magnetic fields up to 10 kOe increased with higher Gd concentration, the linear nature of all Gd-doped magnetic hysteresis loops suggests that the Gd substitution at the A-site does not influence the magnetic state of the parent $Bi_5FeTi_3O_{15}$ phase.

By measuring the magnetization of BFTG10 under magnetic field of ±50 kOe and at 5 K, the nonlinear, hysteretic behavior was confirmed (Fig. 6(b)). This very weak, parasitic magnetism characterizes a well-known effect called canted antiferromagnetism [38, 52]. In canted antiferromagnetic materials, the atomic magnetic moments are aligned in an antiparallel configuration, but are also inclined or tilted relative to one another. This creates a small net magnetization which is perpendicular to the antiferromagnetic ordering. Fig. 6(c) illustrates the variation of magnetization with temperature (5–300 K) in the field cooled-zero field cooled (FC-ZFC) mode for the applied field of 100 Oe. The magnetic interaction can also be reflected by $1/\chi$ against temperature T, where χ is the susceptibility measured after zero-field cooling. As shown in the inset of Fig. 6(c), the relation between $1/\chi$ and T can be well fitted by Curie–Weiss law at high temperature range. The extrapolated Curie–Weiss temperature is about −40 K, indicating that the magnetism of BFTG10 ceramics is dominated by antiferromagnetic interaction [16, 28, 38].

A few previously published papers dealt with the influence of Gd on the magnetic properties of BFT ceramics and showed discrepancies in the results. Our investigation complies with the results of Koval et al. [28], who revealed that substituting Bi^{3+} ions with Gd^{3+} cannot induce any magnetic ordering in the BFT structure. Our previously published paper [23], and some others, confirmed that the enhancement of magnetic properties could be achieved by B-site doping of the perovskite-type units with magnetically active transition-metal ions such as Co, Mn, Ni, and Cr [19-22]. On the other hand, Zou and coauthor [29] illustrated that the remnant magnetization of $Bi_{4.25}Gd_{0.75}Fe_{0.5}Co_{0.5}Ti_3O_{15}$ is about four times higher (18.5 memu/g) than that of $Bi_5Fe_{0.5}Co_{0.5}Ti_3O_{15}$ (~4 memu/g), as if Gd exhibits a synergetic effect when in the presence of Co or other transition-metal ions, interrelated by their strong exchange interaction.

3.6 Dielectric measurements

The temperature dependences of dielectric constant (ε') and dielectric loss ($\tan\delta$) were measured from room temperature to 1070 K. The result at 1 MHz frequency on cooling is shown in Fig. 7. These characteristics were similar for all doped materials and remain almost invariant on temperature changes up to 600 K for both ε' and $\tan\delta$. Starting at a low value near room temperature (approximately 98 for pure BFT), ε' exhibited a noticeable increase as the temperature approached 600 K, indicating enhanced conductivity of the sample. Between 600 and 900 K, all samples displayed a peak in the dielectric constant, which may be associated with a change in the conductivity mechanism. As mentioned earlier, the migration of inherent defects (bismuth and oxygen vacancies) played a significant role in promoting intrinsic ionic conduction, which substantially improved conductivity at elevated temperatures [53]. The dielectric constant around 980 K (for pure BFT) reached a narrow maximum, representing the ferroelectric phase transition. It is worth mentioning that this maximum is clearly seen in dielectric data at higher frequencies as well (see Fig. 8). Moreover, a small (5−10 K) hysteresis between heating (not shown here) and cooling cycles can be noticed what confirms the ferroelectric nature of this anomaly. From Figs. 7 and 8, one can assume that the phase transition peak decreases slightly with the increase of Gd doping even though the dielectric constant value shows the opposite trend for BFTG1-BFTG3 compounds. In the BFTG10 sample, the dielectric anomaly at the phase transition point becomes more like a kink than an anomaly.

The phase transition temperature was shifted toward the high temperatures with an increase of the dopant concentration, from 980 K for BFT to 991, 1006, 1019, 1026 and 1048 K for BFTG1, BFTG2, BFTG3, BFTG5, and BFTG10, respectively. Not many papers deal with the dielectric properties of BFT compounds. What’s more, they report very different results and conclusions. The investigated temperature region is usually narrow, from room temperature up to 800 K. Wu et al. [18] have noticed three different anomalies: one located between 720 and 780 K (that may be related to a change in the conductive model), the second around 1007 K (related to phase transition), and the third at 1090 K (associated with an abrupt lattice expansion of the tetragonal structure). A similar conductivity-related anomaly but in a lower temperature range (500−700 K) was found by Patri et al. in W/Co co-doped $Bi_4LaFeTi_3O_{15}$ ceramics [50]. Snedden et al. have determined phase transition at 1003 K without evidence of a lower temperature phase transition reported by some other authors [7].

Fig 7. Temperature dependence of the dielectric constant (a) and tanδ (b) of all samples.

The values of dielectric constant vary in different literature data depending on the synthesis conditions (calcination and sintering conditions), densities, structure, dopant concentration, grain size homogeneous nature and so on. In this study, the value of the dielectric constant at room temperature is about 98 for BFT and increase with doping up to 200. In contrast, the relatively low dielectric constant was measured at Curie temperature, about 500, which is similar to an earlier report by Wu et al. [18]. Maximum values of ε_r at Curie temperature firstly increase with Gd doping up to x=0.2 and then decrease with increasing levels of Gd substitution.

Fig. 8. Temperature dependence of the dielectric constant and tanδ at selected frequencies for BFT, BFTG3 and BFTG10 samples

Besides the previously mentioned dielectric peak around 1000 K temperature, a broad anomaly above 500 K temperatures is visible in all compounds (Fig. 8). It is important to mention that the maximum of this anomaly shifts toward higher temperatures with the increase of measurement frequency which is different behavior and cannot be associated with any phase transformation. Usually, ion thermal conduction and accumulation at the grain boundaries may be responsible for this dispersion, accompanied by a nearly exponential increase of values of dielectric loss at temperatures between 500 and 800 K. However, at room temperature, the dielectric losses are very low, below 0.01 for all samples and dielectric dispersion becomes negligible as well. A slight dielectric anomaly can be seen for the BFTG10 sample below 400 K, and it extends below room temperature. Summing up, dielectric studies of Gd-doped BFT compounds demonstrated excellent dielectric behavior with high Curie temperature ($T_C \approx 1008$ K), high dielectric constant ($\varepsilon_r \approx 167$, $\varepsilon_{max} \approx 980$), and low dielectric losses (tan$\delta \approx 0.02$), for an optimum value of Gd dopant (x = 0.2). The doping of Gd decreased epsilon at room temperature, and shifted Curie temperature toward higher temperatures. However, it is not possible to establish a clear correlation between dielectric and ferroelectric behavior due to concomitant changes in structural, microstructural and chemical properties of material induced by Gd doping.

4. Conclusions

In summary, the influence of gadolinium doping on the structural, ferroelectric, magnetic, and dielectric properties of the $Bi_{5-x}Gd_xFeTi_3O_{15}$ ceramic obtained from the solid-state reaction method was investigated in this study. A minimal number of impurities was identified by XRD analysis in the neat BFT and samples with low Gd concentration. However, it is clear that higher concentrations of dopants suppress the formation of the impurity phases. SEM analysis reveals an anisotropic nature of grain growth with the exception of the BFGT3 sample, which possesses significantly shorter grains. Raman spectroscopy results indicate that Gd ions prefer to replacing Bi ions in the pseudo-perovskite layers rather than that in the bismuth-oxide layers.

The ferroelectric loops of all investigated samples are unsaturated even at electric fields close to the sample breakdown. The remnant hysteresis technique reveals that a small but finite remnant ferroelectric polarization is present, and it decreases as Gd content increases at the observed electric field. However, the breakdown strength is enhanced through doping, especially by low level Gd substitution (up to x=0.3). Thus, the BFTG3 sample exhibits the highest remnant polarization of 0.65 μC/cm^2 at 140 kV/cm, which increases up to 1.2 μC/cm^2 at 50 °C. Although the Gd doping is ineffective in decreasing the leakage current, it increases the breakdown strength of the BFT samples at higher electric fields. In general, low Gd concentrations (up to x=0.3) can be considered beneficial to the ferroelectric properties. The magnetization at magnetic fields up to 10 kOe increases with Gd substitution, but it does not lead to the development of ferromagnetic ordering in the four-layered Aurivillius $Bi_{5-x}Gd_xFeTi_3O_{15}$ ceramics. However, very weak, parasitic ferromagnetism is observed at 5 K for sample with the highest concentration of Gd (x=1). Dielectric studies demonstrate that x=0.2 is the optimum value of Gd content when the material shows the highest value of Curie temperature and dielectric constant and low dielectric losses ($\tan\delta \approx 0.02$).

Thus, the doping with Gd can improve the overall properties of BFT ceramics. While higher Gd concentrations induce proportionally higher magnetization under magnetic fields at room temperature, it is not the case with the ferroelectric and dielectric properties that are more dependent on structural and microstructural characteristics, where lower Gd concentrations are beneficial. Therefore, special attention should be given to the synthesis and processing conditions for preparing BFT bulk ceramics to avoid irregularities such as porosity and secondary phases that can deteriorate the ferroelectric properties.

References

[1] Achary SN, Jayakumar OD, Tyagi AK. Multiferroic Materials. In: Banerjee S, Tyagi AK, Eds. Functional Materials. Amsterdam: Elsevier, 2012:155.

[2] Birenbaum AY, Scaramucci A., Ederer C., Magnetic order in four-layered Aurivillus phases, *Phys Rev* B. 2017;95:104419.

[3] Kumar N, Shukla A, Kumar N, Choudhary RNP, Kumar A. Structural, electrical, and multiferroic characteristics of lead-free multiferroic: Bi($Co_{0.5}Ti_{0.5}$)O_3–$BiFeO_3$ solid solution. *RSC Adv.* 2018;8:36939.

[4] Jardiel T, Caballero AC, Villegas M. Aurivillius ceramics, $Bi_4Ti_3O_{12}$-based piezoelectrics. J *Ceram Soc Jpn* 2008;116:511.

[5] Huang K, Xu W, Zheng S, Tian J, Coupling photothermal and piezoelectric effect in $Bi_4Ti_3O_{12}$ for enhanced photodegradation of tetracycline hydrochloride, *Opt Mater*. 2023;145:114352.

[6] Hervoches CH, Snedden A, Riggs R, Kilcoyne SH, Manuel P, Lightfoot P. Structural Behavior of the Four-Layer Aurivillius-Phase Ferroelectrics $SrBi_4Ti_4O_{15}$ and $Bi_5Ti_3FeO_{15}$. *J Solid State Chem*. 2002;164:280.

[7] Snedden A, Hervoches CH, Lightfoot P. Ferroelectric phase transitions in $SrBi_2Nb_2O_9$ and $Bi_5Ti_3FeO_{15}$: A powder neutron diffraction study. *Phys Rev B*. 2003;67:092102.

[8] Srinivas A, Suryanarayana SV, Kumar GS, Mahesh Kumar M. Magnetoelectric measurements on $Bi_5FeTi_3O_{15}$ and $Bi_6Fe_2Ti_3O_{18}$. *J Phys: Condens Matter*. 1999;11:3335.

[9] Singh RS, Bhimasankaram T, Kumar GS, Suryanarayana SV, Dielectric and magnetoelectric properies of $Bi_5FeTi_3O_{15}$, *Solid State Commun*. 1994;91:567.

[10] Chen G, Bai W, Sun L, Wu J, Ren Q, Xu W, et al. J. Processing optimization and sintering time dependent magnetic and optical behaviors of Aurivillius $Bi_5Ti_3FeO_{15}$ ceramics. *J Appl Phys.* 2013;113:034901.

[11] Koval V, Shi Y, Skorvanek I, Viola G, Bures R, Saksl K, et al. Cobalt-induced structural modulation in multiferroic Aurivillius-phase oxides. *J Mater Chem C*. 2020;8:8466.

[12] Li Z, Ma J, Gao Z, Viola G, Koval V, Mahajan A, et al. Room temperature magnetoelectric coupling in intrinsic multiferroic Aurivillius phase textured ceramics. *Dalton Trans*. 2016;45:14049.

[13] Dong XW, Wang KF, Wan JG, Zhu JS, Liu JM. Magnetocapacitance of polycrystalline $Bi_5Ti_3FeO_{15}$ prepared by sol-gel method. *J Appl Phys*. 2008;103:094101.

[14] Jena R, Chandrakanta K, Sahu DP, Madhusmita J, Kaushik SD, Singh AK. Enhanced magnetic, magnetodielectric, and field-dependent magnetoimpedance correlation in the $Bi_5Ti_3FeO_{15}$/$Bi_2Fe_4O_9$ composites. *J Magn Magn Mater*. 2023;580:170910.

[15] Mao XY, Wang W, Chen XB. Electrical and magnetic properties of $Bi_5FeTi_3O_{15}$ compound prepared by inserting $BiFeO_3$ into $Bi_4Ti_3O_{12}$. *Solid State Commun*. 2008;147:186.

[16] Liu J, Bai W, Yang J, Xu W, Zhang Y, Lin T, et al. The Cr-substitution concentration dependence of the structural, electric and magnetic behaviors for Aurivillius $Bi_5Ti_3FeO_{15}$ multiferroic ceramics. *J Appl Phys*. 2013;114:234101.

[17] Jartych E, Pikula T, Mazurek M, Lisinska-Czekaj A, Czekaj D, Gaska K, et al. Antiferromagnetic spin glass-like behavior in sintered multiferroic Aurivillius $Bi_{m+1}Ti_3Fe_{m-3}O_{3m+3}$ compounds. *J Magn Magn Mater*. 2013;342:27.

[18] Wu MS, Tian ZM, Yuan SL, Duan HN, Qiu Y. Dielectric behavior and ac conductivity in Aurivillius $Bi_4Ti_3O_{12}$ doped by antiferromagnetic $BiFeO_3$, *Phys Lett A*. 2012;375:2062.

[19] Zhao H, Wang H, Cheng Z, Fu Q, Tao H, Ma Z, et al. Electric and magnetic properties of Aurivillius-phase compounds: $Bi_5Ti_3XO_{15}$ (X=Cu, Mn, Ni, V). *Ceram Int*. 2018;44:13226.

[20] Bobic J, Ilic N, Veerapandiyan V, Vijatovic Petrovic M, Deluca M, Dzunuzovic A, et al. Tailoring the ferroelectric and magnetic properties of $Bi_5Ti_3FeO_{15}$ ceramics by doping with Co and Y, *Solid State Sci*. 2022;123:106802.

[21] Chena X, Xiao J, Xue Y, Zeng X, Yang F, Su P. Room temperature multiferroic properties of Ni-doped Aurivillus phase $Bi_5Ti_3FeO_{15}$. *Ceram Int*. 2014;40 :2635.

[22] Dias JA, Bretas RES, Marcondes LMS, Raymundo Morelli M. Optical and dielectric properties of Nd and Sm-doped $Bi_5Ti_3FeO_{15}$. *J Mater Sci: Mater Electron*. 2019;30:16812.

[23] Bobic JD, Katiliute RM, Ivanov M, Vijatovic Petrovic MM, Ilic NI, Dzunuzovic AS, et al. Dielectric, ferroelectric and magnetic properties of La doped $Bi_5Ti_3FeO_{15}$ ceramics. *J.Mater Sci: Mater Electron.* 2016;27:2448.

[24] Abbas Y, Kamran M, Anis-ur-Rehman M, Facile synthesis of samarium and cerium doped double perovskite cobaltite with enhanced dielectric response, *J. Rare Earths*. 2024;42:1317.

[25] Lukovic Golic D, Radojkovic A, Dapcevic A, Pajic D, Dragovic J, Toric F, et al. Change in structural, ferroelectric, and magnetic properties of bismuth ferrite induced by doping with gadolinium. *Ceram Int*. 2019;45:19158.

[26] Joshi S, Shukla A, Kumar N, Choudhary RNP. Nd substitution response on structural, dielectric, and electrical features of bismuth iron titanate. *Ceram Int.* 2024;50: 1643.

[27] Supriya S. Research progress, doping strategies and dielectric-ferroelectric anomalies of rare earth-based $Bi_{0.5}Na_{0.5}TiO_3$ perovskites. *J. Rare Earths*. 2024;42:2003.

[28] Koval V, Skorvanek I, Viola G, Zhang M, Jia C, Yan H. Crystal chemistry and magnetic properties of Gd-substituted Aurivillius-type $Bi_5FeTi_3O_{15}$ ceramics. *J Phys Chem C*. 2018;122: 15733.

[29] Zuo XZ, Zhang ML, He EJ, Yang J, Zhu XB, Dai JM. Multiferroic property, dielectric response, and scaling behavior in Aurivillius $Bi_{4.25}Gd_{0.75}Fe_{0.5}Co_{0.5}Ti_3O_{15}$ ceramic. *J Alloys Compd*. 2017;695:2556.

[30] Kezionis A, Kazlauskas S, Petrulionis D, Orliukas AF. Broadband method for the determination of small sample's electrical and dielectric properties at high temperatures. *IEEE Trans. Microwave Theory Tech*. 2014,10:2456.

[31] Diasa JA, Oliveira JA, Renda CG, Morelli MR, Production of nanometric $Bi_4Ti_3O_{12}$ powders: from synthesis to optical and dielectric properties. *Mater Res*. 2018;21:e20180118.

[32] Zhang X, Qi R, Dong S, Yang S, Hong X, Peng H, et al. Ferro-electric and magnetic properties in $Bi_5Ti_3FeO_{15}$ films by Mn doping, *J Mater Chem* C. 2022;10:1003.

[33] Moure A, Review and perspectives of Aurivillius structures as a lead-free piezoelectric system. *Appl Sci.* 2018;8:62.

[34] Snedden A, Lightfoot P, Dinges T, Islam MS, Defect and dopant properties of the Aurivillius phase $Bi_4Ti_3O_{12}$. *J Solid State Chem*. 2004;177:3660.

[35] Rao R, Salke NP, Garg AB. Raman spectroscopic study of phase stability and anharmonicity in $Bi_{12}TiO_{20}$. *Mater Chem Phys*. 2013;139:640.

[36] Guo W, Yang Y, Guo Y, Jia Y, Liu H, Guo Y. Self-assembled hierarchical $Bi_{12}TiO_{20}$–graphene nanoarchitectures with excellent simulated sunlight photocatalytic activity. Phys Chem. Chem Phys. 2014;16:2705.

[37] Salas OA, Getahun YW, Mandujano HC, Manciu F, Castellanos M, Lopez J, et al. Resilience of the Aurivillius structure upon La and Cr doping in a $Bi_5Ti_3FeO_{15}$ multiferroic. *Dalton Trans.* 2024;53:6423.

[38] Silva PHT, Silva MAS, da Silva RB, Correa MA, Bohn F, Ade Menezes AS, et al. Effects of the Bi^{3+} substitution on the structural, vibrational, and magnetic properties of bismuth layer-structured ferroelectrics. *Appl Phys A*. 2020;126:653.

[39] Chen XB, Hui R, Zhu J, Lu WP, Mao XY. Relaxor properties of lanthanum-doped bismuth layer-structured ferroelectrics. *J Appl Phys*. 2004;96:5697.

[40] Osada M, Tada M, Kakihana M, Watanabe T, Funakubo H. Cation distribution and structural instability in $Bi_{4-x}La_xTi_3O_{12}$. *Jpn J Appl Phys*. 2001;40:5572.

[41] Supriya S. Tailoring layered structure of bismuth-based Aurivillius perovskites: Recent advances and future aspects. *Coord Chem Rev*. 2023;479:215010.

[42] Murari NM, Thomas R, Melgarejo RE, Pavunny SP, Katiyar RS. Structural, electrical, and magnetic properties of chemical solution deposited $BiFe_{1-x}Ti_xO_3$ and $BiFe_{0.9}Ti_{0.05}Co_{0.05}O_3$ thin films. *J Appl Phys*. 2009;106:014103.

[43] Sun H, Wu Y, Yao T, Lu Y, Shen H, Huang F, et al. Electrical and magnetic properties of Aurivillius phase $Bi_5Fe_{1-x}Ni_xTi_3O_{15}$ thin films prepared by chemical solution deposition. *J Alloys Compd*. 2018;765:27.

[44] Radojkovic A, Luković Golić D, Ćirković J, Marinković Stanojević Z, Pajić D, Torić F, et al. Tuning of $BiFeO_3$ multiferroic properties by light doping with Nb. *Ceram Int*. 2018;44:16739.

[45] Cain MG. Characterisation of Ferroelectric Bulk Materials and Thin Films, Chapter: Dielectric Breakdown in Dielectrics and Ferroelectric Ceramics. Berlin: Springer, 2014.

[46] Cai Z, Feng P, Zhu C, Wang X. Dielectric breakdown behavior of ferroelectric ceramics: The role of pores. *J Eur Ceram Soc*. 2021;41:2533.

[47] Radojković A, Luković-Golić D, Jović Orsinić N, Nikolić N, Cirković J, Lazarević S, et al. Evolution of ferroelectric and piezoelectric properties of $BiFeO_3$ ceramics doped with lanthanum and zirconium. *J Alloys Compd*. 2024;1009:176901.

[48] Jones JL, Slamovich EB, Bowman KJ, Lupascu DC. Domain switching anisotropy in textured bismuth titanate ceramics. *J Appl Phys* 2005;98:104102.

[49] Nazemian M, Khoshnoud DS, The enhanced of magnetic and electrical properties of $Bi_5FeTi_3O_{15}$ compound with replacing Co for Ti sites. *J Magn Magn Mater*. 2023;565:170243.

[50] Patri T, Kumar JP, Ghosh A, Babu PD. Tunable polarization with enhanced multiferroic response of W/Co co-doped $Bi_4LaFeTi_3O_{15}$ Aurivillius ceramics. *J Appl Phys*. 2020;128:154102.

[51] Lee E, Keum YH, Son JY. Enhanced piezoelectric properties of $Bi_5Ti_3FeO_{15}$ thin films by improving crystallinity of fluorine doped tin oxide bottom electrode: Role of α -domains. *Chin J Phys*. 2024;90:90.

[52] Veenachary V, Ramana EV, Babu SN, Puli VS, Saha S, Srinivasan G, et al. Magnetoelectric Properties of Aurivillius-Layered Perovskites. *Crystals*. 2024;14:299.

[53] Wang Q, Liang EM, Wang CM. High-performance bismuth titanate-ferrite ($Bi_5Ti_3FeO_{15}$) for high-temperature piezoelectric applications. *J Am Ceram Soc*. 2024:107(7):4811.

GRAPHICAL ABSTRACT

Gd^{3+}-modified $Bi_{5-x}FeTi_3O_{15}$ ceramics were successfully synthesized by solid state reaction. It enhances the electrical and magnetic properties of the investigated material.

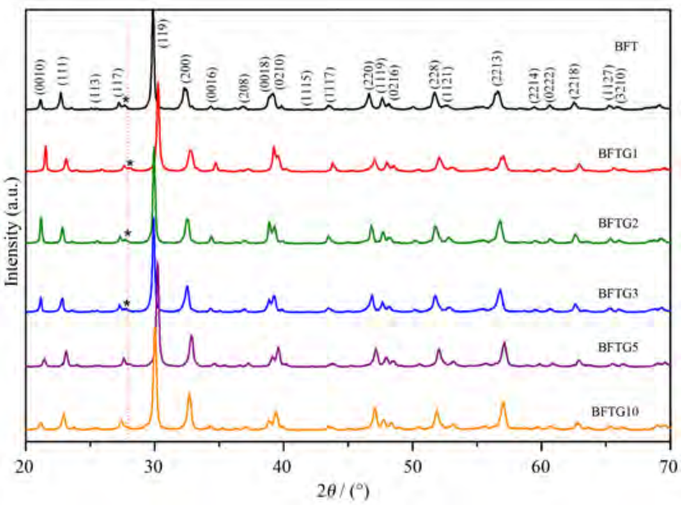

(0010)
(111)
(113)
(117)
(119)
(200)
(0016)
(208)
(0018)
(0210)
(1115)
(1117)
(220)
(1119)
(0216)
(228)
(1121)
(2213)
(2214)
(0222)
(2218)
(1127)
(3210)
*
BFT
BFTG1
BFTG2
BFTG3
BFTG5
BFTG10
Intensity (a.u.)
20
30
40
50
60
70
2θ / (°)

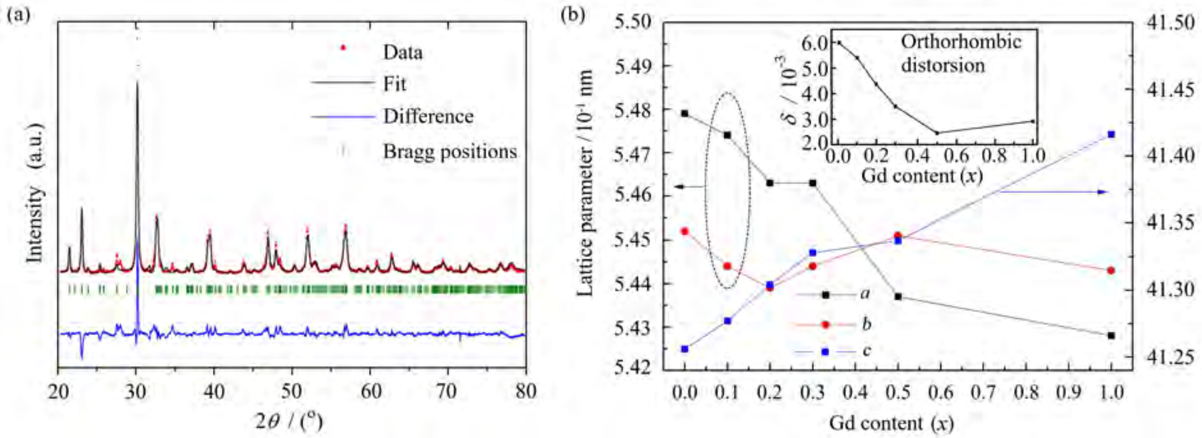
(a)
Data
Fit
Difference
Bragg positions
Intensity (a.u.)
20
30
40
50
60
70
80
2θ / (°)
(b)
Lattice parameter / 10⁻¹ nm
5.42
5.43
5.44
5.45
5.46
5.47
5.48
5.49
5.50
41.25
41.30
41.35
41.40
41.45
41.50
0.0
0.1
0.2
0.3
0.4
0.5
0.6
0.7
0.8
0.9
1.0
Gd content (x)
a
b
c
Orthorhombic distorsion
δ / 10⁻³
2.0
3.0
4.0
5.0
6.0
0.0
0.2
0.4
0.6
0.8
1.0
Gd content (x)

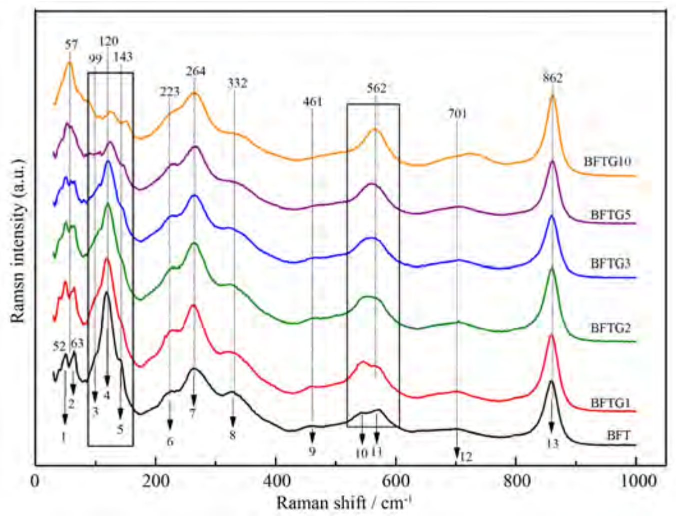
57
120
99
143
264
223
332
461
562
701
862
52
63
1
2
3
4
5
6
7
8
9
10
11
12
13
BFTG10
BFTG5
BFTG3
BFTG2
BFTG1
BFT
Ramsn intensity (a.u.)
0
200
400
600
800
1000
Raman shift / cm⁻¹

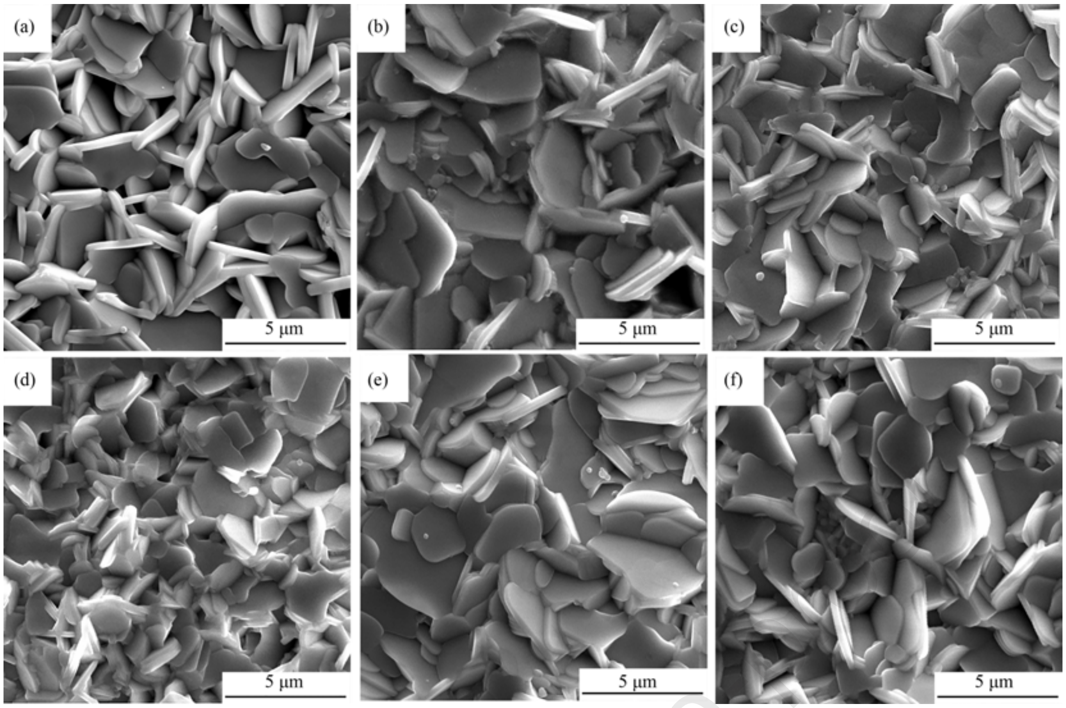
(a)
5 μm
(b)
5 μm
(c)
5 μm
(d)
5 μm
(e)
5 μm
(f)
5 μm

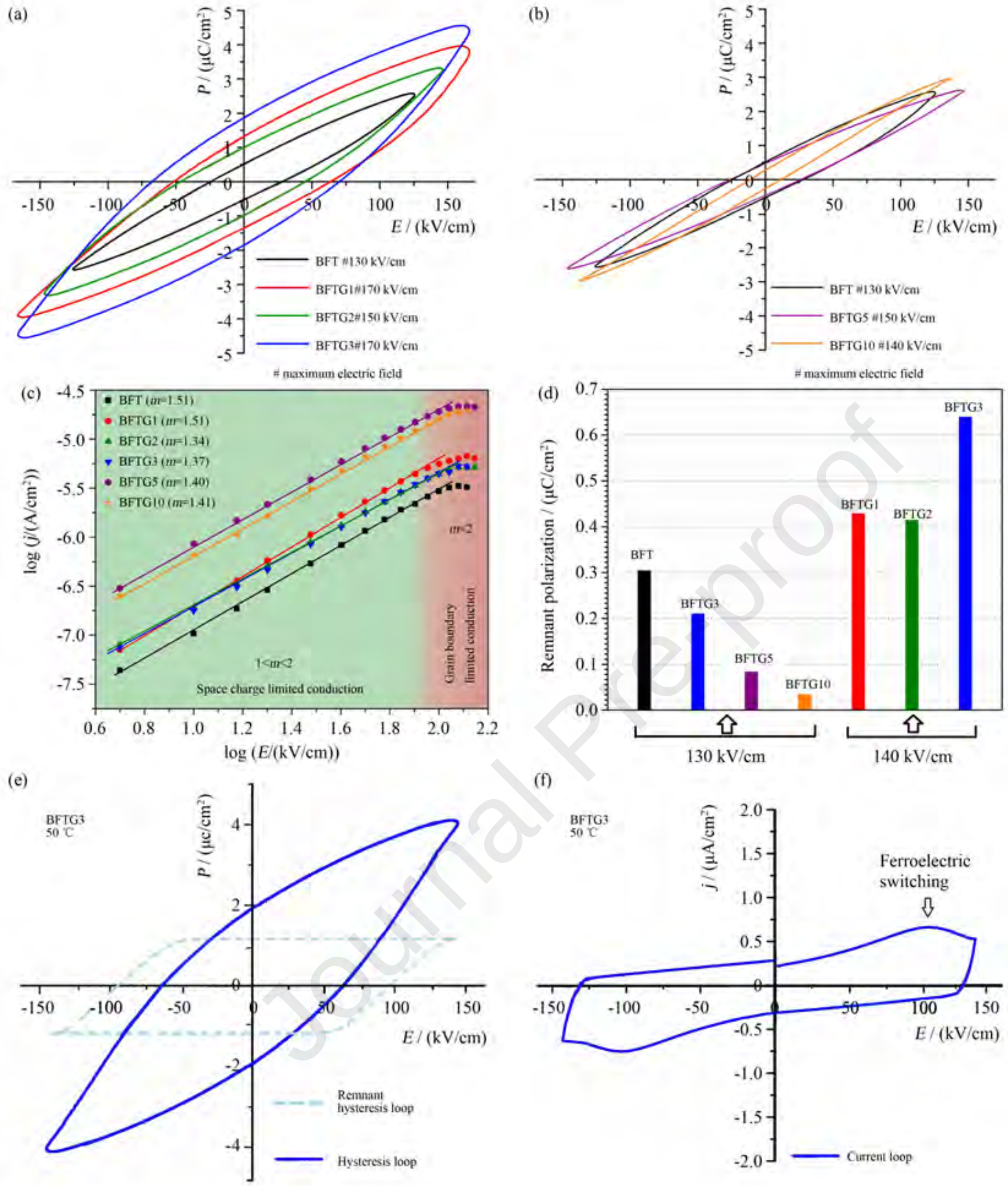
(a)
P / (μC/cm²)
E / (kV/cm)
BFT #130 kV/cm
BFTG1#170 kV/cm
BFTG2#150 kV/cm
BFTG3#170 kV/cm
maximum electric field
(b)
P / (μC/cm²)
E / (kV/cm)
BFT #130 kV/cm
BFTG5 #150 kV/cm
BFTG10 #140 kV/cm
maximum electric field
(c)
log (j/(A/cm²))
log (E/(kV/cm))
BFT (m=1.51)
BFTG1 (m=1.51)
BFTG2 (m=1.34)
BFTG3 (m=1.37)
BFTG5 (m=1.40)
BFTG10 (m=1.41)
m≈2
Grain boundary limited conduction
1<m<2
Space charge limited conduction
(d)
Remnant polarization / (μC/cm²)
BFT
BFTG3
BFTG5
BFTG10
BFTG1
BFTG2
BFTG3
130 kV/cm
140 kV/cm
(e)
BFTG3
50 ℃
P / (μc/cm²)
E / (kV/cm)
Remnant hysteresis loop
Hysteresis loop
(f)
BFTG3
50 ℃
j / (μA/cm²)
E / (kV/cm)
Ferroelectric switching
Current loop

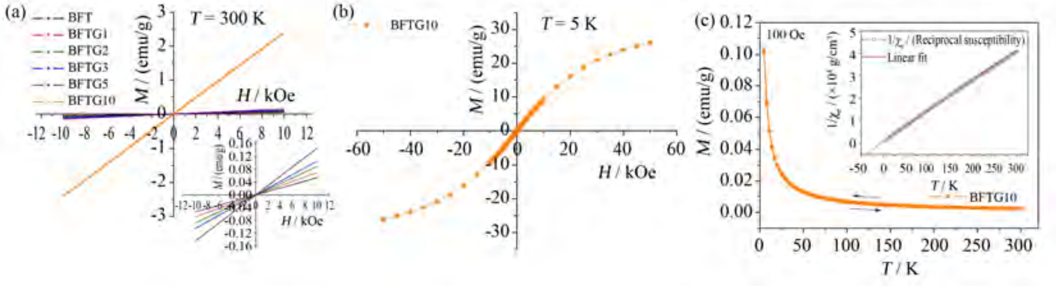
(a)
BFT
BFTG1
BFTG2
BFTG3
BFTG5
BFTG10
T = 300 K
M / (emu/g)
H / kOe
3
2
1
0
-1
-2
-3
-12
-10
-8
-6
-4
-2
0
2
4
6
8
10
12
0.16
0.12
0.08
0.04
0.00
-0.04
-0.08
-0.12
-0.16
M / (emu/g)
H / kOe
(b)
BFTG10
T = 5 K
M / (emu/g)
30
20
10
0
-10
-20
-30
-60
-40
-20
0
20
40
60
H / kOe
(c)
100 Oe
M / (emu/g)
0.12
0.10
0.08
0.06
0.04
0.02
0.00
0
50
100
150
200
250
300
T / K
BFTG10
1/χ_v / (Reciprocal susceptibility)
Linear fit
1/χ_v / (×10⁴ g/cm³)
5
4
3
2
1
0
-50
0
50
100
150
200
250
300
T / K

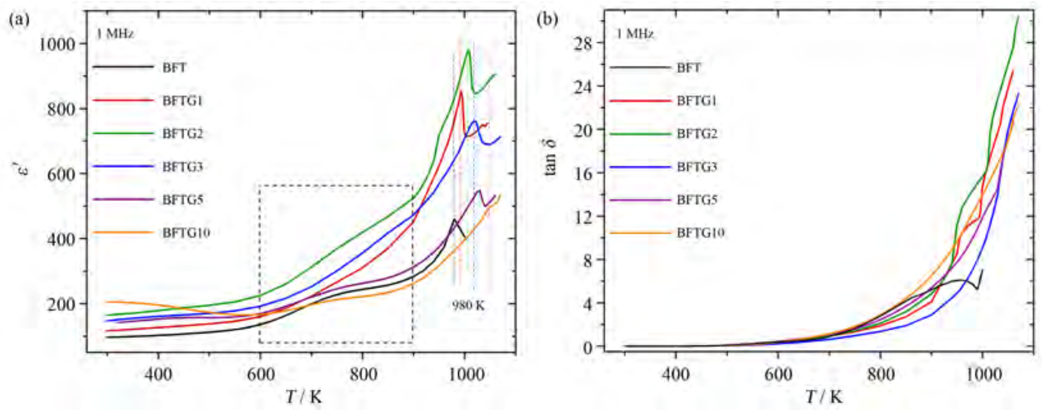
(a)
1 MHz
BFT
BFTG1
BFTG2
BFTG3
BFTG5
BFTG10
ε'
1000
800
600
400
200
400
600
800
1000
T / K
980 K
(b)
1 MHz
BFT
BFTG1
BFTG2
BFTG3
BFTG5
BFTG10
tan δ
28
24
20
16
12
8
4
0
400
600
800
1000
T / K

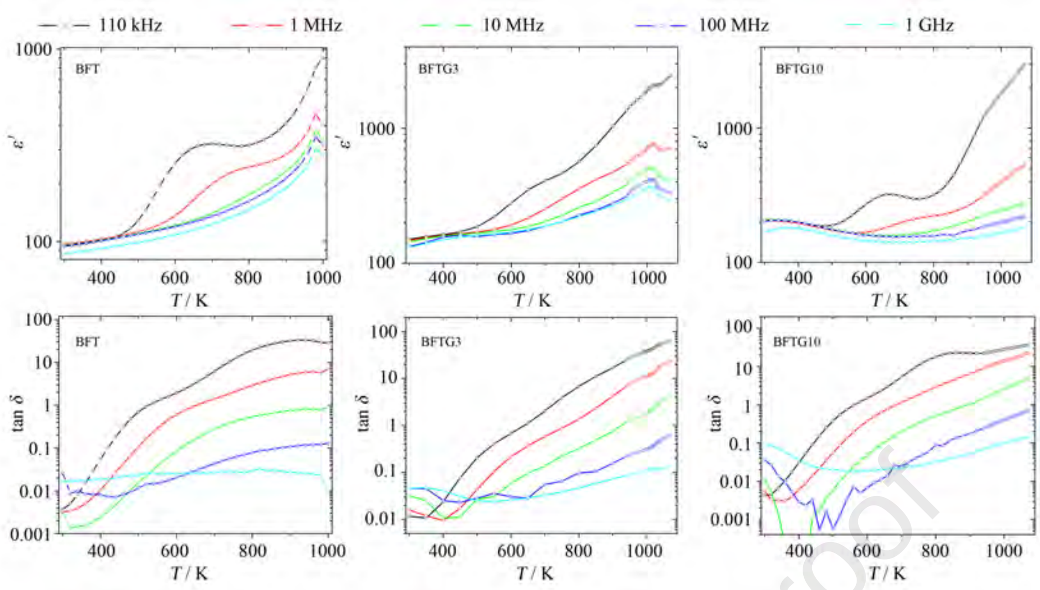
110 kHz
1 MHz
10 MHz
100 MHz
1 GHz
BFT
BFTG3
BFTG10
ε′
tan δ
T / K
1000
100
10
1
0.1
0.01
0.001
400
600
800
1000

Highlights:

- Pure and Gd^{3+} modified ceramics were successfully synthesized by solid state reaction.
- Raman analysis confirmed that Gd^{3+} replaces Bi^{3+} in the BFT structure.
- Up to 6 mol% Gd enhanced the dielectric and ferroelectric properties of BFT.
- The magnetization at magnetic fields up to 10 kOe increased with Gd substitution.

Declaration of Interest Statement

☒ The authors declare that they have no known competing financial interests or personal relationships that could have appeared to influence the work reported in this paper.

☐ The author is an Editorial Board Member/Editor-in-Chief/Associate Editor/Guest Editor for this journal and was not involved in the editorial review or the decision to publish this article.

☐ The authors declare the following financial interests/personal relationships which may be considered as potential competing interests:

ARTICLE IN PRESS

Ceramics International xxx (xxxx) xxx

Contents lists available at ScienceDirect

Ceramics International

journal homepage: www.elsevier.com/locate/ceramint

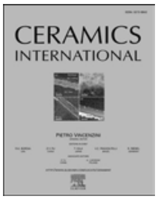

Double magnetization reversal in $Er_3Fe_5O_{12}$ garnet nanocrystals

Novica Paunović [a,*], Zorana Dohčević-Mitrović [a,**], Raneesh Balakrishnan [b], Marko Bošković [c], Marija Perović [c], Bojan Stojadinović [a], Sobi K. Chacko [b,d], Saša Lazović [a], Nandakumar Kalarikkal [e,f,g]

[a] Institute of Physics Belgrade, University of Belgrade, Pregrevica 118, 11080, Belgrade, Serbia
[b] Department of Physics, Catholicate College, Pathanamthitta, Kerala, 689645, India
[c] Vinča Institute of Nuclear Sciences, National Institute of the Republic of Serbia, University of Belgrade, P.O.Box 522, Belgrade, 11351, Serbia
[d] Department of Physics, NSS Hindu College, Changanassery, Kerala, 686 102, India
[e] School of Pure and Applied Physics, Mahatma Gandhi University, Kottayam, Kerala, 686560, India
[f] International and Inter University Centre for Nanoscience and Nanotechnology, Mahatma Gandhi University, Kottayam, Kerala, 686560, India
[g] International Centre for Ultrafast Studies, Mahatma Gandhi University, Kottayam, Kerala, 686560, India

ARTICLE INFO

Keywords:
$Er_3Fe_5O_{12}$ garnet
Rare-earth garnets
Magnetization reversal
Negative magnetization
Magnetization compensation
Magnetization switching

ABSTRACT

$Er_3Fe_5O_{12}$ nanoparticles were synthesized via the sol-gel method, yielding an *Ia3d* garnet structure, as confirmed by XRD, HRTEM, EDX, and Raman spectroscopy. Magnetic measurements showed that the temperature of magnetic compensation is 75 K (T_{comp1}), and that the coercive field exhibits a single peak near T_{comp1}. Above T_{comp1}, the coercive field was found to be proportional to the susceptibility of the Er^{3+} paraprocess. Zero-field-cooled (ZFC) and field-cooled (FC) measurements were performed, including both cooling (FCC) and warming (FCW) cycles. FCC measurements revealed double magnetization reversal, with two compensation temperatures, observed for the first time in $Er_3Fe_5O_{12}$. At T_{comp1}, the magnetization switches from positive to negative, whereas at the lower T_{comp2}, it switches from negative to positive. T_{comp2} depends on the applied field and increases with increasing field, and for fields above 1000 Oe, the magnetization reversal no longer occurs. In contrast, these magnetization reversals are completely absent in the FCW regime. Additionally, $Er_3Fe_5O_{12}$ nanoparticles exhibit magnetization switching, where the magnetization orientation can be reversed by changing only the magnitude of the applied field while keeping its direction fixed. The observed double magnetization reversal is attributed to a strong magnetocrystalline anisotropy opposing the Zeeman-driven realignment of magnetization.

1. Introduction

Magnetization reversal (MR), also known as negative magnetization, is a phenomenon in which the magnetization changes its direction, transitioning from a positive state (aligned with the external field) to a negative state (opposite to the field) within a specific temperature range. The temperature at which the magnetization becomes zero is referred to as the compensation temperature. Such an effect was first predicted by Néel [1] as a phenomenological possibility in certain ferrimagnetic materials. It arises from the different temperature dependencies of magnetization in two antiferromagnetically coupled magnetic sublattices, which result from different molecular fields acting on magnetic ions positioned at two different crystallographic sites. This behavior was later experimentally observed in spinel ferrites [2]. This unusual and intriguing effect has attracted significant attention due to its importance in fundamental physics and its potential applications in magnetic data storage, spin valves, magnetic switches, thermomagnetic switching, bipolar magnetocaloric devices, and advanced spintronic and memory technologies [3–9]. MR has been experimentally reported in various magnetically ordered materials, such as spinels [2,10–13], perovskites [14–17], particularly in orthochromites [18–22] and orthoferrites [8,23,24]. In contrast, it has been reported in a relatively small number of cases for garnets, e.g., Refs. [25–32].

Erbium iron garnet (ErIG) belongs to the rare-earth iron garnet family, a class of ferrimagnetic materials with a cubic garnet structure. These materials are known for their complex magnetic interactions, magnetization compensation effects, and spin reorientation transitions, making them highly relevant for both fundamental research and

---

* Corresponding author.
** Corresponding author.
E-mail addresses: paun@ipb.ac.rs (N. Paunović), zordoh@ipb.ac.rs (Z. Dohčević-Mitrović).

https://doi.org/10.1016/j.ceramint.2025.12.301
Received 29 September 2025; Received in revised form 4 December 2025; Accepted 18 December 2025

Please cite this article as: Novica Paunović et al., *Ceramics International,* https://doi.org/10.1016/j.ceramint.2025.12.301

spintronic applications. ErIG crystallizes in a cubic garnet structure with space group *Ia3d*, where Er^{3+} ions occupy dodecahedral (24c) sites, Fe^{3+} ions are distributed between octahedral (16a) and tetrahedral (24d) sites, while O^{2-} ions reside at the 96h positions. The Fe^{3+} ions in octahedral and tetrahedral sites form distinct magnetic sublattices that are antiferromagnetically coupled but unequal in magnitude, resulting in a net magnetization that gives rise to the ferrimagnetic behavior of ErIG. The Er^{3+} ions at dodecahedral sites form a separate magnetic sublattice that weakly antiferromagnetically couples to the resultant magnetization of the Fe sublattices. The Curie temperature in iron garnets is largely independent of the rare-earth ion, as it is primarily determined by the strong exchange interaction between the Fe sublattices. For ErIG, as well as other iron garnets, the Curie temperature is approximately 560 K [33,34]. The magnetizations of the Er and Fe sublattices in ErIG exhibit different temperature dependencies, with the Er sublattice dominating at low temperatures and the Fe sublattices dominating at high temperatures. The temperature at which their opposing magnetizations cancel each other, resulting in zero net magnetization, is known as the compensation temperature (T_{comp}), which for ErIG is approximately 80 ± 5 K [35–37]. At high temperatures, ErIG exhibits an easy magnetization axis along [111], while at low temperatures, it undergoes a spin reorientation toward the [100] direction, and also adopts the so-called double-umbrella structure, in which the Er moments on magnetically inequivalent sites form two canted cones around the Fe axis [37]. This complex spin behavior makes ErIG interesting for both fundamental research and potential applications.

In this paper, we synthesized ErIG nanoparticles and characterized them using XRD, HRTEM, EDX, and Raman spectroscopy. We also performed detailed field- and temperature-dependent magnetic measurements. ErIG was found to exhibit a double MR, a phenomenon not previously reported for this material and observed in only a few other garnets [30–32]. We found that the MR effect is present only in FCC measurements, and completely absent in FCW measurements. Such asymmetry has been reported in systems such as chromates [18,21], but never before in garnets. Additionally, magnetization switching was observed, where the direction of magnetization reverses solely due to changes in the magnitude of the applied field, without altering its direction. These results advance knowledge of ErIG properties and play an important role in the broader understanding of MR in garnets.

2. Experimental

ErIG nanoparticles were prepared by the polyvinyl alcohol (PVA)-mediated sol-gel method. For the preparation of the precursor solution, constituent nitrates $Er(NO_3)_3 \cdot 5H_2O$ and $Fe(NO_3)_3 \cdot 9H_2O$ were used (Sigma-Aldrich). Stoichiometric amounts of the precursors were dissolved in deionized water. The chelating agent PVA was added to the solution in a 1:1 M ratio relative to the total content of metal ions, and the mixture was continuously stirred and maintained at 80 °C to ensure homogeneous gel formation. The resulting gel was dried in an oven at 110 °C for 5 h, and then calcined at 800 °C for 3 h to obtain ErIG nanoparticles.

The crystalline structure of nanocrystalline ErIG was characterized by X-ray diffraction (XRD) using a Rigaku MiniFlex diffractometer with a Cu-Kα radiation source. XRD data were collected over a 2θ range of 10°–80°. The Rietveld refinement of the XRD data was performed using the FullProf Suite. Transmission electron microscopy (TEM), high-resolution transmission electron microscopy (HRTEM) images, and selected area electron diffraction (SAED) patterns were acquired using a JEOL JEM-2100 transmission electron microscope operated at 200 kV. Elemental analysis was performed with an Oxford EDX system attached to the TEM. The room-temperature micro-Raman spectrum was measured in backscattering geometry using a Jobin Yvon T64000 triple spectrometer equipped with a liquid nitrogen-cooled CCD detector and an Ar^+/Kr^+ ion laser operating at a wavelength of 514.5 nm as the excitation source. Magnetic measurements were performed using a Quantum Design MPMS XL5 SQUID magnetometer.

3. Results and discussion

ErIG crystallizes in a body-centered cubic crystal structure with space group *Ia3d* (O_h^{10}, No. 230), schematically presented in Fig. 1. The conventional unit cell contains eight formula units, corresponding to 160 atoms in total. In this structure, the Fe ions occupy two distinct sites: octahedral 16a sites (Fe^O) with sixfold oxygen coordination, and tetrahedral 24d sites (Fe^T) with fourfold oxygen coordination, thus the formula unit can also be represented as $Er_3\left[Fe_2^O\right]\left[Fe_3^T\right]O_{12}$. The Er ions are located at the 24c dodecahedral sites, each surrounded by eight oxygen ions, while the oxygen ions reside at the 96h positions. The room-temperature XRD pattern of the ErIG nanocrystalline sample, along with the Rietveld refinement, is shown in Fig. 2. The diffraction peaks correspond to the body-centered cubic crystal structure of ErIG, indexed to the *Ia3d* space group (JCPDS standard pattern 23–0240). The parameters obtained from the refinement are summarized in Table 1. The obtained crystal lattice constant is 12.34 Å, which is close to previously reported values [38]. Using the Scherrer equation, the average crystallite size was estimated to be approximately 43 nm.

The TEM image in Fig. 3(a) shows a loose agglomeration of irregularly shaped nanoparticles. The histogram of the particle size distribution was analyzed and fitted to a log-normal distribution function, yielding an average grain size of 47 nm. The HRTEM image (Fig. 3(b)) shows distinct lattice fringes with an interplanar spacing of 0.276 nm, corresponding to the (420) planes in the ErIG crystal structure, indicating high crystallinity of the nanoparticles. The SAED pattern (Fig. 3(c)) displays multiple bright rings, characteristic of a polycrystalline sample. EDX analysis was performed to investigate the elemental composition of the synthesized sample, and a representative EDX spectrum of the top surface layers of the nanoparticles is shown in Fig. 3(d). Aside from the Cu peak, which originates from the grid used to disperse the nanoparticles for measurement, only peaks corresponding to Er, Fe, and O were detected, with no impurities observed. The quantitative results are summarized in Table 2, indicating that the elemental composition is close to the stoichiometrically expected values.

The crystalline structure and purity of the ErIG sample were further confirmed by the room-temperature Raman spectrum shown in Fig. 4. Factor-group analysis for the body-centered cubic rare-earth garnet structure with space group *Ia3d* predicts 25 Raman-active phonon modes, classified as $3A_{1g}$, $8E_g$, and $14T_{2g}$ [40–43]. The measured Raman spectrum closely matches those of other rare-earth iron garnets, and the symmetry assignments of the prominent Raman modes are indicated in Fig. 4 according to the literature data [42]. The high-frequency modes (>500 cm^{-1}) are attributed to internal vibrations of the tetrahedral and octahedral units [40,41,44]. In the intermediate region (300–500 cm^{-1}), the E_g modes correspond to internal vibrations involving Er, tetrahedral Fe, and oxygen ions, where Er and Fe vibrate either in phase or out of phase. The T_{2g} modes represent a combination of internal and rotational vibrations of the tetrahedral and octahedral units [44]. The low-frequency modes (<300 cm^{-1}) correspond to translational motions of Er^{3+} ions and the tetrahedral and/or octahedral structural units [40,44,45].

Magnetization curves M(H) were measured at various temperatures between 5 and 300 K, and for clarity, only the selected representative curves are shown in Fig. 5(a). The sample exhibits clear ferrimagnetic behavior at 300 K, with a coercive field of 47 Oe and a remanent magnetization of 1.59 emu/g. Superimposed on the ferrimagnetic behavior is a linear component arising from the paraprocess contribution of Er^{3+} ions. The ferrimagnetic component reaches most of its saturation magnetization of 11.6 emu/g in fields around 2 kOe, and at higher fields, the magnetization is dominated by the linear component. In ErIG, the spin arrangement is governed by a complex interplay among three distinct magnetic sublattices, schematically illustrated in the inset

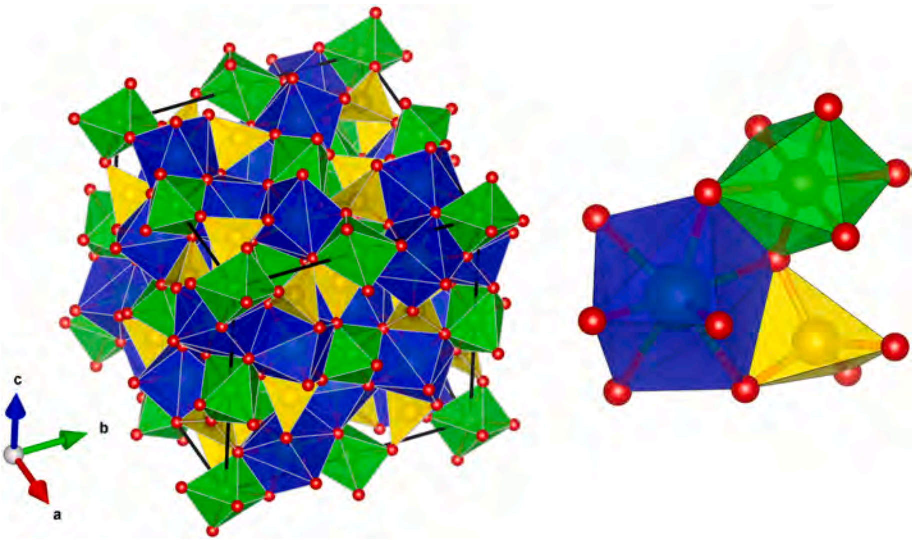

Fig. 1. Crystal Structure of $Er_3Fe_5O_{12}$ ($Er_3\left[Fe_2^O\right]\left[Fe_3^T\right]O_{12}$) erbium iron garnet. The dodecahedral (Er, blue), octahedral (Fe^O, green), and tetrahedral (Fe^T, yellow) local polyhedra environments are shown, with oxygen atoms in red. An enlarged view of one representative set of polyhedra is also included for clarity. The crystal structure was visualized using VESTA 3 [39]. (For interpretation of the references to colour in this figure legend, the reader is referred to the Web version of this article.)

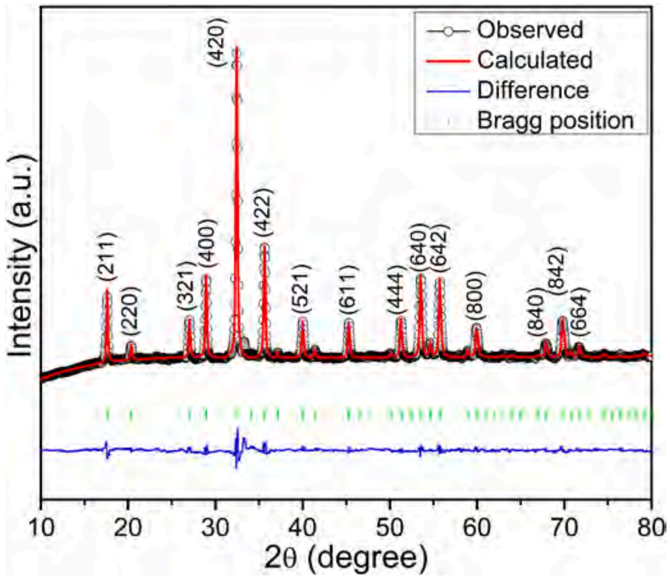

Fig. 2. Rietveld refinement of the XRD pattern of the $Er_3Fe_5O_{12}$ nanocrystalline sample.

Table 1
Crystallographic parameters obtained from the Rietveld refinement of $Er_3Fe_5O_{12}$ at room temperature.

Space group = *Ia3d*, a = 12.3427 Å. χ^2 = 2.856.

Atom	Position	x	y	z
Fe^O	16a	0.000	0.000	0.000
Fe^T	24d	0.375	0.000	0.250
Er	24c	0.125	0.000	0.250
O	96h	−0.0270	0.0568	0.1504

of Fig. 5(b), with magnetizations denoted as M_a, M_d, and M_c. The Fe^{3+} ions occupying octahedral (16a) and tetrahedral (24d) sites are antiferromagnetically coupled due to superexchange interactions mediated by O^{2-} ions. Because the tetrahedral sites host a greater number of Fe^{3+}

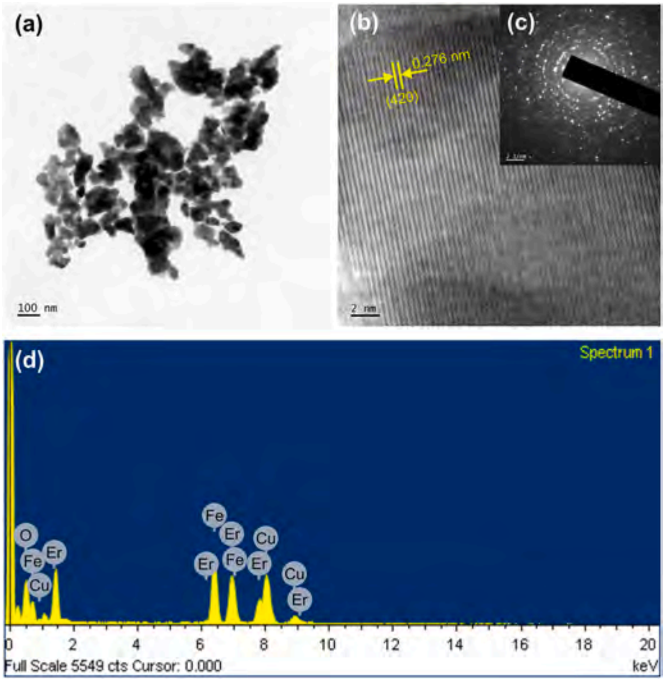

Fig. 3. (a) TEM image, (b) HRTEM image, (c) SAED pattern, and (d) EDX pattern of nanocrystalline $Er_3Fe_5O_{12}$.

Table 2
Elemental composition of the nanocrystalline $Er_3Fe_5O_{12}$ sample obtained from EDX analysis.

Element	Weight % ±5 %	Atomic % ±5 %
O	16.6	55.1
Fe	28.9	27.5
Er	54.5	17.4
Total	100	100

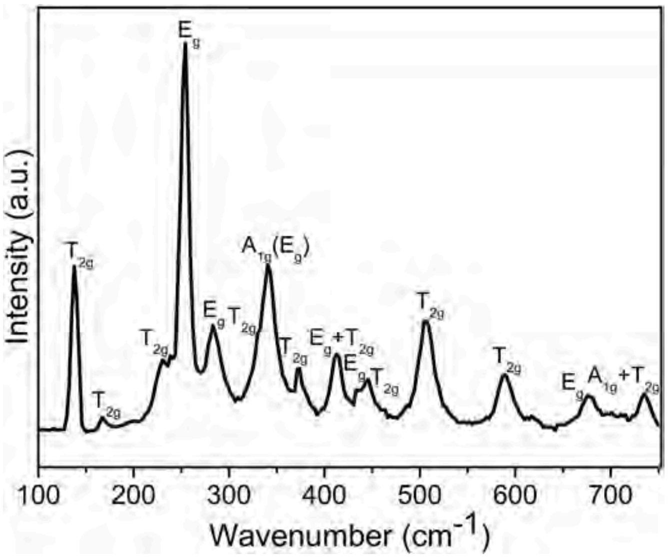

Fig. 4. Room-temperature Raman spectrum of the $Er_3Fe_5O_{12}$ nanocrystalline sample.

ions than the octahedral ones, the magnetization M_d of the tetrahedral sublattice is stronger than the magnetization M_a of the octahedral sublattice, resulting in a net iron sublattice magnetization of $M_d - M_a$. The Er^{3+} ions at the dodecahedral (24c) sites, with magnetization M_c, are antiferromagnetically coupled to the resultant magnetization of the Fe sublattices, leading to a total net moment of $(M_d - M_a) - M_c$. The magnetizations of the Er and Fe sublattices exhibit different temperature dependencies. At low temperatures, the Er sublattice dominates. As the temperature rises, the Er sublattice magnetization decreases more rapidly than that of the Fe sublattices. At the compensation temperature (T_{comp}), the magnetizations of the Er and Fe sublattices cancel each other out, resulting in net zero magnetization. Above T_{comp}, the Fe sublattices dominate the net magnetization of the system. At high temperatures, the Er^{3+} ions exhibit a paramagnetic-like behavior known as the paraprocess, subject to the influence of thermal fluctuations, the external magnetic field, and a weak exchange field produced by the iron sublattices [46–49]. This paraprocess leads to the linear high-field behavior observed in the hysteresis curves at these temperatures (Fig. 5(a)). Fig. 5 (b) shows the temperature dependence of the spontaneous magnetization (M_s), obtained by linear extrapolation of the high-field magnetization to zero field. With decreasing temperature, the spontaneous magnetization decreases and becomes zero at the compensation temperature T_{comp}, below which it increases again. The obtained compensation temperature T_{comp} is approximately 75 K, which is similar to previous findings for ErIG [35–37].

From the linear high-field regions of the hysteresis curves measured at different temperatures, we obtained the susceptibility of the superimposed Er^{3+} paraprocess. The temperature dependence of the inverse susceptibility is shown in Fig. 5(c). It can be seen that this dependence is linear from T_{comp} to room temperature. This linear region was fitted with the Curie-Weiss law (which also applies to paraprocesses [50]), $\chi = C/(T - \theta)$, where C is the Curie constant and θ is the Curie-Weiss temperature. The fit, shown as the red dashed line, yielded a Curie constant of 39.5 emu·K·mol^{-1} Oe^{-1}. The obtained Curie-Weiss temperature in

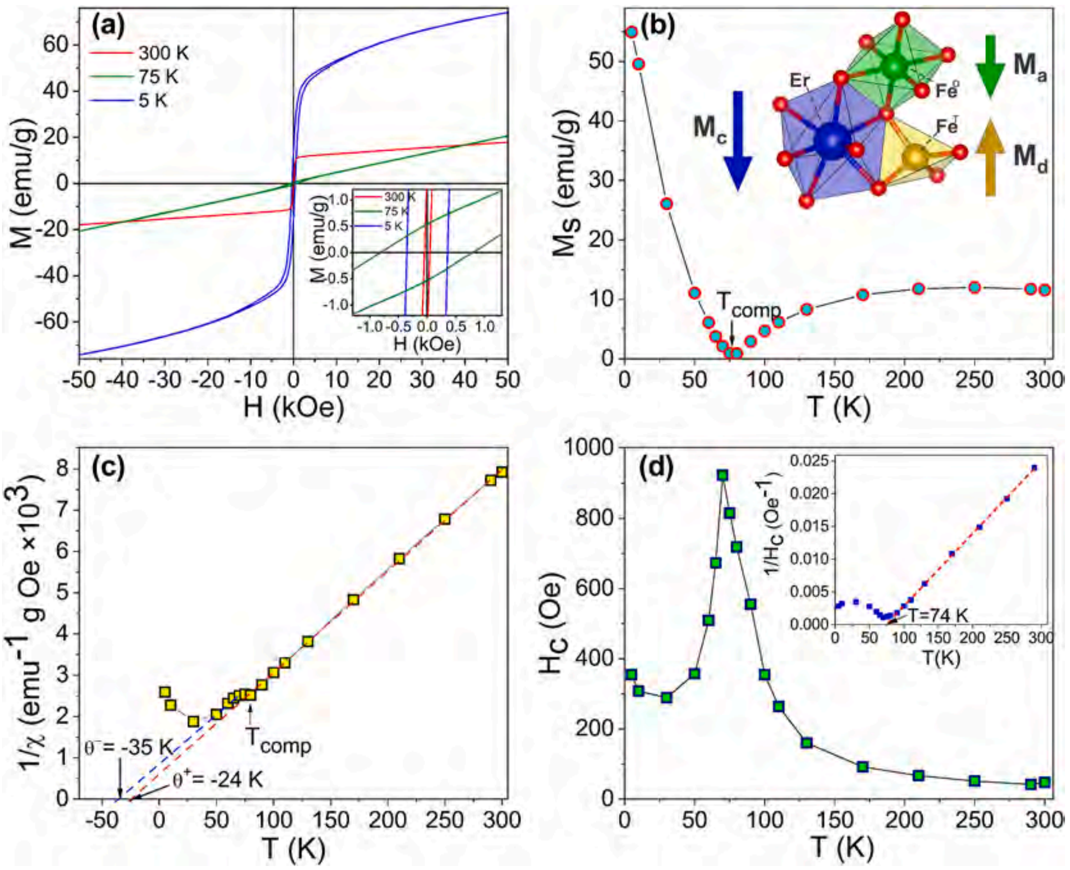

Fig. 5. (a) Magnetization curves M(H) of nanocrystalline $Er_3Fe_5O_{12}$ at selected characteristic temperatures. Inset: a magnified view of the central region of the magnetization curves. (b) Temperature dependence of spontaneous magnetization. Inset: schematic representation of three distinct magnetic sublattices in $Er_3Fe_5O_{12}$. (c) Temperature dependence of the inverse susceptibility, along with Curie–Weiss fits. (d) Temperature dependence of the coercive field. Inset: temperature dependence of its inverse.

this range was $\theta^{+} = -24$ K, indicating a weak antiferromagnetic interaction, and is close to the −19.6 K value reported by Guillot et al. for ErIG single crystal [34,51]. Below T_{comp}, the inverse susceptibility deviates from linear behavior but then enters another short temperature range with linear paraprocess behavior, fitted by the blue dashed line and characterized by a second Curie-Weiss temperature of $\theta^{-} = -35$ K, which is close to the −33 K value reported by Guillot et al. [34,51]. A similar behavior, with two distinct linear paraprocess regions above and below T_{comp} and different Curie-Weiss temperatures, has also been observed in other rare-earth garnets, such as DyIG and HoIG. This has been interpreted as a consequence of differing exchange interactions acting upon rare-earth ions in the respective temperature ranges, with an increasing importance of rare-earth-to-rare-earth exchange interactions at low temperatures [34,51–53].

Fig. 5(d) shows the temperature dependence of the coercive field H_c derived from the hysteresis curves. It can be seen that H_c exhibits a sharp maximum in the vicinity of T_{comp}. This maximum in H_c correlates with the minimum of M_s, indicating that H_c varies approximately inversely with M_s, which is in line with the Stoner–Wohlfarth model [54], where $H_c = 2K/M_s$ and K is the anisotropy constant. Similar behavior has been observed in other rare-earth iron garnets which exhibit either single or double peaks in coercivity near the compensation temperature. In the literature, some confusion remains regarding this behavior. Although the underlying mechanism is generally expected to be the same across all rare-earth iron garnets, reports have shown two coercivity peaks in some compounds [31,46,47,55,56], while others exhibit only a single peak [47,55,57–59]. Moreover, for the same rare-earth iron garnets, certain studies have reported double coercivity peaks, while others have observed only a single peak. For instance, GdIG has been reported to exhibit either a single peak [55,57,59] or double peaks [46,56]. Similarly, HoIG shows a single peak in some studies [55,58] and double peaks in others [31,46,47,55], and DyIG has also been reported with either a single [47,55] or double peak [46]. In the case of ErIG, we observed a single peak in our measurements, while Refs. [46,55] reported double peaks.

Goranskiĭ and Zvezdin [50] proposed a theory based on the Stoner–Wohlfarth model to explain the emergence of a double peak in coercivity near the compensation temperature, which was later extended by Uemura et al. [46]. These models, developed within the molecular-field approximation, assume that near the compensation temperature, the net spontaneous magnetization becomes very small, effectively suppressing magnetostatic interactions. As a result, the system behaves as a single domain, and magnetization reorientation is governed predominantly by coherent rotation under the influence of crystalline anisotropy, rather than by domain wall motion characteristic of multidomain structures. The characteristic double peak in coercivity arises from the interplay between the vanishing net spontaneous magnetization of the iron and rare-earth sublattices at the compensation point, and the paraprocess response of the rare-earth ions, which are influenced by both the external magnetic field and their weak exchange coupling with the iron sublattice. In real materials, however, variations in composition, shape, orientation, compensation temperature, magnetic anisotropy, structural disorder, and other properties across grains and nanoparticles can smear or merge the two peaks, often resulting in a single broadened maximum in the experimental coercivity curve.

The inset in Fig. 5(d) shows the temperature dependence of the inverse coercive field, $1/H_c$. Above the compensation temperature T_{comp}, $1/H_c$ varies linearly with temperature, and a linear extrapolation intersects the temperature axis at 74 K, i.e., near T_{comp}. Since both $1/H_c$ and the inverse paraprocess susceptibility of Er^{3+} ions, $1/\chi$ (Fig. 5(c)), exhibit linear temperature dependence above T_{comp}, this implies that in this range, the coercive field H_c is proportional to susceptibility χ. According to the theories of Goranskiĭ and Zvezdin [50] and Uemura et al. [46], as the temperature moves away from T_{comp} and net magnetization increases, multi-domain structures are expected to form, allowing magnetization reorientation via both domain wall motion and coherent rotation. However, the observed proportionality $H_c \propto \chi$ even well above T_{comp} indicates that coercivity in this range remains governed by the paraprocess of the Er sublattice. This behavior likely reflects the nanostructured nature of the sample, where small particle size suppresses domain wall formation or movement and stabilizes single-domain behavior.

The temperature dependence of the magnetization M(T) was measured under an external magnetic field of 100 Oe using ZFC, FCC, and FCW protocols, as shown in Fig. 6. In the ZFC measurement, the sample was first cooled to 3 K in the absence of a magnetic field, and the magnetization was recorded upon warming under the applied field. Subsequently, the FCC measurement was carried out by cooling the sample from 300 K to 3 K in the presence of the same field, followed by the FCW measurement taken during the warming cycle.

The ZFC curve shows a sharp maximum around 11 K, after which it decreases, reaches zero, and then increases again. Above 11 K, the ZFC curve qualitatively resembles the behavior of the spontaneous magnetization shown in Fig. 5(b), as both are governed by similar underlying dynamics between the Er and Fe sublattices. At low temperatures, the Er sublattice dominates, but its magnetization decreases with increasing temperature more rapidly than that of the Fe sublattice. At a certain temperature, the magnetizations of the two sublattices cancel each other out, and at higher temperatures, the Fe sublattice becomes dominant.

A notable feature in the FCC measurements is the appearance of MR at two compensation temperatures. As can be seen from Fig. 6, with decreasing temperature, the 100 Oe FCC curve exhibits the first MR, crossing zero at $T_{comp1} \approx 75$ K. This temperature corresponds to the T_{comp} determined from the M_s vs. T measurements (Fig. 5(b)), at which the Er and Fe sublattice magnetizations are mutually compensated. Below T_{comp1}, the magnetization becomes negative, i.e., opposite to the direction of the external field. Upon further cooling, the magnetization reaches a maximum negative value, then increases and exhibits the second MR at $T_{comp2} \approx 27$ K, below which it becomes positive again. The FCC curves measured under different applied fields are shown in Fig. 7, with an enlarged view of the region between T_{comp1} and T_{comp2} presented in inset (a). The lower compensation temperature, T_{comp2}, increases with increasing field (inset (b) of Fig. 7), whereas the higher compensation temperature, T_{comp1}, is practically independent of the applied magnetic field. For fields of approximately 1000 Oe and above, T_{comp2} merges with T_{comp1}, and the FCC curve no longer exhibits the MR.

The observed behavior of the FCC curves can be explained as a consequence of competition between the anisotropy energy and Zeeman

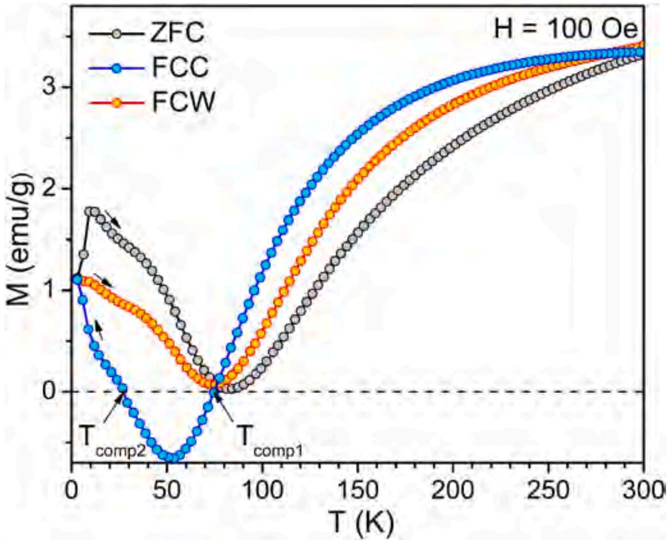

Fig. 6. Temperature-dependent magnetization curves in ZFC, FCC, and FCW measurements at an applied field of 100 Oe.

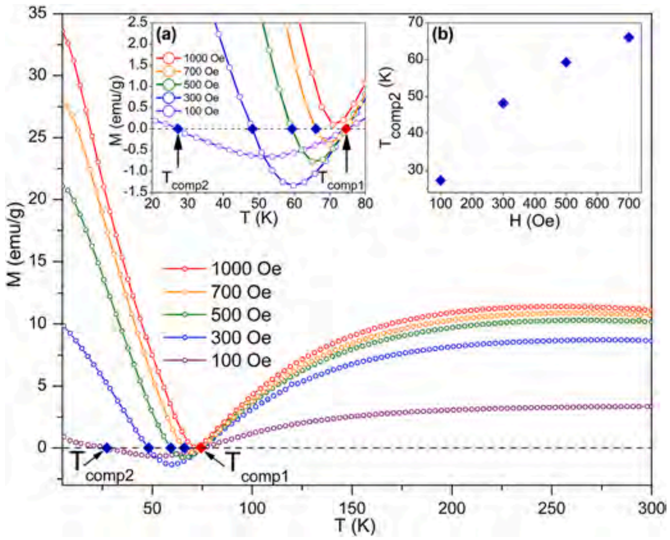

Fig. 7. FCC magnetization curves under various applied fields. Inset (a): enlarged section of the FCC curves in the range between T_{comp1} and T_{comp2}. Inset (b): Variation of T_{comp2} with the applied field.

energy. At high temperatures, above T_{comp1}, the easy axis in ErIG lies along the [111] direction, and the resultant net magnetization is dominated by the Fe sublattices. When an external magnetic field is applied, the net magnetization tends to align with the field direction. The Er and Fe sublattices have antiparallel magnetizations with different temperature dependencies, and at T_{comp1}, their opposing contributions cancel each other. Around T_{comp1}, the easy axis shifts from the [111] to the [100] direction [35,37,60]. With further temperature decrease, the Er sublattice magnetization becomes stronger than that of the Fe sublattices. However, due to the strong magnetocrystalline anisotropy of Er ions, the net magnetization cannot readily reorient along the applied field direction. Instead, it continues to increase in the direction opposite to the applied field, resulting in negative magnetization. Due to the Zeeman energy, this antiparallel orientation of the net magnetization and the field is energetically unfavorable, and below T_{comp1}, as the Er sublattice magnetization becomes increasingly dominant, the net magnetization begins to rotate toward a more favorable parallel alignment with the field. Eventually, the Zeeman energy overcomes the anisotropy barrier, resulting in reorientation of the net magnetization along the direction of the external field, becoming positive again below T_{comp2}. The stronger the applied field, the greater is the Zeeman energy relative to the anisotropy energy, and the increasing magnetization can overcome the anisotropy barrier at higher temperatures, which explains why T_{comp2} shifts to higher temperatures with increasing applied field (Fig. 7). For sufficiently strong fields (~1000 Oe), the Zeeman energy is large enough to rotate the net magnetization, thus preventing the development of negative magnetization. Fig. 8 presents a simplified schematic illustrating only the main features of this evolution. In contrast, the FCW curves do not exhibit negative magnetization at any field. The fact that the FCC starts from a system with the easy axis along the [111] direction, while the FCW starts from a system with the easy axis along the [100] direction, likely plays an important role in the asymmetry between the cooling and warming curves. Related to this, it is also possible that the system exhibits much lower anisotropy when starting from a low temperature and easy axis along the [100] direction, allowing the magnetization to align more readily with the applied field and thereby suppressing the negative magnetization observed in the FCC case.

The MR phenomenon is rare in itself, but MR with two or more compensation temperatures has been reported in an even more limited number of materials, e.g., Refs. [9,11–13,16,18,19,21,31,32], associated with a broad spectrum of different explanatory mechanisms. For instance, in $NdCr_{1-x}Fe_xO_3$, the MR was attributed to the competition between the weak ferromagnetism of Cr^{3+} ions and the paramagnetic moments of Nd^{3+} and Fe^{3+} ions under the effect of a negative internal magnetic field [9]. In YVO_3, the two magnetization reversals were attributed to the competition between single-ion anisotropy and the Dzyaloshinsky–Moriya–driven canting of the antiferromagnetic sublattices [16]. In ErIG, we attribute the double MR to the competition between Zeeman-driven realignment of the magnetization and magnetocrystalline anisotropy. In most materials, the FCW and FCC curves look essentially the same. However, in our ErIG sample, the FCW curve differs markedly from the FCC curve and does not exhibit any MR, remaining positive at all temperatures. Reports that show significantly different behavior between FCC and FCW curves are also relatively rare, e.g., Refs. [18,21,22]. Among garnets, only a few reports have documented the presence of two compensation temperatures [30–32]. However, to the best of our knowledge, no rare-earth garnet compound has been reported to exhibit significantly different behavior between FCW and FCC curves. The presence of spin reorientation certainly plays an important role in this asymmetry. At the same time, spin reorientation is not unique to ErIG, but occurs in other rare-earth garnets as well. However, Er^{3+} has very high anisotropy, particularly at low temperatures, and considering that ErIG has the lowest T_{comp} in this family and that magnetocrystalline anisotropy generally increases with decreasing temperature, and given the importance of anisotropy in the double MR of ErIG, all of this may contribute to the distinct behavior of ErIG relative to other rare-earth garnets.

The appearance of a sharp maximum near 11 K in the ZFC magnetization curve is intriguing. We believe that this feature is related to the different temperature dependencies of the Er sublattice moments in this temperature range. As mentioned earlier, the easy axis shifts from the

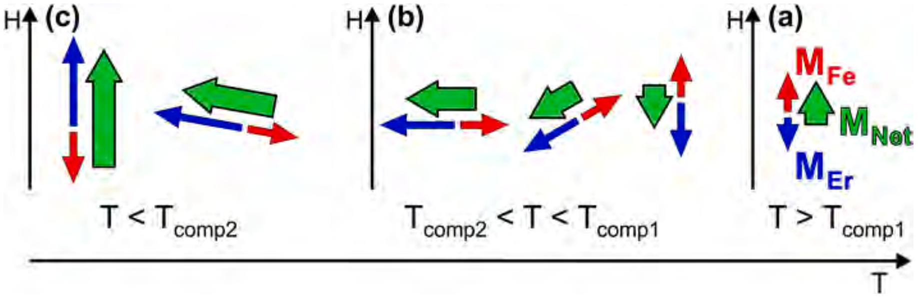

Fig. 8. Schematic illustration of the evolution of magnetic moments in ErIG during FCC, responsible for the observed double magnetization reversal. From right to left, the progression with decreasing temperature is shown. (a) At $T > T_{comp1}$, the Fe sublattice (red) dominates over the Er sublattice (blue), and the net magnetization (M_{Net}, green) is in the direction of the external magnetic field H. (b) Below T_{comp1}, the Er sublattice magnetization begins to dominate. Due to strong anisotropy, M_{Net} does not reorient in the direction of the field, but remains opposite, producing the observed negative magnetization. With further temperature decrease, as the Zeeman energy associated with the growing M_{Net} increases, M_{Net} gradually rotates toward H. (c) Below T_{comp2}, the net magnetization is again oriented toward H and positive. (For interpretation of the references to colour in this figure legend, the reader is referred to the Web version of this article.)

[111] to the [100] direction around and below T_{comp} [35,37,60]. Moreover, below T_{comp}, ErIG also adopts the so-called double-umbrella structure, in which the Er moments form two conical arrangements around the Fe spin axis, with different canting angles and magnetic moments for the two magnetically inequivalent Er sites (8b and 16e). This complex magnetic structure arises from the interplay of crystal-field anisotropy at the Er sites and Fe–Er superexchange interactions. Such a magnetic structure has been observed in ErIG, as well as in several other rare-earth iron garnets, based on neutron diffraction and Mössbauer spectroscopy studies [37,61–65]. From neutron diffraction measurements, Tcheou et al. found that these magnetically inequivalent Er sites form two cones with angles of 14° and 42° relative to the [111] direction [61]. Hock et al. also conducted neutron diffraction studies on ErIG and performed a detailed refinement of its magnetic and crystallographic structure [37]. They found that ErIG adopts the rhombohedral magnetic space group ($R3c'$) above T_{comp}, transitions to a tetragonal magnetic symmetry ($I4_1/ac'd'$) below 65 K, and that the symmetry of the magnetic structure is possibly further lowered to an orthorhombic configuration below 5 K. They also observed that multiple neutron diffraction reflections, most notably the {200} line, display a pronounced intensity maximum near 12 K, which was attributed to the different temperature dependencies of the erbium moments at the 8b and 16e sites. These findings strongly suggest that the 11 K peak observed in the ZFC magnetization curve essentially reflects the same underlying sublattice dynamics responsible for the 12 K intensity maximum observed in neutron diffraction, and arises from the differing temperature evolutions of the Er sublattice moments at the 8b and 16e sites.

Fig. 9 shows the magnetization switching behavior observed in ErIG. The sample was cooled under a magnetic field of 200 Oe down to 73 K (below T_{comp1}), resulting in a negative magnetization (−0.08 emu/g). The magnetization was then monitored as a function of time. When the field was increased to 1000 Oe without changing its direction, the magnetization switched to a positive value (+0.380 emu/g). This MR is achieved by changing only the magnitude of the field while keeping it in the same direction, which is in stark contrast to conventional magnetic materials, where MR would require reversing the field direction. Repeated field cycling between 200 Oe and 1000 Oe induces fully reversible and stable switching between these two magnetization states. As shown in Fig. 9, the magnetization remains constant at each field level, with no time-dependent relaxation, indicating robust and reproducible field-induced reversal. Similar magnetization switching has been reported in other systems such as chromites [6,7,11,18,19], and is considered an attractive property for potential applications.

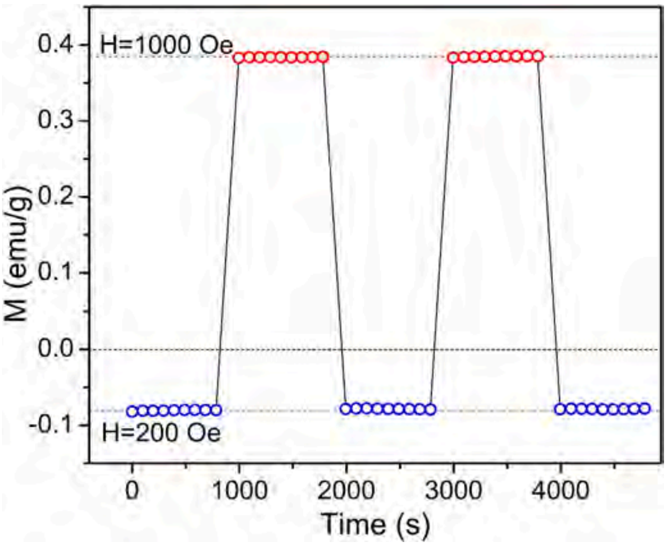

Fig. 9. Magnetization switching in nanocrystalline $Er_3Fe_5O_{12}$ induced by cycling the magnetic field magnitude (200 Oe to 1000 Oe) at 73 K, demonstrating reversible and stable switching under a constant field direction.

4. Conclusions

In summary, $Er_3Fe_5O_{12}$ nanoparticles with the *Ia3d* garnet structure were synthesized via the sol-gel method. M(H) measurements showed that the compensation temperature T_{comp1} is 75 K, and that the coercive field exhibits a single peak near T_{comp1}, indicating that the double coercivity peak often observed in iron garnets is smeared out by variations in grain properties. Two distinct linear paraprocess regions above and below T_{comp1}, each characterized by a different Curie-Weiss temperature, were found, originating from different exchange interactions acting on the rare-earth ions in the respective temperature ranges. Above T_{comp1}, the coercive field was found to be proportional to the paraprocess susceptibility of the Er ions, indicating that coercivity in this temperature range is governed by the paraprocess of the Er sublattice. FCC measurements revealed a double magnetization reversal at two temperatures. The higher T_{comp1} is independent of the applied field, while the lower T_{comp2} increases with increasing field, and for fields above 1000 Oe, the magnetization reversal no longer appears. We interpreted this behavior as a consequence of strong magnetocrystalline anisotropy opposing Zeeman-driven realignment of the net magnetization of the competing Er and Fe sublattices. The magnetization reversals occur only during FCC measurements and are completely absent in the FCW regime. The ZFC curve exhibits a peak at 11 K, which we attributed to the different temperature dependencies of the Er sublattice moments at the 8b and 16e sites. We also observed magnetization switching behavior, in which the magnetization orientation can be reversed by changing only the magnitude of the applied field while keeping its direction fixed. These results reveal interesting and previously unreported aspects of magnetization behavior in ErIG and contribute to the broader understanding of magnetization compensation and reversal processes in rare-earth iron garnets.

CRediT authorship contribution statement

Novica Paunović: Writing – review & editing, Writing – original draft, Visualization, Validation, Project administration, Methodology, Investigation, Funding acquisition, Formal analysis, Data curation, Conceptualization. **Zorana Dohčević-Mitrović:** Writing – review & editing, Writing – original draft, Supervision, Project administration, Methodology, Funding acquisition, Data curation, Conceptualization. **Raneesh Balakrishnan:** Writing – review & editing, Writing – original draft, Visualization, Supervision, Project administration, Methodology, Investigation, Funding acquisition, Formal analysis, Data curation, Conceptualization. **Marko Bošković:** Writing – review & editing, Validation, Resources, Methodology, Investigation, Data curation. **Marija Perović:** Writing – review & editing, Validation, Resources, Methodology, Investigation, Data curation. **Bojan Stojadinović:** Writing – review & editing, Visualization, Methodology, Investigation. **Sobi K. Chacko:** Writing – review & editing, Resources, Methodology, Investigation. **Saša Lazović:** Writing – review & editing, Conceptualization. **Nandakumar Kalarikkal:** Writing – review & editing, Supervision, Project administration, Funding acquisition.

Declaration of competing interest

The authors declare that they have no known competing financial interests or personal relationships that could have appeared to influence the work reported in this paper.

Acknowledgement

The authors gratefully acknowledge funding provided by the Institute of Physics Belgrade, through the grant by the Ministry of Science, Technological Development and Innovation of the Republic of Serbia (Grants No. 451-03-136/2025-03/200024 and 451-03-47/2025-03/200017), and the Serbia-India bilateral project (2022–2024, No. 2). The authors B. R. and N. K. acknowledge the support from the Department of Science and Technology, Govt. of India through India-Serbia Joint S and T project (DST/INT/IND-SERBIA/2022/2). The author N. K. acknowledges SERB: CRG (Grant No. CRG/2021/001506), UGC: Special Assistance Programme (SAP Grant Nos. F.530/12/DRS/2009; F.530/13/DRS II/2016), Scheme for Promotion of Academic and Research Collaboration (SPARC Grant Nos. P930, P1400, P1429, P1460) by MHRD-Govt of India, DST: Nano Mission (Grant No. SR/NM/NS-1420-2014(C)), DST: Fund for Improvement of S&T Infrastructure (FIST Grant No. SR/FST/P SI-143/2009), DAE: UGC-Consortium for Scientific Research (CSR Grant No. UGC-DAE-CSR-KC/CRS/19/RC08/0983/1018), RUSA 2.0 scheme supported by Department of Higher Education, Govt. of India, DAE-Board of Research in Nuclear Sciences (BRNS Grant No. 39/29/2015-BRNS/39009), and DST Promotion of University Research and Scientific Excellence (PURSE Grant No. SR/S9/Z-23/2010/22(C, G)), Government of India programmes for providing facilities for research and development in IIUCNN, MGU.

References

[1] M.L. Néel, Propriétés magnétiques des ferrites; ferrimagnétisme et antiferromagnétisme, Ann. Phys. 12 (3) (1948) 137–198.

[2] E.W. Gorter, J.A. Schulkes, Reversal of spontaneous magnetization as a function of temperature in LiFeCr spinels, Phys. Rev. 90 (3) (1953) 487–488.

[3] A. Kumar, S.M. Yusuf, The phenomenon of negative magnetization and its implications, Phys. Rep. 556 (2015) 1–34.

[4] P. Mandal, A. Sundaresan, C.N.R. Rao, A. Iyo, P.M. Shirage, Y. Tanaka, C. Simon, V. Pralong, O.I. Lebedev, V. Caignaert, B. Raveau, Temperature-induced magnetization reversal in $BiFe_{0.5}Mn_{0.5}O_3$ synthesized at high pressure, Phys. Rev. B 82 (10) (2010) 100416.

[5] S.M. Yusuf, A. Kumar, J.V. Yakhmi, Temperature- and magnetic-field-controlled magnetic pole reversal in a molecular magnetic compound, Appl. Phys. Lett. 95 (18) (2009).

[6] J. Krishna Murthy, A. Venimadhav, Magnetization reversal phenomena and bipolar switching in $La_{1.9}Bi_{0.1}FeCrO_6$, Phys. B Condens. Matter 448 (2014) 162–166.

[7] J. Mao, Y. Sui, X. Zhang, Y. Su, X. Wang, Z. Liu, Y. Wang, R. Zhu, Y. Wang, W. Liu, J. Tang, Temperature- and magnetic-field-induced magnetization reversal in perovskite $YFe_{0.5}Cr_{0.5}O_3$, Appl. Phys. Lett. 98 (19) (2011).

[8] S. Cao, H. Zhao, B. Kang, J. Zhang, W. Ren, Temperature induced spin switching in $SmFeO_3$ single crystal, Sci. Rep. 4 (1) (2014) 5960.

[9] T. Bora, S. Ravi, Sign reversal of magnetization and tunable exchange bias field in $NdCr_{1-x}Fe_xO_3$ (x=0.05–0.2), J. Magn. Magn Mater. 386 (2015) 85–91.

[10] R. Padam, S. Pandya, S. Ravi, A.K. Nigam, S. Ramakrishnan, A.K. Grover, D. Pal, Magnetic compensation effect and phase reversal of exchange bias field across compensation temperature in multiferroic $Co(Cr_{0.95}Fe_{0.05})_2O_4$, Appl. Phys. Lett. 102 (11) (2013).

[11] C. Li, T. Yan, G. Zerihun, Q. Fu, R. Zhang, X. Chen, S. Huang, S. Yuan, Magnetization reversal induced by Mn substitution in spinel chromite $NiCr_2O_4$, J. Am. Ceram. Soc. 101 (12) (2018) 5571–5577.

[12] H.-g. Zhang, W.-h. Wang, E.-k. Liu, X.-d. Tang, G.-j. Li, H.-w. Zhang, G.-h. Wu, Compensation effect and magnetostriction in $CoCr_{2-x}Fe_xO_4$, Phys. Status Solidi 250 (7) (2013) 1287–1292.

[13] Y. Qiu, S.S. Zheng, C.L. Li, G.O. Barasa, M.L. Chen, L. Wang, Y.F. Zhao, Y. Lu, Y. S. Luo, Size-dependent compensation effect and negative magnetization in $Co(Cr_{0.9}Fe_{0.1})_2O_4$ annealed at different temperatures, J. Alloys Compd. 901 (2022) 163692.

[14] J. Mantilla, M. Morales, W. Venceslau, L. Corredor, P.C. Morais, F.F.H. Aragón, S. William da Silva, J.A. Coaquira, Field-driven spin reorientation in $SmMnO_3$ polycrystalline powders, J. Alloys Compd. 845 (2020) 156327.

[15] J. Hemberger, S. Lobina, H.A. Krug von Nidda, N. Tristan, V.Y. Ivanov, A. A. Mukhin, A.M. Balbashov, A. Loidl, Complex interplay of 3d and 4f magnetism in $La_{1-x}Gd_xMnO_3$, Phys. Rev. B 70 (2) (2004) 024414.

[16] Y. Ren, T.T.M. Palstra, D.I. Khomskii, A.A. Nugroho, A.A. Menovsky, G. A. Sawatzky, Magnetic properties of YVO_3 single crystals, Phys. Rev. B 62 (10) (2000) 6577–6586.

[17] A.N. Ulyanov, D.-S. Yang, S.V. Savilov, Negative magnetization, shielding current effect and divalent manganese in $CaMn_{1-x}Ta_xO_3$ manganites, J. Alloys Compd. 967 (2023) 171686.

[18] K. Yoshii, Magnetization reversal in $TmCrO_3$, Mater. Res. Bull. 47 (11) (2012) 3243–3248.

[19] P. Gupta, P. Poddar, Temperature and magnetic field-assisted switching of magnetization and observation of exchange bias in $YbCrO_3$ nanocrystals, Inorg. Chem. 54 (19) (2015) 9509–9516.

[20] Y. Su, J. Zhang, Z. Feng, L. Li, B. Li, Y. Zhou, Z. Chen, S. Cao, Magnetization reversal and Yb^{3+}/Cr^{3+} spin ordering at low temperature for perovskite $YbCrO_3$ chromites, J. Appl. Phys. 108 (1) (2010).

[21] P. Jain, S. Sharma, R. Baumbach, A.K. Yogi, I. Ishant, M. Majumder, T. Siegrist, M. K. Chattopadhyay, N.P. Lalla, Structural role in temperature-induced magnetization reversal revealed in distorted perovskite $Gd_{1-x}Y_xCrO_3$, Phys. Rev. B 109 (9) (2024) 094410.

[22] N. Sharma, B.K. Srivastava, A. Krishnamurthy, A.K. Nigam, Hysteresis in magnetization–temperature curves of the orthochromite $La_{0.1}Gd_{0.9}CrO_3$, J. Alloys Compd. 545 (2012) 50–52.

[23] S.J. Yuan, W. Ren, F. Hong, Y.B. Wang, J.C. Zhang, L. Bellaiche, S.X. Cao, G. Cao, Spin switching and magnetization reversal in single-crystal $NdFeO_3$, Phys. Rev. B 87 (18) (2013) 184405.

[24] T. Bora, S. Ravi, Study of magnetization reversal in $LaCr_{1-x}Fe_xO_3$ compounds, J. Appl. Phys. 114 (3) (2013) 033906.

[25] B. Lüthi, Anomalous magnetizations in the yttrium gallium iron garnet System and the exchange constant of yttrium iron garnet, Phys. Rev. 148 (2) (1966) 519–521.

[26] Y.G. Chukalkin, V.R. Shtirts, Peculiairities of magnetic properties of the garnet $Y_{2.25}Gd_{0.75}Fe_5O_{12}$ irradiated by fast neutrons, Phys. Status Solidi 173 (2) (1999) 459–465.

[27] I.J. Park, K.U. Kang, C.S. Kim, Temperature-Dependent magnetic properties of bismuth substituted terbium–iron garnets, IEEE Trans. Magn. 42 (10) (2006) 2882–2884.

[28] I.J. Park, C.S. Kim, Structural and magnetic characteristics of bismuth substituted holmium iron garnet, Phys. Status Solidi 244 (12) (2007) 4562–4565.

[29] S. Ravi Aakansha, Investigation of negative magnetization and impedance spectroscopy of Sm-substituted gadolinium iron garnets, Mater. Res. Express 6 (12) (2019) 126113.

[30] C. Li, G.O. Barasa, Y. Qiu, S. Yuan, Magnetocaloric effect and sign reversal of magnetic entropy change across the spin reorientation temperature in $R_3Fe_5O_{12}$ (R = Gd, Dy), J. Alloys Compd. 820 (2020) 153138.

[31] M. Ghanathe, A. Kumar, I. da Silva, S.M. Yusuf, Magnetic ordering of Ho and its role in the magnetization reversal and coercivity double peaks in the $Ho_3Fe_5O_{12}$ garnet, J. Magn. Magn Mater. 523 (2021) 167632.

[32] S. Verma, S. Ravi, Analysis of negative magnetization and dielectric studies in holmium substituted samarium iron garnet, Solid State Sci. 139 (2023) 107189.

[33] R. Pauthenet, Spontaneous magnetization of some garnet ferrites and the aluminum substituted garnet ferrites, J. Appl. Phys. 29 (3) (1958) 253–255.

[34] M. Guillot, A. Marchand, F. Tchéou, P. Feldmann, H. Le Gall, Magnetic properties of erbium iron garnet in high magnetic fields up to 150kOe, Z. Phys. B Condens. Matter 44 (1) (1981) 41–52.

[35] M. Guillot, D. Rodic, M. Mitric, Temperature dependencies of the lattice constants and thermal expansion coefficients of $Sm_3Fe_5O_{12}$ and $Er_3Fe_5O_{12}$ single crystals, J. Appl. Phys. 73 (10) (1993) 6304–6306.

[36] K. Abdulvakhidov, A. Soldatov, I. Dmitrenko, Z. Li, S. Kallaev, Z. Omarov, The influence of the structural defects on the physical properties of $Er_3Fe_5O_{12}$ ferrite-garnet, Results Phys. 22 (2021) 103905.

[37] R. Hock, H. Fuess, T. Vogt, M. Bonnet, Low temperature magnetic structure of erbium iron garnet, Z. Phys. B Condens. Matter 82 (2) (1991) 283–294.

[38] J. Zheng, Q. Fu, X. Chen, C. Chakrabarti, P. Wang, H. Yin, C. Li, Y. Qiu, S. Yuan, Colossal dielectric response in erbium iron garnet ceramics, J. Mater. Sci. Mater. Electron. 32 (2020) 290–298.

[39] K. Momma, F. Izumi, VESTA 3 for three-dimensional visualization of crystal, volumetric and morphology data, J. Appl. Crystallogr. 44 (6) (2011) 1272–1276.

[40] G. Mace, G. Schaack, T. Ng, J.A. Koningstein, Optical phonons of terbium-, dysprosium-, and ytterbium-garnet, Zeitschrift für Physik A Hadrons and nuclei 230 (5) (1970) 391–402.

[41] J.P. Hurrell, S.P.S. Porto, I.F. Chang, S.S. Mitra, R.P. Bauman, Optical phonons of yttrium aluminum garnet, Phys. Rev. 173 (3) (1968) 851–856.

[42] J.-J. Song, P.B. Klein, R.L. Wadsack, M. Selders, S. Mroczkowski, R.K. Chang, Raman-active phonons in aluminum, gallium, and iron garnets, J. Opt. Soc. Am. 63 (9) (1973) 1135–1140.

[43] B. Stojadinović, Z. Dohčević-Mitrović, S. Aškrabić, N. Paunović, M.T. Rahul, B. Raneesh, N. Kalarikkal, Spin-phonon interaction in nanocrystalline $Dy_3Fe_5O_{12}$ probed by Raman spectroscopy: effects of magnetic ordering, J. Sci. Adv. Mater. Devices 8 (3) (2023) 100600.

[44] K. Papagelis, G. Kanellis, S. Ves, G.A. Kourouklis, Lattice dynamical properties of the rare Earth aluminum garnets ($RE_3Al_5O_{12}$), Phys. Status Solidi 233 (1) (2002) 134–150.

[45] P.B.A. Fechine, E.N. Silva, A.S. de Menezes, J. Derov, J.W. Stewart, A.J. Drehman, I.F. Vasconcelos, A.P. Ayala, L.P. Cardoso, A.S.B. Sombra, Synthesis, structure and vibrational properties of $GdIG_X$:YIG_{1-X} ferrimagnetic ceramic composite, J. Phys. Chem. Solid. 70 (1) (2009) 202–209.

[46] M. Uemura, T.E.S.C.S. Y, S. Nagata, A double peak of the coercive force near the compensation temperature in the rare earth iron garnets, Philos. Mag. 88 (2) (2008) 209–228.

[47] D.T.T. Nguyet, N.P. Duong, T. Satoh, L.N. Anh, T.T. Loan, T.D. Hien, Crystallization and magnetic characterizations of DyIG and HoIG nanopowders fabricated using citrate sol-gel, J. Sci. Adv. Mater. Devices 1 (2) (2016) 193–199.

[48] D.T.T. Nguyet, N.P. Duong, T. Satoh, L.N. Anh, T.D. Hien, Magnetization and coercivity of nanocrystalline gadolinium iron garnet, J. Magn. Magn Mater. 332 (2013) 180–185.

[49] M. Lahoubi, B. Ouladdiaf, Anomalous magnetic reordering in magnetodielectric terbium iron garnet at low temperatures, J. Magn. Magn Mater. 373 (2015) 108–114.

[50] B.P. Goranskiĭ, A.K. Zvezdin, Temperature dependence of the coercive force of ferrimagnets near the compensation temperature, Sov. Phys. - JETP 30 (1970) 299–301.

[51] M. Guillot, A. Marchand, P. Feldmann, H. Le Gall, J.M. Desvignes, Magnetic properties of single crystal erbium iron garnet, J. Appl. Phys. 50 (B3) (1979) 2112–2114.

[52] M. Guillot, P. Feldmann, H.L. Gall, M. Fadly, Molecular field coefficients of terbium, dysprosium and holmium iron garnets, IEEE Trans. Magn. 14 (5) (1978) 909–911.

[53] M. Fadly, P. Feldmann, H.L. Gall, M. Guillot, H. Makram, Magnetooptical coefficients of Ho3+ ions induced by electric and magnetic dipole transitions in single crystal HoIG, IEEE Trans. Magn. 14 (5) (1978) 448–450.

[54] E.C. Stoner, E.P. Wohlfarth, A mechanism of magnetic hysteresis in heterogeneous alloys, Philos. Trans. R. Soc. Lond., Ser. A Math. Phys. Sci. 240 (826) (1948) 599–642.

[55] J. Hanton, Intrinsic coercive force of rare earth iron garnets near the compensation temperature, IEEE Trans. Magn. 3 (3) (1967) 505–509.

[56] K.P. Belov, Rare-earth magnetic materials, Sov. Phys. Usp. 15 (1) (1972) 130.

[57] P. Coeure, J.C. Gay, J. Carcey, Thermomagnetic properties of fine-grain polycrystalline GdIG, IEEE Trans. Magn. 7 (3) (1971) 397–401.

[58] A.M. Kalashnikova, V.V. Pavlov, A.V. Kimel, A. Kirilyuk, T. Rasing, R.V. Pisarev, Magneto-optical study of holmium iron garnet $Ho_3Fe_5O_{12}$, Low Temp. Phys. 38 (9) (2012) 863–869.

[59] W. Doyle, G. Goldberg, W. Flannery, Thermomagnetic writing in GdIG, IEEE Trans. Magn. 6 (3) (1970) 548–553.

[60] Z.M. Stadnik, G.H.M. Calis, H.V. Lipko, Spin reorientation in erbium iron garnet, Solid State Commun. 38 (1981) 719–722.

[61] F. Tcheou, E.F. Bertaut, H. Fuess, II — neutron diffraction study of some rare earth iron garnets RIG (R = Dy, Er, Yb, Tm) at low temperatures, Solid State Commun. 8 (21) (1970) 1751–1758.

[62] S.J. Pickart, H.A. Alperin, A.E. Clark, Rare-Earth sublattice canting in DyIG, ErIG, and YbIG, J. Appl. Phys. 41 (3) (1970) 1192–1193.

[63] F. Sayetat, Huge magnetostriction in $Tb_3Fe_5O_{12}$, $Dy_3Fe_5O_{12}$, $Ho_3Fe_5O_{12}$, $Er_3Fe_5O_{12}$ garnets, J. Magn. Magn Mater. 58 (3) (1986) 334–346.

[64] H. Young Jun, K. Jun Sig, S. In-Bo, K. Chul Sung, Spin rotation at compensation point studies of $Tb_3Fe_5O_{12}$ by Mössbauer spectroscopy, IEEE Trans. Magn. 40 (4) (2004) 2808–2810.

[65] M. Lahoubi, M. Guillot, A. Marchand, F. Tcheou, E. Roudault, Double umbrella structure in terbium iron garnet, IEEE Trans. Magn. 20 (5) (1984) 1518–1520.

CERTIFICATE OF VISITING PROFESSORSHIP

This is to certify that the School of Pure & Applied Physics (SPAP), International Centre for Ultrafast Studies (ICUS) and International & Inter University Centre for Nanoscience & Nanotechnology (IIUCNN) of Mahatma Gandhi University, Kottayam, Kerala, India bestows the title of **Honorary Visiting Professor** upon

Dr. Bojan Stojadinovic

Institute of Physics, Belgrade, Serbia

as part of the Indo-Serbian Project No: DST/ICD/Serbia/P-02/2021(G) in order to take part in the research and academic activities of SPAP, ICUS and IIUCNN to strengthen our international collaboration.

Prof. (Dr.) Nandakumar Kalarikkal
Hon. Director, ICUS
Senior Professor, SPAP
Mahatma Gandhi University

P. D. HILLS
PIN: 686 560

07-02-2024
Kottayam, Kerala, India

INTERNATIONAL CENTRE FOR ULTRAFAST STUDIES
ICUS
MAHATMA GANDHI UNIVERSITY

विद्यया अमृतमश्नुते

INTERNATIONAL AND INTER UNIVERSITY
IIUCNN
CENTRE FOR NANOSCIENCE AND NANOTECHNOLOGY

International Workshop on Advanced Materials for Emerging Applications (IWAMEA-2024)

January 20-21, 2024

Certificate

This is to certify that Dr. Bojan Stojadinovic, Institute of Physics, Belgrade, Serbia has delivered a plenary talk titled "Insights into Spin-Phonon Interaction in Nanostructures using Raman Spectroscopy" in the International Workshop on Advanced Materials for Emerging Applications (IWAMEA-2024) held on January 20-21, 2024 at the School for Pure and Applied Physics (SPAP), Mahatma Gandhi University, Kottayam, Kerala, India.

Prof. (Dr.) Nandakumar Kalarikkal
Chairman & Convenor, IWAMEA-2024

Subject **Invitation as a plenary speaker for the International Workshop on Advanced Materials for Emerging Applications (IWAMEA-2024)**
From Advanced Materials Laboratory <advancedmaterialslaboratory.mgu@gmail.com>
To <bojans@ipb.ac.rs>
Cc Nandakumar Kalarikkal <nkkalarikkal@mgu.ac.in>
Date 2024-01-10 16:32

- IWAMEA-2024 brochure.jpg (~7.5 MB)
- IWAMEA-2024 schedule.pdf (~144 KB)

Dear Dr. Bojan,

Greetings from Mahatma Gandhi University, Kerala, India!

I hope this email finds you in the best of health and spirits. It is with great pleasure and honour that I extend to you a formal invitation to be a **plenary speaker** for the **"Two Days International Workshop on Advanced Materials for Emerging Applications (IWAMEA-2024)"** jointly organised by the School of Pure & Applied Physics (SPAP), International & Inter University Centre for Nanoscience & Nanotechnology (IIUCNN), International Centre for Ultrafast Studies (ICUS), School of Nanoscience & Nanotechnology (SNSNT) and School of Energy Materials (SEM) of Mahatma Gandhi University in association with the CEFIPRA Project No: 6408-1 and Indo-Serbian Project No: DST/ICD/Serbia/P-02/2021 (G).

IWAMEA-2024 covers a wide range of topics, including nanotechnology, biomaterials, smart materials, renewable energy materials, electronic materials, advanced polymers, and more. This workshop brings together experts and researchers worldwide to discuss and share insights on cutting-edge materials and their potential applications.

As a distinguished researcher in advanced materials for emerging applications, your presence at our workshop would be invaluable in imparting wisdom and expertise to our participants and setting a high standard for the event. We also believe that your extensive experience and accomplishments in advanced materials would give our attendees a unique perspective on the opportunities and challenges within the fields.

Kerala is one of the top tourist destinations in India, known as "God's Own Country", offering a very diverse culture and natural beauty. Kottayam, the heart of Central Kerala, is popularly known as the 'city of letters' and is flanked by the Western Ghats on the east and the Vembanad Lake on the west.

The brochure and tentative schedule of the workshop are also attached for your reference. Thank you for considering our invitation, and we look forward to the possibility of having you as a plenary speaker for IWAMEA-2024.

Best regards,

Prof. Dr. Nandakumar Kalarikkal
Chairman & Convenor, IWAMEA-2024
Senior Professor, School of Pure & Applied Physics
Hon. Director, International Centre for Ultrafast Studies
Mahatma Gandhi University, Kottayam, Kerala, India
www.nandakumarkalarikkal.com

IWAMEA-2024 brochure.jpg
~7.5 MB

International Workshop on Advanced Materials for Emerging Applications (IWAMEA-2024)

JAN 20-21, 2024

Venue: Conference Hall (1st floor), School of Pure & Applied Physics, Mahatma Gandhi University, Kottayam

<u>Tentative Program Schedule</u>

Date	Time	Program
20-01-2024 (FN)	9.30 – 10.00	Inauguration ceremony
	10.00 – 10.45	***Plenary talk 1*** Prof. Kuruvilla Joseph, IIST, Trivandrum
	10.45 – 11.00	Paper presentation 1
	11.00 – 11. 15	Tea break
	11.15 – 12.00	***Plenary talk* 2** Prof. Abhijit Saha, UGC-DAE Consortium, Kolkata
	12.00 – 12.15	Paper presentation 2
	12.15 – 1.00	***Plenary talk* 3** Dr. Novica Paunovic, Institute of Physics, Belgrade, Serbia
20-01-2024 (AN)	1.00 – 2.00	Lunch break
	2.00 – 2.15	Paper presentation 3
	2.15 – 3.00	***Plenary talk* 4** Dr. Bojan Stojadinovic, Institute of Physics, Belgrade, Serbia
	3.00 – 3.15	Paper presentation 4
	3.15 – 3.30	Tea break
	3.30 – 4.15	***Plenary talk* 5** Prof. Sandhyarani, NIT Calicut
	4.15 – 4.30	Paper presentation 5
21-01-2024 (FN)	9.30 – 10.15	***Plenary talk 6*** Prof. Didier Rouxel, Institute of Jean Lamour, Nancy, France
	10.15 – 10.30	Paper presentation 6
	10.30 – 11.05	***Plenary talk* 7** Prof. Sreekala M. S., Mahatma Gandhi University, Kottayam
	11.05 – 11.20	Paper presentation 7
	11.20 – 11.30	Tea break
	11.30 – 12.15	***Plenary talk* 8** Prof. Sabu Thomas, Mahatma Gandhi University, Kottayam
	12.15 – 12.30	Paper presentation 8
	12.30 - 12.45	Paper presentation 9
	12.45 – 1.00	Valedictory ceremony

Total number of plenary talks: 08
Total number of paper presentations: 09

2nd INTERNATIONAL CONFERENCE ON ADVANCED NANOSTRUCTURES (ICAN-2024)

22 - 23 January 2024

Organized by

Post Graduate and Research Department of Physics

Catholicate College, Pathanamthitta, Kerala, 689645

Certificate

This is to Certify that Prof./Dr./Ms./Mrs./Mr. BOJAN STOJADINOVIC

INSTITUTE OF PHYSICS BELGRADE, SERBIA

has presented a paper plenary/invited/short invited/oral/poster/participated at the 2nd INTERNATIONAL CONFERENCE ON ADVANCED NANOSTRUCTURES **(ICAN-2024)** held at Catholicate College, Pathanamthitta, Kerala, India on 22nd & 23rd January 2024.

Dr. Raneesh B.
(Convenor, ICAN 2024)

Dr. George Thomas
(Coordinator, ICAN 2024)

Dr. Sindu Jones
(Principal, Catholicate College)

Post Graduate and Research Department of Physics
Catholicate College, Pathanamthitta, Kerala-689645
Phone: 0468-222 2223, www.catholicatecollege.com

Dr. Raneesh B
Assistant Professor

22.10.2023

To,

Dr. Bojan Stojadinovic
Center for Solid State Physics and New Materials
Institute of Physics Belgrade, Serbia

Dear Dr. Bojan Stojadinovic

Sub: Invitation to 2nd International conference on advanced nanostructures (ICAN-2024)

Greetings from the Post Graduate & Research Department of Physics, Catholicate College, Pathanamthitta, Kerala, India.

I invite you to be an honoured speaker at our upcoming International Conference on Advanced Nanostructures (ICAN-2024). The conference is scheduled to take place on 22 -23 January 2024 at Catholicate College, Pathanamthitta, and we believe that your expertise and insights would greatly contribute to the success of our event. The ICAN-2024 is dedicated to Integrating advancing nanostructures for sustainable applications. Our conference aims to bring together leading experts and researchers worldwide to exchange ideas, foster collaborations, and advance the discourse on nanoscience and nanotechnology. Your presence as a distinguished speaker would undoubtedly enhance the intellectual richness of our program. We kindly request you to confirm your availability at your earliest convenience. We understand the demands on your schedule and greatly appreciate your consideration of this invitation. Please let us know if you require any additional information or have specific preferences. We sincerely hope that you can join us and contribute to the success of this international conference. Thank you for considering our invitation. We look forward to your positive response.

Yours Sincerely

Dr. Raneesh B
(Convener, ICAN-2024)

Dr. RANEESH B
ASSISTANT PROFESSOR
P.G & RESEARCH DEPARTMENT OF PHYSICS
CATHOLICATE COLLEGE
PATHANAMTHITTA, KERALA-689645
E-mail: raneesh.b@gmail.com
Mob: 9645904101

सत्यमेव जयते

भारतीय अंतरिक्ष विज्ञान एवं प्रौद्योगिकी संस्थान
(वि.अ.आयोग अधिनियम 1956 की धारा-3 के अधीन मानित विश्वविद्यालय घोषित)
भारत सरकार, अंतरिक्ष विभाग, वलियमला पोस्ट, तिरुवनंतपुरम 695 547 भारत

INDIAN INSTITUTE OF SPACE SCIENCE AND TECHNOLOGY
(A Deemed to be University u/s 3 of the UGC Act, 1956)
Government of India, Department of Space
Valiamala P. O, Thiruvananthapuram 695 547 India

www.iist.ac.in

Certificate of Appreciation

This certificate is presented to

Dr. Bojan Stojadinović

For sharing his valuable knowledge as a guest speaker in Department of Chemistry on 25th January 2024. The title of the lecture was **"Spin-Phonon Interaction in Multiferroic Nanostructures".**

Dr. K.Y Sandhya
Head
Department of Chemistry
Indian Institute of Space Science and Technology
Thiruvananthapuram, Kerala, India

School of Nanoscience & Nanotechnology (SNSNT)

Mahatma Gandhi University
Kottayam, Kerala, India

CERTIFICATE

of Appreciation

Dr Bojan Stojadinović

Institute of Physics, Belgrade, Serbia

For Delivering a talk
at SNSNT
on the topic Raman Spectroscopy & Magnetic Materials

30th January 2024

Prof. Dr. Sabu Thomas
Hon. Director
SNSNT
MG University
Kottayam, Kerala
India - 686560

Dr Sreekala M S
Joint Director
SNSNT
MG University
Kottayam, Kerala
India - 686560

Department of Physics, Sacred Heart College, Thevara	
Nanomaterials International Symposium 2024 (NIS-24)	
Venue: Fr. Melisius Hall	
Opening Ceremony	9:30 - 9:45 am
Invited talk 1 **Dr. Novica Paunović** Centre for Solid State Physics and New Materials, Institute of Physics, Belgrade, Serbia "Application of far-infrared reflectivity spectroscopy for characterizing nanomaterials"	9:45 - 10:20 am
Invited talk 2 **Dr. Bojan Stojadinović,** Centre for Solid State Physics and New Materials, Institute of Physics, Belgrade, Serbia "Unveiling Spin-Phonon Coupling in Multiferroic Nanostructures through Raman Spectroscopy"	10:20 - 11:00 am
Tea break	11:00 - 11:15 am
Invited talk 3 **Prof. Nandakumar Kalarikkal,** School of Pure and Applied Physics, Mahatma Gandhi University, Kottayam, Kerala, India "Novel nanostructured materials for emerging applications"	11:15 - 12:00
Valedictory function	12:00 -12:30 pm

SACRED HEART COLLEGE
Autonomous

Dr. Bojan Stojadinovic

We, the Sacred Heart Family acknowledge
***Dr. Bojan Stojadinovic**,*
Centre for Solid State Physics and New Materials,
Institute of Physics, Belgrade, Serbia,
for the outstanding contributions as an
Invited Speaker** at the **Nanomaterials
International Symposium, 2024.

We appreciate your pioneering
insights and commitment
to advancing the frontiers of
science and technology.

Application of far-infrared reflectivity spectroscopy for characterizing materials

Novica Paunovic

Institute of Physics Belgrade, University of Belgrade, Pregrevica 118, 11080 Belgrade, Serbia

Abstract

Far-infrared reflectivity spectroscopy is a powerful and nondestructive technique for investigating materials. It can offer valuable insights into the behavior of phonons, plasmons, and other quasiparticles in various materials. The reflectivity spectra can be analyzed by fitting it to appropriate theoretical models, such as the 3-parameters model (also known as the classical oscillator/Lorenz model) or the 4-parameters model (also known as the factorized model) for phonons. In the case of presence of free charges, models like Drude or Extended Drude can be applied, or the coupled plasmon-phonon model. On the other hand, the spectra can also be analyzed by the application of the Kramers-Kronig analysis. For heterogeneous or porous samples, the sample's heterogeneity must be considered through the application of an effective medium approximation, such as Maxwell-Garnett or Bruggeman. This is exemplified through our investigations of far-infrared spectra of CeO_2 and $MgFe_2O_4$ nanoparticles.

Exploring Raman Spectroscopy: A Special Focus on Spin-Phonon Interaction in Multiferroic Nanostructures

Bojan Stojadinović[1], Novica Paunović[1], Zorana Dohčević-Mitrović[1], M. T. Rahul[2], B. Raneesh[2], Nandakumar Kalarikkal[3, 4]

[1] Institute of Physics Belgrade, University of Belgrade, Pregrevica 118, 11080 Belgrade, Serbia

[2] Department of Physics, Catholicate College, Pathanamthitta, Kerala, 689 645, India

[3] School of Pure and Applied Physics, Mahatma Gandhi University, Kottayam, 686 560, India

[4] International & Inter University Centre for Nanoscience and Nanotechnology, Mahatma Gandhi University, Kottayam, Kerala, 686 560, India

Abstract

Raman spectroscopy is a powerful technique for investigating the vibrational properties of materials, providing valuable information about their structural and electronic properties. In the context of magnetic nanostructures, Raman

spectroscopy offers a unique opportunity to delve into the intricate interplay between spin and lattice degrees of freedom, known as spin-phonon coupling. This coupling plays a crucial role in manipulating the magnetic, ferroelectric, and magneto-electric properties of composite nanostructures. In magnetic systems, the spin-phonon interaction often results in anomalous temperature dependencies in the frequencies of optical phonons. These deviations from conventional behavior are attributed to the influence of exchange coupling between magnetic ions, particularly near and below the temperatures of magnetic phase transitions. The complex nature of magnetic interactions in nanomaterials leads to varying coupling strengths between lattice vibrations and magnetic order for different phonon modes, even when the spin-spin interactions are identical. Raman spectroscopy enables the observation of deviations from anharmonic behavior in phonon frequencies, which are reflected as positive or negative frequency shifts in the Raman spectra below the magnetic ordering temperature. The magnitude and direction of these shifts depend on the relative strengths of antiferromagnetic (AFM) or ferromagnetic (FM) exchange interactions. By analyzing these frequency shifts, estimates for the spin-phonon coupling strength can be obtained.

To illustrate the spin-phonon coupling mechanism, we will focus on two distinct types of magnetic nanomaterials: antiferromagnetic bismuth ferrite (BiFeO3) and ferrimagnetic iron garnets (Dy3Fe5O12). Through a mean field approach, we elucidate the spin-phonon interaction in these materials, allowing for the extraction of the spin-spin correlation function. Moreover, this approach facilitates a quantitative assessment of the spin-phonon coupling strength for different phonon modes, shedding light on the underlying mechanisms governing the magnetic properties of these systems.

Call for PAPERS

Final call

INTERNATIONAL CONFERENCE *ON* LIGHT MATTER INTERACTION & ULTRAFAST PROCESSES

1-4 MARCH 2024

Jointly organised by International Centre for Ultrafast Studies (ICUS), International and Inter University Centre for Nanoscience and Nanotechnology (IIUCNN), and School of Pure and Applied Physics (SPAP), Mahatma Gandhi University, Kottayam-686 560, Kerala, India

AIM OF THE CONFERENCE

Over the past decade, significant advancements have propelled the field of ultrafast phenomena to new heights. From enhancing our grasp of fundamental physics to driving innovations in photonics, materials science, and quantum computing, the study of light-matter interaction and ultrafast processes holds vast potential and is a swiftly evolving and thrilling field. The central objective of ICLMIUP 2024 is to furnish a comprehensive overview of the current status of developments in systems that encompass both light-matter interaction and ultrafast processes. This extends to the need for organisational principles, detailed material investigations, and the emergence of cutting-edge sources for generating ultrashort pulses of light, including technologies like high-harmonic generation, few-cycle optical pulses, x-ray-free electron lasers, and new material development. Another integral aim of ICLMIUP 2024 is to establish an international forum for gathering the community of scientists, engineers, and researchers in a unified framework, fostering novel ideas and collaborations in understanding the physics of light-matter interaction and ultrafast phenomena. Hence, ICLMIUP 2024 will be a platform for younger minds to interact with the pioneers of this field, the hot topic of discussion currently in the limelight of the Nobel Prize in Physics 2023.

CONFERENCE ORGANISATION

PATRON: Prof. (Dr.) C.T. Aravindakumar
Hon.Vice-Chancellor, Mahatma Gandhi University
CHAIRMAN & CONVENOR
Prof. (Dr.) Nandakumar Kalarikkal
Hon.Director, International Centre for Ultrafast Studies (ICUS)
Mahatma Gandhi University

LOCAL ADVISORY COMMITTEE

Prof. (Dr.) Sabu Thomas
Former Vice-Chancellor, Hon. Director, IIUCNN, SNSNT & SEM
Mahatma Gandhi University

Prof. (Dr.) Cyriac Joseph
Director, SPAP, Mahatma Gandhi University

Dr. Sreekala M S
Joint Director, IIUCNN & SNSNT Mahatma Gandhi University

School of Pure and Applied Physics
Mahatma Gandhi University, PD Hills PO, Kottayam Kerala

ACCOMMODATION

Accommodations for students and young researchers will be provided in the limited dormitory facilities available in the university guest house on a first-come, first-served basis. Other delegates and participants can contact the hotels near the university for their accommodations, as suggested in the conference website.

SCOPE OF THE CONFERENCE

- Ultrafast Processes
- Ultrafast Spectroscopy
- Ultrafast Photochemistry
- Light Matter Interaction
- Novel Sources of Lasers
- Imaging, Communication and Defense Applications
- Nonlinear Optics
- Laser Plasma Interaction
- Laser Ablation
- Laser Material Processing
- Spin Lasers
- Lasing from Disordered Systems
- Attophysics
- Ultrashort Laser Pulse Technologies
- Medical Photonics
- Novel Nanomaterials
- Additive Manufacturing
- Computational/ Theoretical Modeling

REGISTRATION FEE

*International delegate: € 400
*International student: € 300
*Accompanying person: € 300
Indian delegate: ₹ 5000
Student delegate from India: ₹ 3000
Accompanying person: ₹ 2500
Industrial delegate: ₹ 10000

Early bird registration

**International delegate: € 300*
**International student: € 275*
**Accompanying person: € 275*
Indian delegate: ₹ 4000
Student delegate from India: ₹ 2500
Accompanying person: ₹ 2000
Industrial delegate: ₹ 9000

As a registered delegate, you'll receive a conference kit, complimentary meals, a boat cruise on Vembanadu Lake, and a conference banquet featuring traditional Kerala cultural programs

* In the case of foriegn delegates, registration fee covers accommodation also

The conference registration fee may be sent in favour of:
The Director, University Centre for Ultrafast Studies (UCUS)
Mahatma Gandhi University
Account No: 42391888610
IFSC CODE: SBIN0070669
Branch Code :70669
Payable at State Bank of India, MG University Campus, Kottayam, Kerala-686560, India (Full address of the sending person should be included during money transfer)

FOR MORE INFORMATION
https://iiucnn.in/conferences/iclu2024 www.mgu.ac.in
Email: iclmiup@gmail.com

KEY DATES

Abstract Submission Deadline	Acceptance Intimation	Registration Deadline	Pre-conference Workshop	Conference
25 February 2024	27 February 2024	28 February 2024	1 March 2024	2-4 March 2024

Science and Engineering Research Board (SERB)
Department of Science and Technology (DST)
Govt. of India

KERALA STATE COUNCIL FOR SCIENCE, TECHNOLOGY AND ENVIRONMENT

SPEAKERS GALLERY

Prof. Carlo Spartaco Casari
Politecnico di Milano, Italy

Dr. Murukeshan Vadakke Matham
Nanyang Technological University, Singapore

Prof. M K Jayaraj
Hon. Vice Chancellor, University of Calicut, India

Dr. Erik Dujardin
French National Centre for Scientific Research, France

Prof. Reji Philip
Raman Research Institute, India

Dr. Vandana Sharma
Indian Institute of Technology, Hyderabad, India

Prof. Rakesh K Vaid
University of Jammu, India

Prof. Alika Khare
Indian Institute of Technology, Guwahati, India

Prof. Abhijit Saha
Former Director, UGC-DAE CSR, Kolkata
Visiting Professor, Mahatma Gandhi University, India

Prof. Swapna S Nair
Central University of Kerala, India

Dr. P. Prem Kiran
University of Hyderabad, India

Prof. Sai Santosh Kumar Raavi
Indian Institute of Technology, Hyderabad, India

Dr. R. S. Jayasree
Sree Chitra Tirunal Institute for Medical
Sciences and Technology, India

Prof K L Yadav
Indian Institute of Technology Roorkee, India

Dr. Rajeev N. Kini
Indian Institute of Science Education
and Research (IISER), Thiruvananthapuram, India

Dr Jinto Thomas
Institute For Plasma Research,India

Dr. Bojan Stojadinovic
Institute of Physics, Belgrade, Serbia

Dr. Novica Paunović
Institute of Physics, Belgrade, Serbia

Dr. Riju C Issac
Cochin University of Science & Technology, India

Dr. Gayathri Bharathan
Indian Institute of Technology Delhi, India

Dr. Krishna Kanta Haldar
Central University of Panjab, India

Dr.Sreekanth Perumbilavil
Nanyang Technological University, Singapore

Prof. Olivier J.F. Martin
EPFL STI IMT NAM, Switzerland

Prof Jacob Philip
Former Professor Emeritus at Cochin University of Science and Technology & Visiting Professor
Mahatma Gandhi University, India

Prof. Didier Rouxel
Institute of Jean Lamour, France

Prof. Alex Schechter
Department of Chemical Sciences, Ariel University, Israel

Prof. Soma Venugopal Rao
University of Hyderabad, India

Prof. N. Sandhyarani
Nanional Institute of Technology, Calicut, India

Prof. Anindya Datta
Indian Institute of Technology, Bombay, India

Prof. P.M.G. Nambissan
Saha Institute of Nuclear Physics, DAE
Govt of India

Dr. Isabelle Russier Antoine
Institut Lumière Matière, UMR5306 CNRS, France

Dr. Chaitanya Lekshmi Indira
Plaksha University, India

Dr. Ravi A. V. Kumar
Institute For Plasma Research, India

Dr. Sivarama Krishnan
Indian Institute of Technology Madras, India

Dr. Suchand Sandeep C S
Manipal Institute of Technology, India

Dr. Mukesh Jewariya
CSIR-National Physical Laboratory-New Delhi, India

Dr Anisha Gokarna
University of Technology of Troyes, France

Dr. Akhilesh Kumar Mishra
Indian Institute of Technology Roorkee, India

Dr Bhuvanesh Ramakrishna
Indian Institute of Technology Hyderabad, India

Dr. Subramanyan Namboodiri Varanakkottu
National Institute of Technology, Calicut, India

Dr Arijit K De
Indian Institute of Science Education
and Research (IISER) Mohali, India

Dr. Tapasi Sen
Institute of Nano Science and Technology, Mohali India

Dr Anoop K K
Cochin University of Science & Technology, India

SERB
Science and Engineering Research Board (SERB)
Department of Science and Technology (DST)
Govt. of India

KERALA STATE COUNCIL FOR SCIENCE, TECHNOLOGY AND ENVIRONMENT

LASER SCIENCE
Bringing Tomorrow's Technology Today

ATOS

OXFORD INSTRUMENTS
WITec

Basil Biosolutions

Prof C Vijayan
Indian Institute of Technology, Madras, India

Dr Isabelle Royaud
Institute of Jean Lamour, France

Mr. Jagadesh Obulapuram
Laser Science (I) Pvt. Ltd, India

Mr.Gregory Malinowski
Institute of Jean Lamour, France

Mr. Jon Gorchon
Institute of Jean Lamour, France

CONFERENCE HIGHLIGHTS

- Special focus on Ultrafast Phenomenon
- Prominent speakers and invitees from across the world
- Paper presentation in more than 10 thematic Areas
- Keynote, plenary, contributory and short invited lectures
- Poster presentation
- Industry-academia conclave
- Brain-storming sessions
- Young researcher awards
- Conference publication
- Follow-up programs

PANEL DISCUSSION

To culminate the conference, a comprehensive panel discussion is scheduled on its final day. This session aims to consolidate and summarize the key deliberations and insights garnered throughout the event.

INDUSTRY- ACADEMIA COLLABORATIONS

We aim to facilitate robust business-to-business interactions among numerous companies from both India and abroad. This endeavor seeks to foster new collaborations, joint ventures, and technology transfers among multinational corporations, medium-scale enterprises, and small-scale industrial units worldwide.

EXHIBITION

A prominent exhibition featuring diverse companies within the subject field is scheduled. Additionally, we will extend invitations to ancillary units and companies specializing in supplying key characterization instruments.

ABOUT ICUS

This interdisciplinary research center specializes in ultrafast spectroscopy, photo-physics, and photochemistry, conducting cutting-edge theoretical and experimental investigations into photo-excited state dynamics in functional materials. The center explores applications of pulsed lasers in material processing, femtosecond Laser Induced Breakdown Spectroscopy (fsLIBS), water splitting, optical diagnostics, light-activated advanced cancer therapies, and the laser-assisted fabrication of renewable energy materials. Recognizing the infancy of photon-based technologies in India, the center seeks to contribute to the country's economic and social potential by supporting collaborations between national and international institutions. By generating human resources in ultrafast laser science, the center strives to address the nation's future needs in Photonics, Energy, Communication, and Healthcare.

ABOUT KERALA

Kerala, known as 'God's Own Country,' is a stunning state in southern India. Its lush greenery, backwaters, and beaches attract visitors worldwide. The region boasts diverse landscapes, from mountains to coastlines. Kerala's rich heritage, festivals, and delicious cuisine add to its charm. Whether relaxing on a houseboat or exploring wildlife sanctuaries, Kerala offers unforgettable experiences.

Mr. Anand V Vazhappilly
ATOS Instruments Marketing Services, India

Mr. Vaidotas Stalilionis
Light Conversion, Lithuania

Dr P T Ajith Kumar
Light Logics Holography & Optics Pvt. Ltd, India

Dr. Ponnan Sathiyanathan
Korea Advanced Institute of Science
and Technology (KAIST), Republic of Korea

In view of your excellent contributions to the field of light matter interaction science, we would like to welcome you to give an expert talks and poster presentations at the conference. The scientific committee of the conference is aware of your published works in this field.

We would appreciate if you could submit a one-page abstract of the talk or presentation (in the MS Word format) at the earliest to the conference email:iclmiup@gmail.com or website https://iiucnn.in/conferences/iclu2024.

The Young Researcher Award and Best Poster Award will be presented during the event, distinguishing outstanding achievements among short-invited talks and student posters. An international jury will meticulously assess both the posters and short-invited talks, recognizing excellence and innovation in the contributions made by the participating students.

PUBLICATION OF RESEARCH PAPERS

The selected papers will be published in peer reviewed International Conference Proceedings. The details will be announced soon. We also have got acceptance from renowned publishers and will publish one book based on this conference. All the papers for the journals and for the books will be peer reviewed by international experts before publication. The proposed book and journals are indexed by Scopus database.

ABOUT MAHATMA GANDHI UNIVERSITY

Established on October 2, 1983, Mahatma Gandhi University in Kerala caters to the higher educational needs of Central Kerala through its diverse programs at various academic levels. With 17 University Departments, 1 International and Inter-University Centre, and numerous affiliated colleges and research centers, the university offers research programs in forty disciplines, collaborating with renowned international institutions. The Erudite Scholar in Residence Programme facilitates direct interactions with Nobel Laureates. Notably, MGU has earned accolades, ranking 34th in the National Institution Ranking Framework (NIRF 2018), 11th in IndiaToday–MDRA Ranking 2018, and securing the 30th position in the recent NIRF ranking (April 2019). Additionally, CSIR and NISTADS have recognized the university's intellectual productivity and h-index of the Science faculty, further affirming its academic excellence.

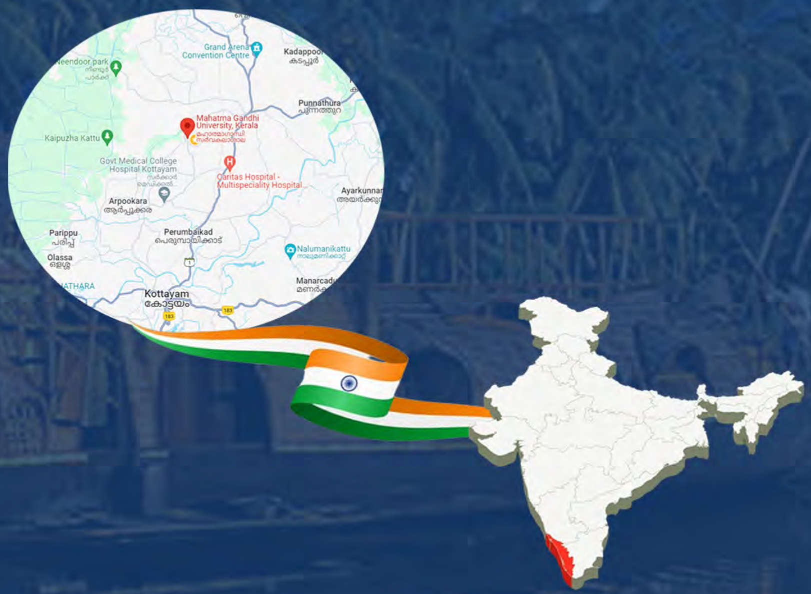

Science and Engineering Research Board (SERB)
Department of Science and Technology (DST)
Govt. of India

KERALA STATE COUNCIL FOR SCIENCE, TECHNOLOGY AND ENVIRONMENT

LASER SCIENCE
Bringing Tomorrow's Technology Today

ATOS

OXFORD INSTRUMENTS
WITec

Basil Biosolutions

ЗАДУЖБИНА

основана 1878.

ЦЕНТАР ЗА ПРЕДАВАЧКУ ДЕЛАТНОСТ

У сарадњи са **Институтом за физику**

Циклус

ДОБА НОВИХ МАТЕРИЈАЛА

1. **Центар за физику чврстог стања**
и нове материјале у свету квантних материјала:
гвоздено доба суперпроводности – случај Fe (Se:S)
Др Ненад Лазаревић (25. март 2025)

2. **Детекција наноскалских скривених фаза**
у квантним материјалима
на великим истраживачким постројењима
Др Емил Божин (1. април 2025)

3. **Револуција 2Д материјала:**
потенцијал полупроводничких наномрежа
Др Јелена Пешић (8. април 2025)

4. **Интеракција јона и електромагнетских поља**
са микро-нано и биоматеријалима са
потенцијалом примене у развоју нових технологија
Др Анђелија Илић (15. април 2025)

5. **Истраживање спин-фононске интеракције у**
мултифероилчним наноструктурама:
улога Рамановe спектроскопије
Др Бојан Стојадиновић (22. април 2025)

Мала сала Коларчеве задужбине, уторком од 18.00
Улаз слободан

Conference Chairs

Nenad Lazarević, *Institute of Physics Belgrade, Serbia*
Emil S. Božin, *Institute of Physics Belgrade, Serbia*
Rudi Hackl, *IFW Dresden, Germany*
Zoran V. Popović, *Serbian Academy of Sciences and Arts (SANU), Serbia* – honorary chair

Organizing Committee

Jelena Pešić - chair
Bojana Višić – chair

Ana Kanjevac
Ana Milosavljević
Andrijana Šolajić
Barbara Bekić
Bojan Stojadinović
Branka Hadžić
Ivana Milošević
Jasmina Lazarević
Jelena Mitrić
Jelena Trajković
Jovan Blagojević
Lenka Filipović
Marko Opačić
Milica Petrović
Nataša Tomić
Novica Paunović
Tea Belojica
Tijana Tomašević Ilić

Role of terbium doping in controlling oxygen vacancies and enhancing conductive performance in $BiFeO_3$ thin films

Bojan Stojadinović [a], Igor Popov [b], Borislav Vasić [a], Dejan Pjević [c],
Milena Rosić [c], Nenad Tadić [d], Zorana Dohčević-Mitrović [a]

[a] *Institute of Physics Belgrade, University of Belgrade, Pregrevica 118, 11080 Belgrade, Serbia*
[b] *Institute for Multidisciplinary Research, University of Belgrade, Kneza Višeslava 1, 11000 Belgrade, Serbia*
[c] *Institute of Nuclear Sciences, "Vinča", University of Belgrade, P. O. Box 522, 11000 Belgrade, Serbia*
[d] *Faculty of Physics, University of Belgrade, Studentski trg 12-16, 11000 Belgrade, Serbia*

Abstract. The influence of Tb doping on structural and electrical properties of $BiFeO_3$ thin films is investigated, combining the experimental observations and density functional theory. With such an approach we aimed to elucidate the influence of Tb dopant and defects in the form of oxygen vacancies on electronic structure and electrical conductivity of $BiFeO_3$ films. X-ray diffraction confirmed that the rhombohedral (*R3c*) crystal structure remains stable in the whole doping range without any impurity phases. Relatively large leakage current was generated in pure $BiFeO_3$ and 5% and 20% Tb-doped films. Significant reduction of electrical conductivity was seen only in 10% Tb-doped film. Conductive atomic force microscopy (C-AFM) allowed us to investigate local electrical conduction properties at the microscale level. The 10% Tb doped film exhibited the smallest conductive surface confirming that this sample has the smallest conductivity, whereas the current maps revealed that the conduction takes place across spatially inhomogeneous grain boundaries with enhanced concentration of defects. The Raman and XPS measurements have shown that oxygen vacancies are the dominant defects in $Bi_{1-x}Tb_xFeO_3$ films. The higher concentration of oxygen vacancies, found in pure, 5% and 20% Tb-doped films can be responsible for higher conductivity of these films. A reduction in oxygen vacancy concentration was registered in 10% Tb-doped film which is in accordance with much lower conductivity of this sample. Density functional theory calculations provide atomic-level insights into the electronic transport mechanisms and are consistent with experimental findings. Undoped and low level Tb-doped samples (~5%) are conductive due to n-type dopants in the form of oxygen vacancies which are primarily localized on surface. For intermediate Tb doping (~10%), the balance between the effects of oxygen vacancies and dopant-induced states results in the highest electrical resistivity. Increased conductivity at higher doping levels (~20%) can be attributed to the denser population of Tb states around the Fermi level, which can overlap, presenting dispersive, conducting states. This work underlines the complex interplay of doping concentration, oxygen vacancies, and electronic transport, suggesting that 10% of Tb is an optimal dopant concentration for enhancing the electrical performances of $BiFeO_3$ thin films.

Subject **Submission Receipt - Structural, ferroelectric and magnetic properties of Bi5Ti3FeO15 Aurivillius-based multiferroic materials**
From electroceramicsxix <notifications@exordo.com>
To <bojans@ipb.ac.rs>
Reply-To electroceramicsxix <electroceramics@ecers.org>
Date 2024-04-29 15:45

19 - 22 August 2024

Electroceramicsxix

https://electroceramicsxix.exordo.com

Dear Bojan,

You have received this email receipt, as you are listed as one of the co-authors on the submission below. Please take a moment to review the submission.

You can make changes by logging in to your Ex Ordo Dashboard and using the 'Edit' prompt on your My Submissions card (on or before Sunday, 5th May 2024 @ 23:59 Europe/Brussels). Further information on how to edit your submission can be found in the article below:

https://support.exordo.com/article/474-editing-your-submission

Structural, ferroelectric and magnetic properties of Bi5Ti3FeO15 Aurivillius-based multiferroic materials

- Jelena Bobic (University of Belgrade, Institute for Multidisciplinary Research, Kneza Viseslava 1, 11 000 Belgrade, Serbia)
- Nikola Ilic (Vinča Institute of Nuclear Sciences, National Institute of the Republic of Serbia, University of Belgrade, Mike Petrovića Alasa 12-14, 11000 Belgrade, Serbia)
- Roberats Grigalaitis (Faculty of Physics, Vilnius University)
- Adis Džunuzović (University of Belgrade, Institute for Multidisciplinary Research, Kneza Viseslava 1, 11 000 Belgrade, Serbia)
- Mirjana Vijatović Petrović (University of Belgrade, Institute for Multidisciplinary Research, Kneza Viseslava 1, 11 000 Belgrade, Serbia)
- Ivan Stijepović (Faculty of Technology Novi Sad, University of Novi Sad)
- Bojan Stojadinovic (Institute of Physics, University of Belgrade)
- Biljana Stojanović (University of Belgrade, Institute for Multidisciplinary Research, Kneza Viseslava 1, 11 000 Belgrade, Serbia)

Abstract

Lately, considerable attention has been given to developing magnetoelectric-active materials in

microelectronics and spintronics [1]. Among many structures from the Aurivillius family, $Bi_5FeTi_3O_{15}$ (BFT) provides the development of ferroelectricity and magnetism and allows different site substitutions to improve the material's properties [2]. The main motivation was to investigate the influence of partial substitution of isovalent Y^{3+} and rare-earth Gd^{3+} ions on A-site bismuth ions, and Co^{2+} on B-site iron ions to improve magnetic and electric properties [3].

Polycrystalline ceramics of pure and doped BFT were prepared by conventional solid-state reaction (according to formulas: $Bi_{5-x}Y_xTi_3FeO_{15}$, $Bi_{5-x}Gd_xFeTi_3O_{15}$; x = 0.1, 0.2, 0.3 and $Bi_5Ti_3Fe_{1-y}Co_yO_{15}$, y = 0.1, 0.3, 0.5). Crystal structure, phase purity, and structural evaluation were investigated via X-ray diffraction, Rietveld refinement, and Raman spectroscopy. The size of unmodified BFT plate-like grains was approximately 3–5 µm in length and 0.5 µm in thickness. With Y, Gd, and Co incorporation, the grain size decreased while the size reduction was more pronounced for Co substitution than for the other two dopants. Ferroelectric measurements show unsaturated leaky hysteresis loops in all samples. However, the decrease of the leakage current by Y and Gd doping implies a decrease in electrical conductivity. On the other hand, this substitution at A-site is not capable of inducing any magnetic ordering while Co^{2+} substitution enhanced the magnetic response of BFT.

Finally, it can be proposed that the best multiferroic properties at room temperature can only be achieved by co-substitution with aliovalent transition-metal ions in the B-sites ions (Fe and Ti) of the perovskite block of Aurivillius structure.

[1] W. Eerenstein et al. *Nature*, 42 (2006) 17.

[2] A.Y. Birenbaum et al. *Phys. Rev.* B 95 (2017) 104419.

[3] J. Bobic et al. *Solid State Sci.* 123 (2022) 106802

Topics

- Functionalities in electroceramics (piezoelectric, ferroelectric, magnetic, conductivity)

Other Properties

Presentation Format:	Oral
Student Submission:	No
Submission ID:	57

New Phases of $BiFeO_3$ Perovkistes

Igor Popov[1], Maria Čebela[2], Dejan Zagorac[2], Bojan Stojadinović[3], Borislav Vasić[3]

(1) *Institute for Multidisciplinary Research, University of Belgrade, Kneza Višeslava 1, 11030 Belgrade, Serbia*

(2) *Institute of Nuclear Sciences Vinča, University of Belgrade, Mike Petrovića Alasa 12-14, 11351 Vinća, Belgrade, Serbia*

(3) *Institute of Physics, University of Belgrade, Pregrevica 118, 11080, Belgrade, Serbia*

***C*ontact:** E. FamilyName (autor@institution.edu)

Abstract. Bismuth ferrite ($BiFeO_3$) is a prominent multiferroic material, renowned for its simultaneous ferromagnetic and ferroelectric properties. This presentation delves into the theoretical exploration of novel crystalline phases in doped bismuth ferrite structures, specifically focusing on holmium- and silver-doped $BiFeO_3$. Utilizing density functional theory (DFT), we investigate the stability and electronic/magnetic characteristics of these new phases, revealing a diverse array of properties that could enhance their application potential in advanced electronic and spintronic devices.

In the second part of the presentation, we show experimental findings on the change in electric resistance of $BiFeO_3$ upon doping with terbium. Through detailed atomic-level analysis using density functional theory, we elucidate the physical mechanisms underlying this observed phenomenon. This dual approach combining theoretical predictions with experimental validation provides a comprehensive understanding of the structural and functional modifications induced by dopants in bismuth ferrite perovskites.

REFERENCES

[1] M. Čebela, et al. Phys. Chem. Chem. Phys. **25** (2023), 22345-22358.
[2] M. Čebela, et al. Ceram. Int. **43** (2017), 1256–1264.

ORCID: 0000-0002-2030-3530, 0000-0001-6120-6924, 0000-0002-3102-852X, 0000-0002-2711-8821, 0000-0002-1575-8004

MAR IVANIOS COLLEGE (AUTONOMOUS)

TRIVANDRUM, KERALA, INDIA

We cherish the privileged moments of your
Esteemed presence in our Campus......!

VERITAS VOS LIBERABIT
Estd. 1949

Effect of Na doping and substrates type on structure and properties of La1–xNaxMnO3 thin films

BOBIC, Jelena Dr. (Institute for Multidisciplinary Research)
RADOJKOVIC, Aleksandar Dr. (Institute for Multidisciplinary Research)
VUKMIROVIC, Jelena Dr. (Faculty of Technology, University of Novi Sad)
VIJATOVIC PETROVIC, Mirjana Dr. (Institute for Multidisciplinary Research)
STOJADINOVIC, Bojan Dr. (Institute of Physics, Belgrade University)
SRDIC, Vladimir Prof. Dr. (Faculty of Technology, University of Novi Sad)

Perovskite-type $LaMnO_3$ has been identified as a promising candidate for magnetic memory devices due to its unique opto-magnetoelectric properties. The structure of $LaMnO_3$ enables the substitution of La^{2+} and/or Mn^{3+} ions with various cations, allowing for straightforward manipulation of its opto-magnetoelectric properties. La-site doping with lower valence cations is of interest, as it leads to the presence of heterovalent manganese ions (Mn^{3+} and Mn^{4+}) to maintain charge neutrality. The so-called double exchange, i.e. electric charge transfer between Mn^{3+} and Mn^{4+} via oxygen anions, is responsible for the appearance of ferromagnetism, metallic conductivity, and colossal magnetoresistance.

In this study, we prepared polycrystalline and epitaxial thin films of $La_{1-x}Na_xMnO_3$ (x = 0; 0.05; 0.10; 0.15; 0.30) from acetate solution deposited by spin coating technique on various substrates (Si, Si/Pt and $SrTiO_3$ (001)). XRD, FE-SEM, AFM, and Raman spectroscopy analyzed the films' structure and properties. XRD analysis showed a slight shift in the peaks' positions towards high 2?, revealing the incorporation of Na ions (x?0.10) in the structure of $LaMnO_3$. Magnetic measurements confirmed the increase of the Neel temperature with Na substitutions and the decrease of magnetic polarizations. The structure and morphology of the films were examined and correlated with sheet resistance and magnetic properties, considering the type and thickness of the films.

Acknowledgement to the financial support of project program of the Science Fund of the Republic of Serbia (Gant no. 7383, Project - PROMTEH)

ID: 14432

2/11/25 1:54 PM

PhD Jelena Bobic
jelenabobic@yahoo.com
Belgrade University
Institute for Mulidisciplinary Research
Šumadijska 34
11030 Belgrade
Serbia

Upload a picture / photo of the presenter (optional)
Abstract_J.Bobic.docx

Declaration of consent (Submission)
Consent granted / Submitted and accepted short abstracts are published given the contact details in an abstract volume to all participants and interested parties.

Select the topic of your submission
S1 / Innovative ceramic syntheses, processing and shaping / Ceramic coatings / Porous ceramics

Submission
POSTER

УНИВЕРЗИТЕТ У БЕОГРАДУ
ИНСТИТУТ ЗА ФИЗИКУ | БЕОГРАД
ИНСТИТУТ ОД НАЦИОНАЛНОГ
ЗНАЧАЈА ЗА РЕПУБЛИКУ СРБИЈУ

ПОТВРДА О ОБАВЉЕНОЈ СТРУЧНОЈ ПРАКСИ

Назив правног лица у коме је студент обављао стручну праксу: Институт за физику у Београду, Институт од националног значаја за Републику Србију
Седиште и адреса: Улица Прегревица 118, Земун, Београд
Матични број: 07018029
ПИБ: 100105980
Контакт особа и телефон: Љубица Илић Војновић, 0606026004

УНИВЕРЗИТЕТ У БЕОГРАДУ
ИНСТИТУТ ЗА ФИЗИКУ | БЕОГРАД
ИНСТИТУТ ОД НАЦИОНАЛНОГ
ЗНАЧАЈА ЗА РЕПУБЛИКУ СРБИЈУ
www.ipb.ac.rs
Број 0801-2445/1
Датум 25-12-2024

Овим се потврђује да је студенткиња Факултета за физичку хемију, Универзитет у Београду, **Слађана Савић**, број индекса 2020/0013 обављала стручну праксу у Институту за физику у Београду у периоду новембар/децембар 2024. године.

Руководилац стручне праксе др Бојан Стојадиновић, виши научни сарадник Института за физику у Београду обучавао је горе наведену студенткињу у оквиру Лабораторије за наноструктуре, Центра за физику чврстог стања и нове материјале, у трајању од укупно 40 радних сати.

Назив и кратак опис истраживачке теме:
"**Моделовање температурних Раман спектра никл-кобалт ферита: анализа магнетних фазних прелаза**"
Истраживачка тема обухвата анализу температурне еволуције Раман спектра никл-кобалт ферита, материјала из групе мешаних ферита. Студенткиња је применом Лоренцијанских профила моделовала спектралне модове и пратила промене у температурном опсегу од течног азота до преко 600 K. Фокус је био на еволуцији Раман модова и структуралним и магнетним променама током фазних прелаза.

Опис послова које је студенткиња **Слађана Савић** обављала у оквиру стручне праксе:

- Пролазак кроз обуку за примену различитих метода синтезе материјала, као што су сол-гел и хидротермална синтеза, као и техника израде танких филмова методом spin-coating.
- Упознавање са основним концептима температурних ефеката на Раманове модове кроз теоријски и практични курс.
- Обрада температурних Раман спектра мешаних феритних структура, укључујући детаљну анализу, моделовање података и дискусију резултата у контексту температурних промена.

Током стручне праксе, **Слађана Савић** је показала изузетну ангажованост, професионализам и пажњу према детаљима. Њена способност да ефикасно примени теоријска знања у лабораторијском раду била је на високом нивоу. Слађана се посебно истакла у обради и анализи сложених температурних Раман спектра, уз јасно разумевање утицаја температуре на структуру и магнетна својства ферита. Њена иницијатива и тимски дух значајно су допринели успешној реализацији задатака.

Датум и место
25-12-2024

Потпис одговорног лица

УНИВЕРЗИТЕТ У БЕОГРАДУ
ИНСТИТУТ ЗА ФИЗИКУ | БЕОГРАД
ИНСТИТУТ ОД НАЦИОНАЛНОГ
ЗНАЧАЈА ЗА РЕПУБЛИКУ СРБИЈУ

ПОТВРДА О ОБАВЉЕНОЈ СТРУЧНОЈ ПРАКСИ

Назив правног лица у коме је студент обављао стручну праксу: Институт за физику у Београду, Институт од националног значаја за Републику Србију
Седиште и адреса: Улица Прегревица 118, Земун, Београд
Матични број: 07018029
ПИБ: 100105980
Контакт особа и телефон: Љубица Илић Војновић, 0606026004

Број 0801-2446/1
Датум 25-12-2024

Овим се потврђује да је студенткиња Факултета за физичку хемију, Универзитет у Београду, **Соња Молдован**, број индекса 2020/0006 обављала стручну праксу у Институту за физику у Београду у периоду новембар/децембар 2024. године.

Руководилац стручне праксе др Бојан Стојадиновић, виши научни сарадник Института за физику у Београду обучавао је горе наведену студенткињу у оквиру Лабораторије за наноструктуре, Центра за физику чврстог стања и нове материјале, у трајању од укупно 40 радних сати.

Назив и кратак опис истраживачке теме:
"**Раманова спектроскопија никл-кобалт ферита: температурни ефекти на магнетне модове**"
Студенткиња је током праксе обрађивала Раманове спектре никл-кобалт ферита, материјала који припада групи мешаних ферита са интересантним магнетним својствима. Њен задатак је био да примени Лоренцијанске профиле у моделовању спектралних модова, са циљем да анализира промене у спектрима у широком температурном опсегу - од температуре течног азота до преко 600 K. Посебан акценат стављен је на праћење еволуције модова током магнетног фазног прелаза, што је омогућило дубље разумевање температурног утицаја на структурална и магнетна својства ферита.
Опис послова које је студенткиња **Соња Молдован** обављала у оквиру стручне праксе:

- Учествовање у обуци за хемијске методе синтезе, укључујући сол-гел, хидротермалну синтезу и технику израде танких филмова (spin-coating).
- Походила кратак курс о анализи температурног утицаја на Раманове модове, са фокусом на померање спектралних позиција.
- Детаљна обрада температурних Раман спектра мешаних ферита, укључујући анализу и моделовање података коришћењем Лоренцијанских профила.

Соња Молдован се истакла својом посвећеношћу и способношћу брзог усвајања нових знања и техника. Током праксе, показала је висок степен прецизности у обради експерименталних података и посебну пажњу према детаљима. Њен ентузијазам и способност анализе сложених температурних ефеката на Раманове модове значајно су допринели успешности рада. Уз јаку радну етику и иницијативу, Соња је демонстрирала спремност за даље напредовање у истраживачком раду.

Датум и место
25-12-2024

Потпис одговорног лица

УНИВЕРЗИТЕТ У БЕОГРАДУ
ИНСТИТУТ ЗА ФИЗИКУ | БЕОГРАД
ИНСТИТУТ ОД НАЦИОНАЛНОГ
ЗНАЧАЈА ЗА РЕПУБЛИКУ СРБИЈУ
www.ipb.ac.rs
Број 0801-1066/1
Датум 12-06-2024

УНИВЕРЗИТЕТ У БЕОГРАДУ
ИНСТИТУТ ЗА ФИЗИКУ | БЕОГРАД
ИНСТИТУТ ОД НАЦИОНАЛНОГ
ЗНАЧАЈА ЗА РЕПУБЛИКУ СРБИЈУ

ПОТВРДА О ОБАВЉЕНОЈ СТРУЧНОЈ ПРАКСИ

Назив правног лица у коме је студент обављао стручну праксу: Институт за физику у Београду, Институт од националног значаја за Републику Србију
Седиште и адреса: Улица Прегревица 118, Земун, Београд
Матични број: 07018029
ПИБ: 100105980
Контакт особа и телефон: Љубица Илић Војновић, 0606026004

Овим се потврђује да је студент Факултета за физичку хемију, Универзитет у Београду, **Петар Марјановић**, број индекса 2020/0011 обављао стручну праксу у Институту за физику у Београду у периоду мај/јун 2024. године.

Руководилац стручне праксе др Бојан Стојадиновић, виши научни сарадник Института за физику у Београду обучавао је горе наведеног студента у оквиру Лабораторије за наноструктуре, Центра за физику чврстог стања и нове материјале, у трајању од укупно 40 радних сати.

Назив и кратак опис истраживачке теме:

"**Синтеза нанопрахова и танких филмова бизмут ферита: сол-гел, хидротермална и *spin-couting* метода**"
Истраживачка тема је фокусирана на развој и оптимизацију метода за синтезу бизмут ферита ($BiFeO_3$) у облику нанопрахова и танких филмова. Циљ је био применом сол-гел и хидротермалне методе произвести висококвалитетне нано-прахове бизмут ферита, а потом применити *spin-couting* технику за синтезу танких филмова.

Опис послова које је студент обављао у оквиру стручне праксе:

Студент **Петар Марјановић** је обављао следеће активности:

- Припрема реагенаса и раствора за сол-гел и хидротермалну синтезу нано-прахова бизмут ферита, као и за *spin-couting* технику за синтезу танких филмова.
- Праћење и оптимизација процеса синтезе.

Описна оцена рада и ангажованости студента приликом обављања стручне праксе:

Петар Марјановић је показао изузетну радну етику и ангажованост током целокупне стручне праксе. Његова способност да брзо усвоји нове методе и примени их у лабораторијском окружењу је била на високом нивоу. Петар је демонстрирао напредне вештине у лабораторијском раду, као и прецизност у извођењу експеримената и анализи резултата.

Датум и место
12-06-2024 БЕОГРАД

Потпис одговорног лица

Subject **Molba za recenziju predloga projekta sa Slovenijom**
From Prijava Slovenija
To bojan.stojadinovic@ipb.ac.rs
Date Tue 12:15

Poštovani gospodine Stojadinović,

Obraćam Vam se, na osnovu dobijenog predloga Matičnog naučnog odbora, sa molbom da recenzirate jedan predlog projekta. Naime, radi se o predlogu projekta koji je prijavljen na Konkursu za sufinansiranje naučno-tehnološke saradnje između Republike Srbije i Republike Slovenije za period 2025-2027.

U skladu sa navedenim, potrebno je da se recenzira zajednički predlog projekta:

	Oblast istraživanja	**Naslov projekta**	**Ključne reči**	**Institucija**	**Rukovodioc projekta**
130	Natural Sciences	Novel multiferroic composite fibers for improved magnetoelectric coupling	multiferroic, composites, electrospinning, magnetoelectrics	Vinča, Institute of Nuclear Sciences, National Institute of the Republic of Serbia	Marko Bošković

Ukoliko ste zainteresovani da uradite recenziju navedenog projekta (rok 30.09.2024.) molim Vas da potvrdite odgovorom na ovaj mejl.
Predlog projekta i formular za evaluaciju sa definisanim kriterijumima, poslaću Vam pošto potvrdite da li ste u mogućnosti da uradite recenziju projekta.
Obaveštavam Vas, takodje, da Ministarstvo ne plaća recenzije. Ukoliko su Vam potrebne dodatne informacije, mozete me kontaktirati.

Unapred Vam se zahvaljujemo i srdačno Vas pozdravljamo u ime Ministarstva nauke, tehnološkog razvoja i inovacija

Nada Milošević, kontakt telefon 011/3616 529

Нада Милошевић / Nada Milošević
саветник / *advisor*

Сектор за међународну сарадњу и европске интеграције / *Sector for International Cooperation and European Integration*
Министарство науке, технолошког развоја и иновација / *Ministry of Science, Technological Development and Innovation*

Tel: + 381 113616529
E-mail: nada.milosevic@nitra.gov.rs

Subject RE: [PAC] Article Review Completed
From Vladimir V. Srdic <srdicvv@uns.ac.rs>
To 'Dr. Bojan Stojadinovic' <bojans@ipb.ac.rs>
Date 2025-11-24 08:53

webmail

Dear Dr. Stojadinovic,

Thank you very much for the prepared review of the manuscript ID PAC-OJ-2157. I am sure that your comments and suggestions will be very helpful for the authors.

Best wishes
Vladimir V. Srdic, editor

-----Original Message-----
From: Dr. Bojan Stojadinovic [mailto:bojans@ipb.ac.rs]
Sent: Friday, November 21, 2025 11:12 AM
Cc: Vladimir Srdić
Subject: [PAC] Article Review Completed

Vladimir Srdić:

I have now completed my review of "Magnetic Properties of Er–Cr Co-doped Bismuth Ferrite Nanoparticles" for Processing and Application of Ceramics, and submitted my recommendation, "Revisions Required."

Dr. Bojan Stojadinovic
____
Processing and Application of Ceramics
http://ojs.tf.uns.ac.rs/index.php/pac

Subject **Thank you for the review of MLBLUE-D-24-03317**
From Junichi Hojo
Sender em.mlblue.31dc.8d90ff.1bfb729b@editorialmanager.com
To Bojan Stojadinović
Reply-To Junichi Hojo
Date Today 11:45

To protect your privacy, remote images are blocked in this message. Display images

Ref.: Ms. No. **MLBLUE-D-24-03317**
Enhanced magnetocaloric effect in nano-sized $Dy_3Ga_5O_{12}$ garnet: A comparative study on the effect of solid-state and wet-chemical synthesis
Materials Letters

Dear Dr. Bojan Stojadinović,

Thank you for reviewing the above referenced manuscript. I greatly appreciate your contribution and time, which not only assisted me in reaching my decision, but also enables the author(s) to disseminate their work at the highest possible quality. Without the dedication of reviewers like you, it would be impossible to manage an efficient peer review process and maintain the high standards necessary for a successful journal.

I hope that you will consider Materials Letters as a potential journal for your own submissions in the future.

You can access your review comments and the decision letter (when available) by logging onto the Editorial Manager site at:

https://www.editorialmanager.com/mlblue/

As a token of appreciation, we would like to provide you with a review recognition certificate on Elsevier Reviewer Hub (reviewerhub.elsevier.com). Through the Elsevier Reviewer Hub, you can also keep track of all your reviewing activities for this and other Elsevier journals on Editorial Manager.

If you have not yet activated your 30 day complimentary access to ScienceDirect and Scopus, you can still do so via the [Rewards] section of your profile in Reviewer Hub (reviewerhub.elsevier.com).
You can always claim your 30-day access period later, however, please be aware that the access link will expire six months after you have accepted to review.

Kind regards,

Professor Junichi Hojo
Editor
Materials Letters

#REV_MLBLUE#

To ensure this email reaches the intended recipient, please do not delete the above code

Subject	**Thank you for reviewing for Journal of Magnetism and Magnetic Materials**
From	Journal of Magnetism and Magnetic Materials <em@editorialmanager.com>
Sender	<em.magma.0.98e1ae.11c19781@editorialmanager.com>
To	"Bojan S." Stojadinović <bojans@ipb.ac.rs>
Reply-To	Journal of Magnetism and Magnetic Materials <support@elsevier.com>
Date	2026-01-19 10:55

Manuscript Number: **MAGMA-D-26-00009**

Structural, Elastic, Magnetic, and Dielectric Properties of Aluminum-Substituted Dysprosium Iron Garnet Nanoparticles

Samyak M. Bansode; Sagar E. Shirsath; Vaibhav D. Murumkar

Dear Stojadinović,

Thank you for reviewing the above referenced manuscript. I greatly appreciate your contribution and time, which not only assisted me in reaching my decision, but also enables the author(s) to disseminate their work at the highest possible quality. Without the dedication of reviewers like you, it would be impossible to manage an efficient peer review process and maintain the high standards necessary for a successful journal.

I hope that you will consider Journal of Magnetism and Magnetic Materials as a potential journal for your own submissions in the future.

As a token of appreciation, we would like to provide you with a review recognition certificate on Elsevier Reviewer Hub (reviewerhub.elsevier.com). Through the Elsevier Reviewer Hub, you can also keep track of all your reviewing activities for this and other Elsevier journals on Editorial Manager.

If you have not yet activated your 30 day complimentary access to ScienceDirect and Scopus, you can still do so via the [Rewards] section of your profile in Reviewer Hub (reviewerhub.elsevier.com).
You can always claim your 30-day access period later, however, please be aware that the access link will expire six months after you have accepted to review.

Kind regards,

Larissa Panina

Editor

Journal of Magnetism and Magnetic Materials

Have questions or need assistance?
For further assistance, please visit Elsevier Support Center for Reviewer Support. Here you can search for solutions on a range of topics, find answers to frequently asked questions, and learn more about Editorial Manager via interactive tutorials.
You can also talk to our customer support team 24/7 by live chat, email and phone.

#REV_MAGMA#

To ensure this email reaches the intended recipient, please do not delete the above code

---

Certificate

for Reviewer

---

presented to

Bojan Stojadinovic

has reviewed for *Applied Physics Letters, an AIP Publishing journal*

AIP Publishing

РЕПУБЛИКА СРБИЈА
ЗАВОД ЗА УНАПРЕЂИВАЊЕ
ОБРАЗОВАЊА И ВАСПИТАЊА
Број: 2145-3/2022
Датум: 23. новембар 2022. године
Београд, Фабрисова 10

На основу чл. 39, 40. и 41. Закона о основама система образовања и васпитања („Сл. гласник РС“, бр. 88/2017, 27/2018 - др. закон, 10/2019, 6/2020 и 129/2021), члана 6. став 5. Правилника о ближим условима и критеријумима за избор других стручних лица и чланова комисије за припрему стручне оцене квалитета рукописа и стручног мишљења („Сл. гласник РС“, бр. 94/2018), члана 40. Статута Завода за унапређивање образовања и васпитања, Допунског јавног позива од 7. новембра 2022. године, који је расписао Завод за унапређивање образовања и васпитања, записника и предлога Комисије о избору стручних лица број 2145-1/2022 од 9. новембра 2022. године, директор Завода доноси

ОДЛУКУ

о избору стручних лица за припрему стручне оцене квалитета рукописа уџбеника и стручног мишљења о квалитету рукописа приручника, додатних наставних средстава, дидактичких средстава и дидактичких игровних средстава

I

На основу Допунског јавног позива утврђује се листа и врши избор стручних лица за припрему стручне оцене квалитета рукописа уџбеника и стручног мишљења о квалитету рукописа приручника, додатних наставних средстава, дидактичких средстава и дидактичких игровних средстава.

Листа лица која испуњавају услове конкурса (прихватају/усвајају се пријаве, потпуно или делимично):

Ред. бр.	Име	Презиме	Академски/стручни назив	Укупно бодова
1.	Гордана	Петровић	професор географије	35.00
2.	Мира	Јовановић	доктор педагошких наука	31.17
3.	Предраг	Кузмановић	доктор наука-физичке науке	24.72
4.	Нела	Дујић	мастер васпитач	22.27
5.	Даница	Веселинов	доктор наука методике разредне наставе	19.41
6.	Марија	Чоловић Савић	дипломирани педагог	17.60
7.	Ајсела	Хаџиахметовић	дипломирани инжењер информационих технологија, мастер професор технике и информатике за електронско учење	17.56

8.	Весна	Јосиповић	васпитач у предшколским установама	17.21
9.	Неда	Вулићевић	дипломирани географ	16.34
10.	Вукашин	Дедовић	доктор историје	15.76
11.	Оливера	Дишић	васпитач у предшколским установама	15.12
12.	Ивана	Ђорђевић	мастер географ	13.49
13.	Александра	Марцикић	струковни мастер васпитач	13.06
14.	Драгана	Стојадиновић-Рудњанин	мастер васпитач	12.93
15.	Александра	Куч	дипломирани математичар, педагошки саветник	11.87
16.	Далиборка	Живковић	мастер васпитач	10.62
17.	Бојан	Стојадиновић	научни сарадник	9.21
18.	Иван	Петронијевић	доктор наука - физичке науке	8.87
19.	Јелена	Селак	специјалиста струковни васпитач	8.86
20.	Татјана	Шуковић	специјалиста методике наставе руског језика	7.97
21.	Марија	Филиповић	дипломирани музичар - педагог	7.03
22.	Мирко	Ђорђевић	научни сарадник (доктор биолошких наука)	6.68
23.	Марко	Николић	дипломирани географ	6.68
24.	Славољуб	Митић	дипломирани физичар	5.87
25.	Душан	Ђорђевић	мастер биолог	5.27
26.	Александра	Петровић	специјалиста струковни васпитач	4.50
27.	Марија	Вељић	дипломирани професор италијанског језика и књижевности	4.50
28.	Јелена	Тришић Стајић	дипломирани педагог	3.77
29.	Јелена	Ђонић	професор италијанског језика и књижевности	3.04
30.	Горан	Боканић	мастер професор информатике и технике	2.78
31.	Снежана	Миловановић	професор биологије	2.78
32.	Зоран	Шикања	мастер професор језика и књижевности	2.56
33.	Снежана	Замуровић	магистар техничких наука	2.27
34.	Милијана	Ардељан Бошков	професор немачког језика и књижевности	2.05
35.	Марија	Старчевић	дипломирани педагог	2.01
36.	Биљана	Шарановић	просветни саветник	1.79
37.	Маријана	Бугарски	професор техничког образовања и машинства	1.79
38.	Јелена	Живковић	професор италијанског језика и књижевности	1.50
39.	Марија	Младеновић	мастер професор информатике и математике	1.50
40.	Весна	Милићевић	дипломирани географ	1.50
41.	Милан	Николић	мастер професор технике и информатике	1.03
42.	Катарина	Матић	мастер педагог	1.03

43.	Саша	Јовановић	дипломирани физичар за Примењену физику - мастер	0.77
44.	Јелена	Бига	професор технике и информатике	0.77
45.	Марина	Грујичић	дипломирани математичар за теоријску математику и примене	0.51
46.	Мирјана	Никлановић	доктор наука-методика наставе	0.51
47.	Ана	Живковић	дипломирани математичар	0.26
48.	Ивана	Булајић	дипломирани географ	0.26
49.	Данијела	Ивовић	дипломирани математичар	0.26
50.	Сања	Лакић	дипломирани математичар	0.26
51.	Јасмина	Месарић	специјалиста струковни васпитач за методику реализације припремног предшколског програма	0.26
52.	Јелена	Жикелић	васпитач у предшколсским установама	0.26
53.	Мирјана	Аничић	дипломирани историчар	0.00
54.	Јелица	Стојчић	професор немачког језика и књижевности	0.00
55.	Александра	Поповић	доктор уметности - Ликовне уметност	0.00
56.	Невена	Пешић	професор техничког образовања	0.00
57.	Ангелина	Јеротијевић Марковић	мастер професор физике	0.00
58.	Предраг	Цветић	професор техничког образовања	0.00
59.	Неда	Јокановић	дипломирани инжењер електротехнике и рачунарства	0.00
60.	Марија	Гаћиновић	дипломирани математичар - математика финансија	0.00
61.	Ирена	Симић	професор француског језика и књижевности	0.00
62.	Ивица	Шантић	магистар географије	0.00
63.	Нада	Андоноски Полексић	дипломирани музички педагог	0.00
64.	Ђорђе	Чолић	дипломирани математичар-информатичар	0.00
65.	Жаклина	Коругић	дипломирани математичар - математика финансија	0.00
66.	Љиљана	Митровић	мастер васпитач	0.00
67.	Маја	Ковачевић	стручни сарадник педагог	0.00
68.	Марина	Станковић	струковни васпитач	0.00
69.	Јелена	Дубљевић	дипломирани васпитач	0.00
70.	Снежана	Аврамовић	дипломирани инжењер организације за информационе системе	0.00
71.	Јасмина	Ракић	професор информатике	0.00
72.	Драгица	Божиловић	дипломирани васпитач	0.00
73.	Гордан	Станојевић	дипломирани физичар за општу физику	0.00
74.	Сузана	Стоичков Стојанов	мастер професор технике и информатике	0.00
75.	Ивана	Стојиљковић	мастер васпитач	0.00

76.	Александра	Вуковић	дипломирани математичар	0.00
77.	Јованка	Сврчкота	мастер математичар	0.00
78.	Наташа	Мајстровић	професор информатике	0.00

I I

Пријаве се одбијају делимично, јер лица немају одговарајуће високо образовање за одређени предмет, односно стручну област:

Ред. бр.	Име	Презиме	Академски/стручни назив	Пријава се одбације за следеће предмете:
1.	Душан	Ђорђевић	мастер биолог	Математика, Историја, Географија, Информатика и рачунарство, Рачунарство и информатика, Техника и технологија, Физика, Музичка култура, Ликовна култура
2.	Бојан	Стојадиновић	научни сарадник	Математика
3.	Иван	Петронијевић	доктор наука - физичке науке	Информатика и рачунарство, Рачунарство и информатика, Техника и технологија

I I I

Пријаве се одбијају потпуно, јер лица немају одговарајуће високо образовање за пријављени предмет, односно стручну област:

Редни број	Име	Презиме	Академски/стручни назив
1.	Раде	Савић	магистар техничких наука-усмерење Технологија материјала и М.Сц. Аерокосмотехнике
2.	Александар	Алексић	професор физичке културе
3.	Тијана	Милисављевић	професор разредне наставе, мастер дефектолог логопед
4.	Гордана	Вујадиновић	дипломирани инжењер технологије

IV

Одбацују се као непотпуне пријаве следећих стручних лица пријављених на Допунски јавни позив, јер иста нису доставила потребну документацију:

Редни број	Име	Презиме	Академски/стручни назив	Недостаје
1.	Биљана	Николић	наставник предшколског васпитања	потврда о стажу
2.	Јелена	Живковић	дипломирани географ	диплома

3.	Марина	Марјановић	дипломирани географ	изјава о сукобу интереса
4.	Биљана	Глишовић	васпитач у предшколским установама	попуњен и потписан образац пријаве на јавни позив
5.	Гордана	Ђорђевић	дипломирани педагог, специјалиста управљања пројектима	потврда о стажу

V

Одбија се пријава стручног лица приспела у Завод за унапређивање образовања и васпитања на основу Допунског јавног позива, јер пријављена не испуњава услов који се односи на стаж у образовању:

Редни број	Име	Презиме	Академски/стручни назив
1.	Рада	Тадић	мастер педагог

VI

Одбија се пријава стручног лица приспела у Завод за унапређивање образовања и васпитања на основу Допунског јавног позива, јер је увидом у приложену документацију утврђено да је лице у сукобу интереса на основу члана 27. Закона о уџбеницима („Сл. гласник РС“, бр. 27/2018):

Редни број	Име	Презиме	Академски/стручни назив
1.	Аца	Манић	дипл. инж. електротехнике

VII

Стручна лица из тачке I ове Одлуке бирају се на неодређено време, односно, док испуњавају услове прописане законом и Правилником о ближим условима и критеријумима за избор других стручних лица и чланова комисије за припрему стручне оцене квалитета рукописа и стручног мишљења („Сл. гласник РС“, бр. 94/2018).

VIII

Ову Одлуку објавити на званичној интернет страници Завода за унапређивање васпитања и образовања.

IX

Ова Одлука је коначна и ступа на снагу даном објављивања.

Образложење

Правилником о ближим условима и критеријумима за избор других стручних лица и чланова комисије за припрему стручне оцене квалитета рукописа и стручног мишљења („Сл. гласник РС“, бр. 94/2018), одређен је поступак за избор стручних лица за припрему стручне оцене квалитета рукописа уџбеника и стручног мишљења о квалитету рукописа приручника, додатних наставних средстава, дидактичких средстава и дидактичких игровних средстава. Директор Завода за унапређивање образовања и васпитања, је надлежан за доношење такве одлуке, све у складу са чл. 39, 40, и 41. Закона о основама система образовања и васпитања („Сл. гласник РС“, бр. 88/2017, 27/2018 - др. закон, 10/2019, 6/2020 и 129/2021). Завод је расписао Допунски јавни позив, сагласно члану 2. Правилника о ближим условима и критеријумима за избор других стручних лица и чланова комисије за припрему стручне оцене квалитета рукописа и стручног мишљења, дана 7. 11. 2022. године, који је објављен на интернет страници Завода за унапређивање образовања и васпитања.

На Допунски јавни позив који је расписао Завод, пријавило се **89** (словима: осамдесет девет) заинтересованих лица. На основу члана 6. Правилника о ближим условима и критеријумима за избор других стручних лица и чланова комисије за припрему стручне оцене квалитета рукописа и стручног мишљења („Сл. гласник РС“ бр. 94/2018), образована је Комисија решењем директора Завода број 2145-1/2022 од 9. новембра 2022. године. Комисија је размотрила приспеле пријаве, извршила бодовање/рангирање кандидата, сачинила записник и упутила предлог о избору стручних лица директору Завода. Изабрана стручна лица испуњавају услове из члана 3. Правилника.

На основу сачињеног записника Комисије и предлога за избор стручних лица а у складу са надлежношћу из члана 40. Статута Завода за унапређивање образовања и васпитања, одлучено је као у диспозитиву.

Упутство о правном средству: против ове одлуке може се поднети тужба Управном суду у року од 30 дана од дана објављивања исте на званичној интернет страници Завода.

ДИРЕКТОР

Др Златко Грушановић

Изјава руководиоца пројекта о руковођењу радним задатком

Овим потврђујем да др Бојан Стојадиновић на пројекту билатералне сарадње Србија-Индија Министарства просвете, науке и технолошког развоја, “Примена мултифероичних наноструктура на бази перовскита у заштити од електромагнетних сметњи (ЕМС) и фотоволтаичним (ФВ) апликацијама“ (451-02-697/2022-09/02), руководи радним задатком који се односи на синтезу бизмут ферита и мерењима и анализом Рамановиx спектара.

Новица Пауновић

Руководилац пројекта
Др Новица Пауновић
Виши научни сарадник